STUDIES OF PHASE BEHAVIOR AND HOST-GUEST BINDING IN AQUEOUS SYSTEMS CONTAINING MACROMOLECULES

by

Viviana Cecília Pereira da Costa

Licenciatura in Chemical Engineering, 2005
University of Coimbra, Coimbra, Portugal

Master in Chemical Engineering, 2009
University of Coimbra, Coimbra, Portugal

Submitted to the Graduate Faculty of the
College of Science and Engineering
Texas Christian University
in partial fulfillment of the requirements
for the degree of

Doctor of Philosophy

December, 2015

STUDIES OF PHASE BEHAVIOR AND HOST-GUEST BINDING IN AQUEOUS SYSTEMS CONTAINING MACROMOLECULES

by

Viviana Cecília Pereira da Costa

Dissertation Approved:

Major Professor

Benjamin George Janesko

Kayla N. Green

For The College of Science and Engineering

Author’s Declaration

This is an original work, except where references have been made. No part of this work has been previously submitted as part of a requirement for an academic degree.

Part of this dissertation appeared in the following publications:

1) da Costa, V. C. P; Annunziata, O. Phys. Chem. Chem. Phys., 2015, 17, 28818–28829.

2) da Costa, V. C. P; Hwang, B. J.; Eggen, S. E.; Wallace, M. J.; Annunziata, O. J. Chem. Thermodynamics 2014, 75, 119-127.

ACKNOWLEDGEMENTS

I would like to acknowledge and to thank all the people that directly or indirectly contributed to my Ph.D. dissertation.

I would like to express my deepest gratitude to my research advisor, Dr. Onofrio Annunziata for his constant patience and support during these past five years. Under his guidance, I acquired new knowledge in physical chemistry and I learned how to be a better researcher, chemist and person.

I want to thank the members of my committee: Dr. Kayla Green, Dr. Benjamin Janesko and Dr. Sergei Dzyuba for all the support, encouragement and invaluable time they have given me during these past five years.

I would also like to say thank you to the people in the Chemistry Department at TCU that help me along the way, especially Page Kimbrell, Carolyn Banwart, David Yale and Gerry Katchinska. To Gerry I have to say I am truly grateful for all your help and availability for fixing equipment in our lab.

To my friends Michele, Henry and Paulina I want to say thank you for always being there for me and letting me share this Ph.D. life with you. To Philip, thank you for making this last few years brighter and easier. To Ana, thank you for always being part of my life no matter the distance. I would also like to thank all my other friends and colleagues at TCU specially Nelli, Jhansi and Mirza for the help with SEM.

Aos meus pais e irmã, obrigada por todo o apoio e por sempre acreditarem em mim. Sem vocês nada disto seria possível.

Finally, I would like to thank TCU for the financial support.

TABLE OF CONTENTS

PART I: LIQUID-LIQUID PHASE TRANSITION OF POLY(AMIDO AMINE) DENDRIMERS IN AQUEOUS SOLUTIONS 1

Chapter 1: Background 2

- 1.1. Introduction 3
- 1.2. Dendrimers 5
  - 1.2.1. PAMAM Dendrimers 7
  - 1.2.2. PAMAM in aqueous solutions 9
- 1.3. Chemical Crosslinking of Macromolecules 10
- 1.4. Thermodynamics of Solutions and liquid-liquid phase transition 13
- 1.5. Phase Behavior of Globular Particles 18
- 1.6. Effect of Salting-Out Agents on Globular Macromolecules Solutions 23

Chapter 2: Materials and Experimental Techniques 29

- 2.1. Materials 30
- 2.2. Solutions Preparation 30
- 2.3. Experimental Techniques 32
  - 2.3.1. Measurements of LLPS Temperature 32
  - 2.3.2. Measurements of Dendrimer-Salt Partitioning at 25 °C 33
    - *Spectrophotometric assay* 35
    - *Potentiometric assay* 36
  - 2.3.3. Dynamic Light Scattering, DLS 36
    - *Dynamic Light Scattering Apparatus* 43
  - 2.3.4. Isothermal Titration Calorimetry, ITC 46

2.3.5. Scanning Electron Microscopy, SEM 52
2.4. Phenol Blue Binding Assay. 53
2.5. Crosslinking experiments 54
2.6. Host-Guest Experiments for Crosslinked PAMAM-NH_2 55
Chapter 3: Unusual Liquid-Liquid Phase Transition of PAMAM-OH in Aqueous Mixtures 57
3.1. Introduction 58
3.2. Effect of Salt Concentration on LLPS Temperature 59
3.3. Salt-Dendrimer partitioning. 62
3.4. PAMAM-OH Dendrimer Diffusion Coefficient 64
3.5. Dendrimer-dye binding 66
3.6. Thermodynamic model 68
3.7. Excess internal energy 72
3.8. Binodal Curve for PAMAM-OH System 76
3.9. LLPS Thermal behavior 80
3.10. Theoretical details on the Thermodynamic Model 83
3.11. Conclusions 92
Chapter 4: Formation of Dendrimer Globular Nanoparticles from Oligomerization Induced LLPS 94
4.1. Introduction 95
4.2. Effect of Salt Concentration on LLPS Temperature 97
4.3. Sodium Sulfate – PAMAM-NH_2 Partitioning in Aqueous Solutions 98
4.4. Effect of crosslinker concentration on LLPS temperature 102

4.5. Formation of dendrimer globular particles 104

4.6. Guest encapsulation of crosslinked dendrimer materials................................ 109

4.7. Experimental characterization by ITC and DLS 110

4.7.1. ITC Experiment for PAMAM-NH_2 system 110

4.7.2. DLS Experiments for PAMAM-NH_2 112

4.8. Conclusions 115

Chapter 5: Summary 116

Part II: FORMATION AND THERMODYNAMIC STABILITY OF HOST-GUEST POLYMER-PORPHYRIN SUPRAMOLECULAR ASSEMBLIES 119

Chapter 6: Background 120

6.1. Introduction 121

6.2. Spectroscopic Properties of Porphyrins 124

6.3. Porphyrin Aggregation.. 130

6.4. Meso-tetrakis(4-sulfonatophenyl) porphyrin (TPPS) 132

6.5. Polymer 134

6.6. Binding Models.. 134

Chapter 7: Materials and Experimental Techniques 141

7.1. Materials 142

7.2. Solution Preparation.. 142

7.3. Isothermal Titration Calorimetry 143

7.4. Absorption Spectra... 144

Chapter 8: Formation and Thermodynamic Stability of (PVP+TPPS) Supramolecular Structures in Aqueous Solutions at pH 7.0 145

8.1. Introduction 146

8.2. TPPS self-association 147

8.3. PVP-TPPS Supramolecular Structures 155

8.4. Absorption Spectra 162

8.5. Conclusions 169

Chapter 9: Effect of PVP on TPPS Spectrophotometric Properties in Acidic Conditions 170

9.1. Introduction 171

9.2. TPPS Spectrophotometric Properties at low pH in the presence of PVP 171

9.3. Effect of pH on the PVP-TPPS binding affinity 177

9.4. Conclusions 180

Chapter 10: Summary 182

References 185

Appendices 199

Appendix A 200

Appendix B: Experimental Data for Chapter 3 201

Appendix C: Experimental Data for Chapter 4 207

Vita

Abstract

LIST OF FIGURES

Figure 1. Schematic diagram representing the architecture of a dendrimer generation. 7

Figure 2. Dendrimers, proteins and virus 8

Figure 3. Glutaraldehyde structure. 10

Figure 4. Summary of possible forms of glutaraldehyde in aqueous solution 11

Figure 5. Proposed mechanism for protein crosslinking by glutaraldehyde 12

Figure 6. Typical chemical potential plot as a function of particle volume fraction. 18

Figure 7. Hofmeister series for anions. 24

Figure 8. Two domain model. 26

Figure 9. Scheme for the turbidity meter apparatus 33

Figure 10. Scheme of the dynamic light scattering apparatus. 44

Figure 11. Schematic of an ITC instrument. 47

Figure 12. (A) Sample displacement inside the sample cell and (B) limiting cases 50

Figure 13. (A) Phenol blue absorption at 646.5 nm as a function of ϕ_D at $C_\mathrm{S} = 0$ M (B) Phenol blue absorption at 646.5 nm as a function of C_S at $\phi_\mathrm{D} = 0$. 54

Figure 14. Normalized-transmitted-intensity profile corresponding to a sample at (A) low salt concentration and (B) high salt concentration. 60

Figure 15. T_ph as a function of salt concentration at several constant dendrimer molar fractions 61

Figure 16. Normalized-transmitted-intensity profile observed for the dendrimer-salt-water system at $C_\mathrm{S} = 0.51 \mathrm{mol \cdot dm^{-3}}$ and $\phi_\mathrm{D} = 0.20$ 62

Figure 17. Plots of $(\phi_\mathrm{D}^{(\mathrm{I})}+\phi_\mathrm{D}^{(\mathrm{II})})/2$ as a function of $|\phi_\mathrm{D}^{(\mathrm{II})}-\phi_\mathrm{D}^{(\mathrm{I})}|^{1/\beta}$ 64

Figure 18. Plots of $(\Delta C_\mathrm{S}/\Delta\phi_\mathrm{D})$ as a function of $|\phi_\mathrm{D}^{(\mathrm{II})}-\phi_\mathrm{D}^{(\mathrm{I})}|^{1/\beta}$ 64

Figure 19. Normalized DLS diffusion coefficient as a function of PAMAM-OH dendrimer volume fraction... 66

Figure 20. Absorbance of phenol blue as a function of salt concentration, C_S, at $\phi_\mathrm{D}=0.020$ 67

Figure 21. Scheme describing the dilution process from the dendrimer volume fraction, occurring inside the ITC cell.. 72

Figure 22. Representative ITC Power-time profile associated with consecutive injections of titrant solution into the titrand solution inside the ITC cell................................. 73

Figure 23. Differential heat, q, extracted from the shown power-time profile as function of dendrimer volume fraction inside the ITC cell... 73

Figure 24. Reduced excess internal energy, ω_D, as a function of ϕ_D^0. 76

Figure 25. Binodal data, ϕ_D as a function of C_S, for the dendrimer-salt-water system at 25 ºC. The solid curve is the theoretical binodal with $q=0.35$. 78

Figure 26. Calculated relative binodal curves, $\phi_\mathrm{D}-\phi_\mathrm{D}^{(\mathrm{R})}$, as a function of C_S. 82

Figure 27. Scheme of equilibrium dialysis with two compartments separated by a membrane.. 84

Figure 28. T_ph as a function of salt concentration at several constant dendrimer molar fractions.. 97

Figure 29. Plots of $(\phi_\mathrm{D}^{(\mathrm{I})}+\phi_\mathrm{D}^{(\mathrm{II})})/2$ as a function of $|\phi_\mathrm{D}^{(\mathrm{II})}-\phi_\mathrm{D}^{(\mathrm{I})}|^{1/\beta}$. 99

Figure 30. Binodal data, ϕ_D as a function of C_S, for the dendrimer-salt-water system. 100

Figure 31. LLPS temperature as a function of crosslinker-to-dendrimer molar ratio. ... 103

Figure 32. Normalized light-scattering intensity, i_S, as a function of hydrodynamic radius, R_h, at constant dendrimer volume fraction, sodium sulfate concentration, and four representative crosslinker-to-dendrimer molar ratios, C_{CL} / C_D (A-D)........... 106

Figure 33. Scanning electron micrographs showing dendrimer nanospheres................ 107

Figure 34. Normalized light-scattering intensity, i_S, as a function of hydrodynamic radius, R_h, at 25 °C and constant dendrimer volume fraction, sodium chloride concentration and four representative crosslinker-to-dendrimer molar ratios........ 108

Figure 35. Partition equilibrium of phenol blue... 109

Figure 36. (A) ITC Power-time profile associated with consecutive injections of titrant solution into the titrand solution inside the ITC cell at 25.0 °C. (B) ITC Power-time profile associated with injections with $k \geq 13$. (C) Differential heat, q, extracted from the shown power-time profile as function of dendrimer volume fraction inside the ITC cell, after each injection.. 111

Figure 37. Normalized DLS diffusion coefficient as a function of PAMAM-NH_2 dendrimer volume fraction... 114

Figure 38. Basic structure of the porphyrin.. 121

Figure 39. Schematic representation of the Jablonski diagram.................................... 123

Figure 40. Structures of (A) free base porphine (B) diacid porphine and (C) metalloporphine.. 125

Figure 41. Energy diagram for the (A) four-orbital model and (B) electronic states of DAP or MP. 127

Figure 42. Energy diagram for the (A) four-orbital model and (B) electronic states of FBP. 129

Figure 43. Energy diagram for (A) H-aggregates and (B) J-aggregates. 132

Figure 44. Acid-base equilibrium for TPPS. 133

Figure 45. Structure of polyvinyl pyrrolidone (PVP). 134

Figure 46. Dimerization process. 139

Figure 47. (A) Representative plot of power as a function of time for the titration at 25 °C. (B) Differential heat associated with consecutive injections of titrant solution into the titrand solution as a function of TPPS concentration. 149

Figure 48. Van't Hoff plot for the TPPS dimer dissociation constant as a function of temperature. The inset shows the standard dissociation enthalpy for TPPS dimers as a function of temperature. 150

Figure 49. (A) Representative plot of power as a function of time for the titration at 25 °C. (B) Differential heat associated with consecutive injections of titrant solution into the titrand solution as a function of the PVP to TPPS concentration ratio. 157

Figure 50. Van't Hoff plot for the PVP-TPPS dissociation constant as a function of temperature. The inset shows the standard dissociation enthalpy for PVP-TPPS complexes as a function of temperature 161

Figure 51. Normalized absorption spectra showing the four *Q* bands of TPPS in sodium phosphate buffer (A) Spectra obtained at several TPPS concentrations, C_L in the absence of PVP. The effect of C_L on $\varepsilon$is described by the graphs on the right side

showing the ratio, $\varepsilon/\varepsilon_1$, as a function of C_L (B, C, D) Spectra obtained at several PVP concentrations, C_P, for three constant TPPS concentrations. The effect of the molar ratio, C_P/C_L, on ε is described by the corresponding graphs on the right side showing the ratio, $\varepsilon/\varepsilon_0$, as a function of C_P/C_L 166

Figure 52. Limiting normalized absorption spectra for TPPS in the monomeric, dimeric and bound states. 167

Figure 53. Normalized absorption spectra showing the Soret band for TPPS at C_L= 23 μM for several PVP concentrations. 168

Figure 54. Normalized absorption spectra showing the four Q bands of TPPS and in (A)-(C) acetate buffer for three constant TPPS concentrations and (D)-(F) sodium citrate buffer for three constant TPPS concentrations. 172

Figure 55. Normalized absorption spectra showing the Q bands for TPPS (A) pH 7.0, pH 4.5 and pH 3.0 in the absence of PVP and (B) pH 7.0, pH 4.5 and pH 3.0 in excess of PVP. 175

Figure 56. Normalized absorption spectra showing the Soret band for TPPS in (A) acetate buffer and (B) sodium citrate buffer. 176

Figure 57. Normalized extinction coefficient at 642 nm, $\varepsilon / \varepsilon_0$, of TPPS in acetate buffer, as a function of C_P / C_L for three constant TPPS concentrations. 177

Figure 58. Normalized extinction coefficient at 642 nm, $\varepsilon / \varepsilon_0$, of TPPS in sodium citrate buffer as a function of C_P / C_L for three constant TPPS concentrations................. 178

Figure 59. Number of porphyrin molecules bound per polymer, ν, as a function of free ligand concentration. 180

LIST OF TABLES

Table 1. Salt-Dendrimer partitioning parameters at 25 °C. 63

Table 2. DLS parameters for PAMAM-OH. 66

Table 3. ITC parameters at 25 °C. 76

Table 4. DLS parameters for the analysis of k_D 92

Table 5. Salt-Dendrimer partitioning parameters at 25 °C. 99

Table 6. Values of q for PAMAM-NH_2 and PAMAM-OH at different temperatures.... 102

Table 7. DLS parameters for PAMAM-NH_2. 113

Table 8. Thermodynamic parameters associated with TPPS dimerization..................... 151

Table 9. Thermodynamic parameters associated with PVP + TPPS binding. 159

Table 10. Fractions of DAP, MAP and FBP.. 174

PART I

LIQUID-LIQUID PHASE TRANSITION OF POLY(AMIDO AMINE) DENDRIMERS IN AQUEOUS SOLUTIONS

Chapter 1: Background

1.1. Introduction

Liquid-liquid phase separation (LLPS) in macromolecular solutions is a type of phase transition. In LLPS, a change of conditions such as temperature causes an initially homogenous solution of macromolecules (*e.g.* proteins, polymers) or colloid particles (*e.g.* inorganic, polymer nanoparticles) to reversibly form two separate coexisting liquid phases: a macromolecule-rich phase and macromolecule poor-phase[1–10]. This phenomenon is of great interest in the fields of thermodynamics of liquid mixtures[5,11], materials science[12–15], separation science[16,17], catalysis[18,19] and medicine[2,20–24]. In the case of protein solutions, LLPS has been implicated in diseases such as cataract[2,3,24] and sickle cell anemia[21–23,25].

With respect to separation science, LLPS finds applications in the purification and concentration of macromolecules solutions[10,26–29]. For example, protein purification can be achieved by using the two-phase partitioning method. In this method, additives (e.g. salts or polymers) are added to the protein aqueous solution to induce phase separation. After phase separation, a protein concentrated phase (up to 50% w/w in water) is formed, which can be easily separated from the other phase enriched in impurities and additives.

LLPS finds also applications in homogeneous catalysis[18,19]. Specifically, a catalyst can be separated from the reaction product and recycled by inducing LLPS of the initially homogenous reaction media[18]. Typically, LLPS is reversibly induced by either increasing or lowering the temperature of the system[18]. For example, the catalyst and the substrate are initially dissolved in the reaction medium at high temperature. After the reaction is carried out, the temperature is lowered to induce the formation of two phases that contain the product and the catalyst, respectively. These reaction media are typically formulated by adding two solvents with partial miscibility.

LLPS often occurs through the reversible formation of spherical liquid droplets rich in macromolecules (coacervates[12]). Since these droplets are highly viscous, with a gel-like behavior, a chemical crosslinker can be then added to the suspension so that the macromolecules within a droplet can be covalently bound to each other[12,30–34]. Thus, the coupling of LLPS with crosslinking gives rise to the formation of microspheres. These find applications as therapeutic and diagnostic agents in the field of medicine[12]. Furthermore, in the case of enzymes, the obtained product (crosslinked enzyme aggregates, CLEAs) show improved conformational stability and finds applications as catalyst in non-aqueous media[33].

In the polymer field, LLPS can be used for production of porous hydrogels by adding a crosslinker to a polymer solution after inducing the formation of solvent-rich droplets[12]. LLPS has been also used to produce complex materials consisting of two interconnected bicontinuous phases through a kinetic process known as spinodal decomposition[12,32].

For globular particles (*e.g.* proteins, colloidal suspensions), it has been shown that LLPS is metastable with respect to crystallization[35–38]. Thus, LLPS has been used as a kinetic pathway for the formation of crystals. In the case of proteins, LLPS is also a kinetic pathway for the formation of fibers, aggregates and gels[35]. Thus, this phase transition has been related to diseases such as cataracts[3,24] and sickle cell anemia[21,23,25].

Solutions of globular macromolecules that possess LLPS in their phase diagram will also exhibit strong local heterogeneities even in the one-phase region of the diagram[39]. Specifically, it has been shown that macromolecules form transient nanoclusters reminiscent of the macromolecular-rich droplets that occur during the LLPS process[39–41]. Moreover, these nanoclusters are also believed to be intermediates for the formation of other condensed phases such as crystals and aggregates[39–41].

Although LLPS has been studied for many proteins[2,3,24,36,42] and synthetic polymers[11,43–52], to date, there is no reported experimental investigation for dendrimers. As it will be discussed in Section 1.2, there is a strong overlap between the applications of LLPS and those of dendrimers. One goal of this dissertation, is to investigate LLPS for two well-known poly(amido amine) (PAMAM) dendrimers. Since chemical crosslinking is often combined to LLPS for drug delivery and catalytic applications, the effects of coupling this phase transition with dendrimer crosslinking will be also explored. Chemical crosslinking will be reviewed in Section 1.3.

1.2. Dendrimers

Dendrimers, from the Greek "*dendron*" meaning "tree" and "*meros*' meaning "part", are an interesting class of hyperbranched polymers with considerable differences from classical random coils[53–55]. These hyperbranched macromolecules have a highly controlled symmetrical tree-like structure[53–55] resulting in unique structural and chemical properties that find applications as nanoreactors[56–59], chemical sensors[60,56], extracting agents[61] and drug delivery[62–65].

The dendrimer structure consists of a multifunctional central core, to which branching units are sequentially added. As a result, the structure of a dendrimer molecule can be divided in three main components[65,66] (Figure 1): (1) the core, which consists of an initiator core and interior shells (generations) composed of repeating units radially attached to the initiator, where the generation (G) is defined as the number of branching points when going radially from the core towards the surface; (2) the outer shell beneath the dendrimer surface; and (3) the multivalent surface which contains a high number of functional groups. The initiator core can have different multiplicities (4 in Figure 1), which will eventually determine the number of branches in the dendrimer. The dendrimer core possesses a unique microenvironment composition with interesting physicochemical properties (e.g. polarity) that may be different from those of the outer shell and/or dendrimer surroundings[54,55,66]. Furthermore, the dendrimer tree-like structure also gives rise to the formation of internal cavities or, in other words, they have an interior volume of solvent-filled void space[55,66,67]. Thus, the dendrimer core is well-suited for encapsulation of guest molecules, such as drugs[64,65]. Furthermore, the high number of functional groups (either non-reactive or reactive) situated on the outer shell and surface of the dendrimer also play an important role, for example, in host-guest interactions and catalysis[55,65,66]. Overall, all parts of the dendrimer can be tailored for the desired purposes resulting in the wide range of applications.

Vögtle and co-workers, in 1978, were the first to report and describe the synthesis of this type of macromolecules[55]. Yet, dendrimers only received a wide-spread attention in 1985, when Tomalia's group published the synthesis of poly(amidoamine) (PAMAM) dendrimers[68].

In contrast to polymers, the preparation techniques and the properties of dendrimers are unique and involve synthesis under well-controlled conditions giving rise to monodisperse and well-defined branched structures[53,55]. Dendrimers can be synthesized using various strategies, with the divergent and convergent methods being the most common[53,55,66]. The divergent method consists of a stepwise procedure where the dendrimer is grown from a multifunctional central core molecule to whose monomers (building blocks) are sequentially attached[53,55,66]. The alternative convergent approach consists of first creating individual dendritic segments (dendrons) and then coupled to a multifunctional central core molecule[53,55,66].

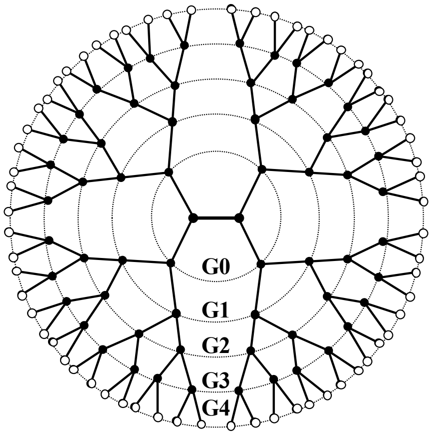

Figure 1. Schematic diagram qualitatively representing the architecture of a dendrimer generation (G) 4 with tetrafunctional core. The space confined by a dashed circle describes a given dendrimer generation and the number associated with each circle is the generation number. The closed circles represent branching units and the open circles correspond to the surface functional group. The full lines correspond to the spacer functional group. Note that the white area inside the dendrimer corresponds to the dendrimer cavities.

1.2.1. PAMAM Dendrimers

The dendrimers chosen in this work are two poly(amido amine) dendrimers (PAMAM) of forth generation (G4) with a hydroxyl-functionalized surface (PAMAM-OH) and amino-functionalized surface (PAMAM-NH_2) (see Figure A.1 in Appendix A). Several generations (1≤G≤10) of both dendrimers are commercially available. The original synthesis[68] was done through a divergent method using ethylenediamine (EDA) or ammonia (multiplicity of 4 and 3, respectively) as the initiator core and repeating units derived from N-(2-aminoethyl) acrylamide. The repeating units were sequentially constructed by alternating two reactions: (1) Michael addition of an acrylate ester to the amine functionality of the initiator core; and (2) coupling the resulting ester moieties with an alkylene diamine (e.g. ethylene diamine) through amidation to create a new amino-terminated functionality.

The relative efficacy and low cost of synthesis of PAMAM as well as the possibility to readily modify their peripheral amine groups to the desired functionality (*e.g.* solubility, biocompatibility/immunogenicity) has made this type of dendrimers to be extensively used in catalysis, drug delivery and as template for metal nanoclusters synthesis[53,55,69,70]. Furthermore, PAMAM dendrimers are also often referred to as protein mimics due to their globular structure, comparable molecular-weight range and hydrodynamic behavior[70]. For example, size and shape similarities between PAMAM dendrimers of different generations and some well-known proteins[70] and even a small virus[71] have been drawn (Figure 2). One interesting application of dendrimers as protein biomimics is to use the functional groups on the surface of to mimic protein behavior in solution and to study protein-protein interactions[70].

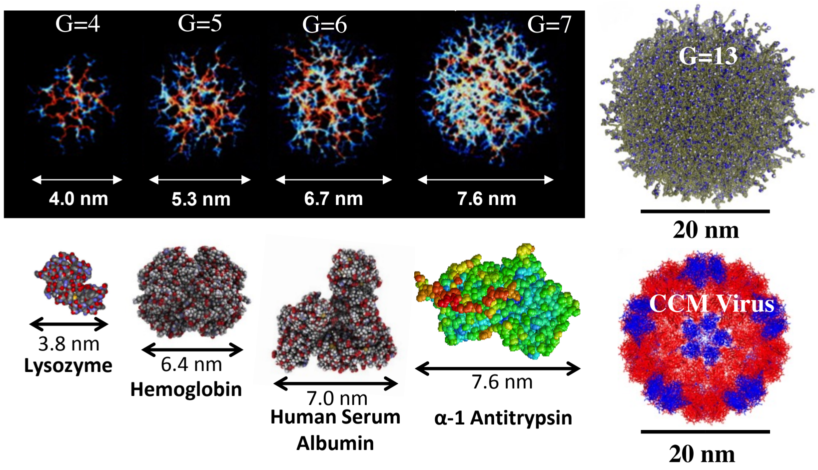

Figure 2. Dendrimers, proteins and virus [Adapted from[70,71]].

1.2.2. PAMAM in aqueous solutions

The behavior of dendrimers in aqueous solutions, including that of PAMAMs, in aqueous solutions has been studied mostly with respect to their size and conformation in solution[67,72–76]. In these studies, it was observed that the dendrimer surface density of terminal groups increases with generation and, consequently, high-generation dendrimers (G≥7) show a pronounced back folding of these groups due to steric hindrance[67]. This results in an increase of dendrimer conformational rigidity and a corresponding decrease of cavity volume. On the other hand, low-dendrimer generations (G=1–3) are generally open and, consequently, do not possess well-defined cavities[67]. Thus, intermediate-generation dendrimers (G=4–6) are usually the most suitable for host-guest applications[55,67]. Furthermore, their flexibility can lead to significant conformational changes due to external stimuli[72,73,75–79]. This aspect is important for applications such as environment-sensitive host-guest binding and chemical sensing. Clearly, it becomes important to identify approaches that would circumvent the loss of cavity volume for high-G dendrimers and will lead to the preparation of dendrimer materials that retain the advantages of both high- and low-G dendrimers. One approach is the preparation of nanoclusters of low-G dendrimers.

Regarding dendrimer conformation, several theoretical[75–77,79] and experimental[72,73,80] studies have demonstrated that flexible dendrimers can undergo conformational changes due to external stimuli such as pH, ionic strength and solvent polarity. For instance, Welch and Muthukumar theoretically showed that a significant change in the conformational state of a charged dendrimer (G=5) occurs as the ionic strength of the solvent increases[75]. Specifically, at high ionic strength, they observed backfolding of the end groups resulting in dense-core compact structure. On the other hand, the dendrimer exhibits a more open conformation at low ionic strength[75].

In relation to phase transitions, there are a few studies on thermoresponsive dendrimers, which report temperature-induced dendrimer aggregation in aqueous solutions[81–86]. The aggregation is induced by *ad hoc* modifications of the dendrimer structure by either incorporating well-known thermo-responsive groups[81,82,86,87] or by an appropriate balance of hydrophilic and hydrophobic moieties[84]. In relation to LLPS, there are a few theoretical studies[88–90]. However, to our knowledge, there are no experimental reports.

1.3. Chemical Crosslinking of Macromolecules

Glutaraldehyde is a crosslinking agent widely use in the fields of pharmaceutical sciences, biomedical technology, enzyme technology and microscopy[91]. This crosslinking agent has a high reactivity towards proteins and certain polymers and it can effectively crosslink these macromolecules in aqueous solutions over a wide pH range (≥ 3) without significantly affecting the macromolecule structure[91].

Glutaraldehyde is a linear 5-carbon dialdehyde (see Figure 3) very soluble in water. It is usually commercially available as an acidic aqueous solution (pH 3.0-4.0, 2% to 70% w/v).

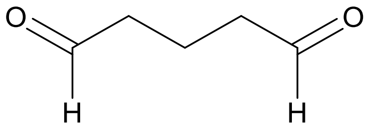

Figure 3. Glutaraldehyde structure.

Glutaraldehyde reactivity increases with pH and it rapidly reacts with macromolecule primary and secondary amino groups, but it can also react with other functional groups such as thiol, phenol and hydroxyl groups[91].

Despite the widely use of glutaraldehyde, its crosslinking chemistry is still quite controversial mainly because of the complexity of its behavior in aqueous solution and reactivity[91]. In fact, the glutaraldehyde structure in aqueous solution is not limited to the monomeric form, depending on the pH of the solution. In Figure 4, we show several possible structures for glutaraldehyde[91]. For instance, we can observe that glutaraldehyde can also exist has α-β-unsaturated aldehydes which can undergo spontaneous polymerization (*e.g.* dimer, trimer or polymer) and are able to form various structures. In acidic conditions, glutaraldehyde can also exist as a mixture of hydrated forms.

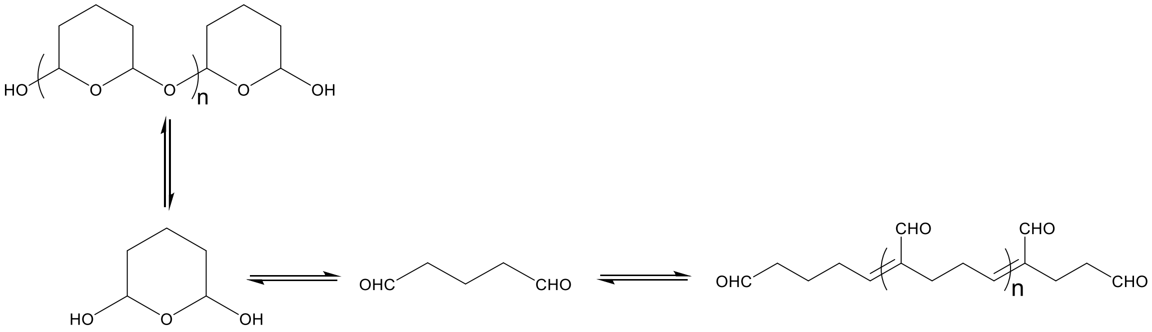

Figure 4. Summary of possible forms of glutaraldehyde in aqueous solution.

Glutaraldehyde has been widely used to crosslinking enzymes and other proteins through a reaction between α,β-unsaturated aldehydes and amino groups on the protein surface[13,91]. Monsan *et al.* proposed a mechanism of addition on the aldehydic part of the α,β-unsaturated aldehydes, which gives a Schiff base stabilized by conjugation (see Figure 5 A scheme 1)[91,92]. Richards and Knowles proposed a slightly different mechanism of addition to ethylenic double bonds (see Figure 5 A scheme 2)[91,92]. However, Hardy *et al.* and Lubig *et al.* proposed a different mechanism in which two glutaraldehyde monomers react with two protein molecules to form a pyridinium compound (see Figure 5 B)[91,92]. Therefore, the mechanism of protein cross-linking by glutaraldehyde is complicated and still not well understood. Indeed, it is possible that several reaction mechanisms are simultaneously present during crosslinking[91,92]. Reactions between glutaraldehyde and amine groups form robust cross-linking linkages and generate chromophores absorbing light in the visible range[91]. They also have a strong UV absorbance at 260-280 nm.

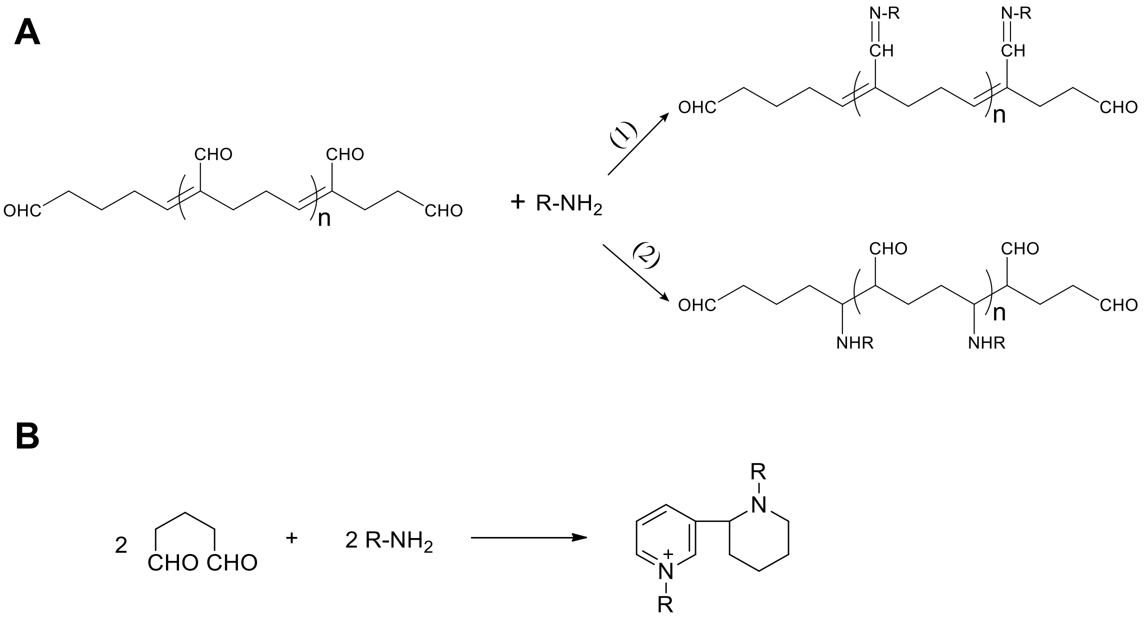

Figure 5. Representative examples of protein crosslinking by glutaraldehyde [Adapted from[91]].

Regardless of the mechanistic details glutaraldehyde is an efficient crosslinking agent for a dendrimer with primary amino groups as its surface functionalities (*e.g.* PAMAM-NH$_2$). Interestingly, there are no reports on the reactions of glutaraldehyde with dendrimers to our knowledge. Therefore, the studies on protein crosslinking represent our main guide for designing experiments involving dendrimer crosslinking.

1.4. Thermodynamics of Solutions and liquid-liquid phase transition

In order to understand and control LLPS of macromolecule aqueous solutions and to develop new strategies to optimize the applications outlined in Section 1.1, it is necessary to examine these complex mixtures from a thermodynamic point of view. Furthermore, in many cases, the binary macromolecule-water system does not undergo LLPS. Here, additives such as salts are added in order to induce and modulate this phase transition. Thus, it becomes particularly important to develop thermodynamic models that allow us to predict the effect of additives on the topology of the LLPS boundary in the phase diagram.

Mixing of solutions and their phase transitions are processes that occur or are examined at constant temperature and pressure[93–95]. These processes can be described by examining the behavior of the Gibbs free energy, G as a function of the composition of the liquid mixture. However, for many solutions of macromolecules or colloidal particles, the total volume of the system is not appreciably changing during phase transitions[94,95]. Thus, the Helmholtz free energy, F, becomes an appealing thermodynamic function to describe these nearly isochoric processes. Here, we will focus on the behavior of F. The fundamental equation for F, for an open system, is as follows[93]:

$$dF = -SdT - pdV + \sum_i \mu_i dn_i \tag{1. 1}$$

where S is the entropy, T is the temperature, p is the pressure, V is the total volume of the system, μ_i is the chemical potential of component i and n_i is the molar number of component *i*. The chemical potential μ_i is defined as[93]:

$$\mu_i = \left(\frac{\partial F}{\partial n_i}\right)_{T,V,n_{j,j\neq i}} = \left(\frac{\partial G}{\partial n_i}\right)_{T,P,n_{j,j\neq i}} \tag{1. 2}$$

It will be now shown that, when the system is not undergoing a change in volume, the thermodynamics of a binary liquid mixture can be equivalently described as that of a one-component in the gas phase[94,95].

We start by considering the change in Helmholtz free energy (see Eq. (1. 1)) at constant *T* and *p*, for our binary two component open system, solute particles (P) + solvent molecules (W)[94,95]:

$$dF = -pdV + \mu_{\mathrm{P}} dn_{\mathrm{P}} + \mu_W dn_{\mathrm{W}} \tag{1. 3}$$

We now write the following differential for V:

$$dV = V_{\mathrm{P}} dn_{\mathrm{P}} + V_{\mathrm{W}} dn_{\mathrm{W}} \tag{1. 4}$$

where V_i is the molar volume of the component i ($i = \mathrm{P}$ and W). Note that V_i is assumed to be constant and independent of composition, consistent with the assumption of fluid incompressibility[94,95]. If we multiply Eq. (1. 4) by the factor $\mu_{\mathrm{W}} / V_{\mathrm{W}}$ and then subtract the resulting equation to Eq. (1. 3), we obtain:

$$dF = -\left(p - \frac{\mu_{\mathrm{W}}}{V_{\mathrm{W}}}\right) dV + \left(\mu_{\mathrm{P}} - \mu_{\mathrm{W}} \frac{V_{\mathrm{P}}}{V_{\mathrm{W}}}\right) dn_{\mathrm{P}} \tag{1. 5}$$

As a reference case, we consider that of a pure solvent system with molar volume $\bar{V}_{\mathrm{W}}$ occupying the same total volume V. From Eq. (1. 5) it follows that the corresponding free energy is:

$$dF^{*} = -\left(p - \mu_{\mathrm{W}}^{*} / V_{\mathrm{W}}\right) dV \tag{1. 6}$$

where μ_{W}^{*} is the chemical potential of pure solvent. By subtracting Eq. (1. 5) from Eq. (1. 6) we obtain:

$$d\tilde{F} = -\left(\frac{\mu_{\mathrm{W}}^{*} - \mu_{\mathrm{W}}}{\bar{V}_{\mathrm{W}}}\right) dV + \tilde{\mu}_{\mathrm{P}} dn_{\mathrm{P}} \tag{1. 7}$$

where $\tilde{\mu}_{\mathrm{P}} \equiv \mu_{\mathrm{P}} - \mu_{\mathrm{W}}(V_{\mathrm{P}} / V_{\mathrm{W}})$. Here, the difference $\tilde{F} \equiv F - F^{*}$ is the change in the free energy when a given amount of solvent molecules is replaced by the same volumetric amount of solute particles at constant T and V [94,95].

The term $(\mu_{\mathrm{W}}^{*} - \mu_{\mathrm{W}}) / V_{\mathrm{W}}$ in Eq. (1. 7) is the osmotic pressure Π [93–95]. Therefore, we can rewrite Eq. (1. 7) as:

$$d\tilde{F} = -\Pi dV + \tilde{\mu}_{\mathrm{P}} dn_{\mathrm{P}} \tag{1. 8}$$

According to Eq. (1. 1), Eq. (1. 8) describes a one-component compressible gas system, with chemical potential $\tilde{\mu}_{\mathrm{P}}$, and pressure Π [94,95].

In conclusion, a binary incompressible system can be equivalently treated as a compressible fluid consisting of one effective component with pressure Π and chemical potential $\tilde{\mu}_{\mathrm{P}}$. Furthermore, the liquid-liquid phase transition of a binary liquid mixture can be equivalently treated as the gas-liquid phase transition (condensation) of a one-component gas system.

The particles of our effective one-component gas system can undergo condensation (*i.e.* the liquid-liquid phase separation of the binary solution) when the osmotic pressure is not an increasing function of the particle concentration in all concentration domain[5,9,93,96,97]. At equilibrium, it is possible to determine the composition of the two coexisting phases (I and II) by solving the chemical (Eq. (1. 9)) and the mechanical equilibrium (Eq. (1. 10)) conditions at any given T [93,95,97]:

$$\tilde{\mu}_{\mathrm{P}}(\phi_{\mathrm{P}}^{(\mathrm{I})}) = \tilde{\mu}_{\mathrm{P}}(\phi_{\mathrm{P}}^{(\mathrm{II})}) \tag{1. 9}$$

$$\Pi(\phi_{\mathrm{P}}^{(\mathrm{I})}) = \Pi(\phi_{\mathrm{P}}^{(\mathrm{II})}) \tag{1. 10}$$

where the volume fraction is defined as $\phi_{\mathrm{P}} = n_{\mathrm{P}}\bar{V}_{\mathrm{P}} / V$ and the superscripts (I) and (II) denote phase I and II, respectively.

Note that we can describe the mechanical equilibrium condition on a $\tilde{\mu}_{\mathrm{P}}(\phi_{\mathrm{P}})$ diagram using Maxwell equal-area rule equation[93,97]:

$$\left(\phi_{\mathrm{P}}^{(\mathrm{II})} - \phi_{\mathrm{P}}^{(\mathrm{I})}\right) \cdot \tilde{\mu}_{\mathrm{P}}(\phi_{\mathrm{P}}^{(\mathrm{I})}) = \int_{\phi_{\mathrm{P}}^{(\mathrm{I})}}^{\phi_{\mathrm{P}}^{(\mathrm{II})}} \tilde{\mu}_{\mathrm{P}}(\phi_{\mathrm{P}}) d\phi_{\mathrm{P}} \tag{1. 11}$$

The phase boundary for LLPS can be constructed by solving Eq. (1. 9) and (1. 10) with respect to $\phi_{\mathrm{P}}^{(\mathrm{I})}$ and $\phi_{\mathrm{P}}^{(\mathrm{II})}$ at various temperatures[11,93,97]. In Figure 6, we show a typical plot of $\tilde{\mu}_{\mathrm{P}}$ as a function of ϕ_{P} (Figure 6A) and several curves obtained at several temperatures (Figure 6B). In Figure 6A it can be seen that $\tilde{\mu}_{\mathrm{P}}$ significantly increases with ϕ_{P} at low concentrations due to the ideal-gas contribution ($\ln\phi_{\mathrm{P}}$). However, as the concentration increases, ϕ_{P} passes trough a maximum (b) and then a minimum (c) due to particle-particle attractive interactions; note that the fulfillment of the chemical equilibrium condition implies that there are two values of ϕ_{P} for which $\tilde{\mu}_{\mathrm{P}}$ is the same. In Figure 6A the points (a) and (d) satisfy the mechanical condition (see Eq. (1. 11)); between these points any hypothetical solution with a composition within this range will undergo LLPS. The points (b) and (c) define the domain in which $\left(\partial\tilde{\mu}_{\mathrm{P}} / \partial\phi_{\mathrm{P}}\right)_T < 0$. Between a-b and c-d the solution is metastable with respect to phase separation. In these conditions, the separation is occurs through a nucleation process. Here, the new phase grows as spherical droplets in order to minimize surface tension effects. Note that the region between the points (b) and (c) is thermodynamically unstable ($\left(\partial\tilde{\mu}_{\mathrm{P}} / \partial\phi_{\mathrm{P}}\right)_T < 0$) and points (b) and (c) define the spinodal boundary[93,97]. In Figure 6B, several representative $\tilde{\mu}_{\mathrm{P}}$ curves are shown at different T. The top curve, which corresponds to the highest temperature, has one horizontal inflection point that defines the critical point. At the critical point the composition of the system is $\phi_{\mathrm{P}}^{\mathrm{c}}$ and T^{c} . This point can be obtained by applying the conditions $(\partial\tilde{\mu}_{\mathrm{P}} / \partial\phi_{\mathrm{P}})_{\phi_{\mathrm{P}}^{\mathrm{c}},T^{\mathrm{c}}} = 0$ and $(\partial^2\tilde{\mu}_{\mathrm{P}} / \partial{\phi_{\mathrm{P}}}^2)_{\phi_{\mathrm{P}}^{\mathrm{c}},T^{\mathrm{c}}} = 0$. At $T > T^{\mathrm{c}}$ the chemical potential curves are monotonically increasing with concentration. In this T domain the system remains homogeneous stable at any ϕ_{P}. For the chemical potential curves calculated at $T < T^{\mathrm{c}}$ the immiscibility gap where LLPS occurs is defined by the solid circles. Furthermore, there is a region within the immiscibility gap for which $(\partial\tilde{\mu}_{\mathrm{P}} / \partial\phi_{\mathrm{P}})_T < 0$. This region is thermodynamically unstable and is delimited by the spinodal boundary $(\partial\tilde{\mu}_{\mathrm{P}} / \partial\phi_{\mathrm{P}})_T = 0$.

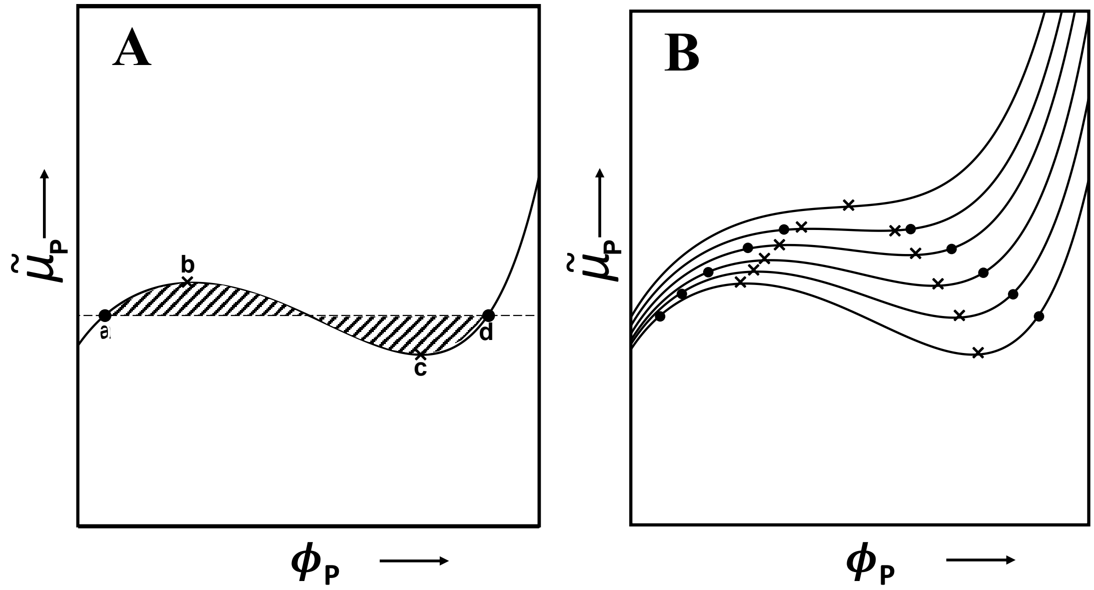

Figure 6. Typical chemical potential plot as a function of particle volume fraction at (A) constant temperature and (B) as a function of temperature (each curve is obtained at a different temperature). In (A) we show the Maxwell equal-area rule to describe phase equilibrium. In (B) the circle points denote the LLPS boundary points and the crosses denote the points that belong to the spinodal boundary. [Adapted from[97]].

1.5. Phase Behavior of Globular Particles

We will now discuss an important thermodynamic model for globular particles. As discussed in section 1.4, the expression of the chemical potential and the pressure are needed to characterize the phase behavior of the one-component gas system as a function of particle volume fraction, $\tilde{\mu}_P(\phi_P)$, at a temperature T.

It is convenient to start from the general equation of state of a gas system[96]:

$$\frac{V_P\Pi}{k_BT} = \phi_P\left[1 + b\cdot\phi_P\right] \tag{1. 12}$$

where the first term in the square brackets is the ideal-gas contribution, while b is a function of ϕ_{P} and T in general ($b(\phi_{\mathrm{P}},T)$) and it describes deviation from ideality. The expression for the chemical potential can be derived from Eq. (1. 12) in the following way.

The starting point is to split the effective chemical potential into an ideal contribution, $\tilde{\mu}_{\mathrm{P}}^{\mathrm{id}}$, and an excess term, $\tilde{\mu}_{\mathrm{P}}^{\mathrm{ex}}$:

$$\tilde{\mu}_{\mathrm{P}} = \tilde{\mu}_{\mathrm{P}}^{\mathrm{id}} + \tilde{\mu}_{\mathrm{P}}^{\mathrm{ex}} \tag{1. 13}$$

From statistical thermodynamics[9,96], an expression for the ideal chemical potential for a system with a number of particles, N_{P}, can be derived from the classical canonical partition function, $Q_{\mathrm{P}}^{\mathrm{id}}$, using the following relationship:

$$\frac{\tilde{\mu}_{\mathrm{P}}^{\mathrm{id}}}{k_B T} = -\left(\frac{\partial \ln Q_{\mathrm{P}}^{\mathrm{id}}}{\partial N_{\mathrm{P}}}\right)_{T,N_{\mathrm{P}}} \tag{1. 14}$$

where $Q_{\mathrm{P}}^{\mathrm{id}} = \frac{1}{N_{\mathrm{P}}!}\left(\frac{V}{\Lambda_{\mathrm{P}}{}^{3}}\right)^{N_{\mathrm{P}}}$ and Λ is the De Broglie wavelength[93].We have ignored internal-motion contributions (e.g. vibrational and electronic motion) because they are normally not affected by the liquid-liquid phase transition[5,96].

From Eq. (1. 14) and using the Stirling's approximation[93] we obtain:

$$\frac{\tilde{\mu}_{\mathrm{P}}^{\mathrm{id}}}{k_B T} = \ln\left(\frac{\Lambda_{\mathrm{P}}{}^{3}}{V_{\mathrm{P}}}\right) + \ln \phi_{\mathrm{P}} \tag{1. 15}$$

From the Gibbs-Duhem relation[93], we can relate the effective chemical potential to the osmotic pressure:

$$\left(\frac{\partial\tilde{\mu}_{\mathrm{P}}}{\partial\phi_{\mathrm{P}}}\right)_T=\frac{V_{\mathrm{P}}}{\phi_{\mathrm{P}}}\left(\frac{\partial\Pi}{\partial\phi_{\mathrm{P}}}\right)_T \tag{1. 16}$$

Eq. (1. 16) can be also applied to ideal chemical potential contribution alone:

$$\left(\frac{\partial\tilde{\mu}_{\mathrm{P}}^{\mathrm{id}}}{\partial\phi_{\mathrm{P}}}\right)_T=\frac{V_{\mathrm{P}}}{\phi_{\mathrm{P}}}\left(\frac{\partial\Pi^{\mathrm{id}}}{\partial\phi_{\mathrm{P}}}\right)_T=\frac{k_BT}{\phi_{\mathrm{P}}} \tag{1. 17}$$

Using Eqs. (1. 16) and (1. 17), we can deduce that $\tilde{\mu}_{\mathrm{P}}^{\mathrm{ex}}$ (see eq. (1. 13)) is given by:

$$\frac{1}{k_BT}\left(\frac{\partial\tilde{\mu}_{\mathrm{P}}^{\mathrm{ex}}}{\partial\phi_{\mathrm{P}}}\right)_T=\frac{1}{\phi_{\mathrm{P}}}\left[\left(\frac{\partial(V_{\mathrm{P}}\Pi/k_BT)}{\partial\phi_{\mathrm{P}}}\right)_T-1\right] \tag{1. 18}$$

We can now rewrite Eq. (1. 18) using (1. 12) and obtain:

$$\frac{\tilde{\mu}_{\mathrm{P}}^{\mathrm{ex}}}{k_BT}=\tilde{b}+b\cdot\phi_{\mathrm{P}} \tag{1. 19}$$

with $\tilde{b}\equiv\int_0^{\phi_{\mathrm{P}}}b(x,T)\,dx$.

Using Eq. (1. 19), we can rewrite Eq. (1. 13) and obtain an expression for the chemical potential:

$$\frac{\tilde{\mu}_{\mathrm{P}}}{k_{\mathrm{B}}T}=\ln\left(\frac{\Lambda_{\mathrm{P}}{}^3}{V_{\mathrm{P}}}\right)+\ln\phi_{\mathrm{P}}+\tilde{b}+b\cdot\phi_{\mathrm{P}} \tag{1. 20}$$

In this expression the first two terms represent the ideal part and the last two are corrections for taking into account non-ideality.

An important reference model for globular particles is the hard-sphere model[96]. This is described by the following pairwise potential energy, $u(r)$, expression:

$$u(r)=\begin{cases}+\infty, \text{ for } 0\le r<\sigma\\ 0, \text{ for } r\ge\sigma\end{cases} \tag{1. 21}$$

where σ is the diameter of the spheres and r is the particle-particle distance. Note that $u(r<\sigma)=+\infty$ in Eq. (1. 21) implies that there is no overlapping between hard spheres. For this system, Carnahan and Starling[5,96,98] showed that

$$b(\phi_P)=\frac{4-2\phi_P}{(1-\phi_P)^3} \tag{1. 22}$$

and $\tilde{b}=[(4-3\phi_P)/(1-\phi_P)^2]\phi_P$ independent of temperature.

Eq. (1. 22) was deduced from the virial expansion of the pressure:

$$\frac{V_P\Pi}{k_BT}=\phi_P\left[1+\left(\sum_{m=1}B_{m+1}\phi_P{}^{m-1}\right)\cdot\phi_P\right] \tag{1. 23}$$

where the coefficients B_{m+1} are the virial coefficients[96,98]. The first term on Eq. (1. 23) represents ideal-gas behavior and it is valid at low ϕ_P. At increasing volume fractions, the particle-particle steric interactions also increase and deviation from ideality is expressed through the virial coefficients, B_{m+1}. The second virial coefficient, B_2, describes the interaction energy for isolated particle pairs, while the third virial coefficient, B_3, describes three-body solvent-mediated interactions and so on. For hard-spheres, we can analytically obtain the exact values of B_2, B_3 and B_4 (*e.g.* $B_2=4$). For the determination of the values of B_5 and higher order coefficients, numerical calculations based on the Monte Carlo method are needed. All these calculations have shown that, to a good approximation, virial coefficients can be represented by the relation $B_{m+1}=(m^2+3m)$. The substitution of this result into Eq. (1. 23) leads to Eq. (1. 22).

Using Eq. (1. 22) we can rewrite Eq. (1. 20) and obtain the result for the effective chemical potential of a hard-sphere in a “gas-fluid” with particle volume fraction ϕ_P:

$$\frac{\tilde{\mu}_\mathrm{P}}{k_\mathrm{B}T}=\ln\left(\frac{{\Lambda_\mathrm{P}}^3}{V_\mathrm{P}}\right)+\ln\phi_\mathrm{P}+\frac{(8-9\phi_\mathrm{P}+3{\phi_\mathrm{P}}^2)\phi_\mathrm{P}}{(1-\phi_\mathrm{P})^3} \tag{1. 24}$$

The hard-sphere model contains only an entropic steric term due to particle-particle steric repulsion. Thus, this model does not show the liquid-gas phase transition, since it does not contain an energy term describing particle-particle attraction. In order to introduce this ingredient, we should consider a potential-energy expression that contains an attractive well around the particle. An example of this type of potential energy expressions is given by the square-well potential[95,96]:

$$u(r)=\begin{cases}+\infty,\ \text{for } 0\le r\le\sigma\\ -\varepsilon,\ \text{for } \sigma\le r\le\lambda\sigma\\ 0,\ \text{for } r\ge\lambda\sigma\end{cases} \tag{1. 25}$$

where $\varepsilon>0$ characterizes the depth of the well (magnitude of interaction) and $\lambda>1$ range of the interaction. According to statistical thermodynamics, the excess internal energy[96] of the system, U^ex, is related to $u(r)$ by:

$$U^\mathrm{ex}=\frac{{N_\mathrm{P}}^2}{2V}\int_0^\infty(4\pi r^2)g(r)u(r)dr \tag{1. 26}$$

where $g(r)$ is the radial distribution function, with $g(r<\sigma)=0$ and $g(\infty)=1$. This function, which also depends on ϕ_P and T, describes the probability to find a particle at a distance r away from a reference particle. The chemical potential is then obtained by using[96]:

$$\tilde{\mu}=\tilde{\mu}_\mathrm{HS}+T\left(\frac{\partial}{\partial N}\int_0^{T^{-1}}U^\mathrm{ex}\,dT^{-1}\right)_{T,V} \tag{1. 27}$$

In the van-der-Waals approximation, $g(r)$ is assumed to be equal to one when $r \geq \sigma$, independent of ϕ_{P} and T[96]. Thus, Eq. (1. 26) becomes:

$$U^{\mathrm{ex}} = -aN\phi_{\mathrm{P}} \tag{1. 28}$$

where $a \equiv -\frac{1}{2V_{\mathrm{P}}}\int_{\sigma}^{\infty}(4\pi r^2)u(r)dr$ is the van-der-Waals constant. In the case of a square-well potential, $a \equiv 4\varepsilon(\lambda^3 - 1)$. If we insert Eq. (1. 28) in Eq. (1. 27), we obtain:

$$\tilde{\mu}_{\mathrm{P}} = \tilde{\mu}_{\mathrm{P,\,HS}} - 2a\phi_{\mathrm{P}} \tag{1. 29}$$

Using the Gibbs-Duhem relation and Eq. (1. 29) we can also determine the osmotic pressure of the system:

$$\Pi = \Pi_{\mathrm{HS}} - \frac{a{\phi_{\mathrm{P}}}^2}{V_{\mathrm{P}}} \tag{1. 30}$$

Eqs. (1. 29) and (1.30) can be used to calculate the phase behavior of a system of hard spheres by solving the coexistence equilibrium equations for phase I in equilibrium with phase II (see Eqs. (1. 9) and (1. 10)) and Figure 6.

1.6. Effect of Salting-Out Agents on Globular Macromolecules Solutions

The effect of salting-out agents on macromolecule aqueous solutions has been extensively studied, especially in the case of proteins and polymers[48,52,99–108]. It has been shown that salting-out anions favor the compact states of hydrophilic macromolecules and promote their precipitation from aqueous solution[100,101]. On the other hand, salting-in anions favor expanded conformational states of these macromolecules (*e.g.* unfolding for proteins) and increase their solubility[100,101]. Typically, the effectiveness of anions in precipitating macromolecules according to their salting-out strength follows the Hofmeister series (Figure 7)[99–101].

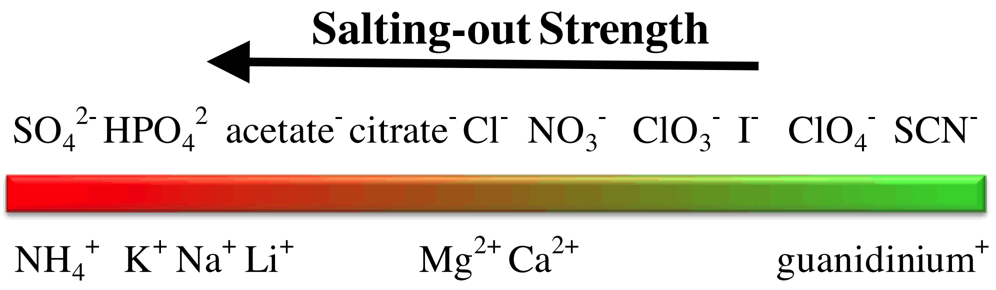

Figure 7. Hofmeister series for anions.

According to this series, the sulfate anion, SO_4^{2-}, has the highest salting-out strength while the thiocyanate anion, SCN^-, exhibits strong salting-in effects. Chloride, Cl^-, is often considered to have minor salting-in effects and it is the midpoint in the series. Cations such as Na^+ and K^+ display strong salting-out effects.

It was originally believed that the effect of salt anions on macromolecules aqueous solutions was due to interactions between anions and water that cause changes in the hydrogen-bonding network of water[100,101]. Specifically, salting-out anions were described as water structure makers and they would strength hydrogen-bonding, while salting-in anions acted as water structure breakers. However, recent studies have shown that the behavior observed in the Hofmeister series is the result of a direct interaction of anions with the macromolecule/aqueous interface[100,101].

The effect of salting-out anions on the thermodynamic properties of macromolecules can be described using a two-domain model[9,109–112] represented in Figure 8. It is assumed that both the salt component and the macromolecule are hydrophilic and they will preferentially interact with water. This implies that there is a layer surrounding the globular macromolecule that is depleted of the salt component. Thus, we can describe the macromolecule-salt-water system by considering two domains. The first domain is the "local" domain surrounding the macromolecules in which the salt is depleted (inside the dashed circle). The second domain is the "bulk" domain (outside the dashed circle), which is represented by the unperturbed binary salt-water system with a composition equal to that of a salt-water system in equilibrium dialysis with our ternary system through a membrane that is not permeable to the macromolecule. The salt depletion in the "local" domain is the result of macromolecule-salt net repulsive interactions in water. The corresponding increase in macromolecule chemical potential can be described as the reversible expansion work against the salt osmotic pressure to remove salt ions from the local domain. We will derive below a thermodynamic relation describing how the chemical potential of the macromolecule increases with salt concentration and its consequences on the macromolecule solubility.

According to the two-domain description, the chemical potential of the salt, $\tilde{\mu}_\mathrm{S}$, is that of the bulk domain which is given by[113]:

$$\tilde{\mu}_\mathrm{S} = \tilde{\mu}_\mathrm{S}^0 + \nu RT \ln C_\mathrm{S}^* \gamma_\mathrm{S}^* \tag{1. 31}$$

where ν is the stoichiometric coefficient, C_S^* and γ_S^* are the concentration and the activity coefficient of the salt in the bulk domain, respectively. We can relate C_S^* to the total concentration of salt, C_S, using $C_\mathrm{S} = C_\mathrm{S}^* \alpha$ where α is the volume fraction of the "bulk" domain in the ternary system. As ϕ_P increases, α decreases. In the limit of $\phi_\mathrm{P} \to 0$,

$\alpha = 1-(1+q)^3\phi_{\mathrm{P}}$, where q is the ratio of the thickness of the local domain to the particle radius, and $(1+q)^3 V_{\mathrm{P}}$ is the volume of the local domain associated with each particle.

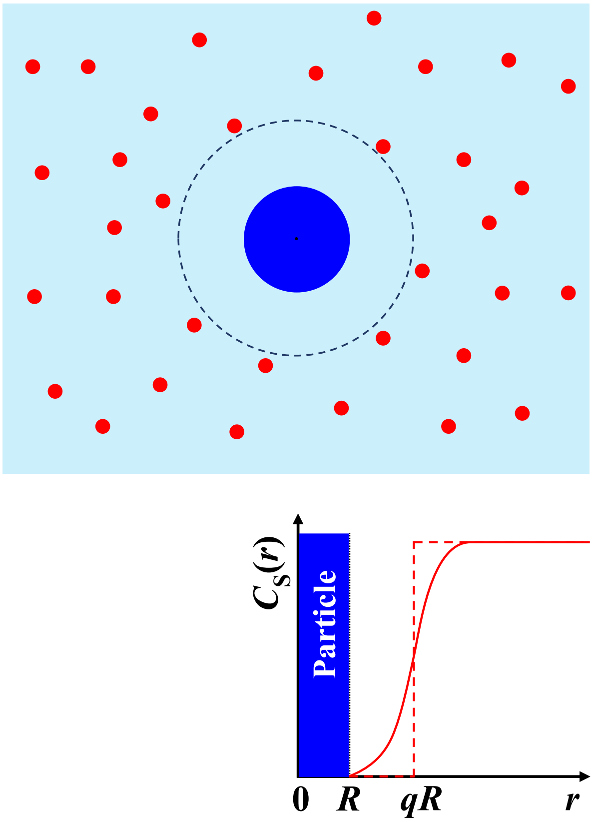

Figure 8. Two domain model. The blue circle represents the particle and the red circles represent the salt ions. The local domain is inside the dashed circle while the bulk domain is outside the dashed circle. The graph represents the salt concentration gradient: salt is partially depleted (solid red line) and is completely depleted (dashed red line) from the local domain. R is the radius of the particle and q is the ratio of the thickness of the local domain to the particle radius.

We will know show that in the presence of a salting-out salt the macromolecule chemical potential increases[113]. We start using the following Maxwell relation,

$$\left(\frac{\partial\tilde{\mu}_{\mathrm{P}}}{\partial C_{\mathrm{S}}}\right)_{\phi_{\mathrm{P}},T}=\left(\frac{\partial\tilde{\mu}_{\mathrm{S}}}{\partial\phi_{\mathrm{P}}}\right)_{C_{\mathrm{S}},T}V_{\mathrm{P}} \tag{1. 32}$$

The derivative on the right side of Eq. (1. 32) can be rewritten in the following way,

$$\left(\frac{\partial\tilde{\mu}_{\mathrm{S}}}{\partial\phi_{\mathrm{P}}}\right)_{C_{\mathrm{S}},T}=\left(\frac{\partial\tilde{\mu}_{\mathrm{S}}}{\partial C_{\mathrm{S}}^{*}}\right)_{T}\left(\frac{\partial C_{\mathrm{S}}^{*}}{\partial\phi_{\mathrm{P}}}\right)_{C_{\mathrm{S}},T} \tag{1. 33}$$

An expression for the first factor on the right side of Eq. (1. 33) can be derived from Eq. (1. 31) while the second factor is obtained from $C_{\mathrm{S}}=C_{\mathrm{S}}^{*}\alpha$. Starting from Eq. (1. 32), we obtain:

$$\left(\frac{\partial\tilde{\mu}_{\mathrm{P}}}{\partial C_{\mathrm{S}}}\right)_{\phi_{\mathrm{P}},T}=\frac{\nu RT}{C_{\mathrm{S}}}\left(1+\frac{d\ln\gamma_{\mathrm{s}}^{*}}{d\ln C_{\mathrm{S}}}\right)\left(-\frac{C_{\mathrm{s}}V_{\mathrm{P}}\alpha'}{\alpha^{2}}\right) \tag{1. 34}$$

where $\alpha'\equiv(\partial\alpha/\partial\phi_{\mathrm{P}})_{T}$. Eq. (1. 34) can be examined in the limit of $\phi_{\mathrm{P}}\rightarrow 0$, where we can set $\alpha=1$, $C_{\mathrm{s}}^{*}=C_{\mathrm{s}}$ and $\alpha'=-(1+q)^{3}$. Here, Eq. (1. 32) becomes:

$$\left(\frac{\partial\tilde{\mu}_{\mathrm{P}}}{\partial C_{\mathrm{S}}}\right)_{\phi_{\mathrm{P}},T}=\nu RT\left(1+\frac{d\ln\gamma_{\mathrm{s}}}{d\ln C_{\mathrm{S}}}\right)\left(1+q\right)^{3}V_{\mathrm{P}} \tag{1. 35}$$

In salting-out conditions, $(\partial\tilde{\mu}_{\mathrm{P}}/\partial C_{\mathrm{s}})_{\phi_{\mathrm{P}},T}$ is a positive parameter which is directly proportional to the volume of the local domain surrounding the macromolecule[113]. Eq. (1. 35) can be integrated to yield a relation between the chemical potential of the macromolecule and the salt concentration. If we neglect the salt non-ideality term for simplicity, integration gives

$$\tilde{\mu}_{\mathrm{P}}=\tilde{\mu}_{\mathrm{P,W}}+\int_{0}^{C_{\mathrm{s}}}\left(\partial\tilde{\mu}_{\mathrm{P}}/\partial C_{\mathrm{s}}\right)_{\phi_{\mathrm{P}},T}dC_{\mathrm{s}}\approx\tilde{\mu}_{\mathrm{P,W}}+RTKC_{\mathrm{s}} \tag{1. 36}$$

where $\tilde{\mu}_{\mathrm{P,W}}$ represents the macromolecule chemical potential in the absence of salt. Eq. (1. 36) shows that the chemical potential of the macromolecule approximately linearly increases with salt concentration with a slope $K \equiv \nu(1+q)^3 V_\mathrm{P}$ describing the salting-out effectiveness of the salt[113]. Note that, νRTC_S in Eq. (1. 36) represents the salt osmotic pressure (assuming ideal behavior) while $(1+q)^3 V_\mathrm{P}$ represents the cavity volume depleted in the salt component[113]. Thus, the second term in Eq. (1. 36) describes the reversible work needed to remove the salt component from the local domain.

The effect of salts on macromolecule solubility can be described using Eq. (1. 36). We start from the liquid-solid chemical-equilibrium condition[113]:

$$\tilde{\mu}_\mathrm{P} = \tilde{\mu}_\mathrm{P,C} \tag{1. 37}$$

where $\tilde{\mu}_\mathrm{P,C}$ is the macromolecule chemical potential in the condensed phase, which is here assumed to be independent of salt concentration. At low macromolecule concentration, we can write[113]:

$$\frac{\tilde{\mu}_\mathrm{P}}{RT} = \frac{\tilde{\mu}^0_\mathrm{P,W}}{RT} + \ln S_\mathrm{P} + KC_\mathrm{s} \tag{1. 38}$$

where $\tilde{\mu}^0_\mathrm{P,W}$ is the standard chemical potential of the macromolecule in the liquid phase, S_P is the macromolecule solubility in solution. If we combine Eq. (1. 37) and Eq. (1. 38), we obtain:

$$\ln S_\mathrm{P} = \frac{\tilde{\mu}_\mathrm{P,C} - \tilde{\mu}^0_\mathrm{P,W}}{RT} - KC_\mathrm{s} \tag{1. 39}$$

According to Eq. (1. 39), the logarithm of macromolecule solubility linearly decreases as the concentration of the salting-out agent increases. The parameter K is typically denoted as the salting-out constant[113].

Chapter 2: Materials and Experimental Techniques

2.1. Materials

Hydroxyl- and amino-functionalized poly(amido amine) dendrimers, generation 4 (G=4), were purchased from Dendritech, Inc (Midland) as a methanol solution. Methanol was removed by drying dendrimer samples in a vacuum oven, at 50 ºC and moderate vacuum. After drying, water was added to dried dendrimer samples and the drying procedure was repeated to remove any residual amounts of methanol. Deionized water was passed through a four-stage Millipore filter system to provide high-purity water for all experiments. Dendrimer-water stock solutions were then prepared by weight.

Sodium Sulfate was purchased from J.T. Baker (New Jersey, USA). Stock solutions of sodium sulfate were prepared by weight and their exact concentration was determined from density measurements using a digital density meter (Mettler/Paar, DMA40), thermostated at 25.00±0.01 ºC. Density values were converted into the corresponding concentrations using the known[114] relation between density and salt composition.

Copper Sulfate (98%) and N,N-Dimethylindoaniline (Phenol Blue) were purchased from Sigma Aldrich (Missouri, USA). Triethanolamine (98%), Sodium Chloride and silicone oil were purchased from Fisher Scientific (New Hampshire, USA).

2.2. Solutions Preparation

The known weigh fractions of dendrimer and salt in the ternary mixture were then converted into dendrimer volume fraction, ϕ_{D}, and salt molar concentration, C_{S}, after estimating the sample density using the known volumetric properties of binary sodium sulfate-water solutions the dendrimer specific volume specific volume of 0.817 g cm^{-3}.

Sample density was estimated in the following way. We start by considering dendrimer and salt weight fractions, w_{D} and w_{S} respectively. Salt molality m_{S} was calculated according to

$$m_{\mathrm{S}} = 1000(w_{\mathrm{S}} / M_{\mathrm{S}}) / (1 - w_{\mathrm{S}} - w_{\mathrm{D}}) \tag{2. 1}$$

where $M_{\mathrm{S}} = 142.037\,\mathrm{g\,mol^{-1}}$. The density d_{S} of the corresponding binary salt-water solution was calculated from the literature expression $d_{\mathrm{S}}(m_{\mathrm{S}})$ [114]:

$$\begin{aligned} &d_{\mathrm{S}} / \mathrm{g\,cm^{-3}} = 0.997045 + 0.129483(m_{\mathrm{S}} / m^0) \\ &-0.0086616(m_{\mathrm{S}} / m^0)^{1.5} - 0.0061207(m_{\mathrm{S}} / m^0)^2 + 0.0007909(m_{\mathrm{S}} / m^0)^{2.5} \end{aligned} \tag{2. 2}$$

where $m^0 \equiv 1\,\mathrm{mol\,kg^{-1}}$. The specific volume, v, of the ternary dendrimer-salt-water solution was the calculated using the following expression:

$$v = w_{\mathrm{D}}\, v_{\mathrm{D}} + (1 - w_{\mathrm{D}}) / d_{\mathrm{S}}(m_{\mathrm{S}}) \tag{2. 3}$$

where v_{D} is the dendrimer specific volume reported above[74]. Dendrimer volume fraction and salt molar concentrations were then calculated using

$$\phi_{\mathrm{D}} = w_{\mathrm{D}}\, v_{\mathrm{D}} / v \tag{2. 4}$$

$$C_{\mathrm{S}} = 1000(w_{\mathrm{S}} / M_{\mathrm{S}}) / v \tag{2. 5}$$

2.3. Experimental Techniques

2.3.1. Measurements of LLPS Temperature

The phase boundary of the dendrimer-salt-water system is described by the LLPS temperature, T_{ph}, as a function of salt concentration, C_{S} and dendrimer volume fraction, ϕ_{D}. Turbidity measurement experiments allow us to obtain the T_{ph} of our system samples.

The turbidity meter apparatus (Figure 9) is comprised of a programmable circulating bath (1197P,VWR) connected to a homemade optical cell where the homogenous dendrimer-salt-water sample (optical path of 0.4 cm) and thermocouple are located a calibrated thermocouple (±0.1 ºC). Collimated light, from a solid-state laser (633 nm, 5 mW, Coherent) passes through the sample and the transmittance is measured using a photodiode detector coupled with a computer-interfaced optical meter (1835-C Newport). A continuous airflow was directed to the optical cell lateral walls to prevent condensation of moisture.

In this method, we start by measuring the transmittance intensity, I_0, of a homogenous single-phase sample at a specific temperature. Afterwards, the temperature is slowly decreased (0.5 °C/min) or increased at a specific rate and the corresponding transmitted intensity, I, is measured. We identify T_{ph} as the temperature at which a sharp decrease in intensity is observed (cloud point).

To measure T_{ph}, homogenous samples $(\approx 100\ \mu\mathrm{L})$ were prepared by mixing known amounts of water, dendrimer and salt stock solutions. The known weigh fractions of dendrimer and salt in the ternary mixture were then converted into ϕ_{D} and C_{S}, after calculating the sample density using the known volumetric properties of the binary sodium sulfate-water solutions and the dendrimer specific volume specific volume of 0.817 g cm^{-3}. All samples prepared for turbidity measurements were allowed to equilibrate for two days at a temperature at which they were homogeneous. We note that T_{ph} was found to strongly depend on salt concentration. Thus, errors on T_{ph} values due to water evaporation were minimized by layering silicon oil on our small samples.

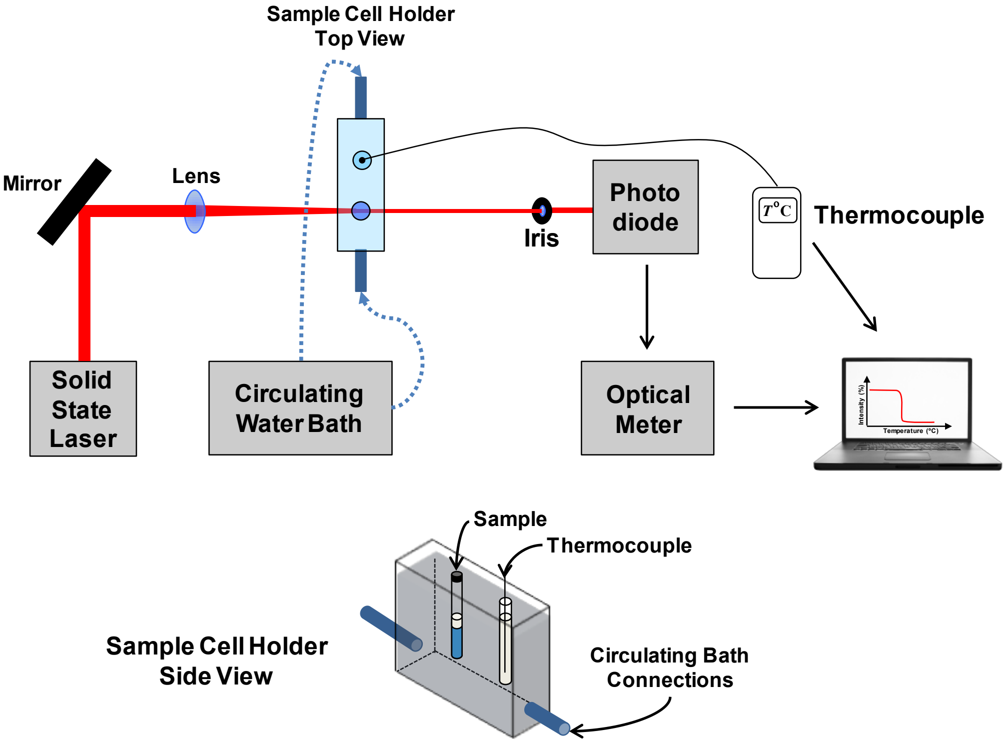

Figure 9. Scheme for the turbidity meter apparatus.

2.3.2. Measurements of Dendrimer-Salt Partitioning at 25 °C

The experimental procedure to characterize dendrimer-salt partitioning in water involved two steps: the first step was sample mixing and equilibration, and the second one was the separation of the two coexisting liquid phases. Both steps required the development of new experimental procedures in order to circumvent challenges related to the small sample size (500 μL) and viscosity. Samples for partitioning measurements were prepared as follows: a known amount of dendrimer and salt stock solutions, and water were mixed together, in a small test tube, so that the final system consisted of two coexisting liquid phases at room temperature. The test tube was capped and samples were mixed vigorously using a vortex stirrer for 5 min at room temperature to facilitate equilibration. These samples were then immersed in a temperature-controlled water bath at 25.0 ºC. It is important to note that sample shaking did not lead to appreciable sample mixing due to the sample small volume and viscosity. To improve mixing we assembled a test-tube rotation device (see figure) with adjustable speed. Thus, sample mixing was achieved by test-tube rotation (0.2 rpm for two days) leading to cyclic sample inversions inside the water bath. Afterwards, samples were positioned vertically and held stationary to allow for macroscopic phase separation of the two coexisting liquid phases by gravity. When the interface between the two coexisting phases was clear, aliquots from the top phase I and bottom phase II were transferred into small test tubes and weighted. The aliquot from the bottom solution was taken after the section containing liquid-liquid interface was removed by suction using a needle connected to a vacuum pump. The two separated samples taken from the bottom and top phases were both centrifuged (Allegra^{TM} 25R centrifuge, Beckman Coulter) to verify their homogeneity, at 25.0 ºC.

The composition of the two phases was then characterized using a spectrophotometric assay (for dendrimer) and a potentiometric assay (for salt). Both methods are described in the two following sub-sections. The composition of the two coexisting phases I and II were reported as dendrimer volume fraction and salt molar concentration, $(\phi_{\mathrm{D}}^{(\mathrm{I})}, C_{\mathrm{S}}^{(\mathrm{I})})$ and $(\phi_{\mathrm{D}}^{(\mathrm{II})}, C_{\mathrm{S}}^{(\mathrm{II})})$, respectively.

Spectrophotometric assay

The determination of the dendrimer concentration in aqueous solution was based on a copper-dendrimer binding assay[115]. These studies show that, in aqueous solutions copper ions exist primary as $[\mathrm{Cu(H_2O)_6}]^{2+}$ with a weak absorption band at 810 nm. However, in the presence of PAMAM-OH, this peak blue shifts to 610 nm with a significant increase in absorbance with increasing dendrimer concentration. Thus, a calibration curve was prepared by measuring copper absorbance at 610 nm (DU 800 spectrophotometer, Beckman Coulter) as a function of dendrimer concentration. Samples were prepared by mixing aqueous stock solutions of dendrimer and copper. The concentration of the copper stock solution was found to influence the formation of copper aggregates. Thus, we prepared a copper stock solution of 0.06 M to avoid aggregation. The final copper concentration of our samples was always kept constant at 0.006 M. This concentration allowed for only a small excess of copper but ensured that all dendrimer binding sites were occupied. The order by which stock solutions were mixed was also found to be critical to avoid the formation of copper aggregates. To avoid aggregation, copper solution was always added at the end.

For salt-dendrimer partitioning characterization, a small aliquot of a phase was first diluted in water following copper addition. We also evaluated the effect of the presence of sodium sulfate on the dendrimer-copper binding and we found that, within our experimental salt concentration range, the presence of salt had no effect on the absorbance of our solutions.

Potentiometric assay

Sodium sulfate concentration was measured by utilizing a sodium ion-selective electrode (Accumet). We first prepared a calibration curve based on the Nernst equation. This equation expresses the sodium ions concentration as a function of the system potential: $E = a + c\ln C_\mathrm{S} + b(\ln C_\mathrm{S})^2$ where E is the measured potential of the system and a , b, and c are fitting constants. To prepare the samples, a small aliquot was taken and properly diluted with water. A known excess (90%) of an ionic strength adjustor (triethanolamine-water solution, 5.3% v/v, pH 9.5) was then added to the diluted sample. A calibration curve was obtained by preparing samples with known amounts of sodium sulfate and measuring the electrode electric potential as a function of salt concentration (reported as $\ln C_\mathrm{S}$). Since our samples from the partitioning experiments had both salt ions and the dendrimer, we also evaluated the effect of dendrimer concentration on the electrode electric potential. All the measurements were performed under moderate stirring at room temperature. Because the electrical potential depends on temperature, the calibration procedure was repeated every time we made measurements.

2.3.3. Dynamic Light Scattering, DLS

Dynamic light scattering (DLS) is a technique that can be used to determine the diffusion coefficient, D, of macromolecules in solutions[116,117]. One important application of diffusion coefficients is the determination of the hydrodynamic radius, R_h, of particles. This link can be appreciated, if we observe that small particles tend to diffuse faster than large particles.

The mathematical relation between D and R_h can be derived using the following approach[116].

We start by considering the generalized equation for diffusion specifically, the Fick's first law of diffusion[116]:

$$J_\mathrm{P} = -D\nabla C_\mathrm{P} \tag{2. 6}$$

in which the flux, J_P (the net amount of molecules that flow per unit area and per unit time) is directly proportional to the concentration gradient, ∇C_P. Here, the diffusion coefficient is the proportionality constant. It is also convenient to relate the diffusion coefficient to the kinetic evolution of particle concentration. This equation which can be derive from the Fick's first law, is called Fick's second law of diffusion[116]:

$$\frac{\partial C_\mathrm{P}}{\partial t} = \nabla\left(D\nabla C_\mathrm{P}\right) \tag{2. 7}$$

where t is the time. In general, D depends on particle concentration due to particle-particle interactions[116,117]. At infinite dilution, D is denoted as D_0, the tracer diffusion coefficient of the particle[116].

We then introduce the theory of Brownian motion that provides a microscopic view of diffusion[116,117]. This theory describes the random motion of non-interacting particles suspended in a fluid as a result of their random collisions with solvent molecules. There are two important equations in this theory. The first relates the mean squared displacement, $\langle [r(t)-r(0)]^2 \rangle$, of a Brownian particle with its tracer diffusion coefficient, D_0 as follows:

$$D_0 = \lim_{t\to\infty} \frac{\langle [r(t)-r(0)]^2 \rangle}{6t} \tag{2. 8}$$

The second equation, which can be derived from Eq. (2. 8) using Newton equation of motion, establishes a relationship of D_0 to the collisional force of solvent molecules (thermal energy) and the opposing frictional force experienced by the moving particle inside the fluid. This equation is known as the Stokes-Einstein equation[116,117]:

$$D_0 = \frac{k_{\mathrm{B}}T}{f} = \frac{k_{\mathrm{B}}T}{6\pi\eta R_{\mathrm{h}}} \tag{2. 9}$$

where f is the friction coefficient, η is the solvent viscosity and R_{h} is the radius of the particle in the special case of a sphere. The Stokes-Einstein equation is important because it allows us to convert the measured diffusion coefficient into the hydrodynamic radius of the particle.

Diffusion can be also introduced by using the principles of non-equilibrium thermodynamics[116–118]. According to this theory, the vector flux, J_{P}, of a solute component immersed in a binary solute-solvent fluid is directly proportional to the chemical potential gradient, $\nabla\tilde{\mu}_{\mathrm{P}}$, of the solute:

$$J_{\mathrm{P}} = -L\nabla\tilde{\mu}_{\mathrm{P}} \tag{2. 10}$$

where L is denoted Onsager diffusion coefficients. It is however convenient to relate the diffusion flux to the measurable gradient of particle concentration (see Eq. (2. 6)). If we rearrange Eq. (2. 10) as follows:

$$J_{\mathrm{P}} = -L\left(\frac{\partial\tilde{\mu}_{\mathrm{P}}}{\partial C_{\mathrm{P}}}\right)\nabla C_{\mathrm{P}} \tag{2. 11}$$

we can then deduce from Eq. (2. 6) that

$$D = L\left(\frac{\partial \tilde{\mu}_{\mathrm{P}}}{\partial C_{\mathrm{P}}}\right) \tag{2. 12}$$

Eq. (2. 12) can be rearranged to express D as a product of a mobility factor (first factor in parenthesis) and a thermodynamic factor (second factor in parenthesis)[116,117]:

$$D = \left(\frac{k_{\mathrm{B}}T}{C_{\mathrm{P}}}L\right)\left(\frac{C_{\mathrm{P}}}{k_{\mathrm{B}}T}\frac{\partial \tilde{\mu}_{\mathrm{P}}}{\partial C_{\mathrm{P}}}\right) \tag{2. 13}$$

In the limit of $C_{\mathrm{P}} \to 0$, the mobility factor becomes D_0 and the thermodynamic factor is equal to 1. It is therefore convenient to rewrite Eq. (2. 13) in the following way:

$$D = D_0 H(C_{\mathrm{P}}) s(C_{\mathrm{P}}) \tag{2. 14}$$

where $s(C_{\mathrm{P}})$ and $H(C_{\mathrm{P}})$ are the thermodynamic and hydrodynamic factors, respectively with $H(0) = s(0) = 1$ [116,117]. Note that, $H(C_{\mathrm{P}})$ represents a corrective factor characterizing the deviation of the mobility factor from D_0.

When measurements of D are performed as a function of C_{P}, the experimental data are examined according to[116,117]:

$$D = D_0\left(1 + kC_{\mathrm{P}} + \ldots\right) \tag{2. 15}$$

where the tracer diffusion coefficient D_0 is graphically represented by the intercept of Eq. (2. 15), while the normalized slope, k, characterizes the net effect of the hydrodynamic and thermodynamic interactions.

We will now focus on how we can obtain the diffusion coefficient of a particle using DLS. Fundamentally, this technique probes concentration fluctuations caused by the Brownian motion of solute particles in a solution[116]. If the polarizability of these particles is different from that of the surrounding medium (solvent), the photons of an incident light beam are observed to be scattered in all directions by the investigated sample[116].

We will now consider a system with N identical scattering particles where each particle produces a scattered electromagnetic wave of amplitude E_0. This amplitude value is directly proportional to the molecular weight of the particle.

The total scattered electromagnetic field, E, resulting from the scattering of N identical particles, is given by[116]:

$$E = E_0 \sum_{i}^{N} e^{iq \cdot r_i} \tag{2. 16}$$

where r_i is the position vector of the i particle and q is the scattering vector defined as $q = (4\pi n / \lambda_0)\sin(\theta / 2)$. Here, n is the refractive index, λ_0 is the wavelength of the light in vacuum and θ is the scattering angle.

The intensity of the scattered light, I, is proportional to the square of the amplitude of the electromagnetic field[116,117]:

$$I = I_0 \left| \sum_{i=1}^{N} e^{iq \cdot r_i} \right|^2 = I_0 \left[N + 2 \sum_{i=1}^{N} \sum_{j>i}^{N} \cos q \cdot \left(r_i - r_j \right) \right] \tag{2. 17}$$

where $r_i - r_j$ is the difference in position between particle i and particle j. The last term on Eq. (2. 17) is a stochastic function of time due to particle random motion. Thus, the measured intensity, $I(t)$, fluctuates as a function of time. If we consider the time average of $I(t)$, we obtain $\langle I \rangle = NI_0$ because the last term in the square bracket of Eq. (2. 17) is zero on average.

For interacting particles, the deviation from $\langle I \rangle = NI_0$ is accounted for by introducing the static structure facture, $S(C_{\mathrm{P}},q)$ [116,117]:

$$\langle I \rangle = NI_0 S(C_{\mathrm{P}},q) \tag{2. 18}$$

where the static structure factor is:

$$S(C_{\mathrm{P}},q) = \left\langle \frac{1}{N} \left| \sum_{i=1}^{N} e^{iq\cdot r_i} \right|^2 \right\rangle \tag{2. 19}$$

The static structure factor describes equilibrium properties. For instance, $S(0,0)=1$ for ideal particles[116,117]. In general, when particles are small compared to the wavelength of the incident light, λ_0, $S(C_P,q) = S(C_P,0) = (k_B T / C_P)(\partial C_P / \partial \tilde{\mu}_P)_T$ [116,117].

To investigate diffusion it is convenient to introduce the dynamic structure factor[116,117], $F(C_{\mathrm{P}},q,\tau)$ defined as follows,

$$F(C_{\mathrm{P}},q,\tau) \equiv \left\langle \frac{1}{N} \sum_{k=1}^{N} e^{iq\cdot r_k(\tau)} \sum_{j=1}^{N} e^{-iq\cdot r_j(0)} \right\rangle = \left\langle \frac{1}{N} \sum_{k=1}^{N} e^{iq\cdot\left(r_k(\tau)-r_k(0)\right)} \right\rangle + \left\langle \frac{1}{N} \sum_{k=1}^{N} \sum_{j>k}^{N} e^{iq\cdot\left(r_j(\tau)-r_k(0)\right)} \right\rangle \tag{2. 20}$$

where $r_k(\tau)-r_j(0)$ is the difference in position between particle k at time $\tau>0$ and particle j at time $\tau=0$. Note that $F(C_{\mathrm{P}},q,0)=S(C_{\mathrm{P}},q)$ (see Eq. (2. 19) and Eq. (2. 20)). In the absence of particle-particle interactions the cross-term $k \neq j$ vanishes and Eq. (2. 20) becomes:

$$F(0,q,\tau) \equiv \left\langle \frac{1}{N} \sum_{k=1}^{N} e^{iq\cdot\left(r_k(\tau)-r_k(0)\right)} \right\rangle \tag{2. 21}$$

This equation describes single particle motion and $F(0,q,\tau)$ is called the self-dynamic structure factor[116,117].

Brownian motion theory and Fick's second law can be then used for non-interacting particles to relate their position displacement to the tracer diffusion coefficient by:

$$F(0,q,\tau) = S(0,q)e^{-q^2 D_0 \tau} \tag{2. 22}$$

In relation to DLS experiments at a given particle concentration and scattering angle, it is convenient to introduce the normalized correlation function of the electromagnetic field:

$$g^{(1)}(\tau) = \frac{\langle E(t)E^*(t+\tau)\rangle}{\langle E(t)^2\rangle} = \frac{F(c,q,\tau)}{S(c,q)} \tag{2. 23}$$

where we also used Eq. (2. 16), Eq. (2. 19) and Eq. (2. 20). If we then consider Eq. (2. 22), we can appreciate that:

$$g^{(1)}(\tau) = e^{-q^2 D_0 \tau} \tag{2. 24}$$

with $g^{(1)}(\infty) = 0$. Because $E(t)$ is a stochastic function as a result of Brownian motion, all the information is contained in the temporal correlations of the electromagnetic field. According to Brownian motion theory, correlation is lost more rapidly for smaller molecules due to their higher diffusion coefficient as described by Eq. (2. 24).

In the case of a polidisperse particle system the normalized correlation function of the electromagnetic field becomes[116,117],

$$g^{(1)}(\tau) = \sum_{i=1}^{N} W_i e^{-q^2 D_i \tau} \tag{2. 25}$$

where D_i is the tracer-diffusion coefficient associated with type *i* particles and W_i is the corresponding normalized scattering contribution, with W_i being proportional to $N_i M_i^2$ where N_i is the number of type *i* particles and M_i their corresponding molecular weight.

In order to experimentally determine D_0, we need to link the measured scattered intensity $I(t)$ to $g^{(1)}(\tau)$. This is achieved by introducing the normalized correlation function for the scattered intensity[116,117]:

$$g^{(2)}(\tau)=\frac{\langle I(t)I(t+\tau)\rangle}{\langle I\rangle^2} \tag{2. 26}$$

Because $I(t)$ is also a stochastic function as a result of Brownian motion, correlation is lost for long times. In the absence of correlation, $\langle I(t)I(t+\infty)\rangle=\langle I\rangle^2$ and $g^{(2)}(\infty)=1$.

The normalized intensity correlation function $g^{(2)}(\tau)$ is related to the electric field correlation function $g^{(1)}(\tau)$ by the Siegert equation as follows:

$$g^{(2)}(\tau)=1+A\left|g^{(1)}(\tau)\right|^2 \tag{2. 27}$$

where A is the coherence factor; $A=1$ when scattered light is collected by the detection system from an infinitesimal solid angle and $A<1$ for any finite value of this angle.

Dynamic Light Scattering Apparatus

DLS experiments were performed on a light scattering apparatus (Figure 10) built using the following main components: He-Ne laser (35 mW, 632.8 nm, Coherent Radiation), manual goniometer and thermostat (Photocor Instruments), multi-tau correlator, APD detector and software (PD4042, Precision Detectors). The laser is polarized and perpendicular to the plane of all the apparatus components (sample, detector and correlator). The laser beam width at the focus point is around $10\ \mu\text{m}$. The scattered light from the scattering volume is collected at a scattering angle $\theta=90^\circ$ and focused by a condenser lens and an iris placed between the sample and the lens. The scattered light is then transmitted to a photodiode detector through an optical fiber. The photodetector receives the photons and converts them to electrical pulses so they can be processed and analyzed by the 256 channel correlator. The correlator collects the measured intensities $I(t)$ as a function of time (from 10^{-9} to 10^{-3} seconds apart) and computes $g^{(2)}(\tau)$ using a discrete integration method based on Eq. (2. 27). The correlation functions are calculated every 2 seconds and averaged over 300-3200 accumulation times to minimize statistical errors. Indeed, the precision of the correlation function increases with the square root of accumulation time.

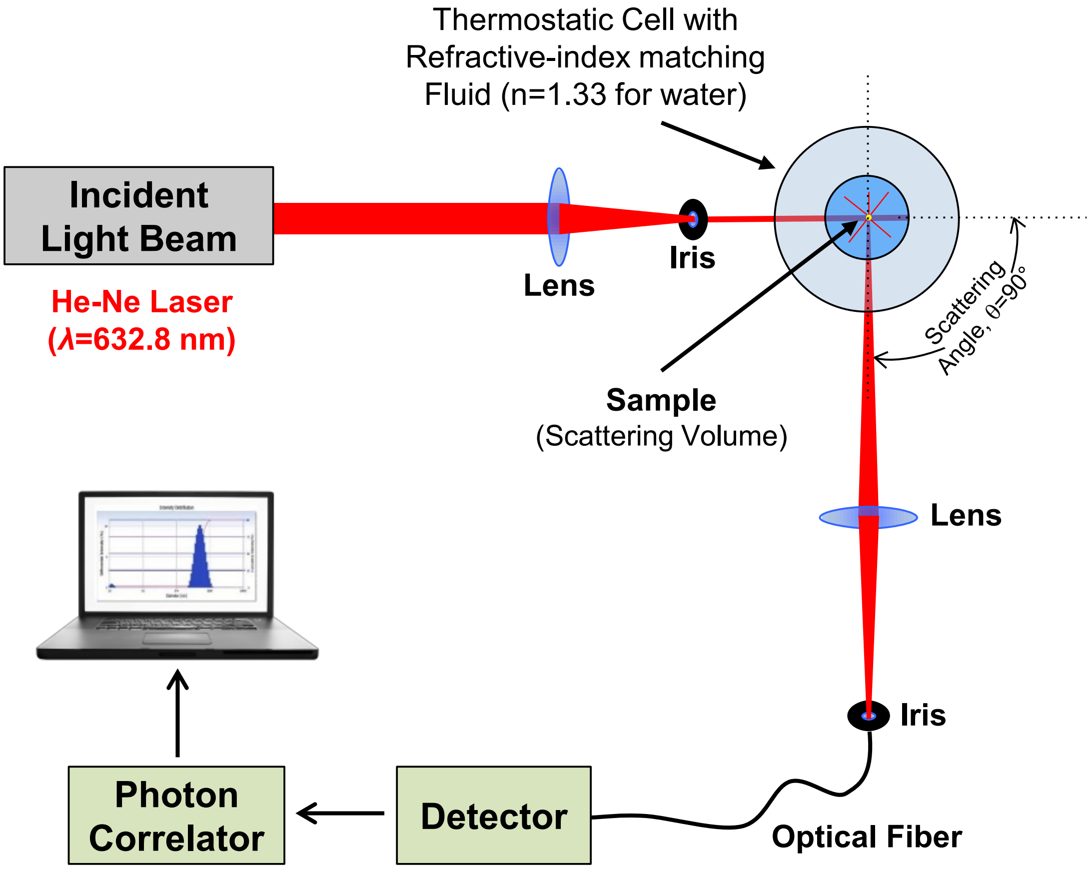

Figure 10. Scheme of the dynamic light scattering apparatus.

The experimental $g^{(2)}(\tau)$ is then examined according to[116]

$$g^{(2)}(\tau) = B + A\left(\sum_i W_i e^{-D_i q^2 \tau}\right)^2 \tag{2. 28}$$

where particles are assumed to be polydisperse (see Eqs. (2.25) and (2.27)). In Eq. (2. 28), a grid of diffusion coefficients $\{D_i\}$ is constructed, and the corresponding $\{W_i\}$ are determined. This gives the normalized light-scattering distribution $W(D)$ of diffusion coefficients. This can be also converted in the corresponding size distribution $W(R_\mathrm{h})$ by using the Stokes-Einstein Equation (see Eq. (2.9)). The average diffusion coefficient of the distribution is determined as

$$\langle D\rangle_z = \sum_{i=1}^{n} W_i D_i \tag{2. 29}$$

where the subscript z specifies that this is a z-average[116].

Note that the procedure to obtain $\{W_i\}$ from a linear combination of exponential decays is an inverse Laplace transformation. It is known that this procedure is an ill-posed problem, since any small perturbation in $g^{(2)}(\tau)$ can give very different distributions $\{W_i\}$. To solve this problem, two conditions are imposed: (1) W_i can only assume positive values and (2) $\{W_i\}$ is smooth. The latter is achieved by including in the method of least squares the minimization of the summation $\alpha\sum_{k=1}^{n} W_i^2$, where α is a regularization parameter. The experimentalist chooses the lowest value of α that makes independent consecutive measurements on the same sample reproducible. In our case, the software Precision Deconvolve 32 is used for the extraction of $\{W_i\}$.

The DLS experiments on dendrimer-salt-water solutions were performed at 25.0±0.1 and 37.0±0.1 ºC. All samples were filtered through a 0.02-μm filter (Anotop 10, Whatman) and placed in an optically cleaned test tube. In the case of the measurements of dendrimer diffusion coefficient as a function of dendrimer and salt concentration, all experimental correlation functions give monomodal diffusion-coefficient distributions. In these cases, the *z*-average diffusion coefficient was determined.

For DLS experiments on dendrimer solutions in the presence of crosslinker, experiments were performed at 25.0±0.1 ºC and samples were filtered through a 0.45-μm filter (Anotop 10, Whatman). The corresponding correlation functions yielded mono and bimodal diffusion-coefficient distributions.

2.3.4. Isothermal Titration Calorimetry, ITC

Isothermal Titration Calorimetry (ITC) (MicroCal iTC200 System, GE Healthcare Life Sciences) was used to characterize the dendrimer-dendrimer interaction energy. ITC is a technique often used in host-guest interactions studies to directly determine thermodynamic parameters such as enthalpy changes, binding affinity and stoichiometry in solution (see Part II Chapter 8 for this application)[119]. In our case, we specifically developed a model to relate the excess internal energy of our dendrimer solutions to the heat of dilution measured by ITC.

This instrument[119] consists of two identical cells: the reference (R) and the sample (S) cell, coupled to highly sensitive thermocouple circuits (Figure 11). The ITC cells are made of a Hastelloy alloy for an efficient thermal conduction, chemical resistance and compatibility. The sensitive thermocouples are used to detect temperature differences between the reference and sample cell as low as 0.1 mC. A syringe at the top of the sample cell is used to inject small aliquots of a titrant. Typically, the titrant solution contains a reacting solute component (*e.g.* a guest ligand or a host macromolecule). In the ITC experiments discussed in this section, the titrant solution consists of a concentrated dendrimer solution. Correspondingly, the sample cell contains the solution to be titrated (titrand). Typically, the titrand solution contains the other reacting solute component (*e.g.*, a host macromolecule or a guest ligand). However, in our case, which aims at measuring the heat of dilution of dendrimer-dendrimer interaction, the titrand is a dendrimer-free solution. The reference cell usually contains water or a buffer solution.

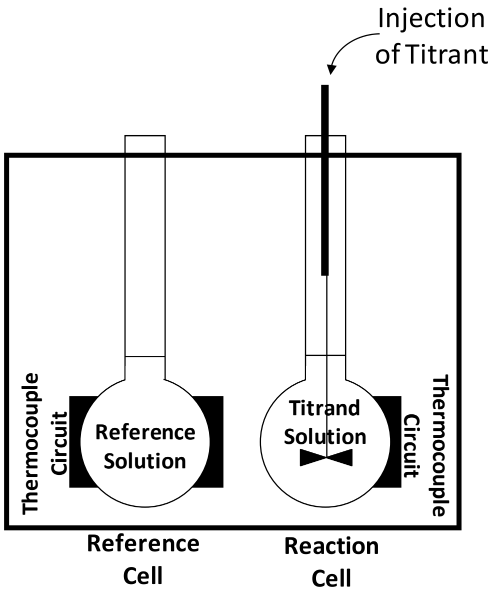

Figure 11. Schematic of an ITC instrument.

At the beginning of the experiment *i.e.*, before addition of the titrant, both cells are at a constant power (w) of the order of 5 mW. The electrical powers of the sample cell, w_{S}, and reference cell, w_{R}, maintain the temperature of the sample T_{S} and the reference cell T_{R} at an equal value (*e.g.* 25 °C). Upon addition of the titrant, the instrument will adjust w_{S} accordingly so that $T_{\mathrm{S}} = T_{\mathrm{R}}$ during the isothermal titration. The mixing of the titrant to the titrand solution gives rise to exothermic or endothermic events. For example, if the event is endothermic, heat is absorbed in the sample cell and, consequently, more power w_{S} is needed to maintain the target T_{S}.

In an ITC experiment, the changes of power $w_{\mathrm{S}} - w_{\mathrm{R}}$ are plotted as a function of time, t (see Section 3.7). Thus, this power plot consists of a series of peaks associated with heat flow, corresponding to multiple titrant injections into the sample cell. If the titrant injection leads to an exothermic (endothermic) event, a depression (bump) peak is observed[119].

The concentrations of titrand, C_{titrand}, and titrant, C_{titrant}, inside the sample cell need to be corrected for the displaced volume $\Delta V = kv$ [119,120]. In other words, each injection drives the liquid solution, in the sample cell, out of the working volume, V up to the inactive tube as shown in Figure 12A by the darkened portion representing ΔV. Here, only the solution contained within V is probed by the ITC instrument. These small volumetric displacements are taken into account by introducing minor corrections in the calculation of C_{titrand} and C_{titrant}. To determine C_{titrand} and C_{titrant}, we can consider two limiting cases Figure 12B[120]. If stirring is not effective *i.e.*, no mixing, the addition of ΔV titrant solution displaces a corresponding

ΔV of the initial (before injection) titrand solution to the cell neck. Thus the corresponding mass balance for the total titrant solution $C_{titrant}^{(k)}$ with each injection k is:

$$C_{\text{titrant}}^{0} kv = C_{\text{titrant}}^{(k)} V \tag{2. 30}$$

On the other hand, if we consider complete mixing (very effective stirring), the mixing of the titrant inside the cell will occur before sample volume displacement (Figure 12B). Here, the corresponding mass balance is,

$$C_{\text{titrant}}^{0} kv = C_{\text{titrant}}^{(k)} \left(V + kv \right) \tag{2. 31}$$

To consider both cases, we take the average of these two mass balances (Eq. (2. 30) and Eq. (2. 31)) and obtain:

$$C_{\text{titrant}}^{(k)} = C_{\text{titrant}}^{0} \frac{kv}{V(1+0.5kv/V)} \tag{2. 32}$$

where the factor in parentheses represents a small correction to titrant concentration inside the cell associated with the volume displacement.

Note that similar mass balances can be derived for the titrand molecules and we obtain:

$$C_{\text{titrand}}^{0} \left(V - kv \right) = C_{\text{titrand}}^{(k)} V \tag{2. 33}$$

for the limiting case no mixing and:

$$C_{\text{titrand}}^{0} V = C_{\text{titrand}}^{(k)} \left(V + kv \right) \tag{2. 34}$$

for the limiting case of complete mixture.

The average mass balance for the titrand using Eq. (2. 33) and Eq. (2. 34) corresponds to:

$$C_{\text{titrand}}^{(k)} = C_{\text{titrand}}^{0}\left(\frac{V-0.5kv}{V+0.5kv}\right) \tag{2. 35}$$

where the two factors in parentheses are close to 1.

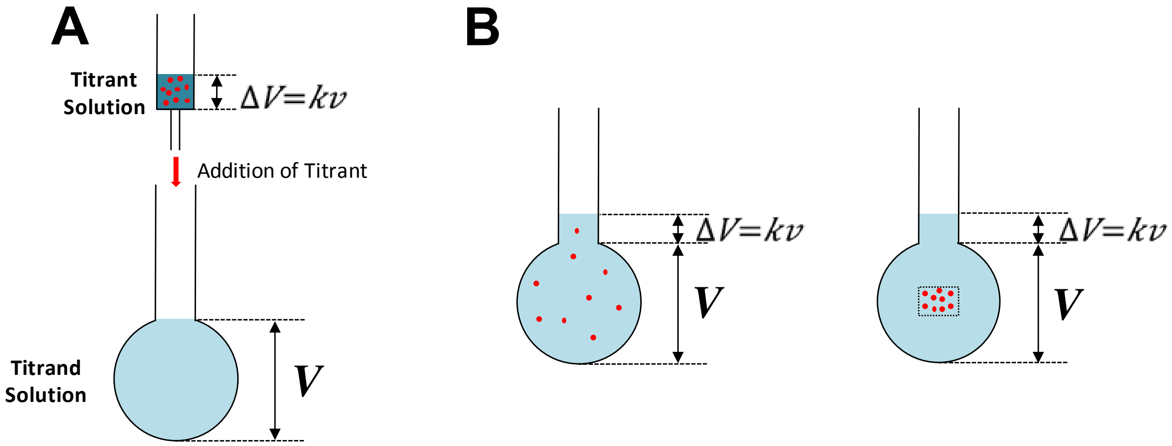

Figure 12. (A) Sample displacement inside the sample cell and (B) limiting cases.

The differential heat $q^{(k)}$ associated with each injection, k, is calculated as the area of the corresponding measured peak and normalized with respect to the titrant number of moles[119,120]. The cumulative heat, $Q^{(k)}$, absorbed or released by the sample after injection k can be linked to $q^{(k)}$ by applying[119,120]:

$$q^{(k)} = \left[\left(V+v/2\right)\left(Q^{(k)}/V\right)-\left(V-v/2\right)\left(Q^{(k-1)}/V\right)\right]\Big/\left(vC_{\text{titrant}}^{0}\right) \tag{2. 36}$$

where V is the working volume of the cell, v is the volume of each injection and C_{titrant}^{0} is the concentration of titrant in the syringe. Typically, we have: $v/V \approx 0.01$. The volumetric factors $(V+v/2)/V$ and $(V-v/2)/V$ represent small corrections taking into account that the titrant addition to the sample cell displaces a small fraction of solution outside the stirred cell. Thus, the experimentally recorded differential heat corresponds to an overestimated of $Q^{(k)}$ because a small contribution to heat will also come from the sample displaced outside the cell and an underestimated $Q^{(k-1)}$ because this displaced sample contributed to the cumulative heat after injection $k-1$. Thus $Q^{(k-1)}$ does not represent the correct starting point for injection k.

To determine thermodynamic parameters from ITC, a model-based mathematical expression for the cumulative heat as a function of system composition (inside the cell) is used (see excess internal model Section 3.7 and self-association and host-guest binding models in part II, Chapter 8). The mathematical expression for $Q^{(k)}$ is then inserted in Eq. (2. 36) and the method of least squares is applied to the differential heat $q^{(k)}$. Specifically, the summation of the square residuals over N experimental points, $\sum_{k=1}^{N}\left(q_{\text{exp}}^{(k)}-q_{\text{cal}}^{(k)}\right)^2$, is minimized using MatLab software[120].

All experiments were performed at 25.0 °C and atmospheric pressure. In these experiments, dendrimer solutions were exhaustively dialyzed (membrane) against an aqueous salt-buffer (ACES, pH 7.0, 0.10 M; sodium sulfate, 0.03 M; ionic strength, 0.14 M) and concentrated by ultrafiltration. The final dendrimer concentration was determined using the spectrophotometric assay described in Section 2.3.2. Dendrimer volume fractions ranged from $\phi_{\text{D}}^{0}=0.10$ to $\phi_{\text{D}}^{0}=0.19$. Small aliquots ($v=2.0\ \mu\text{L}$) of these dendrimer solutions were sequentially injected (19 injections, titrant) from a rotating syringe into the vigorously stirred sample cell (syringe rotation, 1000 rpm) containing the aqueous salt-buffer (titrand). The ITC sample cell volume is $V=203.4\ \mu\text{L}$ (factory specifications). To minimize effects related to minor differences in the thermodynamic activities of the buffer components, ionic strength and pH, the "waste" obtained from the ultrafiltration procedure was used as the titrand. The dendrimer volume fraction inside the ITC cell after injection k was calculated using Eq. (2. 32) in terms of dendrimer volume fraction,

$$\phi_{\mathrm{D}}^{(k)} = \phi_{\mathrm{D}}^{0} \frac{kv}{V + 0.5kv} \qquad (2.\ 37)$$

Each injection corresponds to an exothermic peak on a plot showing the power required to maintain the sample and reference cells at the same temperature as a function of time. The differential heat associated is calculated using Eq. (2. 36) in terms of dendrimer volume fraction:

$$q^{(k)} = \left[\left(V + v/2\right)\left(V_{\mathrm{D}} Q^{(k)}/V\right) - \left(V - v/2\right)\left(V_{\mathrm{D}} Q^{(k-1)}/V\right) + k_{\mathrm{ITC}} \phi_{\mathrm{D}}^{(k)} \right] \Big/ \left(v \phi_{\mathrm{D}}^{0}\right) \qquad (2.\ 38)$$

where $Q^{(0)} = 0$ and k_{ITC} is a parameter characterizing a baseline correction.

2.3.5. Scanning Electron Microscopy, SEM

Samples for field-emission SEM were prepared by adding 100 µl of the samples previously prepared for DLS measurements to 1 ml of water. These solution were then dialyzed against water using an ultrafiltration membrane (10 kDa cut-off) in order to remove any salt from the samples. A small aliquot (≈10 µl) of the filtered samples was directly placed on the specimen stub and let to dry overnight under vaccum. After drying, all samples were coated with a 10 nm layer of 60/40 gold/palladium by low-vacuum sputter coating and analyzed with a JSM-7800F field-emission SEM (JEOL).

2.4. Phenol Blue Binding Assay.

Our binding assay was based on measuring the absorbance of phenol blue at 646.5 nm[121] (DU 800 spectrophotometer, Beckman Coulter). A stock solution of phenol blue in water (0.02 mM) was prepared by extensively stirring dye-water suspensions at room temperature in dark conditions. The obtained stock solution was then filtered (Nalgene filter, 0.2 μm pore size). Solutions were then prepared by mixing the phenol blue stock solution with water, dendrimer and sodium sulfate stock solutions. For all solutions, the dye concentration was kept constant at 0.01 M. The dendrimer concentration was also kept constant at 1.73 mM. This concentration was chosen by verifying that the absorbance at 646.5 nm of 0.01-M dye solutions significantly decreases as dendrimer concentration increases up to about 1.7 mM (see Figure 13A). Thus, the fraction of the dye bound to dendrimer is close to maximum in these conditions. The sodium sulfate concentration in our solutions was increased up to 0.7 M. Solutions with higher salt concentrations could not be prepared due to solubility limitations of phenol blue and sodium sulfate in their corresponding aqueous stock solutions. All absorbance measurements were promptly performed on the freshly prepared solutions and then repeated after 24 hours to allow for binding to occur and reach equilibrium. Control experiments on dendrimer-free dye solutions were also performed (see Figure 13B). All samples were stored in dark conditions during the incubation time of 24 hours.

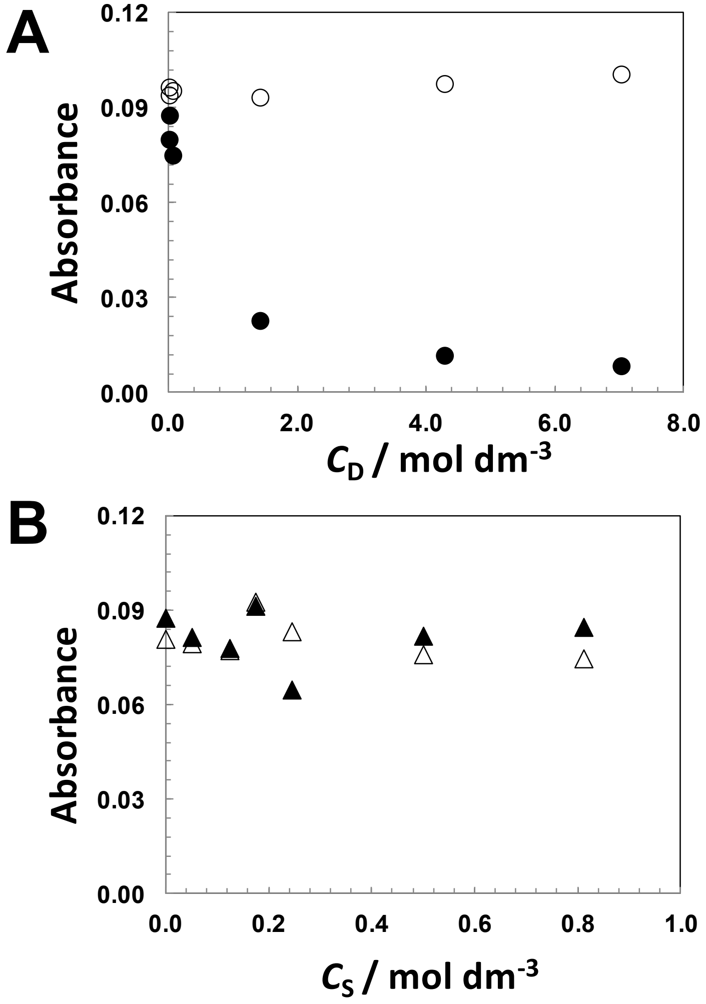

Figure 13. (A) Phenol blue absorption at 646.5 nm as a function of ϕ_D at $C_S = 0$ M and at time 0 (open circles) and time 24 h (closed circles). (B) Phenol blue absorption at 646.5 nm as a function of C_S at $\phi_D = 0$ and at time 0 (open triangles) and time 24 h (closed triangles).

2.5. Crosslinking experiments.

Samples for crosslinking experiments were prepared by mixing known amounts of water, dendrimer and salt stock solutions. Glutaraldehyde-water solutions were prepared by weight. Small aliquots (<40 μL) of glutaraldehyde stock solutions were slowly added to the dendrimer-salt solutions under 100 rpm stirring. Cross-linked dendrimer samples were characterized by measuring the and by using dynamic light scattering (DLS) and field-emission scanning electronic microscopy (SEM).

2.6. Host-Guest Experiments for Crosslinked PAMAM-NH_2

An aqueous stock solutions of phenol blue (11 mM) was prepared by mixing a known weight of this dye with water in a 1-L volumetric flask. A dendrimer-water stock solution (1.9% w/w, 1.3 mM, 1 mL) was also prepared by weight and mixed with an equal volume of phenol blue stock solution so that the dendrimer molar concentration was 0.65 mM. The molar ratio of dye to dendrimer in the resulting mixture of 2 mL was ≈0.01. This mixture was stirred at room temperature in the dark during the incubation time of 48 hours. The absorbance spectrum of the mixture was recorded (DU800, Beckman Coulter) before and after the incubation time. The binding of blue phenol to dendrimer is verified by the occurrence of the wavelength shift of the maximum absorbance from 635 nm to 545 nm[121]. Control measurements, directly performed on the phenol blue stock solution before and after the incubation time (also stored in the dark), show no detectable change in the absorption spectrum. After the sample incubation time, toluene (2 mL) was added to the dendrimer-dye aqueous solution[122]. The biphasic sample was thoroughly shaken for 10 min. The sample was then allowed to achieve macroscopic phase separation first by gravity and then by centrifugation (10 min at 2500 rpm, AllegraTM 25 R centrifuge, Beckman Coulter) until a clear interface is observed between the organic (top) and the aqueous (bottom) phases. Aliquots from both organic and aqueous phases were transferred into different vials and the visible spectrum of each phase was recorded. No phenol blue could be detected in the organic phase by spectrophotometry. In a control experiment, a 2-mL solution of phenol blue, which was prepared by mixing 1 mL of the stock solution with water, was added to an equal volumetric amount of toluene. After the equilibration procedure, the dye transferred to the organic phase and no phenol blue could be detected in the aqueous phase by spectrophotometry. The dye-loaded dendrimer aqueous solution was then crosslinked using glutaraldehyde in the presence of sodium sulfate. Specifically, a 1-mL aliquot of the dye-loaded dendrimer solution was first concentrated by evaporation in a vacuum oven at room temperature and then mixed with a sodium sulfate stock solution and water so that the final sample volume remained of 1 mL. A small amount (60 mL) of aqueous stock solution of glutaraldehyde (5% w/w) was then steadily added to ensure that dendrimer crosslinking and aggregation occurred. The equilibration procedure in the presence of 1 mL of toluene was repeated. After the equilibration procedure, no phenol blue could be detected in the organic phase by spectrophotometry.

Chapter 3: Unusual Liquid-Liquid Phase Transition of PAMAM-OH in Aqueous Mixtures

---

3.1. Introduction

In this chapter, the phase behavior of aqueous solutions containing the hydroxyl-functionalized PAMAM of forth generation (PAMAM-OH, G4) will be experimentally and theoretically investigated.

Due to the hydrophilic nature of the hydroxyl surface groups, this dendrimer is predicted to be preferentially hydrated in aqueous solutions. Thus, LLPS is not expected to be observed in water but it may be observed in the presence of salting-out agents as described for proteins and polymers (Section 1.6). Our exploratory experiments confirm that no phase separation occurs in water. Furthermore, no phase separation was observed in the presence of sodium chloride, a mild salting-out agent according to the Hofmeister series (see Section 1.6). On the other hand, we found that LLPS can be induced in the presence of sodium sulfate, a stronger salting-out agent.

LLPS occurred at ionic strengths of the order of one or higher. At these high ionic strengths, the salting-out action of salt ions on the somewhat positively charged dendrimer macro-ions is not expected to be related to electrostatic interactions but rather to dendrimer preferential hydration.

In our experiments, the composition of the ternary dendrimer-salt-water system is given by the dendrimer volume fraction, ϕ_{D}, and salt (sodium sulfate) molar concentration, C_{S}. Here, we will characterize the effect of sodium sulfate on the phase behavior of PAMAM-OH aqueous solutions by characterizing two thermodynamically independent properties of the phase boundary: (1) the LLPS temperature T_{ph} as a function of C_{S} and ϕ_{D}, and (2) salt-dendrimer partitioning between the two coexisting phases at constant temperature (25 °C).

To support our experimental findings and develop a model describing the observed behavior, thermodynamic and transport properties of ternary dendrimer-salt-water solutions were also characterized using ITC, DLS and a dendrimer-dye binding spectrophotometric assay.

3.2. Effect of Salt Concentration on LLPS Temperature

We have experimentally characterized T_{ph} as a function of C_{S} at several values of ϕ_{D}. Interestingly, these experiments revealed a peculiar temperature behavior. Specifically, LLPS switches from being induced by lowering temperature to being induced by increasing temperature as salt concentration increases and dendrimer concentration correspondingly decreases.

In Figure 14 (A, B), we report two representative turbidity profiles obtained at low (Figure 14 A) and high (Figure 14 B) salt concentration. As we can see, at low salt concentration LLPS is induced by lowering the temperature while at high salt concentration it is induced by increasing the temperature. Interestingly, these experiments show that LLPS switches from being induced by cooling to being induced by heating as the salt concentration increases. Thus, this phase transition exhibits a lower and upper critical solution temperature-type behavior.

From the turbidity profiles, we obtained the correspondent T_{ph} for the corresponding sample. In Figure 15 (A,B), we report our phase-boundary, $T_{\mathrm{ph}}(C_{\mathrm{S}})$, results obtained at relatively low (A, 0.3-0.5 mol·dm^{-3}) and high (B, 0.7-1.2 mol·dm^{-3}) salt concentrations. The numbers associated with each curve identify the corresponding value of ϕ_D. The solid lines are linear fits to the experimental data as a function of C_S at several constant dendrimer ϕ_D. In all cases, T_{ph} was found to strongly depend on salt concentration. In Figure 15 (A, B), the T_{ph} curves associated with cooling-induced and heating-induced LLPS have positive and negative slopes, respectively. Since the two-phase domain is located below a given T_{ph} curve in Figure 15A, a positive slope implies that the two-phase domain increases with salt concentration. On the other hand, the two-phase domain is located above a given T_{ph} curve in Figure 15B. This implies that the two-phase domain increases with salt concentration if the slope is negative.

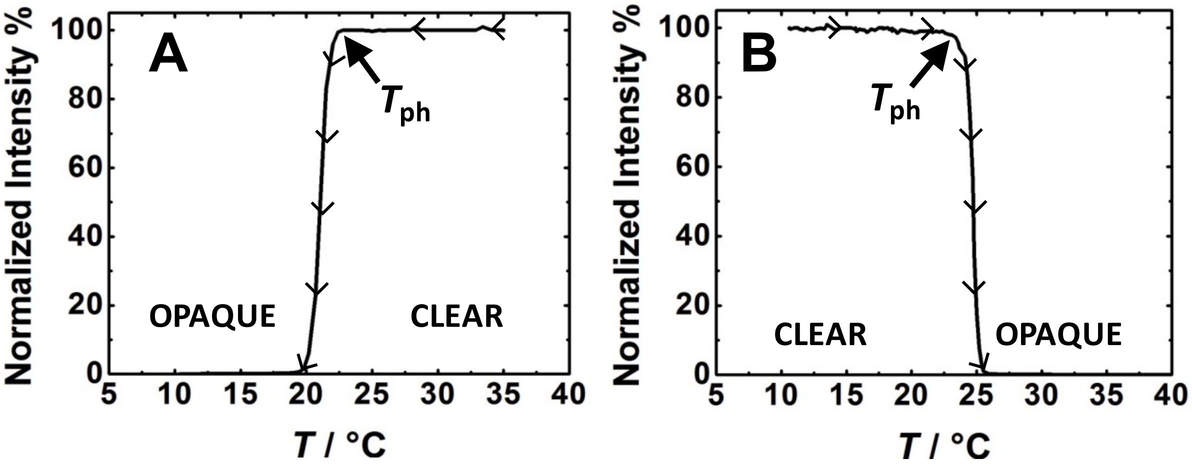

Figure 14. Normalized-transmitted-intensity profile corresponding to a sample at (A) low salt concentration ($\phi_D = 0.29$ and $C_S = 0.38$ M) and (B) high salt concentration ($\phi_D = 0.049$ and $C_S = 0.98$ M). The LLPS temperature, T_{ph}, was identified as the temperature at which a sharp decrease in intensity is observed.

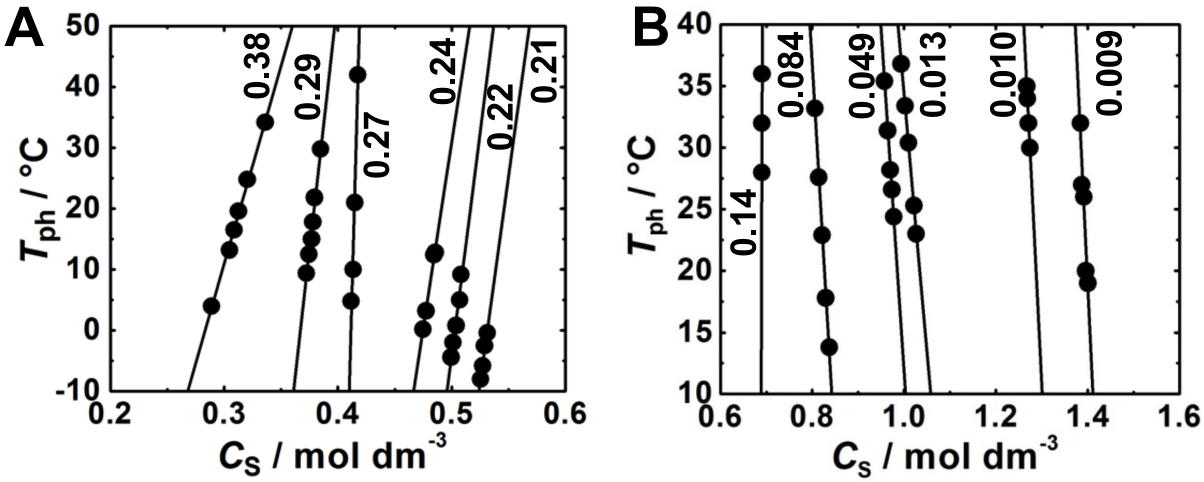

Figure 15. T_{ph} as a function of salt concentration at several constant dendrimer molar fractions. The numbers associated with each curve identify the corresponding value of ϕ_D. The solid lines are linear fits to the experimental data.

Experiments in a narrow range of intermediate salt concentrations revealed that the turbidity of initially homogenous samples was found to increase by both cooling and heating as shown in Figure 16. This behavior, which implies that $T_{ph}(C_S)$ can assume two values at the same salt concentration, could of the detected only in a narrow range of salt concentrations due to the steepness of the $T_{ph}(C_S)$ curves. In Section 3.9, we further explain the observed thermal behavior by using our thermodynamic model.

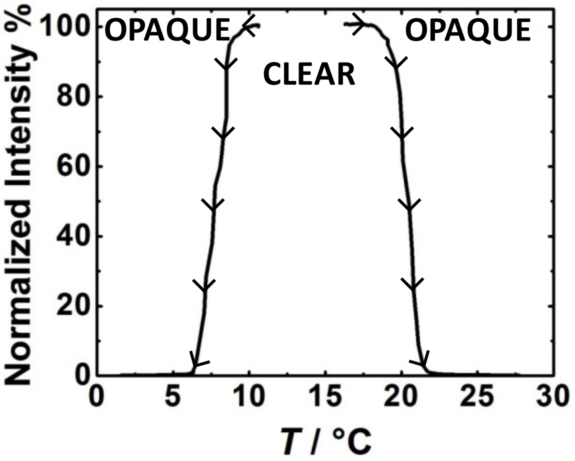

Figure 16. Normalized-transmitted-intensity profile observed for the dendrimer-salt-water system at $C_\mathrm{S} = 0.51 \mathrm{mol \cdot dm^{-3}}$ and $\phi_\mathrm{D} = 0.20$.

3.3. Salt-Dendrimer partitioning.

At a fixed temperature, LLPS yields the formation of two coexisting liquid phases with compositions $(C_\mathrm{S}^{(\mathrm{I})}, \phi_\mathrm{D}^{(\mathrm{I})})$ and $(C_\mathrm{S}^{(\mathrm{II})}, \phi_\mathrm{D}^{(\mathrm{II})})$ for phases I and II, respectively. We have experimentally characterized these compositions at 25 ºC. Our results are reported in Table 1 together with the corresponding partitioning coefficients defined as

$$\frac{\Delta C_\mathrm{S}}{\Delta \phi_\mathrm{D}} \equiv \frac{C_\mathrm{S}^{(\mathrm{II})} - C_\mathrm{S}^{(\mathrm{I})}}{\phi_\mathrm{D}^{(\mathrm{II})} - \phi_\mathrm{D}^{(\mathrm{I})}} \tag{3. 1}$$

The negative values of $\Delta C_\mathrm{S} / \Delta \phi_\mathrm{D}$ reflect a salting-out mechanism. Specifically, the preferential hydration of both solute components leads to salt-rich (I) and dendrimer-rich (II) coexisting phases[123]. Turbidity experiments revealed that the separated coexisting phases display opposite temperature responses, consistent with our results reported in Section 3.2.

Thus, this phase transition exhibits a simultaneous lower and upper critical solution temperature-type behavior.

Table 1. Salt-Dendrimer partitioning parameters at 25 °C.

$C_{\mathrm{S}}^{(\mathrm{I})}$ / mol·dm^{-3}	$\phi_{\mathrm{D}}^{(\mathrm{I})}$	$C_{\mathrm{S}}^{(\mathrm{II})}$ / mol·dm^{-3}	$\phi_{\mathrm{D}}^{(\mathrm{II})}$	$(\Delta C_{\mathrm{S}} / \Delta\phi_{\mathrm{D}})$ / mol·dm^{-3}	q
1.01	0.030	0.36	0.36	-2.0	0.25
1.19	0.038	0.33	0.35	-2.8	0.34
1.47	0.031	0.31	0.40	-3.1	0.32
1.66	0.003	0.18	0.52	-2.9	0.26

Our values in Table 1 can be used to estimate the critical dendrimer volume fraction, $\phi_{\mathrm{D}}^{(\mathrm{c})}$. This was obtained by the linear extrapolation of $(\phi_{\mathrm{D}}^{(\mathrm{I})} + \phi_{\mathrm{D}}^{(\mathrm{II})})/2$ to $|\phi_{\mathrm{D}}^{(\mathrm{II})} - \phi_{\mathrm{D}}^{(\mathrm{I})}|^{1/\beta} \to 0$, with $\beta = 0.325$ (Ising exponent) and $\beta = 0.5$ (mean-field exponent). In Figure 17, we plot $(\phi_{\mathrm{D}}^{(\mathrm{I})} + \phi_{\mathrm{D}}^{(\mathrm{II})})/2$ as a function of $|\phi_{\mathrm{D}}^{(\mathrm{II})} - \phi_{\mathrm{D}}^{(\mathrm{I})}|^{1/\beta}$ where a linear extrapolation to $|\phi_{\mathrm{D}}^{(\mathrm{II})} - \phi_{\mathrm{D}}^{(\mathrm{I})}|^{1/\beta} = 0$ yields estimates of the $\phi_{\mathrm{D}}^{(\mathrm{c})}$ value. We estimate that $\phi_{\mathrm{D}}^{(\mathrm{c})}$ is between 0.15 and 0.18, which correspond to a salt critical concentration, $C_{\mathrm{S}}^{(\mathrm{c})}$, ranging from 0.6 to 0.7 mol·dm^{-3}. Similarly, we have also used the $(\Delta C_{\mathrm{S}} / \Delta\phi_{\mathrm{D}})$ values to extract the limiting partition coefficient at the critical point, $(\partial C_{\mathrm{S}} / \partial\phi_{\mathrm{D}})_T$. In Figure 18 we plot $(\Delta C_{\mathrm{S}} / \Delta\phi_{\mathrm{D}})$ as a function of $|\phi_{\mathrm{D}}^{(\mathrm{II})} - \phi_{\mathrm{D}}^{(\mathrm{I})}|^{1/\beta}$. Linear extrapolation to $|\phi_{\mathrm{D}}^{(\mathrm{II})} - \phi_{\mathrm{D}}^{(\mathrm{I})}|^{1/\beta} = 0$ yields estimates of $(\partial C_{\mathrm{S}} / \partial\phi_{\mathrm{D}})_T$. Since $(\Delta C_{\mathrm{S}} / \Delta\phi_{\mathrm{D}})$ ratios show an error of ≈20%, the corresponding extrapolation error is also large. We estimate $(\partial C_{\mathrm{S}} / \partial\phi_{\mathrm{D}})_T$ to be in the range between -3 and -2 mol·dm^{-3}.

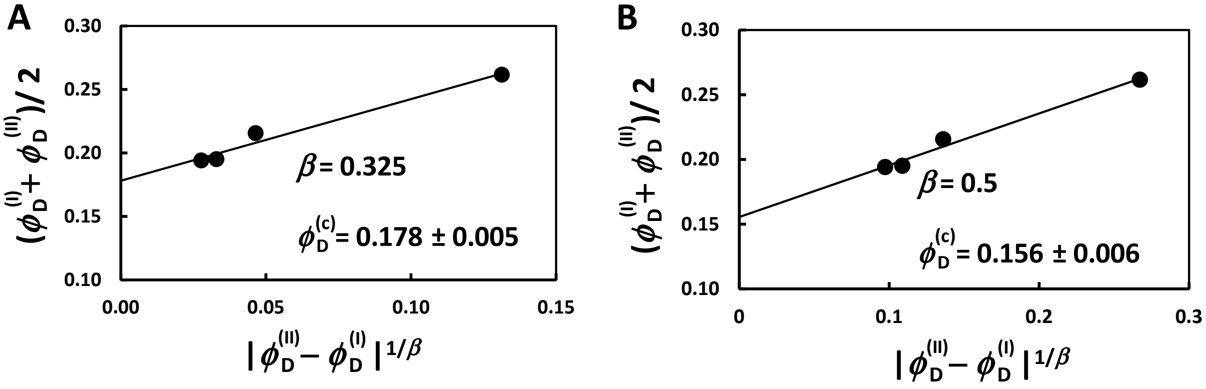

Figure 17. Plots of $(\phi_{\mathrm{D}}^{(\mathrm{I})}+\phi_{\mathrm{D}}^{(\mathrm{II})})/2$ as a function of $|\phi_{\mathrm{D}}^{(\mathrm{II})}-\phi_{\mathrm{D}}^{(\mathrm{I})}|^{1/\beta}$, where $\beta=0.325$ and $\beta=0.5$ are the Ising (A) and mean-field (B) exponents, respectively.

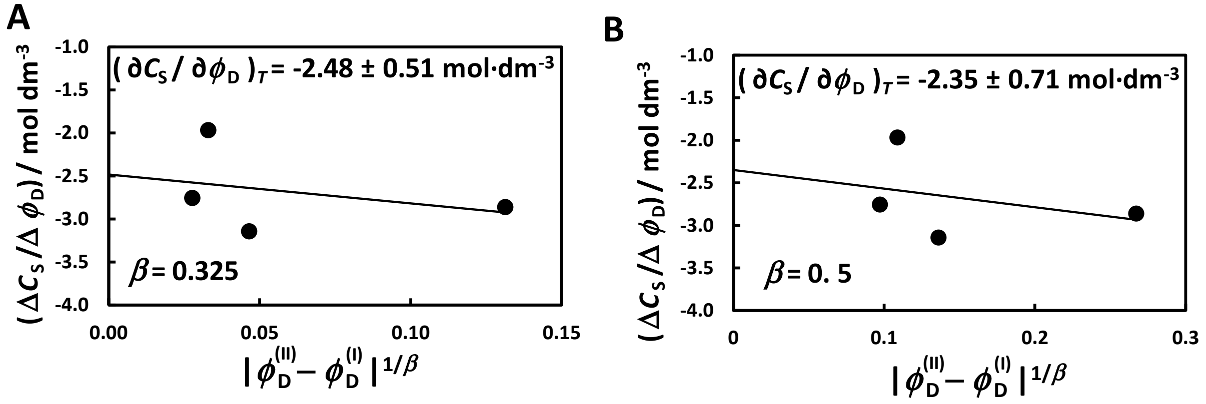

Figure 18. Plots of $(\Delta C_{\mathrm{S}}/\Delta\phi_{\mathrm{D}})$ as a function of $|\phi_{\mathrm{D}}^{(\mathrm{II})}-\phi_{\mathrm{D}}^{(\mathrm{I})}|^{1/\beta}$, where $\beta=0.325$ and $\beta=0.5$ are the Ising (A) and mean-field (B) exponents, respectively.

3.4. PAMAM-OH Dendrimer Diffusion Coefficient

The peculiar temperature behavior of this phase transition may be caused by salt-induced conformational changes in flexible dendrimers such as PAMAM. To examine this hypothesis, we determined the dendrimer hydrodynamic radius, R_{h}, at both low and high salt concentration by measuring the DLS dendrimer diffusion coefficient, D, as a function of ϕ_{D}.

At $\phi_\mathrm{D} = 0$, D becomes the dendrimer tracer-diffusion coefficient, D_0, and the Stokes-Einstein equation (see Eq. (2. 9)) can be applied, with η being the known viscosity of the salt-water system[124].

Figure 19, shows the inverse of the hydrodynamic radius, $(6\pi\eta D)/k_\mathrm{B}T$, as a function of ϕ_D at low (0.044 mol·dm^{-3}) and high (0.95 mol·dm^{-3}) salt concentrations and two temperatures, 25 and 37 °C. Experimental data were examined according to Eq. (2. 15), which was rewritten in terms of dendrimer volume fraction:

$$D = D_0(1 + k_\mathrm{D}\phi_\mathrm{D}) \tag{3. 2}$$

The intercept, D_0, and the normalized unitless slope, k_D, are obtained by applying the method of least squares and they are reported in Table 2 together with the corresponding values of R_h. In all cases, the hydrodynamic radius was found to be 2.6 nm within the experimental error. Thus, salt and temperature changes have no appreciable effect on dendrimer size.

We now turn our attention to the values of k_D in Table 2. Since these are positive at low salt concentration, dendrimer-dendrimer interactions are repulsive in these conditions[125,126]. On the other hand, k_D becomes negative at high salt concentration. This indicates that dendrimer-dendrimer interactions become more attractive as salt concentration increases, consistent with the salting-out mechanism. In Table 2, we can also see that the effect of temperature on k_D is small.

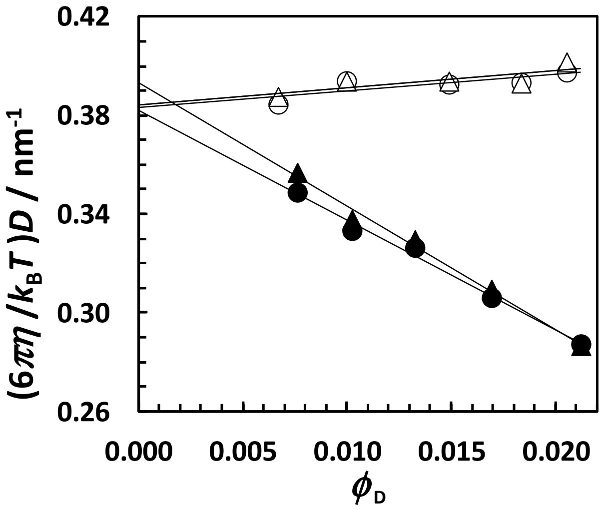

Figure 19. Normalized DLS diffusion coefficient as a function of PAMAM-OH dendrimer volume fraction, ϕ_D, at two salt concentrations, $C_S = 0.044\ \mathrm{mol \cdot dm^{-3}}$ (open circles, 25 ºC; open triangles, 37 ºC), and $C_S = 0.949\ \mathrm{mol \cdot dm^{-3}}$ (closed circles, 25 ºC; closed triangles, 37 ºC). The solid lines are linear fits through the data.

Table 2. DLS parameters for PAMAM-OH.

C_S / mol·dm^{-3}	T / °C	D_0 / 10^{-9}·m^2·s^{-1}	η / 10^{-3}·kg·m^{-1}·s^{-1}	R_h / nm	k_D
0.044	25.0	0.0920±0.0010	0.909	2.61±0.03	1.8±0.4
0.949	25.0	0.0615±0.0006	1.357	2.62±0.03	-11.6±0.4
0.044	37.0	0.1236±0.0014	0.706	2.60±0.03	1.8±0.4
0.949	37.0	0.0852±0.0009	1.048	2.54±0.03	-12.7±0.4

3.5. Dendrimer-dye binding

We also characterized the effect of salt concentration on the binding affinity of dendrimer to phenol blue since it is possible to have dendrimer conformational changes without having large changes in dendrimer size. Phenol blue is a dye that has been shown to bind to

PAMAM dendrimers[121,122]. This dye possesses an absorption band with a maximum at 646.5 nm in water[121]. However, as the polarity of the dye environment decreases, the intensity of the absorbance at 646.5 nm correspondingly decreases. Thus, the binding of dye to dendrimers will reduce the absorbance at 646.5 nm due to its less polar properties. Since dendrimer cavity accessibility and surface properties are expected to change in the presence of conformational changes, we expect that the dye spectrophotometric properties be sensitive to these changes. Our results in Figure 20 show that dendrimer-dye binding occurs. However, no appreciable change in absorbance is observed as salt concentration increases. Thus, our experimental results are consistent with salt having no appreciable effect on the dendrimer conformational state.

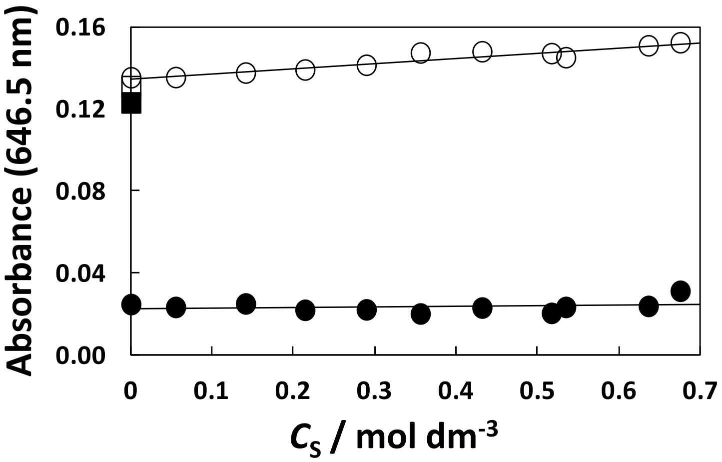

Figure 20. Absorbance of phenol blue as a function of salt concentration, C_S, measured for freshly prepared solutions (open circles) and after 24 hours (solid circles) at room temperature at $\phi_D = 0.020$ (solid circles, dye-to-dendrimer molar ratio, $\approx 6\times10^{-3}$). The solid lines are linear fits through the data. The open and the solid squares at $C_S = 0$, represent the absorbance of the dendrimer-free solution measured for a freshly prepared solution and after 24 hours, respectively.

3.6. Thermodynamic model

In this section, we develop a thermodynamic model that can be used to describe the phase behavior of ternary dendrimer-salt-water systems. For the purpose of clarity, we shall focus on the main aspects of the model in this section and skip some technical details. A more comprehensive description of this model is reported as Section 3.10 at the end of this Chapter.

Our thermodynamic model assumes that dendrimers have a globular compact conformational state consistent with the presence of a strong salting-out agent. For these globular particles, the hard-sphere suspension was chosen as the reference system in the proposed model[96,95]. As we describe in Section 1.5, our goal is to identify an equation of state for the dendrimer particles, which can be then used to compute the LLPS boundary. In our case, we add an energy term to the equation of state for hard spheres. This extra term describes an energetic contribution due to dendrimer-dendrimer interactions. Our ITC experiments (see section 3.7) confirm this energetic contribution.

In Section 1.6 we also described the effect of salt on globular macromolecules using the preferential-hydration formalism based on the existence of two domains[109,112]. Since dendrimers interact with the salt and water molecules in their vicinity (within a distance of a few Å), the concentration of salt in the local domain is different from that of the unperturbed bulk domain. If dendrimer preferential hydration occurs, the salt concentration in the local domain is lower than that of the bulk domain, which corresponds to salting-out conditions. Thus, the local domain will consist of dendrimer particles and their adjacent salt-depleted aqueous layer. For strong salting-out agents such as sodium sulfate, the salt concentration in the local domain can be considered negligible.

The existence of the salt-depleted layer increases the chemical potential of the dendrimer by an amount that is equal to the reversible work performed against salt osmotic pressure in order to maintain salt ions outside the local domain. The presence of salt-depleted layers favors LLPS because the contacts between macromolecules reduce the overall volume of the local domain, thereby reducing the work contribution to the macromolecule chemical potential.

According to the two-domain model (see Section 1.6), the thermodynamic properties of the salt in the bulk domain are the same as those of a binary salt-water reservoir in equilibrium dialysis with our dendrimer-salt-water system through a membrane nor permeable to the dendrimer[109–111]. The pressure difference between the ternary mixture and the binary reservoir is the osmotic pressure of the dendrimer particles. It can be then shown that (see Section 3.10 for details):

$$p = p_{\mathrm{D}} - (1 - \alpha + \alpha' \phi_{\mathrm{D}}) p_{\mathrm{S}} \tag{3. 3}$$

where $p \equiv \Pi V_{\mathrm{D}} / RT$, $p_{\mathrm{D}} \equiv \Pi_{\mathrm{D}} V_{\mathrm{D}} / RT$, and $p_{\mathrm{S}} \equiv \Pi_{\mathrm{S}} V_{\mathrm{D}} / RT$ are the unitless reduced pressure parameters; Π is the osmotic pressure of the dendrimer particles, Π_{D} is the corresponding contribution in the absence of bulk domain, Π_{S} is the salt osmotic pressure of the binary reservoir (and the bulk domain) in the ternary mixture and $V_{\mathrm{D}} = 11.7$ dm^3·mol^{-1} is the dendrimer molar volume[74]. Note that α is the volume fraction of the bulk domain with $\alpha' \equiv (\partial \alpha / \partial \phi_{\mathrm{D}})_T$.

The salt osmotic pressure contribution, p_{S}, can be related to the known temperature-dependent osmotic coefficient $\varphi(C_{\mathrm{S}}^{*},T)$ using[127]:

$$p_{\mathrm{S}} = \gamma_{\mathrm{D}} \nu_{\mathrm{S}}\, \varphi(C_{\mathrm{S}}^{*},T)\, C_{\mathrm{S}}^{*} / C_{\mathrm{W}}^{*} \tag{3. 4}$$

where $\gamma_{\mathrm{D}} \equiv V_{\mathrm{D}} / V_{\mathrm{W}} = 645$, $\nu_{\mathrm{S}} = 3$ for sodium sulfate, C_{W}^{*} is the water molar concentration in the binary reservoir. At a given $C_{\mathrm{S}}^{*} / C_{\mathrm{W}}^{*}$, the salt osmotic coefficient is known to increase with temperature for sodium sulfate. If the salt molar concentration in the binary reservoir is C_{S}^{*}, then the salt concentration in the ternary mixture is $C_{\mathrm{S}} = C_{\mathrm{S}}^{*} \cdot \alpha(\phi_{\mathrm{D}},T)$.

For a suspension of identical hard spheres with volume fraction, ϕ_{D}, the bulk-domain volume fraction, $\alpha(\phi_{\mathrm{D}},T)$, can be described as the probability of a successful insertion of a distinct test hard sphere with radius equal to the thickness of the salt-depleted layer (local domain). This implies that $\alpha(\phi_{\mathrm{D}},T)$ can be obtained from the excess chemical potential of the test particle, $(-RT\ln\alpha)$ (see section 3.10). We choose the temperature-independent expression of α obtained from the Mansoori-Carnahan-Starling-Leland equation of state for a binary hard-sphere mixture[128,129]

$$\alpha = (1-\phi_{\mathrm{D}})\exp\left[-A\eta_{\mathrm{D}} - B\eta_{\mathrm{D}}{}^{2} - C\eta_{\mathrm{D}}{}^{3} + D\ln(1+\eta_{\mathrm{D}})\right] \tag{3. 5}$$

where $\eta_{\mathrm{D}} \equiv \phi_{\mathrm{D}} / (1-\phi_{\mathrm{D}})$, $A \equiv 3q + 6q^{2} - q^{3}$, $B \equiv 3q^{2} + 4q^{3}$, $C \equiv 2q^{3}$, $D \equiv 3q^{2} - 2q^{3}$ and q is the ratio of the thickness of the salt-depleted layer to the particle radius. In the limit of $\phi_{\mathrm{D}} \to 0$, the volume fraction of bulk domain is given by $\alpha = 1-(1+q)^{3}\phi_{\mathrm{D}}$. As ϕ_{D} increases, particle-particle contacts reduce the volume of the local domain, which implies that

$\alpha'' \equiv d^2\alpha / d\phi_{\mathrm{D}}^2$ is positive. The parameter, q, characterizes the strength of the salting-out interactions in our model.

For the osmotic pressure for the dendrimer in the absence of bulk domain, we propose the following expression:

$$p_{\mathrm{D}} = \left(1 + b\ \phi_{\mathrm{D}} + \frac{e}{RT}\phi_{\mathrm{D}}\right)\phi_{\mathrm{D}} \tag{3. 6}$$

where the first term in parenthesis represents the ideal contribution to osmotic pressure while $b(\phi_{\mathrm{D}})$ and $e(\phi_{\mathrm{D}})$ are temperature-independent functions describing the steric entropic term and the energetic contribution of dendrimer-dendrimer interactions, respectively. The expression for $b(\phi_{\mathrm{D}})$ was already stated in Section 1.5 (see Eq. (1. 22)). The quantity $e(\phi_{\mathrm{D}})$ can be linked to the excess internal energy, U_{D}, of the dendrimer particles in the absence of bulk domain. This will be described by introducing the intensive property, $\omega_{\mathrm{D}} \equiv U_{\mathrm{D}} V_{\mathrm{D}} / V$ where $V_{\mathrm{D}} = 11.7\ \mathrm{dm}^3 \cdot \mathrm{mol}^{-1}$ is the dendrimer molar volume and V the total volume. The thermodynamic link between $\omega_{\mathrm{D}}(\phi_{\mathrm{D}})$ and $e(\phi_{\mathrm{D}})$ is given by:

$$\omega_{\mathrm{D}} = \phi_{\mathrm{D}}\, \tilde{e}(\phi_{\mathrm{D}}) \tag{3. 7}$$

where $\tilde{e}(\phi_{\mathrm{D}}) \equiv \int_0^{\phi_{\mathrm{D}}} e(x)\,dx$, with x being the integration variable and $\tilde{e}(0) = 0$ (see Section 3.10 for details).

3.7. Excess internal energy

The excess internal energy associated with dendrimer-dendrimer interactions can be obtained from measurements of heat associated with the dilution of the dendrimer particles (see Figure 21). Specifically, we have measured the differential heat associated with consecutive injections of concentrated dendrimer solutions (titrant) into an initially dendrimer-free solution (titrand). Since the proposed model does not take into account electrostatic and pH effects associated with the dendrimer net charge and acid-base properties of the tertiary amines, we have used a buffer aqueous solution with pH=7.0 and an ionic strength of 0.14 instead of pure water as the titrand.

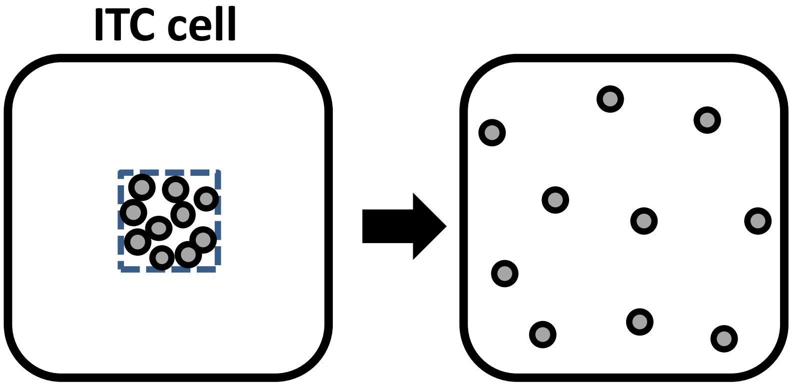

Figure 21. Scheme describing the dilution process from the dendrimer volume fraction, ϕ_D^0 (left) to ϕ_D (right) occurring inside the ITC cell.

As it can be seen from the dilution power peaks (see Figure 22), and the corresponding values of differential heats (see Figure 23) in dendrimer dilution is an exothermic process. As dendrimer concentration decreases, dendrimer-dendrimer contacts correspondingly decrease thereby increasing the average exothermic hydration per dendrimer particle. This implies that dendrimer-dendrimer interactions are endothermic.

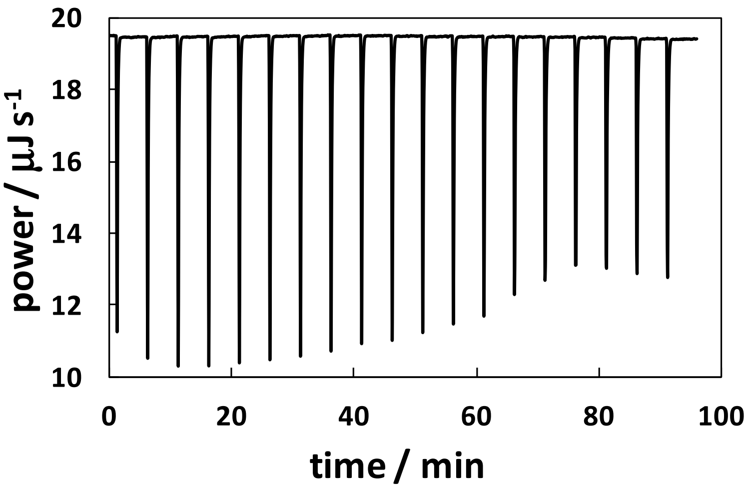

Figure 22. Representative ITC Power-time profile associated with consecutive injections of titrant solution ($\phi_{\mathrm{D}}^{0} = 0.191$) into the titrand solution inside the ITC cell.

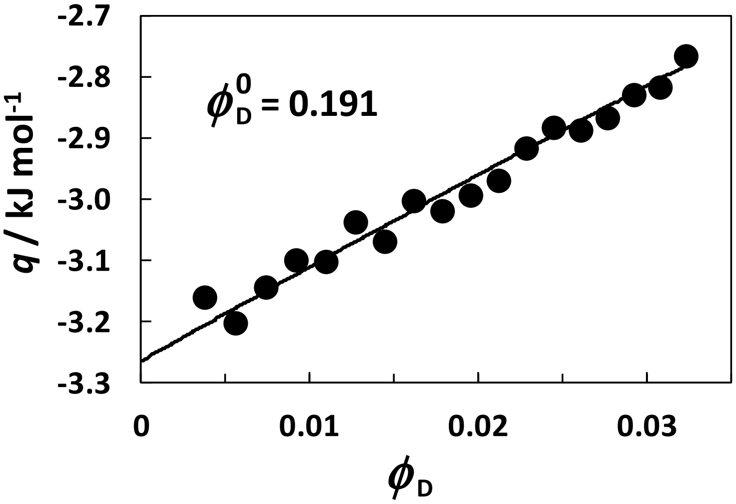

Figure 23. Differential heat, q, extracted from the shown power-time profile as function of dendrimer volume fraction inside the ITC cell, ϕ_{D}, after each injection. The solid curve is a fit through the data based on (2. 38), (3. 8), (3. 11).

The cumulative heat $V_{\mathrm{D}}Q/V$ in Eq. (2. 38) (see Section 2.3.4) is linked to ω_{D} by applying:

$$\frac{V_{\mathrm{D}}Q}{V} = \omega_{\mathrm{D}}(\phi_{\mathrm{D}}) - \frac{\phi_{\mathrm{D}}}{\phi_{\mathrm{D}}^{0}}\omega_{\mathrm{D}}(\phi_{\mathrm{D}}^{0}) \tag{3. 8}$$

where ϕ_{D}^{0} is the dendrimer volume fraction of the titrant solution, and $\phi_{\mathrm{D}} << \phi_{\mathrm{D}}^{0}$ is the dendrimer volume fraction inside the ITC cell after a given titrant injection. Note that a simple extrapolation of differential-heat values to $\phi_{\mathrm{D}} \to 0$ give estimates of $\omega_{\mathrm{D}}(\phi_{\mathrm{D}}^{0})$. However, to extract accurate energy values from our ITC data, an analytical expression of ω_{D} in Eq. (3. 8) is needed.

We start by linking the excess internal energy to microscopic properties (see Section 1.5) by using

$$U_{\mathrm{D}} = \frac{N_{\mathrm{D}}^{2}}{2V}\int_{0}^{\infty}(4\pi r^{2})u(r)g(r)\,dr \tag{3. 9}$$

where $u(r)$ is the pairwise particle-particle potential energy, r is the particle-particle distance and $g(r)$ is the corresponding radial distribution function[96]t (see Section 3.10 for details). It follows that ω_{D} is given by,

$$\omega_{\mathrm{D}} = \frac{2\pi\phi_{\mathrm{D}}^{2}}{V_{\mathrm{D}}}\int_{0}^{\infty} r^{2}u(r)g(r)\,dr \tag{3. 10}$$

In our case, we examine the accuracy of two simple expressions of $g(r)$ associated with the two limiting cases of infinitely long and infinitely short range of interactions using the observed dependence of ω_{D} on ϕ_{D}. Using Eq. (3. 10), we have first examined the Van-der-Waals[125] limiting expression of $\omega_{\mathrm{D}} = \varepsilon\phi_{\mathrm{D}}^{2}$, obtained by setting $g(r) \equiv 1$ in Eq. (3. 10), where ε is a constant energy parameter (positive for repulsive interactions). However, the ITC experimental dependence of ω_{D} on ϕ_{D} was found to be appreciably stronger than that predicted by this simple quadratic expression. A more accurate representation of our ITC results is achieved by considering the range of dendrimer-dendrimer interactions as infinitely short. In other words, we assume that dendrimer dehydration occurs only when dendrimer particles are in close contact. To obtain the corresponding analytical expression of ω_{D}, we set $u(r) = \varepsilon V_{\mathrm{D}} \delta(r-\sigma)$ with $r \geq \sigma$, where σ is the particle diameter, ε is the energy parameter and $\delta(r-\sigma)$ is the radial Dirac function with $4\pi\int_0^{\infty} r^2\delta(r-\sigma)\,dr = 1$. For $g(r)$ in Eq. (3. 10), we take the Carnahan-Starling contact value of $g(\sigma) = (1-\phi_{\mathrm{D}}/2)/(1-\phi_{\mathrm{D}})$ [96,130]. Thus Eq. (3. 10) becomes:

$$\omega_{\mathrm{D}}(\phi_{\mathrm{D}}) = \frac{\varepsilon}{8} b(\phi_{\mathrm{D}})\phi_{\mathrm{D}}^{2} \tag{3. 11}$$

and, consequently,

$$U_{\mathrm{D}} = N\frac{\varepsilon}{8} b\phi_{\mathrm{D}} \tag{3. 12}$$

The expressions of $\omega_{\mathrm{D}}(\phi_{\mathrm{D}})$ and $\omega_{\mathrm{D}}(\phi_{\mathrm{D}}^{0})$ given by Eq. (3. 11) are first inserted into Eq. (3. 8). The resulting expression for $V_{\mathrm{D}}Q/V$ is then inserted into Eq. (2. 38) so that a value of ε and $\omega_{\mathrm{D}}(\phi_{\mathrm{D}}^{0})$ can be determined for a given ITC experiment. As we can see in Table 3, the values of ε are in good agreement with each other, thereby supporting the validity of Eq. (3. 11). A unique value of ε is obtained by applying the method of least squares based on Eq. (3. 11) to the $\omega_{\mathrm{D}}(\phi_{\mathrm{D}}^{0})$ data in Figure 24. We obtain: $\varepsilon = (19.9 \pm 0.3)$ kJ $\cdot$mol^{-1}, which corresponds to $\varepsilon / RT = 8.0 \pm 0.1$ at 25 °C.

Table 3. ITC parameters at 25 °C.

ϕ_D^0	ε / kJ·mol^{-1}	w_D / kJ·mol^{-1}
0.103	18.1	0.127
0.130	18.8	0.227
0.173	20.6	0.500
0.191	19.8	0.612

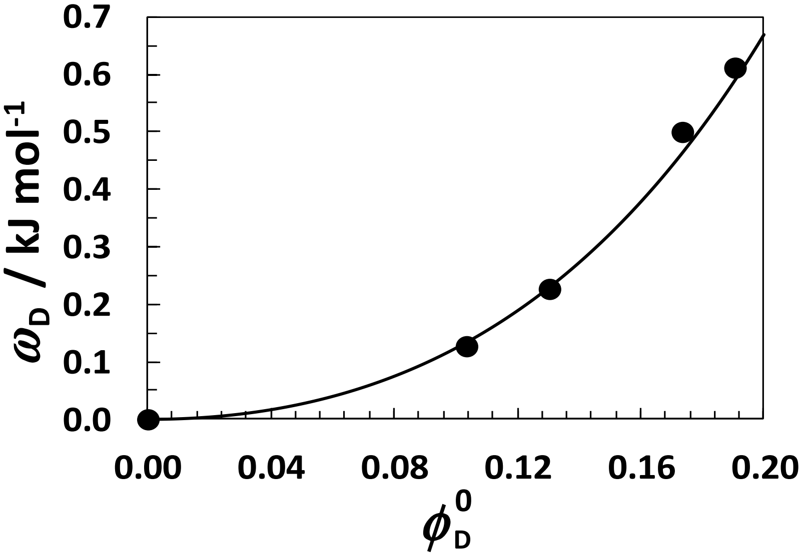

Figure 24. Reduced excess internal energy, ω_D, as a function of ϕ_D^0. The solid curve is a fit through the data based on Eq. (3. 11).

3.8. Binodal Curve for PAMAM-OH System

The experimental LLPS properties at 25 °C are described by an isothermal curve in the (C_S, ϕ_D) phase diagram known as the binodal. We extract the experimental binodal at 25 °C by interpolating the turbidity data in Figure 15. The corresponding experimental data are shown in Figure 25. We then construct a theoretical binodal starting from the equation of state discussed in Section 3.6. After inserting Eq. (3. 6) into Eq. (3. 3), we obtain:

$$p = (1 + b\phi_{\mathrm{D}})\phi_{\mathrm{D}} + \frac{1}{8}\frac{\varepsilon}{RT}(b + b'\phi_{\mathrm{D}})\phi_{\mathrm{D}}{}^{2} - (1 - \alpha + \phi_{\mathrm{D}}\alpha')\, p_{\mathrm{S}} \tag{3. 13}$$

with $e(\phi_{\mathrm{D}}) = (\varepsilon/8)(b + b'\phi_{\mathrm{D}})\phi_{\mathrm{D}}$ from Eqs. (3. 7), (3. 11). The corresponding expression for $\mu \equiv (\mu_{\mathrm{D}} - \mu_{\mathrm{D}}^{0})/RT$, where μ_{D} is the dendrimer chemical potential (the effective chemical potential $\tilde{\mu}_{\mathrm{P}}$ in Section 1.4) and μ_{D}^{0} its standard value, is obtained from Eq. (3. 13) by applying the Gibbs-Duhem condition: $\phi_{\mathrm{D}}\,(\partial\mu/\partial\phi_{\mathrm{D}})_{T,p_{\mathrm{S}}} = (\partial p/\partial\phi_{\mathrm{D}})_{T,p_{\mathrm{S}}}$:

$$\mu = (\ln\phi_{\mathrm{D}} + \tilde{b} + b\phi_{\mathrm{D}}) + \frac{1}{8}\frac{\varepsilon}{RT}(2b + b'\phi_{\mathrm{D}})\phi_{\mathrm{D}} - \alpha' p_{\mathrm{S}} \tag{3. 14}$$

where $\tilde{b}(\phi_{\mathrm{D}}) \equiv \int_0^{\phi_{\mathrm{D}}} b(x)\,dx$.

To construct the theoretical binodal, q in the expression of α is left as the only parameter to be varied. For a given value of q, the theoretical binodal is calculated in the following way. We start from a value of p_{S} that is just high enough to produce a non-monotonic behavior of $p(\phi_{\mathrm{D}})$ and $\mu(\phi_{\mathrm{D}})$. At this value of p_{S}, we numerically determine the values of $\phi_{\mathrm{D}}^{(\mathrm{I})}$ and $\phi_{\mathrm{D}}^{(\mathrm{II})}$ that satisfy the equilibrium conditions: $p(\phi_{\mathrm{D}}^{(\mathrm{I})}) = p(\phi_{\mathrm{D}}^{(\mathrm{II})})$ and $\mu(\phi_{\mathrm{D}}^{(\mathrm{I})}) = \mu(\phi_{\mathrm{D}}^{(\mathrm{II})})$. This procedure is then repeated for higher values of p_{S}. The corresponding salt concentrations are obtained by first extracting C_{S}^{*} from Eq. (3. 4) and then applying $C_{\mathrm{S}}^{(\mathrm{I})} = C_{\mathrm{S}}^{*}\,\alpha(\phi_{\mathrm{D}}^{(\mathrm{I})})$ and $C_{\mathrm{S}}^{(\mathrm{II})} = C_{\mathrm{S}}^{*}\,\alpha(\phi_{\mathrm{D}}^{(\mathrm{II})})$. The compositions of the two coexisting phases, $(C_{\mathrm{S}}^{(\mathrm{I})}, \phi_{\mathrm{D}}^{(\mathrm{I})})$ and $(C_{\mathrm{S}}^{(\mathrm{II})}, \phi_{\mathrm{D}}^{(\mathrm{II})})$, are connected by tie lines (solid lines in Figure 25). The critical point is calculated by the linear extrapolation of $(\phi_{\mathrm{D}}^{(\mathrm{I})} + \phi_{\mathrm{D}}^{(\mathrm{II})})/2$ and p_{S} to $|\phi_{\mathrm{D}}^{(\mathrm{II})} - \phi_{\mathrm{D}}^{(\mathrm{I})}|^{1/\beta} \to 0$, where $\beta = 0.5$ is the appropriate exponent for this model.

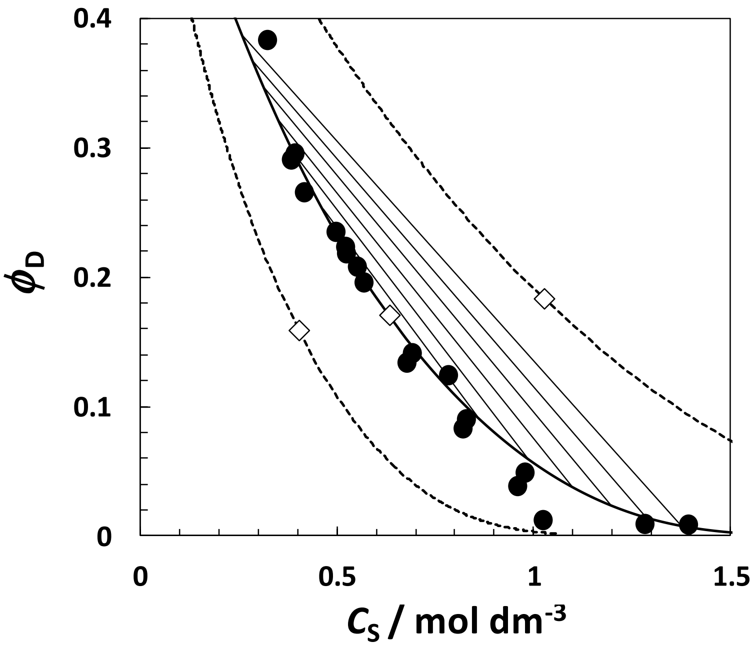

Figure 25. Binodal data, ϕ_D as a function of C_S, for the dendrimer-salt-water system at 25 ºC (solid circles). The solid curve is the theoretical binodal with $q = 0.35$. The solid lines are the corresponding calculated tie-lines. The dashed curves on the left and right sides are theoretical binodal with $q = 0.40$ and $q = 0.30$, respectively. The open diamonds represent the location of the critical point for each binodal curve.

As q increases, the theoretical binodal curve horizontally shifts towards lower salt concentrations, together with the critical salt concentration, $C_S^{(c)}$. This reflects the increasing strength of the salting-out agent. As shown in Figure 25, the theoretical binodal is in good agreement with the experimental data when $q = 0.35$. Correspondingly, we obtain $C_S^{(c)} = 0.63\,\text{mol·dm}^{-3}$ and $\phi_D^{(c)} = 0.17$, in good agreement with our experimental findings (see Section 3.3). The proposed model also predicts the experimental slope, $(\partial C_S / \partial \phi_D)_T$, at the critical point. We obtain $(\partial C_S / \partial \phi_D)_T = -(2.4 \pm 0.1)$ mol·dm^{-3} by fitting our experimental data in Figure 18 around the critical point (see Section 3.3 for details), which is in excellent agreement with the value of -2.37 mol·dm^{-3} calculated from the model with $q = 0.35$. Thus, the proposed one-parameter model can predict two features of the binodal that are thermodynamically independent of each other: the location of the critical point and the boundary slope around the critical point. However, some deviation between the experimental and the model appears at salt concentrations around ≈ 1 mol·dm^{-3}.

The slope, $(\partial C_{\mathrm{S}} / \partial \phi_{\mathrm{D}})_T$, at the critical point also represents the limiting value of the salt-dendrimer partitioning coefficient, $\Delta C_{\mathrm{S}} / \Delta \phi_{\mathrm{D}}$, at this point as discussed in Section 3.3. It is important to note that the value obtained from the turbidity data is in agreement with that obtained from partitioning data within the experimental error. Furthermore, these salt-dendrimer partitioning data can be also used to extract values of q by applying the condition:

$$C_{\mathrm{S}}^{*} = \frac{C_{\mathrm{S}}^{(\mathrm{I})}}{\alpha(\phi_{\mathrm{D}}^{(\mathrm{I})})} = \frac{C_{\mathrm{S}}^{(\mathrm{II})}}{\alpha(\phi_{\mathrm{D}}^{(\mathrm{II})})} \tag{3. 15}$$

The calculated q values, which are also included in Table 1, are comparable with $q = 0.35$ and range from 0.25 to 0.34. These variations can be attributed to the large experimental error associated with the partitioning coefficients in Table 1.

Finally, we have also used our thermodynamic model to examine the behavior of the DLS diffusion coefficient. In the limit of $\phi_{\mathrm{D}} \to 0$, D can be written as

$$D = D_0 [1 + (k_H + k_S) \phi_{\mathrm{D}}] \tag{3. 16}$$

where k_H and k_S are two parameters describing hydrodynamic and thermodynamic interactions, respectively[125,126]. Since $(\partial p / \partial \phi_{\mathrm{D}})_{T,p_{\mathrm{S}}} = 1 + k_S\, \phi_{\mathrm{D}}$ in the limit of $\phi_{\mathrm{D}} \to 0$, Eq. (3. 13) yields

$$k_S = 8 + \frac{\varepsilon}{k_\mathrm{B}T} - \alpha''(0)\,p_\mathrm{S} \qquad (3.\ 17)$$

with $\alpha''(0) = (12 + 15q + 6q^2 + q^3)\,q^3$. If we assume that the hydrodynamic parameter, k_H, is independent of salt concentration and temperature, and set the value of k_D at C_S =0.05 mol·dm^{-3} and 25 °C as the reference, the agreement of the other values of k_D in Table 2 with theoretical predictions is achieved when $q = 0.33$. When, instead, we set $q = 0.35$, the predicted value of k_D at C_S =0.95 mol·dm^{-3} is about 20% lower than that reported in Table 2. This is still an acceptable result considering that we have approximated k_H as a constant. Our model also predicts that the temperature dependence of k_D is small, consistent with our findings (see Section 3.10 for details).

3.9. LLPS Thermal behavior

We now examine the anomalous temperature response discussed in Section 3.3. The observed thermal behavior can be thought as the net result of at least two thermodynamic factors of comparable contribution, but with opposite temperature responses. Thus, a quantitative prediction of the behavior of $T_\mathrm{ph}(C_\mathrm{S}, \phi_\mathrm{D})$ is difficult to achieve. However, our model can be used to understand the two main features of LLPS: 1) LLPS switches from being induced by cooling to being induced by heating as C_S increases and ϕ_D correspondingly decreases (see Figure 14 and Figure 15) and 2) the existence of a narrow composition domain in which LLPS can be induced by both increasing and decreasing temperature (see Figure 16).

According to Eq. (3. 3), p_{D} , p_{S} and α are the three quantities regulating the thermodynamic behavior of the ternary dendrimer-salt-water system. The first quantity, p_{D}, describes the net dendrimer-dendrimer interactions in the absence of bulk domain. Since our ITC results show that dendrimer-dendrimer interactions are endothermic, dendrimer-dendrimer repulsion decreases as temperature increases. The second quantity, p_{S}, describes salt thermodynamic non-ideality. According to osmotic-coefficient data,[127] p_{S} increases with temperature at a any given salt concentration. Thus, the salt effectiveness in inducing LLPS increases with temperature. Clearly, the thermal behavior of both p_{D} and p_{S} indicate that LLPS should be induced only by heating. While this analysis is in agreement with the experimental behavior observed at low ϕ_{D}, it fails to predict the thermal behavior observed at high ϕ_{D}. To address this aspect within the framework of our model, we assume that the parameter q in the expression of α increases as temperature decreases. This implies that the salting-out strength of salt increases as temperature decreases.

As a numerical example, we compute the binodal at three representative temperatures, 25, 15 and 5 °C. In order to reproduce our experimental findings, the values of $q(T)$ are taken to be 0.3500, 0.3544 and 0.3604 at 25, 15 and 5 °C, respectively. In Figure 26, we plot $\phi_{\mathrm{D}} - \phi_{\mathrm{D}}^{(\mathrm{R})}$ as a function of C_{S}, where $\phi_{\mathrm{D}}^{(\mathrm{R})}(C_{\mathrm{S}})$ represents the binodal curve at 25 °C set to be the reference. The three relative boundaries are shown in this figure with that at 25 °C being located at $\phi_{\mathrm{D}} - \phi_{\mathrm{D}}^{(\mathrm{R})} \equiv 0$. Points below and above a given boundary correspond to homogenous mixtures and biphasic systems at the boundary temperature, respectively.

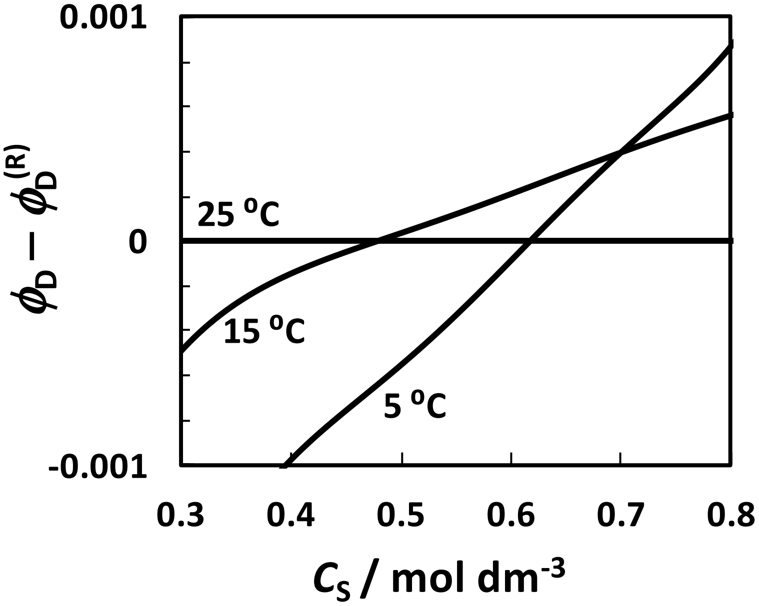

Figure 26. Calculated relative binodal curves, $\phi_D - \phi_D^{(R)}$, as a function of C_S, where $\phi_D^{(R)}$ represents the binodal at 25 °C. The numbers associated with each curve identify the corresponding value of temperature. The values of q for the binodal curves at 25, 15 and 5 °C are 0.3500, 0.3544 and 0.3604, respectively.

According to the computed curves, a point on the 15 °C binodal at $C_S \approx 0.3$ mol·dm^{-3} represents a homogeneous mixture at 25 °C, but a biphasic system at 5 °C. On the other hand, a point on the same binodal at $C_S \approx 0.8$ mol·dm^{-3} is associated with the opposite thermal behavior. This is in agreement with our experiment results in Figure 14 and Figure 15. Moreover, note that the binodal at 15 °C is located above the other two binodals when $C_S \approx 0.5\text{-}0.6$ mol·dm^{-3}. Thus, at these intermediate salt concentrations, a point slightly below the 15 °C binodal represents a homogeneous mixture at 15 °C but a biphasic system at both 5 °C and 25 °C. This is in agreement with the thermal behavior illustrated in Figure 16.

The proposed model successfully predicts that cooling-induced LLPS occurs at high ϕ_D. This can be understood by recognizing that an increase in p_S favors LLPS. Thus, we examine the dependence of p_S on temperature at constant C_S based on the observation that p_S is directly proportional to $\varphi \cdot C_S^*$ (see Eq. (3. 4)) with $C_S^* = C_S / \alpha$. If α is independent of temperature, p_S increases with T due to the corresponding increase in the salt osmotic coefficient, φ. In these conditions, LLPS can be only favored by heating. However, if α is a function of temperature, then the corresponding temperature dependence of C_S^* (at constant C_S) will also contribute to the behavior of p_S. In our numerical example, α increases with T, thereby implying that p_S may decrease as T increases if the temperature dependence of α is sufficiently strong. In these conditions, LLPS will be favored by cooling. It is important to remark that this effect is expected to prevail at relatively high ϕ_D. Indeed, according to the proposed model, LLPS is expected to be always favored by heating at sufficiently low ϕ_D since α becomes independent of temperature in the limit of $\phi_D \to 0$; i.e., $\alpha \to 1$ independent of $q(T)$.

3.10. Theoretical details on the Thermodynamic Model

According to the two-domain model, the salt thermodynamic properties in the bulk domain are the same as those of an infinitely large binary salt-water reservoir in equilibrium dialysis with a ternary dendrimer-salt-water mixture of volume, V, through a membrane not permeable to the dendrimer particles (see Figure 27). The thermodynamic properties of the reservoir are fixed at constant temperature. We denote the pressure difference between the two compartments as Π. This pressure difference between the ternary mixture and the binary reservoir is the osmotic pressure of the dendrimer particles.

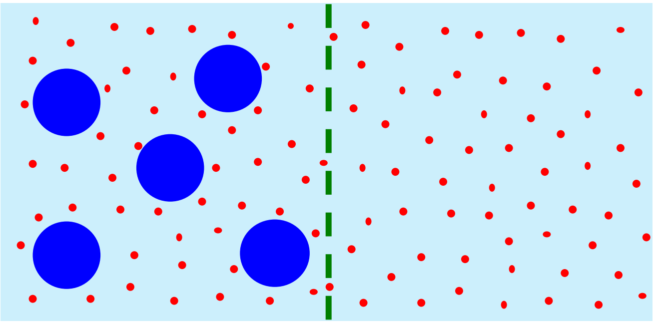

Figure 27. Scheme of equilibrium dialysis with two compartments separated by a membrane (dashed line). The left compartment contains the dendrimer particles (large blue circles) and salt (small red dots) while the right compartment only contains salt. The blue background is water. The membrane is only permeable to salt ions.

To determine Π, we treat the dendrimer solution as a suspension of N_{D} dendrimer gas particles (see Section 1.4 and 1.5). The corresponding canonical partition function, Q, is given by

$$Q = \frac{1}{N_{\mathrm{D}}!}\left(\frac{q_{\mathrm{int}}}{\Lambda_{\mathrm{D}}{}^{3}}\right)^{N} \int_{V} d\mathbf{r}\, e^{-w(\mathbf{r})/k_{\mathrm{B}}T} \qquad (3.\ 18)$$

where Λ_{D} is the thermal wavelength, q_{int} it the particle internal partition function, $\mathbf{r}$ collectively represents the $3N_{\mathrm{D}}$ spatial coordinates of the N_{D} particles and $w(\mathbf{r})$ is the potential of mean force, which is given by

$$w(\mathbf{r}) = w_{\mathrm{DD}}(\mathbf{r}) + w_{\mathrm{DS}}(\mathbf{r}) \qquad (3.\ 19)$$

where $w_{\mathrm{DD}}(\mathbf{r})$ is the potential contribution associated with dendrimer-dendrimer interaction in the absence of bulk domain, with $w_{\mathrm{DD}}(\infty) = 0$, where "∞" denotes that all particle-particle distances are infinitely large. The remaining contribution in Eq. (3. 19), $w_{\mathrm{DS}}(\mathbf{r})$, describes the effect of salt on dendrimer-dendrimer interactions. Using Eqs. (3. 18) and (3. 19), Eq. (3. 18) can be rewritten in the following way:

$$Q = Q_{\mathrm{D}} \left\langle e^{-w_{\mathrm{DS}}(\mathbf{r})/k_{\mathrm{B}}T} \right\rangle \tag{3. 20}$$

with

$$Q_{\mathrm{D}} = \frac{1}{N_{\mathrm{D}}!}\left(\frac{q_{\mathrm{int}}}{\Lambda_{\mathrm{D}}{}^{3}}\right)^{N_{\mathrm{D}}} \int_{V} d\mathbf{r}\, e^{-w_{\mathrm{DD}}(\mathbf{r})/k_{\mathrm{B}}T} \tag{3. 21}$$

and

$$\left\langle e^{-w_{\mathrm{DS}}(\mathbf{r})/k_{\mathrm{B}}T} \right\rangle = \frac{\int_{V} d\mathbf{r}\, e^{-w_{\mathrm{DD}}(\mathbf{r})/k_{\mathrm{B}}T} e^{-w_{\mathrm{DS}}(\mathbf{r})/k_{\mathrm{B}}T}}{\int_{V} d\mathbf{r}\, e^{-w_{\mathrm{DD}}(\mathbf{r})/k_{\mathrm{B}}T}} \tag{3. 22}$$

The osmotic pressure of the dendrimer particles is given by,

$$\Pi = k_{\mathrm{B}}T\left(\frac{\partial \ln Q}{\partial V}\right)_{T,N} = \Pi_{\mathrm{D}} + k_{\mathrm{B}}T\left(\frac{\partial \ln\left\langle e^{-w_{\mathrm{DS}}(\mathbf{r})/k_{\mathrm{B}}T}\right\rangle}{\partial V}\right)_{T,N} \tag{3. 23}$$

where $\Pi_{\mathrm{D}} = k_{\mathrm{B}}T(\partial \ln Q_{\mathrm{D}} / \partial V)_{T,N}$.

We start by considering the osmotic pressure of the dendrimer particles in the absence bulk domain ($w_{\mathrm{DS}} = 0$). Here, we propose the following type of equation of state:

$$\frac{\Pi_{\mathrm{D}} v_{\mathrm{D}}}{k_{\mathrm{B}}T} = \left(1 + b\phi_{\mathrm{D}} + \frac{e}{k_{\mathrm{B}}T}\phi_{\mathrm{D}}\right)\phi_{\mathrm{D}} \tag{3. 24}$$

where v_{D} is the particle volume and the first term in parenthesis represents the ideal contribution to osmotic pressure while $b(\phi_{\mathrm{D}})$ and $e(\phi_{\mathrm{D}})$ are temperature-independent functions describing the steric entropic term and the energetic contribution of dendrimer-

dendrimer interactions, respectively. The expression of $b(\phi_{\mathrm{D}})$ is obtained from the Carnahan-Starling equation of state for hard spheres (see Eq. (1. 22)). Expressions for related functions are reported below:

$$b'(\phi_{\mathrm{D}}) \equiv \frac{db}{d\phi_{\mathrm{D}}} = \frac{10-4\phi_{\mathrm{D}}}{(1-\phi_{\mathrm{D}})^4} \tag{3. 25}$$

$$b''(\phi_{\mathrm{D}}) \equiv \frac{d^2b}{d\phi_{\mathrm{D}}{}^2} = \frac{36-12\phi_{\mathrm{D}}}{(1-\phi_{\mathrm{D}})^5} \tag{3. 26}$$

$$\tilde{b}(\phi_{\mathrm{D}}) \equiv \int_0^{\phi_{\mathrm{D}}} b(x)\,dx = \frac{4-3\phi_{\mathrm{D}}}{(1-\phi_{\mathrm{D}})^2}\phi_{\mathrm{D}} \tag{3. 27}$$

The quantity $e(\phi_{\mathrm{D}})$ can be linked to the excess internal energy of the dendrimer particles, U_{D}, in the absence of bulk domain. This quantity will be described by introducing the intensive property,

$$\omega_{\mathrm{D}} \equiv U_{\mathrm{D}} V_{\mathrm{D}} / V \tag{3. 28}$$

This can be obtained by first introducing the excess internal energy using,

$$U_{\mathrm{D}} = < w_{\mathrm{DD}}(\mathbf{r}) >= \frac{\int_V d\mathbf{r}\, w_{\mathrm{DD}}(\mathbf{r}) e^{-w_{\mathrm{DD}}(\mathbf{r})/k_{\mathrm{B}}T}}{\int_V d\mathbf{r}\, e^{-w_{\mathrm{DD}}(\mathbf{r})/k_{\mathrm{B}}T}} \tag{3. 29}$$

To obtain an expression for U_{D}, we apply thermodynamic relations starting from the expression of Π_{D} in Eq. (3. 24) and derive an expression for the Helmoholtz free energy, F_{D} :

$$\frac{F_{\mathrm{D}} - F_{\mathrm{D}}^{(\mathrm{id})}}{N k_{\mathrm{B}} T} = \int_0^{\phi_{\mathrm{D}}} \frac{Z-1}{\phi_{\mathrm{D}}} d\phi_{\mathrm{D}} = \tilde{b} + \frac{\tilde{e}}{k_{\mathrm{B}}T} \tag{3. 30}$$

where $Z \equiv v_{\mathrm{D}} \Pi_{\mathrm{D}} / (\phi_{\mathrm{D}} k_{\mathrm{B}} T)$ is the compressibility factor, $\tilde{e} \equiv \int_0^{\phi_{\mathrm{D}}} e(x)\, dx$ (x is the integration variable), and $F_{\mathrm{D}}^{(\mathrm{id})}$ are the ideal-state Helmoholtz free energy. The excess internal energy is then obtained from:

$$U_{\mathrm{D}} = \left[\frac{\partial (F_{\mathrm{D}} - F_{\mathrm{D}}^{(\mathrm{id})}) / T}{\partial (1/T)} \right]_{N,V} = N \tilde{e} \tag{3. 31}$$

From Eqs. (3. 31) and (3. 12) we can also derive:

$$\tilde{e} \equiv \int_0^{\phi_{\mathrm{D}}} e(x)\, dx = \frac{1}{8} \varepsilon\, b\, \phi_{\mathrm{D}} \tag{3. 32}$$

$$e = \frac{1}{8} \varepsilon\, (b + b' \phi_{\mathrm{D}}) \tag{3. 33}$$

$$e' \equiv \frac{de}{d\phi_{\mathrm{D}}} = \frac{1}{8} \varepsilon\, (2b' + b'' \phi_{\mathrm{D}}) \tag{3. 34}$$

To obtain an expression for the second term on the right side of Eq. (3. 23), an expression for $w_{\mathrm{DS}}(\mathbf{r})$ is needed. This is obtained by assuming a two-domain model. Each particle is surrounded by a salt-depleted local domain, v_{L}. When particles are far from each other, the total volume of the local domain has its maximum value of $V_{\mathrm{L}}(\infty) = N v_{\mathrm{L}}$. In general, we have $V_{\mathrm{L}}(\mathbf{r}) < N v_{\mathrm{L}}$ due to presence of particle-particle contacts. The remaining space occupied by the system is represented by the bulk domain with volume: w_{D}. This second domain is assumed to be a homogeneous binary salt-water solution with the same internal composition of that of the reservoir. Due to the presence of the salt component, the change from a generic $\mathbf{r}$ to ∞ results in an increase in $V_{\mathrm{L}}(\mathbf{r})$ and corresponding compression of the bulk-domain volume. This decrease in volume is given by $[V_{\mathrm{L}}(\mathbf{r}) - V_{\mathrm{L}}(\infty)]$. The corresponding positive work performed by the dendrimer particles on the bulk domain is $\Pi_{\mathrm{S}} \cdot [V_{\mathrm{L}}(\infty) - V_{\mathrm{L}}(\mathbf{r})]$, where Π_{S} is the salt osmotic pressure associated with the bulk domain (and the reservoir). If this is the only mechanism of action of salt, we can write:

$$w_{\mathrm{DS}}(\mathbf{r}) = -\Pi_{\mathrm{S}} \cdot [N v_{\mathrm{L}} - V_{\mathrm{L}}(\mathbf{r})] \tag{3. 35}$$

We now introduce the ensemble-average local-domain volume:

$$< V_{\mathrm{L}} > = \frac{\int_V d\mathbf{r}\, V_{\mathrm{L}}(\mathbf{r}) e^{-w_{\mathrm{DD}}(\mathbf{r})/k_{\mathrm{B}}T}}{\int_V d\mathbf{r}\, e^{-w_{\mathrm{DD}}(\mathbf{r})/k_{\mathrm{B}}T}} = (1-\alpha)V \tag{3. 36}$$

where α is the corresponding bulk-domain volume fraction. The ensemble-average of $w_{\mathrm{DS}}(\mathbf{r})$ is then given by

$$< w_{\mathrm{DS}}(\mathbf{r}) > = -\Pi_{\mathrm{S}} \cdot [N v_{\mathrm{L}} - (1-\alpha)V] \tag{3. 37}$$

To link Eq. (3. 37) to Eq. (3. 22), we now make the first-order (mean-field) approximation:

$$\ln\left\langle e^{-w_{\mathrm{DS}}(\mathbf{r})/k_{\mathrm{B}}T} \right\rangle = -\frac{< w_{\mathrm{DS}}(\mathbf{r}) >}{k_{\mathrm{B}}T} \tag{3. 38}$$

which is based on the Taylor's series expansion: $\ln < e^{-x} > = \ln < 1 - x + x^2/2 + \ldots > = - < x > + (< x^2 > - < x >^2)/2 + \ldots$ This gives:

$$\ln\left\langle e^{-w_{\mathrm{DS}}(\mathbf{r})/k_{\mathrm{B}}T} \right\rangle = \frac{\Pi_{\mathrm{S}}}{k_{\mathrm{B}}T} \cdot [N v_{\mathrm{L}} - (1-\alpha)V] \tag{3. 39}$$

We are now in position to write the following expression for Π starting from Eq. (3. 23:

$$\Pi = \Pi_{\mathrm{D}} - \left[\frac{\partial(1-\alpha)V}{\partial V}\right]_{T,N} \Pi_{\mathrm{S}} = \Pi_{\mathrm{D}} - \left[1 - \alpha + \left(\frac{\partial \alpha}{\partial \phi_{\mathrm{D}}}\right)_T \phi_{\mathrm{D}}\right] \Pi_{\mathrm{S}} \tag{3. 40}$$

As previously mentioned, an expression for $\alpha(\phi_{\mathrm{D}},T)$ can be obtained from the excess chemical potential of a hard-sphere test particle (TP) with a radius equal to the thickness of the salt-depleted layer. Specifically, the chemical potential of one test particle μ_{TP} is given by

$$\mu_{\mathrm{TP}} = k_{\mathrm{B}}T \ln \frac{C_{\mathrm{TP}}\Lambda_{\mathrm{TP}}{}^{3}}{\alpha} = \mu_{\mathrm{TP}}^{(id)} - k_{\mathrm{B}}T \ln \alpha \tag{3. 41}$$

where Λ_{TP} is the thermal wavelength of the test particle, C_{TP} is the concentration of the test particle inside the system and C_{TP} / α is the corresponding concentration in the accessible volume (bulk domain). In Eq. (3. 46), the term representing the excess chemical potential is $-k_{\mathrm{B}}T \ln \alpha$.

The chemical potential of a test particle, TP, can be extracted from the Helmholtz free energy of a binary hard-sphere mixture. The Helmholtz free energy depends on the volume fractions of TP particles, ϕ_{TP}, and D particles, ϕ_{D}, and the ratio of TP radius to D radius, q. To obtain the excess chemical potential of the test particle, we can use the following thermodynamic relation:

$$\ln \alpha = -\frac{v_{\mathrm{TP}}}{k_{\mathrm{B}}TV} \lim_{\phi_{\mathrm{TP}}\to 0} \left(\frac{\partial F - F^{(\mathrm{id})}}{\partial \phi_{\mathrm{TP}}} \right)_{\phi_{\mathrm{D}},V,T} \tag{3. 42}$$

where v_{TP} is the volume of test particles, $F^{(\mathrm{id})}$ is the ideal contribution of the Helmholtz free energy and α is a function of ϕ_{D} and q. We choose the expression of α obtained from the Mansoori-Carnahan-Starling-Leland thermodynamic model for a binary hard-sphere mixture (see Eq. (3. 5)).

The expressions of its derivatives, $\alpha'(\phi_{\mathrm{D}}) \equiv d\alpha / d\phi_{\mathrm{D}}$ and $\alpha''(\phi_{\mathrm{D}}) \equiv d^2\alpha / d\phi_{\mathrm{D}}{}^2$ are included below:

$$\alpha' \equiv \frac{d\alpha}{d\phi_{\mathrm{D}}} = -\frac{\alpha}{1-\phi_{\mathrm{D}}}\left[1+\frac{A+2B\eta_{\mathrm{D}}+3C\eta_{\mathrm{D}}{}^2 - D/(1+\eta_{\mathrm{D}})}{1-\phi_{\mathrm{D}}}\right] \tag{3. 43}$$

$$\begin{aligned}\alpha'' \equiv \frac{d^2\alpha}{d\phi_{\mathrm{D}}{}^2} = -\frac{\alpha}{(1-\phi_{\mathrm{D}})^2} \\ \left[1+2\frac{A+2B\eta_{\mathrm{D}}+3C\eta_{\mathrm{D}}{}^2 - D/(1+\eta_{\mathrm{D}})}{1-\phi_{\mathrm{D}}}+\frac{2B+6C\eta_{\mathrm{D}}+D/(1+\eta_{\mathrm{D}})^2}{(1-\phi_{\mathrm{D}})^2}\right]+\frac{\alpha'^2}{\alpha}\end{aligned} \tag{3. 44}$$

The dendrimer chemical potential can be introduced through the Gibbs-Duhem equation (see Eq. (1. 16)) at constant T and Π_{S}:

$$\phi_{\mathrm{D}}\left(\frac{\partial \mu_{\mathrm{D}}}{\partial \phi_{\mathrm{D}}}\right)_{T,\Pi_{\mathrm{S}}} = \left(\frac{\partial \Pi}{\partial \phi_{\mathrm{D}}}\right)_{T,\Pi_{\mathrm{S}}} \tag{3. 45}$$

After inserting Eqs. (3. 24) and (3. 40) in Eq. (3. 45), we obtain:

$$\frac{\Pi v_{\mathrm{D}}}{k_{\mathrm{B}}T} = \left(1+b\phi_{\mathrm{D}}+\frac{e}{k_{\mathrm{B}}T}\phi_{\mathrm{D}}\right)\phi_{\mathrm{D}} - (1-\alpha+\alpha'\phi_{\mathrm{D}})\frac{\Pi_{\mathrm{S}} v_{\mathrm{D}}}{k_{\mathrm{B}}T} \tag{3. 46}$$

$$\frac{v_{\mathrm{D}}}{k_{\mathrm{B}}T}\left(\frac{\partial \Pi}{\partial \phi_{\mathrm{D}}}\right)_{T,\Pi_{\mathrm{S}}} = 1+(2b+b'\phi_{\mathrm{D}})\phi_{\mathrm{D}}+\frac{2e+e'\phi_{\mathrm{D}}}{k_{\mathrm{B}}T}\phi_{\mathrm{D}} - \alpha''\phi_{\mathrm{D}}\frac{\Pi_{\mathrm{S}} v_{\mathrm{D}}}{k_{\mathrm{B}}T} \tag{3. 47}$$

$$\frac{v_{\mathrm{D}}}{k_{\mathrm{B}}T}\left(\frac{\partial \mu_{\mathrm{D}}}{\partial \phi_{\mathrm{D}}}\right)_{T,\Pi_{\mathrm{S}}} = \frac{1}{\phi_{\mathrm{D}}}+(2b+b'\phi_{\mathrm{D}})+\frac{2e+e'\phi_{\mathrm{D}}}{k_{\mathrm{B}}T} - \alpha''\frac{\Pi_{\mathrm{S}} v_{\mathrm{D}}}{k_{\mathrm{B}}T} \tag{3. 48}$$

$$\frac{\mu_{\mathrm{D}}-\mu_{\mathrm{D}}^0}{k_{\mathrm{B}}T} = \ln\phi_{\mathrm{D}}+\tilde{b}+b\phi_{\mathrm{D}}+\frac{\tilde{e}+e\phi_{\mathrm{D}}}{k_{\mathrm{B}}T} - \alpha'\frac{\Pi_{\mathrm{S}} v_{\mathrm{D}}}{k_{\mathrm{B}}T} \tag{3. 49}$$

where we have used the mathematical relation: $\int_0^{\phi_\mathrm{D}} x\, f'(x)\, dx = \phi_\mathrm{D}\, f(\phi_\mathrm{D}) - \tilde{f}(\phi_\mathrm{D})$ with $\tilde{f} \equiv \int_0^{\phi_\mathrm{D}} f(x)\, dx$.

The DLS diffusion coefficient can be written as (see Section 2.3.3)

$$D = D_0 H(\phi_\mathrm{D}, T) S(\phi_\mathrm{D}, T) \tag{3. 50}$$

where $H(\phi_\mathrm{D}, T)$ and $S(\phi_\mathrm{D}, T)$ are the hydrodynamic and thermodynamic factors, respectively[116,117]. Note that $S(\phi_\mathrm{D}, T) = (v_\mathrm{D} / k_\mathrm{B} T)(\partial \Pi / \phi_\mathrm{D})_T$ (see Eqs. (2. 13) and (2. 14)). At low ϕ_D, we can write:

$$H(\phi_\mathrm{D}, T) = 1 + k_H\, \phi_\mathrm{D} + \ldots \tag{3. 51}$$

$$S(\phi_\mathrm{D}, T) = 1 + k_S\, \phi_\mathrm{D} + \ldots \tag{3. 52}$$

where the slopes, k_H and k_S, characterize hydrodynamic and thermodynamic interactions, respectively. The hydrodynamic slope, k_H, is expected to be negative, while the thermodynamic slope, k_S, is positive (negative) for repulsive (attractive) particle-particle thermodynamic interactions. From Eqs. (3. 51) and (3. 52), we can write:

$$D = D_0 \left[1 + (k_H + k_S)\phi_\mathrm{D} + \ldots \right] \tag{3. 53}$$

If the observed slope, $k_D = k_H + k_S$, is positive then particle-particle thermodynamic interactions are repulsive.

The following expression for k_S can be extracted from Eq. (3. 47) in the limit of $\phi_\mathrm{D} = 0$.

$$k_S = 2b(0) + \frac{2e(0)}{k_\mathrm{B} T} - \alpha''(0) \frac{\Pi_\mathrm{S} v_\mathrm{D}}{k_\mathrm{B} T} = 8 + \frac{\varepsilon}{k_\mathrm{B} T} - (12 + 15q + 6q^2 + q^3) q^3 p_\mathrm{S} \tag{3. 54}$$

where $p_{\mathrm{S}} \equiv \Pi_{\mathrm{S}} v_{\mathrm{D}} / k_{\mathrm{B}} T$. If we set the value of k_D at C_{S} / mol dm^{-3} = 0.044 and 25.0 °C as the reference $k_D^{(R)} = 1.8$ and assume that k_H is independent of salt concentration and temperature, Eqs. (3. 53) and (3. 54) yield:

$$k_D = k_D^{(R)} + \frac{\varepsilon}{k_{\mathrm{B}}}\left(\frac{1}{T} - \frac{1}{T_R}\right) - (12 + 15q + 6q^2 + q^3)q^3\left(p_{\mathrm{S}} - p_{\mathrm{S}}^{(R)}\right) \tag{3. 55}$$

In Table 4 (last four columns), we report the values of k_D calculated from Eq. (3. 55) and $q = 0.30$ ($k_{\mathrm{DLS}}^{(q=0.30)}$), $q = 0.33$ ($k_{\mathrm{DLS}}^{(q=0.33)}$), 0.35 ($k_{\mathrm{DLS}}^{(q=0.35)}$) and 0.40 ($k_{\mathrm{DLS}}^{(q=0.40)}$)

Table 4. DLS parameters for the analysis of k_D.

C_{S} /mol·dm^{-3}	T/ °C	$\varepsilon / k_{\mathrm{B}}T$	p_{S}	k_D	$k_D^{(q=0.30)}$	$k_D^{(q=0.33)}$	$k_D^{(q=0.35)}$	$k_D^{(q=0.40)}$
0.044	25.0	8.0	1.28	1.8±0.4				
0.949	25.0	8.0	21.95	-11.6±0.4	-7.7	-11.6	-14.2	-23.4
0.044	37.0	7.7	1.28	1.8±0.4	1.5	1.5	1.5	1.5
0.949	37.0	7.7	22.43	-12.7±0.4	-8.2	-12.2	-14.8	-24.3

3.11. Conclusions

LLPS of aqueous solutions of PAMAM G4-OH dendrimer in the presence of sodium sulfate was observed. To explain the experimental binodal at 25 °C, a thermodynamic model, which includes dendrimer-dendrimer interaction energy (ε), salting-out strength of salt (q) and the available salt osmotic coefficient (φ) of the binary salt-water system, was developed. The parameter ε was characterized by ITC so that q remains the only parameter to be determined. It was shown that the model agrees with both the location of the experimental binodal and its slope around the critical point when $q = 0.35$. The proposed thermodynamic model also predicts that the observed unusual temperature behavior can be explained if $\varphi(T)$ and $q(T)$ have opposite temperature effects on LLPS, with $\varphi(T)$ dominating at low ϕ_{D} and $q(T)$ prevailing at high ϕ_{D}.

Chapter 4: Formation of Dendrimer Globular Nanoparticles from Oligomerization Induced LLPS

4.1. Introduction

In this chapter we report an experimental investigation of the LLPS of aqueous PAMAM-NH_2 in the presence of sodium sulfate. Similarly to PAMAM-OH aqueous solutions, we will demonstrate that sodium sulfate can also induce LLPS on PAMAM-NH_2 solutions. However, LLPS in PAMAM-NH_2 solutions is only observed by cooling. As in the previous chapter, the composition of a ternary dendrimer–salt–water system is described by the dendrimer volume fraction, ϕ_{D}, and the sodium sulfate molar concentration, C_{S}. The phase transition of this system will be also characterized by a surface in the phase diagram, representing the LLPS temperature, T_{ph}, as a function of ϕ_{D} and C_{S} and the dendrimer-salt partitioning will be described by an isothermal coexistence curve, which gives the concentration $(C_{\mathrm{S}}^{(\mathrm{I})},\phi_{\mathrm{D}}^{(\mathrm{I})})$ and $(C_{\mathrm{S}}^{(\mathrm{II})},\phi_{\mathrm{D}}^{(\mathrm{II})})$ of the coexisting liquid phases, I and II. Our experimental results on the LLPS of dendrimer-salt-water mixtures will be also examined using the thermodynamic model described in Chapter 3.

The main goal discussed in this chapter is to show that low-G dendrimers can be used as building blocks for the formation of dendrimer globular nanoparticles through LLPS. High-G dendrimers have the advantage of potentially hosting a relatively high number of guest molecules. However, since the surface density of terminal groups also increases with generation, dendrimers with G≥7 are more difficult to synthesize due to steric hindrance. This also promotes a pronounced backfolding of terminal groups, which causes an increase in conformational rigidity and a decrease of cavity volume per dendrimer mass. Hence, the loading capacity of guest molecules is significantly reduced. Thus, low-G dendrimers (4≤G≤6) are the most suitable for host-guest applications. Furthermore, their flexibility can lead to significant conformational changes due to external stimuli. This aspect is important for applications such as environment-sensitive host-guest binding and chemical sensing. Thus, it is important to identify approaches that would circumvent the need of synthesizing high-G dendrimers and will lead to the preparation of dendrimer materials that retain the advantages of both high- and low-G dendrimers. One approach is the preparation of nanoclusters of low-G dendrimers. In this paper, we examine the use of liquid-liquid phase separation (LLPS) as a means to induce self-assembly of low-G dendrimers.

In this chapter, we will show that the addition of a small amount of glutaraldehyde, a bi-functional crosslinker that mainly reacts with primary amino groups on the protein surface, enhances LLPS due to the oligomerization of PAMAM-NH2 dendrimers. It will be shown that this process leads to the formation of dendrimer globular nanoparticles.

LLPS of solutions of globular macromolecules has been already employed for the formation of crosslinked microspheres. In these experiments, a precipitating agent is typically added to the macromolecule solution to induce the formation of macromolecular-rich spherical droplets, a process usually denoted as coacervation or condensation. A chemical crosslinker is then added to the resulting suspension in order to irreversibly produce microspheres. However, this approach yields, in general, large particles, with radii of the order of 10 μm. This is mainly related to the lag time between the formation and growth of the droplets and the crosslinking step.

The approach discussed in this chapter, which was developed in our laboratory, is distinct from that used to produce microspheres. In our case, the crosslinker is added to the homogeneous macromolecular solution to form soluble dendrimer oligomers and induce LLPS. This approach, which we denote as oligomerization-induced LLPS, removes the lag time between droplet formation and crosslinking and is therefore promising for obtainment of relatively small spherical particles of dendrimer coacervates. As we shall see in this chapter, the successful use of this approach requires that the macromolecular solution to exhibit LLPS at a temperature that is different from the crosslinking temperature. We will show that oligomerization-induced condensation yields dendrimer globular nanoparticles with a radius of ≈ 100 nm.

4.2. Effect of Salt Concentration on LLPS Temperature

To characterize the LLPS boundary we have experimentally measured T_{ph}, as a function of sodium sulfate concentration, C_S, at several values of dendrimer volume fraction, ϕ_D, using the same procedure as described for PAMAM-OH in Chapter 8. Our experiments revealed that LLPS is induced by lowering temperature at all experimental salt concentrations. The obtained values of T_{ph} are reported in Figure 28.

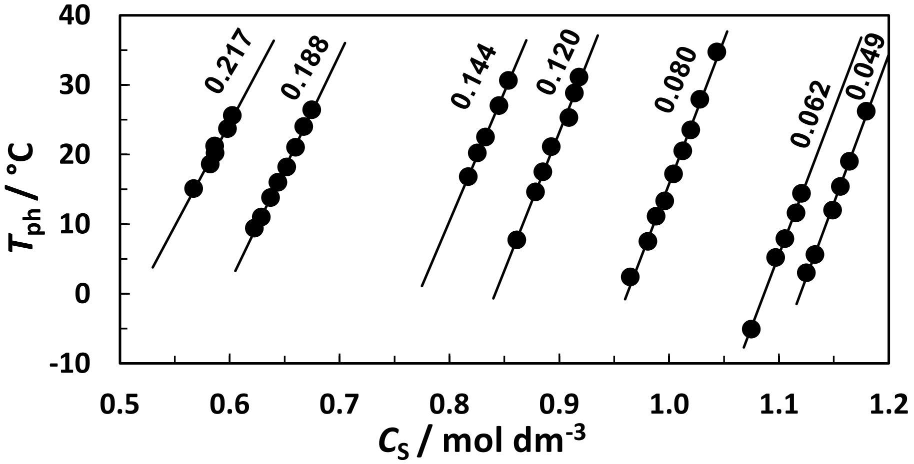

Figure 28. T_{ph} as a function of salt concentration at several constant dendrimer molar fractions. The numbers associated with each curve identify the corresponding value of ϕ_D. The solid lines are linear fits to the experimental data.

In all cases, T_{ph} significantly increases with salt concentration. Specifically, an increment of ≈0.1 mol·dm^{-3} in salt concentration produces a corresponding increment of ≈30 °C in LLPS temperature. This is a different behavior from that observed in the case of the PAMAM-OH system (Section 3.2) where we observed the inversion of temperature behavior.

4.3. Sodium Sulfate – PAMAM-NH$_2$ Partitioning in Aqueous Solutions

At a fixed temperature, LLPS yields the formation of two coexisting liquid phases with compositions $(C_{\mathrm{S}}^{(\mathrm{I})}, \phi_{\mathrm{D}}^{(\mathrm{I})})$ and $(C_{\mathrm{S}}^{(\mathrm{II})}, \phi_{\mathrm{D}}^{(\mathrm{II})})$ for phases I and II, respectively. We have experimentally characterized these compositions at 25 ºC. Our results are reported in Table 5 together with the corresponding partition coefficients defined as $\Delta C_{\mathrm{S}} / \Delta\phi_{\mathrm{D}} \equiv (C_{\mathrm{S}}^{(\mathrm{II})} - C_{\mathrm{S}}^{(\mathrm{I})}) / (\phi_{\mathrm{D}}^{(\mathrm{II})} - \phi_{\mathrm{D}}^{(\mathrm{I})})$. The negative values of $\Delta C_{\mathrm{S}} / \Delta\phi_{\mathrm{D}}$ reflect the salting-out mechanism; i.e., the preferential hydration (see Section 3.3) of both solute components leads to salt-rich (I) and dendrimer-rich (II) coexisting phases. Note that the reported $\phi_{\mathrm{D}}^{(\mathrm{II})}$ values, which are higher than 0.3, correspond to an average dendrimer-dendrimer distance lower than 4 nm, consistent with the formation of a dendrimer condensed phase in which dendrimer particles with a radius of ≈2 nm (see Section 3.3) are essentially in contact with each other. In other words, the dendrimer concentration in phase II is comparable with that of crystals and aggregates of colloidal particles[131]. On the other hand, dendrimer concentration in the salt-rich phase is significantly lower ($\phi_{\mathrm{D}}^{(\mathrm{I})} \leq 0.01$). This shows LLPS effectiveness in removing dendrimers from their initial medium.

Our values in Table 5 can be also used to estimate the critical dendrimer volume fraction, $\phi_{\mathrm{D}}^{(\mathrm{c})}$. This was obtained by the linear extrapolation of $(\phi_{\mathrm{D}}^{(\mathrm{I})}+\phi_{\mathrm{D}}^{(\mathrm{II})})/2$ to $|\phi_{\mathrm{D}}^{(\mathrm{II})}-\phi_{\mathrm{D}}^{(\mathrm{I})}|^{1/\beta}\rightarrow 0$, with $\beta=0.325$ (Ising exponent) and $\beta=0.5$ (Mean-field exponent) (see Figure 29). From the corresponding plots, we found that $\phi_{\mathrm{D}}^{(\mathrm{c})}=0.12\pm 0.03$.

Table 5. Salt-Dendrimer partitioning parameters at 25 °C.

$C_{\mathrm{S}}^{(\mathrm{I})}$ / mol·dm^{-3}	$\phi_{\mathrm{D}}^{(\mathrm{I})}$	$C_{\mathrm{S}}^{(\mathrm{II})}$ / mol·dm^{-3}	$\phi_{\mathrm{D}}^{(\mathrm{II})}$	$(\Delta C_{\mathrm{S}}/\Delta\phi_{\mathrm{D}})$ / mol·dm^{-3}	q
1.23	0.006	0.37	0.34	-2.4	0.29
1.41	0.004	0.39	0.35	-2.7	0.29
1.31	0.010	0.40	0.34	-2.5	0.27
1.61	0.004	0.38	0.38	-3.2	0.31

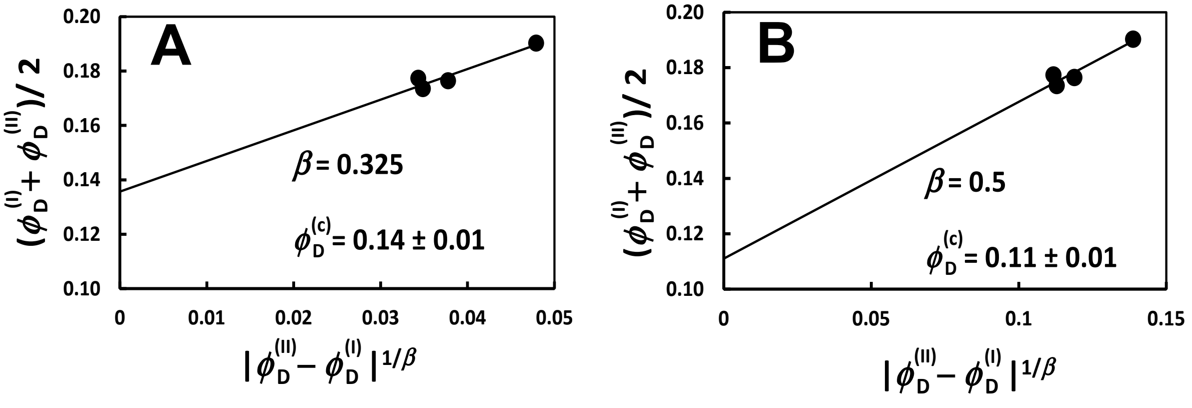

Figure 29. Plots of $(\phi_{\mathrm{D}}^{(\mathrm{I})}+\phi_{\mathrm{D}}^{(\mathrm{II})})/2$ as a function of $|\phi_{\mathrm{D}}^{(\mathrm{II})}-\phi_{\mathrm{D}}^{(\mathrm{I})}|^{1/\beta}$, where $\beta=0.325$ and $\beta=0.5$ are the Ising (A) and mean-field (B) exponents, respectively. Linear extrapolation to $|\phi_{\mathrm{D}}^{(\mathrm{II})}-\phi_{\mathrm{D}}^{(\mathrm{I})}|^{1/\beta}=0$ yield estimates of the critical volume fraction, $\phi_{\mathrm{D}}^{(\mathrm{c})}$.

In Figure 30A, we plot our experimental binodal $\phi_{\mathrm{D}}(C_{\mathrm{S}})$ at T_{ph}=25 °C. This curve, which was obtained by fitting our $T_{\mathrm{ph}}(C_{\mathrm{S}})$ data in Figure 28 at any given ϕ_{D} to a linear equation, shows that an increment of ≈0.1 mol·dm^{-3} in salt concentration reduces dendrimer "solubility" by ≈0.03 in volume fraction units within the experimental salt concentration range.

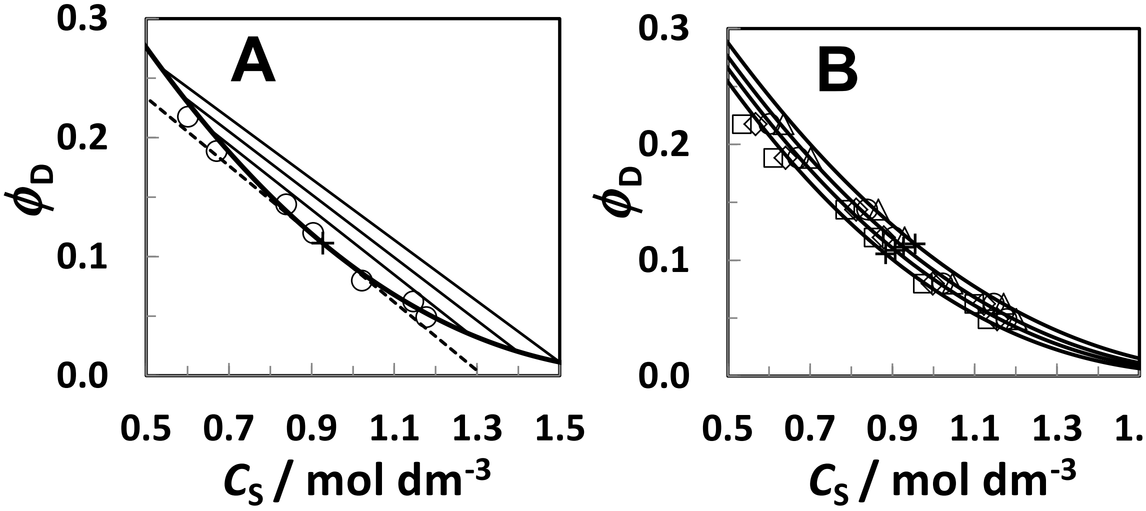

Figure 30. Binodal data, ϕ_D as a function of C_S, for the dendrimer-salt-water system (A) at 25 ºC (circles). The solid curve is the theoretical binodal with $\varepsilon / RT = 25$ ($\varepsilon = 62\ \mathrm{kJ \cdot mol^{-1}}$) and $q = 0.415$. The three solid lines are calculated representative tie-lines. The cross represents the location of the critical point. The dashed line crossing the critical point describes the experimental slope at the critical point and (B) at four representative temperatures (5 ºC, squares; 15 ºC, diamonds; 25 ºC, circles; 35 ºC, triangles). Moving from left to right, the four solid curves are theoretical binodal curves calculated by setting q = 0.4375 (5 ºC), 0.4250 (15 ºC), 0.4150 (25 ºC) and 0.4050 (35 ºC), respectively. The four crosses represent the location of the critical points.

By fitting the binodal data in Figure 30A to a linear equation, the salt critical concentration of $C_S^{(c)} = (0.9 \pm 0.1)\ \mathrm{mol \cdot dm^{-3}}$ is obtained. We have also extracted the corresponding slope, $(\partial C_S / \partial \phi_D)_T = -(3.45 \pm 0.16)\ \mathrm{mol \cdot dm^{-3}}$. This slope also represents the limiting partition coefficient at the critical point and is comparable with the values of $\Delta C_{\mathrm{S}} / \Delta\phi_{\mathrm{D}}$ in Table 5, which range between -3.2 and -2.4 mol·dm^{-3}.

To theoretically describe LLPS, we consider the thermodynamic model described in Section 3.6. In Figure 30A, we include the binodal calculated using the values of $q = 0.415$ and $\varepsilon / RT = 25$ ($\varepsilon = 62\ \mathrm{kJ \cdot mol^{-1}}$). These were chosen to match both the location of the experimental binodal in the phase diagram and the experimental slope $(\partial C_{\mathrm{S}} / \partial\phi_{\mathrm{D}})_T$. The calculated value of $\phi_{\mathrm{D}}^{(\mathrm{c})} = 0.111$ is consistent with our partition results within the experimental error. The positive value of ε, which corresponds to endothermic dendrimer-dendrimer interactions, is in qualitatively agreement with heat-of-dilution experiments by isothermal titration calorimetry at 25 °C. However, the quantitative analysis of our calorimetric data was hindered by the presence of multiple concurring energetic events (see Section 4.7.1).

In Figure 30B, we plot four experimental binodals at the representative temperatures of T_{ph}=5, 15, 25 and 35 °C, respectively. Linear fits through turbidity data were used to extract binodal data at these four representative temperatures. As temperature increases, the binodal shifts towards higher salt concentration. In this figure, we have also included theoretical binodal curves extracted from the thermodynamic model. To reproduce the experimental trend, the value of q was decreased as temperature increases while the value of ε was kept constant. Thus, the observed thermal behavior of LLPS is explained by the increase of salting-out strength of salt as temperature is lowered.

Note that q for PAMAM-NH$_2$ is predicted to increase as temperature is lowered (see Table 6). This change is about two-fold larger than that calculated for PAMAM-OH (Figure 26). This describes why LLPS for PAMAM-NH$_2$ occurs by cooling only.

Table 6. Values of q for PAMAM-NH$_2$ and PAMAM-OH at different temperatures.

T / °C	q(PAMAM-NH$_2$)	q(PAMAM-OH)
5	0.438	0.360
15	0.425	0.354
25	0.415	0.350

4.4. Effect of crosslinker concentration on LLPS temperature

In the previous section, we have shown that LLPS of a dendrimer aqueous system can be induced in the presence of sodium sulfate. In this section, we examine the effect of dendrimer self-association on this LLPS. Specifically, small amounts of glutaraldehyde were added to dendrimer-salt-water mixtures to induce dendrimer oligomerization. This bifunctional crosslinker binds to the terminal amino groups of our dendrimer thereby producing dendrimer soluble oligomers, with the oligomer size increasing with crosslinker concentration (see Section 4.5). To verify that the crosslinking reaction reaches completion, light-scattering intensity was monitored as a function of time. Our light-scattering experiments show that no change in sample light-scattering intensity is observed after 10 min within the experimental error.

To characterize the effect of dendrimer self-association on LLPS, we have measured the LLPS temperature, T_{ph}, as a function of crosslinker concentration, C_{CL}. LLPS measurements performed after 10 and 120 min show no change in T_{ph} within the experimental error. In

Figure 31, we show our results for a ternary mixture ($\phi_{\mathrm{D}} = 0.048, C_{\mathrm{S}} = 1.0\,\mathrm{mol \cdot dm^{-3}}$) that exhibits LLPS at $T_{\mathrm{ph}} = -12.0$ °C in the absence of crosslinker. Specifically, we plot T_{ph} as a function of the molar ratio, $C_{\mathrm{CL}} / C_{\mathrm{D}}$, with $C_{\mathrm{D}} = 4.1 \times 10^{-3}\,\mathrm{mol \cdot dm^{-3}}$ being the dendrimer molar concentration. As we can see in this figure, T_{ph} shows a weak dependence on $C_{\mathrm{CL}} / C_{\mathrm{D}}$ at low crosslinker concentrations and then sharply increases approaching room temperature after $C_{\mathrm{CL}} / C_{\mathrm{D}}$ reaches a value of ≈ 1.5. This behavior can be related to glutaraldehyde oligomerization in solution[13]. Since the concentration of glutaraldehyde oligomeric species increases with C_{CL}, our results are consistent with a reaction mechanism in which the presence of glutaraldehyde oligomers is necessary for dendrimer crosslinking. The same behavior was observed in the case of protein crosslinking[13].

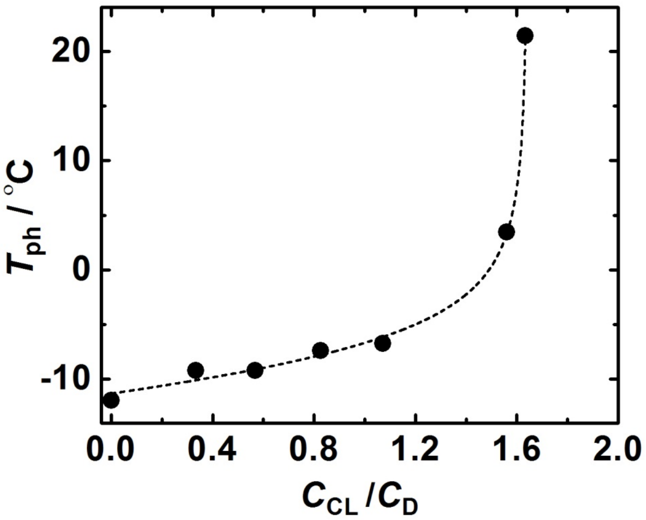

Figure 31. LLPS temperature as a function of crosslinker-to-dendrimer molar ratio, $C_{\mathrm{CL}} / C_{\mathrm{D}}$. Experiments were performed at the constant dendrimer volume fraction of $\phi_{\mathrm{D}} = 0.048$ (molar concentration of C_{D} = 4.1 mmol·dm^{-3}) and sodium sulfate molar concentration of C_{S} = 1.0 mol·dm^{-3}. The dashed curve is a guide to the eye.

It is important to remark that the existence of LLPS for the monomeric dendrimer represents a necessary prerequisite for the observation of LLPS in the presence of crosslinker. Indeed, experiments in which sodium chloride replaces sodium sulfate at the same ionic strength ($C_{\mathrm{S}} = 3.0\,\mathrm{mol \cdot dm^{-3}}$ for NaCl) show that samples remain clear at temperatures as low as -15 °C and $C_{\mathrm{CL}} / C_{\mathrm{D}}$ as high as $C_{\mathrm{CL}} / C_{\mathrm{D}} = 3$.

4.5. Formation of dendrimer globular particles

Our results in Section 4.4 indicate that LLPS of dendrimer aqueous solutions may be isothermally induced at room temperature by dendrimer self-association, which can be achieved by adding small amounts of crosslinker. The oligomerization-induced LLPS should yield globular condensates, i.e. dendrimer-rich droplets (coacervation).

Dendrimer oligomerization and condensation were investigated by DLS at 25 °C. Specifically, we have characterized light-scattering particle-size distributions as a function of $C_{\mathrm{CL}} / C_{\mathrm{D}}$ at the dendrimer concentration of $C_{\mathrm{D}} = 0.75 \times 10^{-3}\,\mathrm{mol \cdot dm^{-3}}$ ($\phi_{\mathrm{D}} = 0.0087$) and sodium sulfate concentration of $C_{\mathrm{S}} = 0.37\,\mathrm{mol \cdot dm^{-3}}$. The dendrimer concentration was chosen to be relatively low in order to justify the use of the Stokes-Einstein equation for the determination of the particle hydrodynamic radius, R_{h}. At the chosen sodium sulfate concentration, equilibrium DLS distributions could be successfully measured for $C_{\mathrm{CL}} / C_{\mathrm{D}}$ ratios as high as 14. At higher values of $C_{\mathrm{CL}} / C_{\mathrm{D}}$, dendrimer crosslinking results in dendrimer macroscopic precipitation. In Figure 32A-D, we show DLS distribution obtained at four representative $C_{\mathrm{CL}} / C_{\mathrm{D}}$ ratios. At low $C_{\mathrm{CL}} / C_{\mathrm{D}}$, DLS distributions are monomodal with the average R_h increasing with $C_\mathrm{CL} / C_\mathrm{D}$ starting from the radius of $R_\mathrm{h} = 2.0$ nm for the dendrimer monomer (see Figure 32A,B). This behavior characterizes the increase of oligomer size with crosslinker concentration. At $C_\mathrm{CL} / C_\mathrm{D} = 10$, the DLS distribution becomes bimodal (see Figure 32C). Specifically, a population of large dendrimer nanoparticles with $R_\mathrm{h} \approx 70$ nm separates from the population of dendrimer oligomers with $R_\mathrm{h} \approx 3$ nm. As the $C_\mathrm{CL} / C_\mathrm{D}$ ratio further increases, the DLS peak associated with dendrimer nanoparticles becomes dominant (see Figure 32D). The dendrimer nanoparticles represent the formation of a new condensed phase with the value $C_\mathrm{CL} / C_\mathrm{D} = 10$ characterizing the corresponding phase boundary.

The dilution of the sample containing nanoparticles and its dialysis against water to remove salt show that the formation of dendrimer nanoparticles is an irreversible process. This can be understood by realizing that the crosslinking reaction is enhanced at the high dendrimer concentration of the condensed phase. SEM images taken after water evaporation show the formation of globular nanoparticles with an average radius of about 100 nm (about 50 times larger than one dendrimer). This is illustrated in Figure 33.

DLS experiments were also performed on dendrimer aqueous solutions in the presence of sodium chloride at the same salt ionic strength of sodium sulfate. The obtained particle-size distributions at four representative $C_\mathrm{CL} / C_\mathrm{D}$ ratios ranging from 0 to 19 are shown in Figure 34A-D. All DLS distributions in the presence of NaCl are monomodal with R_h smoothly increasing with $C_\mathrm{CL} / C_\mathrm{D}$ as expected from dendrimer self-association. Corresponding SEM images show no formation of globular nanoparticles. At higher values of $C_\mathrm{CL} / C_\mathrm{D}$, dendrimer crosslinking results in dendrimer macroscopic precipitation. These results are consistent with NaCl not being able to induce LLPS of dendrimer aqueous solutions.

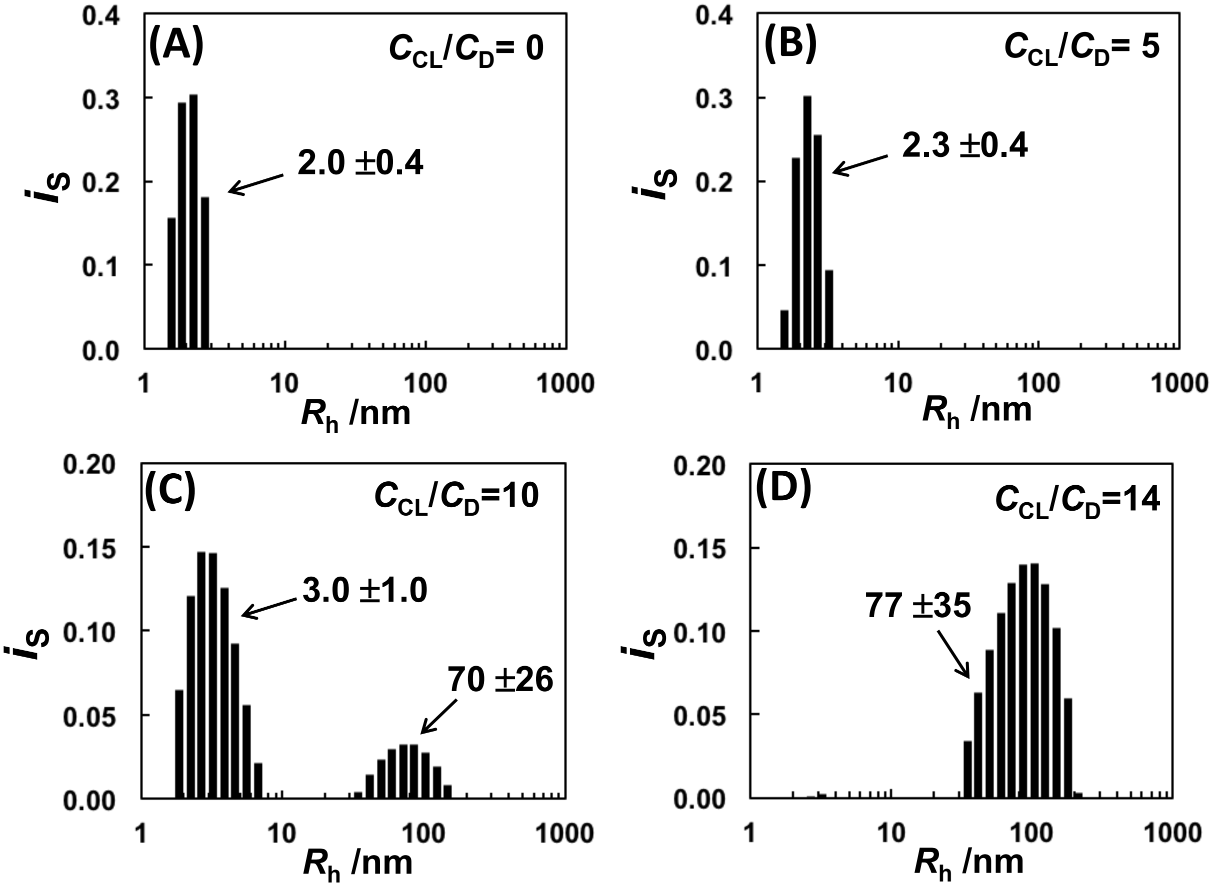

Figure 32. Normalized light-scattering intensity, i_S, as a function of hydrodynamic radius, R_h, at the constant dendrimer volume fraction of $\phi_D = 0.0087$ (C_D = 0.75 mmol·dm^{-3}), sodium sulfate concentration of C_S = 0.37 mol·dm^{-3}, and four representative crosslinker-to-dendrimer molar ratios, C_{CL} / C_D (A-D). The numbers associated with each peak represent the value of R_h/nm calculated from the corresponding *z*-average diffusion coefficient. The associated standard deviations describe the width of the peaks; these values are calculated from the corresponding diffusion-coefficient distributions. Measurements were performed at 25 ºC.

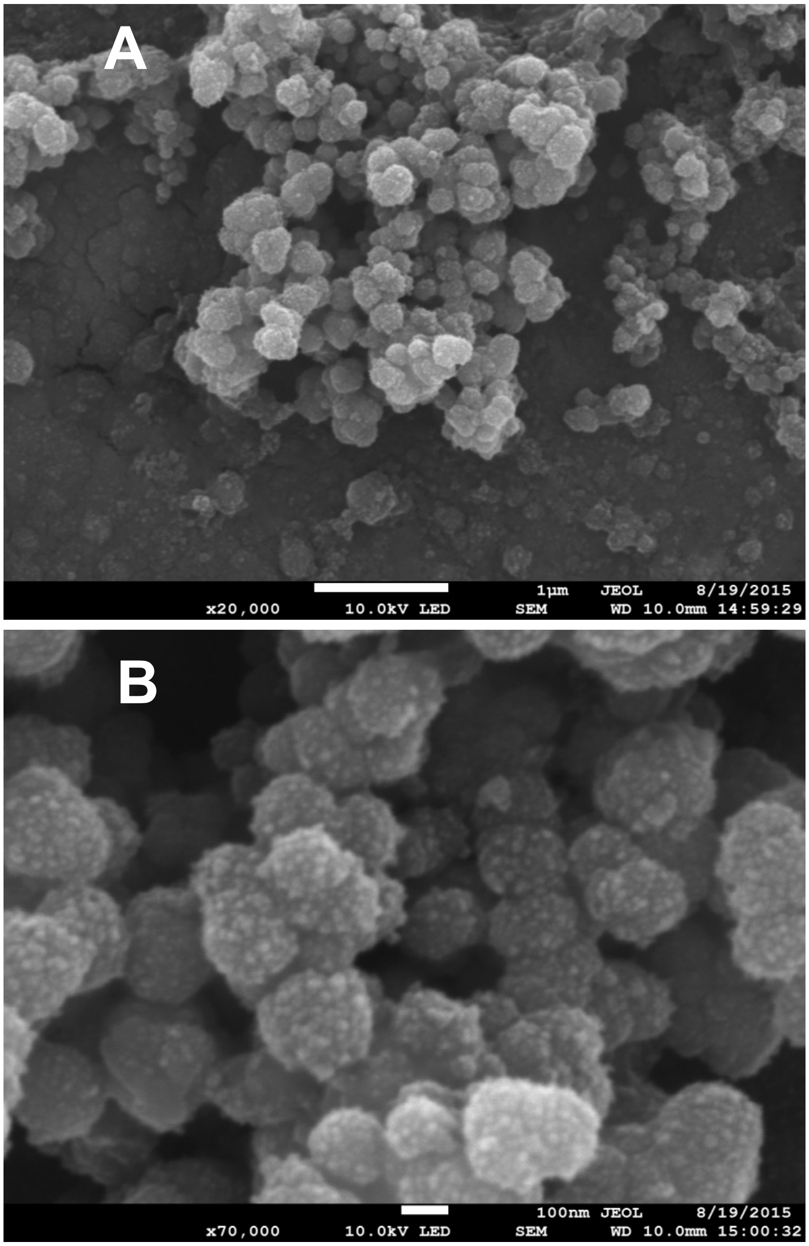

Figure 33. Scanning electron micrographs showing dendrimer nanospheres with a radius of about 100 nm. The horizontal bar represents 1 µm (A) and 100 nm (B). The surface roughness may be attributed to the water removal.

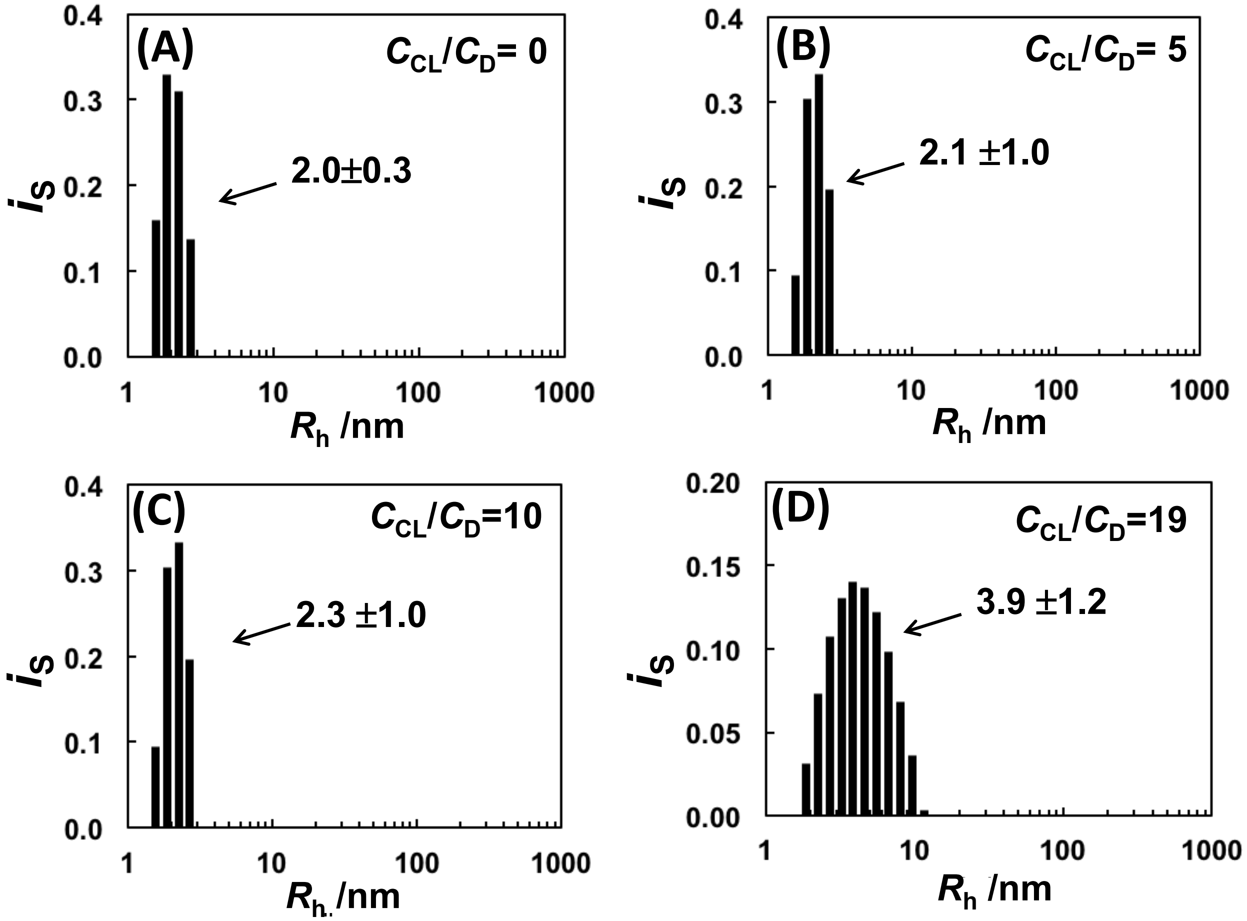

Figure 34. Normalized light-scattering intensity, i_S, as a function of hydrodynamic radius, R_h, at 25 ºC and constant dendrimer volume fraction of $\phi_D = 0.0082$ (C_D = 0.70 mmol·dm^{-3}), sodium chloride concentration of C_S = 0.98 mol·dm^{-3}, and four representative crosslinker-to-dendrimer molar ratios, C_{CL} / C_D (A-D). The numbers associated with each peak represent the value of R_h/nm calculated from the corresponding *z*-average diffusion coefficient. The associated standard deviations describe the width of the peaks; these values are calculated from the corresponding diffusion-coefficient distributions.

4.6. Guest encapsulation of crosslinked dendrimer materials

Polyamidoamine dendrimers are known to bind small organic molecules. This can be shown by evaluating the partitioning of a guest molecule between an aqueous phase containing the host dendrimers and a nonpolar organic phase towards which the guest molecule and the host system exhibit a high and poor affinity, respectively. In our case, we consider phenol blue as the guest molecule, a dye that is known to be encapsulated by the investigated dendrimer and has a high affinity towards toluene[121,122]. As it is shown in Figure 35A, phenol blue undergoes a quantitative transfer from the aqueous to the organic phase in the absence of dendrimer. In the presence of dendrimer, no phenol blue can be detected in the organic phase by spectrophotometry (see Figure 35B). If the guest-loaded dendrimers are crosslinked in the presence of sodium sulfate to yield dendrimer nanoparticles, blue phenol remains in the aqueous phase (see Figure 35C). This experiment demonstrates that dendrimer nanoparticles can encapsulate guest molecules.

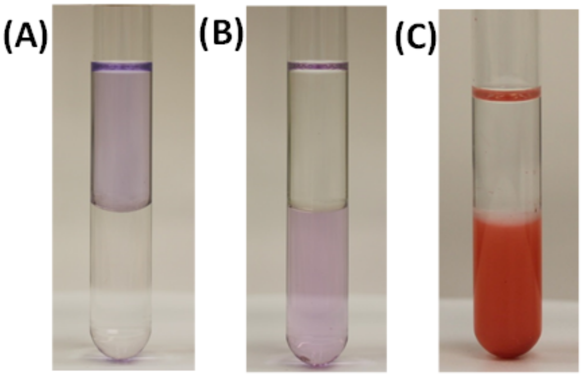

Figure 35. Partition equilibrium of phenol blue (PB) between an organic phase (toluene, top) and an aqueous phase (bottom) at room temperature. PB is initially in the aqueous phase with concentration of 0.5 μM. (A) Aqueous phase is pure water, (B) aqueous phase is a dendrimer+water solution with $\phi_{\mathrm{D}} = 0.0076$ and (C) aqueous phase is a suspension of crosslinked dendrimer nanospheres ($\phi_{\mathrm{D}} = 0.0076$).

4.7. Experimental characterization by ITC and DLS

We also characterized our dendrimer-dendrimer interactions and hydrodynamic radius in aqueous solutions by ITC and DLS, respectively. However, our experimental results could not be easily interpreted. We attribute this problem to the protonation properties of the amino terminal groups.

4.7.1. ITC Experiment for PAMAM-NH$_2$ system

Figure 36A shows the plot of the power required to maintain the sample and reference cells in thermal equilibrium as a function of time during the titration. The ITC power peaks reflect the net effect of two energetic modes both exothermic. As we can see in this figure, a sharp spike (fast mode) is followed by a slowly dissipating exothermic tail (slow mode). As the injection number, k, increases, the contribution of the slow mode significantly decreases as it can be also seen in Figure 36B. Since the heat associated with the energy of particle-particle interactions is not expected to significantly vary with the injection number when particle concentration in the ICT cell is one order of magnitude smaller than that of the titrant, we attribute the fast mode to energy of particle-particle interactions. Thus, data with $k \geq 13$ were used to calculate the corresponding differential heat per mole of titrant, $q^{(k)}$. Since the experiment pH is 9.0±0.1 and the primary amino terminal groups have a pKa of about 9.2 [132], the observed slow mode may be attributed to multiple changes in protonation states of these amino groups. In Figure 36C, we show $q^{(k)}$, as a function of the dendrimer volume fraction inside the ITC cell, $\phi_{\mathrm{D}}^{(k)}$, after injection k (with $k \geq 13$).

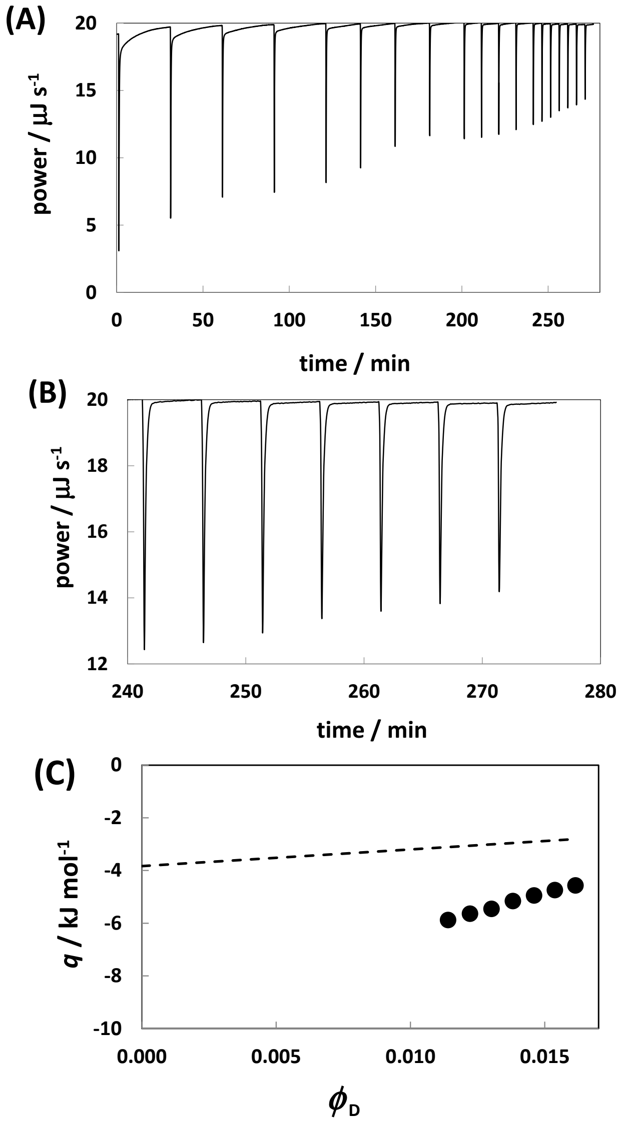

Figure 36. (A) ITC Power-time profile associated with consecutive injections of titrant solution (ϕ_D^0=0.095) into the titrand solution inside the ITC cell at 25.0 °C. (B) ITC Power-time profile associated with injections with $k \geq 13$. (C) Differential heat, q, extracted from the shown power-time profile as function of dendrimer volume fraction inside the ITC cell, ϕ_D, after each injection. The dashed curve represent the differential-heat values of $q^{(k)}$ calculated for $\varepsilon / RT = 25$ by applying the approach discussed in Chapter 3.

Our experimental binodal curve agrees with the thermodynamic model when $\varepsilon / RT = 25$. In Figure 36B, we show the values of $q^{(k)}$ (solid curve) calculated for $\varepsilon / RT = 25$. This energetic parameter is about 70% of the value of $\varepsilon / RT = 35$ (dashed curve) that best fit our ITC data with $k \geq 14$.

4.7.2. DLS Experiments for PAMAM-NH_2

Similarly to the PAMAM-OH dendrimer, we also examined the effect of salt concentration and temperature on the dependence of the DLS dendrimer diffusion coefficient (D) as a function of ϕ_{D} (slope k_{D}, see Chapter 3).

In Figure 37, we plot the normalized diffusion coefficient, $(6\pi\eta D_{\mathrm{DLS}}) / k_{\mathrm{B}}T$, as a function of dendrimer volume fraction, ϕ_{D} at low (0.043 mol·dm^{-3}), intermediate (0.45 mol·dm^{-3}), and high (0.95 mol·dm^{-3}) salt concentrations. Experimental data were examined according to Eq. (3. 2). The intercept, D_0, and the normalized unitless slope, k_{D}, are obtained by applying the method of least squares and they are reported in Table 7 together with the corresponding values of R_{h}. We found values of R_{h} ranging between 2.1 and 2.5. The hydrodynamic radius slightly decreases as salt concentration increases, which is consistent with more charge screening at high salt concentration. Note that in water PAMAM-NH_2 has a positive charge (pKa=9.2[132]). We can also observe that R_{h} decreases at higher temperatures.

We now turn our attention to the values of k_{D} in Table 7. We can observe that at low salt concentrations, k_{D} is more positive in comparison to PAMAM-OH (see Section 3.4). As result of the higher PAMAM-NH_2 charge, we can expect dendrimer-dendrimer interactions to be more repulsive than in the case of PAMAM-OH. This is in agreement with the value of ε for PAMAM-NH_2 being larger than that of PAMAM-OH. As the salt concentration increases, k_D decreases as a result of the salting-out interaction (see Section 3.4).

Table 7. DLS parameters for PAMAM-NH_2.

C_S / mol·dm^{-3}	T / °C	D_0 / 10^{-9}·m^2·s^{-1}	η / 10^{-3}·kg·m^{-1}·s^{-1}	R_h / nm	k_D
0.043	25.0	0.0950±0.0011	0.909	2.53±0.03	6.4±0.9
0.450	25.0	0.0847±0.0014	1.075	2.40±0.04	2.0±0.9
0.947	25.0	0.0705±0.0006	1.342	2.31±0.02	-4.4±0.4
0.043	37.0	0.1308±0.0011	0.706	2.46±0.02	5.2±0.7
0.450	37.0	0.1217±0.0022	0.837	2.23±0.04	-2.3±1.3
0.947	37.0	0.1019±0.0014	1.037	2.15±0.03	-7.7±0.6

In Table 7, we can also see that k_D appreciably decreases as temperature increases. For example k_D decreases by 3.3 as the temperature changes from 25 to 37 °C at $C_\mathrm{S} = 0.947$ M (see Table 7). This suggests that dendrimer-dendrimer interactions become more attractive as temperature increases, in qualitative disagreement with the observed thermal behavior of LLPS. Examination of Eq. (3.55) shows that the temperature behavior of k_D is given by the difference of two contributions. The first contribution contains the energy term, ε, while the second contribution contains the salting-out parameter, q, and the salt osmotic coefficient, φ. Numerical examination shows that the first contribution is expected to decrease by 4%, while the second contribution is predicted to decrease by 8% when the temperature is increase from 25 to 37 °C at $C_\mathrm{S} = 0.947$ M. The net effect on k_D is an increase of the k_D value of about 1.3 in disagreement with our experimental results. However, Eq. (3.55) is based on the assumption that the hydrodynamic-interaction parameter, k_{H} (see Eq. (3.53)), is independent of temperature. For charged particles, k_{H} may appreciably change with temperature since particle mobility is coupled with the mobility of the small ions[133,134].

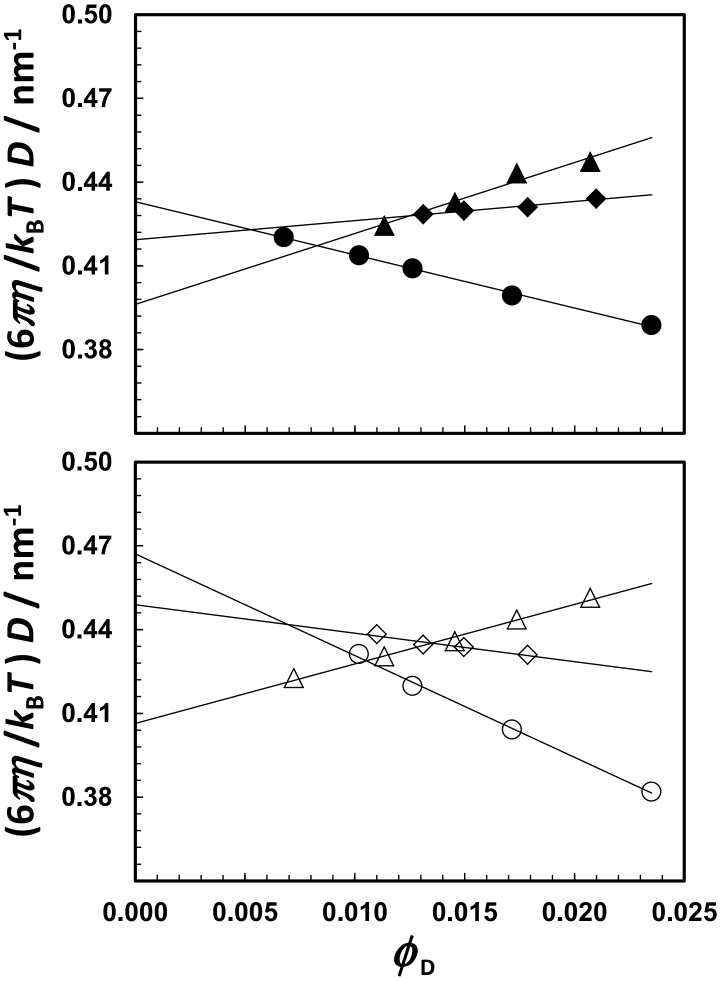

Figure 37. Normalized DLS diffusion coefficient as a function of PAMAM-NH$_2$ dendrimer volume fraction, ϕ_{D}, at 25 °C (A) $C_{\mathrm{S}} = 0.043\ \mathrm{mol \cdot dm^{-3}}$, (closed triangles), $C_{\mathrm{S}} = 0.450\ \mathrm{mol \cdot dm^{-3}}$ (closed diamonds) and $C_{\mathrm{S}} = 0.947\ \mathrm{mol \cdot dm^{-3}}$ (closed circles) and 37 °C (B) $C_{\mathrm{S}} = 0.043\ \mathrm{mol \cdot dm^{-3}}$, (open triangles), $C_{\mathrm{S}} = 0.450\ \mathrm{mol \cdot dm^{-3}}$ (open diamonds) and $C_{\mathrm{S}} = 0.947\ \mathrm{mol \cdot dm^{-3}}$ (open circles). The solid lines are linear fits through the data.

4.8. Conclusions

In this Chapter we showed that LLPS of aqueous solutions of PAMAM G4-NH_2 can also be induced in the presence of sodium sulfate. We were also able to show that our thermodynamic model also agrees with both the location of the experimental bimodal and the slope around the critical point. Furthermore, this model also predicts the observed temperature behavior where we can only induce LLPS by cooling our PAMAM G4-NH_2 + salt + water system.

We also showed that the addition of a small amount of glutaraldehyde enhances the LLPS domain due to dendrimer oligomerization and leads to the formation of spherical dendrimer nanoclusters. The proposed mechanism is that dendrimer self-association reduces the mixing entropy of the homogenous solution, thereby inducing the nucleation of a dendrimer-rich liquid phase; here, dendrimer nano-assemblies are the precursors of the emerging phase. Furthermore, the high dendrimer concentration inside the nanoclusters accelerates dendrimer crosslinking, thereby producing chemically stable dendrimer nanoparticles. Our preliminary results show that dendrimer spherical nanoparticles (radius of ≈ 100 nm) are obtained from this coupling. It is important to remark that crosslinking alone results in the formation of dendrimer oligomers with an average size that smoothly increases with crosslinker concentration.

Chapter 5: Summary

Dendrimers are hyperbranched macromolecules important for host-guest chemistry and self-assembly, relevant to catalysis, medicinal chemistry and nanoscience. This work contributes to the fundamental understanding of the phase behavior of dendrimer aqueous solutions and the effect of salting-out agents on macromolecules in general. Our experimental findings and theoretical model apply to the two dendrimers chosen in this investigation (PAMAM-OH and PAMAM-NH2, G4). Nevertheless, these studies can be used as the starting reference point for LLPS studies on other dendrimer systems. As future work, one important aspect to investigate will be how the LLPS behavior depends on the composition of surface terminal groups.

In Chapter 4 of Part I of this dissertation, we showed that the coupling of dendrimer oligomerization, which is a chemical reaction occurring in homogeneous solution, with a physical process, LLPS, leads to the formation of dendrimer globular nanoparticles. In this process, dendrimer self-association reduces the mixing entropy of the homogenous solution, thereby inducing the nucleation of dendrimer-rich liquid nanodroplets. Our results show that dendrimer globular particles with radius of ≈ 100 nm are irreversibly formed. One future goal is to identify variables that can be used to control the size of these particles. This requires a systematic investigation on the effect of crosslinking temperature, its difference with the LLPS temperature of dendrimer solution, pH and dendrimer concentration.

This investigation provides guidance for the development of novel dendrimer globular nanoparticles obtained through LLPS-induced oligomerization using low generation dendrimers as the building blocks. The preparation of these nanoparticles may circumvent the need of preparing high-generation dendrimers, which are relatively hard to synthesize, sterically hindered and they also possess a reduced guest capacity. To prepare guest-loaded dendrimer nanoparticles, guest molecules are first added into a binary aqueous solution of low generation dendrimers. In these conditions, guest encapsulation is favored by the more open conformational state assumed by dendrimers. In a second step, a salt-water solution is then mixed with the dendrimer solution in order to promote a more compact conformational state of the guest-loaded dendrimers and introduce the LLPS boundary in the system phase diagram. In a third step, a small amount of crosslinker is added to trigger oligomerization-induced LLPS and produce guest-loaded dendrimer nanoparticles.

Finally, we observe that for future work oligomerization-induced LLPS can be also extended to systems containing two distinct macromolecules such as dendrimers and enzymes. The resulting enzyme-dendrimer nanomaterials can potentially find applications in the field of catalysis.

Part II

FORMATION AND THERMODYNAMIC STABILITY OF HOST-GUEST POLYMER-PORPHYRIN SUPRAMOLECULAR ASSEMBLIES

Chapter 6: Background

6.1. Introduction

Porphyrins, from the Greek porphura (*i.e.*, purple), are tetrapyrrolic macrocycles of 20 carbon atoms and four nitrogen atoms (see Figure 38); the macrocycle is built up from four smaller pyrrole subunits[135]. The pyrrolic nitrogen atoms can bind several metal ions and form metalloporphyrins[136–138]. Their structure is fully aromatic and contains 18 π – electrons[135].

Many porphyrins occur in nature where they are synthesized by living systems. Small variations on the basic chemical structure of the tetrapyrrolic macrocycle of porphyrins lead to a wide diversity of biochemical functions[135,138]. Well-known natural compounds utilizing macrocycles equal or similar to porphyrins are, among others, vitamin B_{12}, chlorophyll and heme (ferroprotoporphyrin complex)[135,138]. Many synthetic porphyrins have a substituent in the *meso* position (see Figure 38) to obtain more complex porphyrins[135,138].

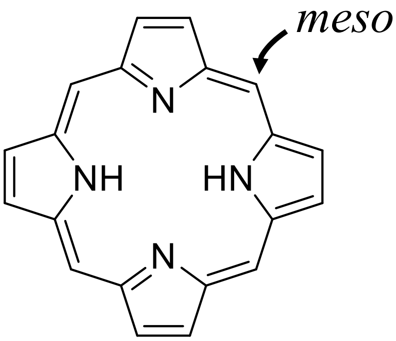

Figure 38. Basic structure of a porphyrin.

Porphyrins and their metal complexes have unique photochemical, spectroscopic and electrochemical properties; they also have applications in catalysis[135,139–142], supramolecular chemistry[135,139,141–143], photoelectrical devices[144,145] and biomedicine[146–151]. In catalysis, metalloporphyrins are known to catalyze a wide range of reactions including the functionalization of saturated C–H bonds[139]. In nature, metalloporphyrins compounds act as centers for significant biochemical events (*e.g.* heme iron complexes, vitamin B12 cobalt complexes, chlorophyll magnesium binding)[138]. Metalloporphyrins are also used as building blocks for the formation of noncovalently connected polymers[142].

Another important application of porphyrins is their use in medicine for photodynamic therapy (PDT). PDT is a form of therapy that uses photochemical phenomena induced by light to treat diseases such as cancer[152]. In fact, PDT has been approved and used against several cancer types such as bladder, brain, breast metastases, skin and oral cancers[146,152]. The therapeutic effect of PDT is based on the formation of reactive oxygen species (ROS) upon activation of a photosensitizer by light[146,152,153]. In turn, ROS causes cytotoxicity (*i.e.*, damage of cell membranes), vascular damage, and inflammatory and immunological responses[146,152,153]. In PDT, the photosensitizer is a substance, which upon absorption of light induces a chemical or physical alteration of another substance[146,152]. Most photosensitizers used in PDT today are metal-free porphyrins or porphyrin related compounds[146,147,151,152]. One of the main advantages of PDT and the use of porphyrins is its tissue selectivity, which mainly affects the target tissue. This selectivity is based on a difference between the photosensitizer retention in tumors and normal tissues[152]. The light source in PDT is in the visible and near-infrared regions and the choice of wavelength depends on the photosensitizer used and how deep light penetration through tissue is necessary. For deeper tissue penetration light with wavelengths in the red to near infrared region is desirable[147,152].

The basic photophysical processes involved in PDT are represented in Figure 39 by using a Jablonski diagram[146]. In this energy diagram, the ground state of the photosensitizer is a singlet state, S_0, and upon absorption of light the photosensitizer is excited to the vibronic level of an excited singlet state, S_1. In order to return to the S_0 – state, the photosensitizer can convert the absorbed energy through different processes such as fluorescence ($S_0 \rightarrow S_1$), internal conversion ($S_0 \rightarrow S_1$) and inter-system crossing ($S_1 \rightarrow T_1$) followed by phosphorescence ($T_1 \rightarrow S_0$). The photodynamic action of the photosensitizer is mostly mediated by the T_1 state since the excited photosensitizer S_1 state does not react directly with surrounding cells and tissues[146,152]. The T_1 photosensitizer can return to S_0 by undergoing a photodynamic reaction. Specifically, the T_1 state reacts first with groundstate (triplet) oxygen, $^3O_2$[146,152,153]. Upon energy exchange, the photosensitizer return to S_0 will correspond to the formation of the excited state (singlet) of oxygen, $^1O_2$. This species is highly cytotoxic and causes irreversible damage to vital structures and functions of cells, which ultimately results in the destruction of tumor tissue.

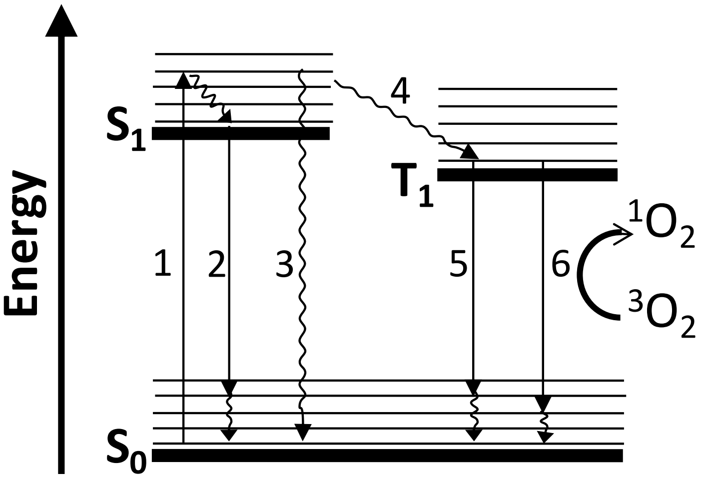

Figure 39. Schematic representation of the Jablonski diagram showing the various photophysical processes: (1) absorption, (2) fluorescence, (3) internal conversion, (4) intersystem crossing, (5) phosphorescence and (6) formation of singlet oxygen $^1O_2$ by energy transfer from T_1 photosensitizer to triplet oxygen $^3O_2$ [adapted from[146]].

6.2. Spectroscopic Properties of Porphyrins

Porphyrin spectroscopic properties depend on their protonation state among other factors such as substitute groups, metal binding and aggregation[135,154–156]. In this section, we will focus on the spectroscopic properties of the basic porphyrin structure known as porphine[135]. In Figure 40, we show the structure of the free base porphine (FBP) (Figure 40 A) where the two protonated nitrogens are located along the *x*-axis as a convention[157]. At relatively low pH, the two nitrogens along the *y*-axis are protonated giving rise to the diacid porphine (DAP) (Figure 40 B). In the case of the metalloporphyrin (Figure 40 C), the two protons of FBP are replaced with a metal ion, M^{2+} (usually).

The spectroscopic properties of porphines are mainly related to the electronic properties of the 18 π electrons of the inner 16-membered ring[135,156]. The typical porphyrin absorption spectrum is dominated by π–π^* electronic transitions. The individual electronic bands may undergo blue or red shifts (*i.e.*, a shift toward the shorter or longer wavelengths, respectively), and hypo- and hyperchromic shifts (*i.e.*, a loss or a gain in intensity, respectively) upon substitution or metalation[154,156–158]. Furthermore, the ring symmetry properties affect the number of electronic bands in the spectrum[156]. We will now discuss symmetry properties of porhines and the related energy diagrams.

In Figure 40, we can see that the symmetry of both DAP and MP is D_{4h} while that of FBP is D_{2h}. We shall see that the reason why FBP has a four-band visible absorption spectrum while DAP and MP have a two-band visible spectrum is a consequence of this difference in symmetry.

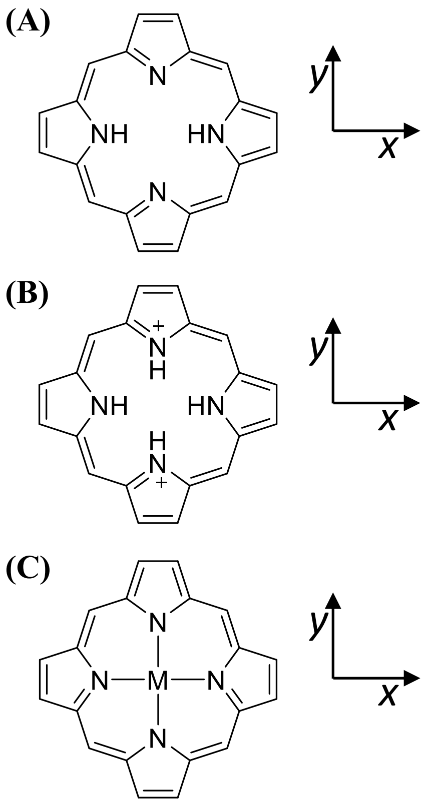

Figure 40. Structures of (A) free base porphine, FBP, (B) diacid porphine, DAB, and (C) metalloporphine, MP.

The interpretation of the electronic states of a D_{4h} porphine is based on Gouterman model[141,156]. This model is based on the results of two quantum-mechanical models: the particle on the ring and the Huckel's theory for conjugated π bonds. According to the particle-on-the ring model, the HOMO and LUMO energy levels are expected to be two-fold degenerate singlet states[156]. Gouterman's model is illustrated in Figure 41 A, where the symmetry properties of the corresponding orbitals were obtained from the shape of the molecular orbitals extracted from Huckel's theory. The symmetry notation for this electronic configuration can be obtained by applying the direct-product rule to the characters of the irreducible representation of individual orbitals. Therefore, the electronic groundstate configuration is $(a_{1u})^2(a_{2u})^2$ and it is labeled as A_{1g}. The two excited configurations,

$(a_{2u})^2(a_{1u})(e_g)$ and $(a_{2u})(a_{1u})^2(e_g)$, are labeled as $(a_{1u})(e_g)$ and $(a_{2u})(e_g)$, respectively. They are both two-fold degenerate, labeled as x and y. Note that both excited configurations follow the E_u symmetry properties. Because the wavefunctions of the two excited configurations share the same symmetry and energy, the variational method can be used to show that more accurate wavefunctions[156,159] are given by

$$\begin{aligned} \left|B\right\rangle &= \frac{1}{\sqrt{2}}\left(\left|a_{1u}e_g\right\rangle + \left|a_{2u}e_g\right\rangle\right) \text{ with } E_B = E_0 + \Delta \\ \left|Q\right\rangle &= \frac{1}{\sqrt{2}}\left(\left|a_{1u}e_g\right\rangle - \left|a_{2u}e_g\right\rangle\right) \text{ with } E_Q = E_0 - \Delta \end{aligned} \qquad (6.\ 1)$$

where E_B and E_Q are the energies associated with excited states $\left|B\right\rangle$ and $\left|Q\right\rangle$, respectively, while $E_0 = \left\langle a_{1u}e_g\right|\hat{H}\left|a_{1u}e_g\right\rangle = \left\langle a_{2u}e_g\right|\hat{H}\left|a_{2u}e_g\right\rangle$ and $\Delta = \left\langle a_{1u}e_g\right|\hat{H}\left|a_{2u}e_g\right\rangle$ with $\hat{H}$ being the Hamiltonian operator. The energy diagram deduced from Gouterman's model is shown in Figure 41 B. This diagram shows that the transition, $\left|Q\right\rangle \leftarrow \left|A_{1g}\right\rangle$ will occur at longer wavelengths compared to $\left|B\right\rangle \leftarrow \left|A_{1g}\right\rangle$. The intensity of the transitions, $\left|Q\right\rangle \leftarrow \left|A_{1g}\right\rangle$ and $\left|B\right\rangle \leftarrow \left|A_{1g}\right\rangle$, can be examined by considering the corresponding transition dipole moments[156]:

$$\begin{aligned} \mu_{B(x,y)} &= \left\langle A_{1g}\right|(x,y)\left|B\right\rangle = \left(\left\langle A_{1g}\right|(x,y)\left|a_{1u}e_g\right\rangle + \left\langle A_{1g}\right|(x,y)\left|a_{2u}e_g\right\rangle\right)/\sqrt{2} \\ \mu_{Q(x,y)} &= \left\langle A_{1g}\right|(x,y)\left|Q\right\rangle = \left(\left\langle A_{1g}\right|(x,y)\left|a_{1u}e_g\right\rangle - \left\langle A_{1g}\right|(x,y)\left|a_{2u}e_g\right\rangle\right)/\sqrt{2} \end{aligned} \qquad (6.\ 2)$$

The integrals $\left\langle A_{1g}\right|(x,y)\left|a_{1u}e_g\right\rangle$ and $\left\langle A_{1g}\right|(x,y)\left|a_{2u}e_g\right\rangle$ in Eqs (6. 2) are predicted to be different from zero because the corresponding representations contain A_{1g}. Eq. (6. 2) shows that $\mu_{Q(x,y)} = 0$ and the $\left|Q\right\rangle \leftarrow \left|A_{1g}\right\rangle$ is predicted to be forbidden. Experimental absorption spectra of MP and DAP show that $\left|Q\right\rangle \leftarrow \left|A_{1g}\right\rangle$ transitions do occur in the visible range but they are significantly weaker than $\left|B\right\rangle \leftarrow \left|A_{1g}\right\rangle$ transitions occurring at shorter wavelengths (uv range)[156]. Furthermore, in the absorption spectra of MP and DAP, the $\left|Q\right\rangle \leftarrow \left|A_{1g}\right\rangle$ transition results in two bands labeled as Q(0,0) and Q(1,0), with the Q(1,0) being of higher energy[141,156]. The notations (0,0) and (1,0) refer to two bands sharing the same electronic origin, but different vibronic component.

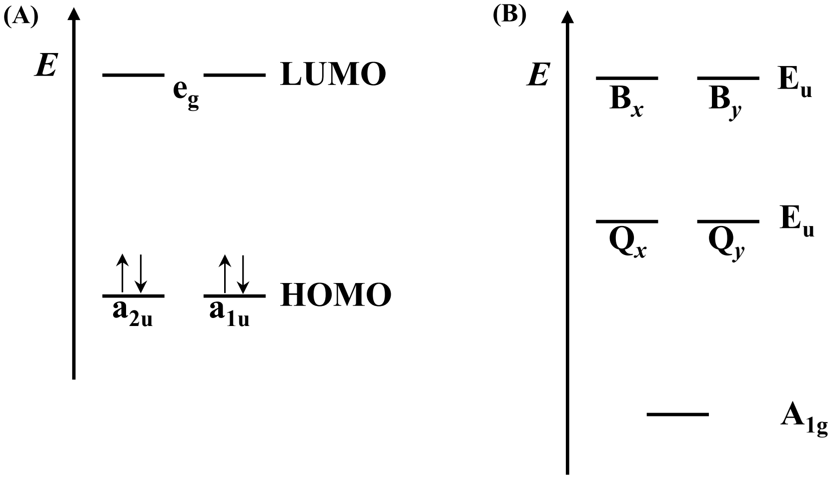

Figure 41. Energy diagram for the (A) four-orbital model and (B) electronic states of DAP or MP.

In the case of FBP, the symmetry changes from D_{4h} to D_{2h}. This implies that the x and y axis are no longer equivalent and the two-fold degenerate Q-bands will split into Q_x and Q_y[141,156]. The orbital energy diagram for the symmetry group D_{2h} is shown in Figure 42 A. The two orbitals with symmetry e_g in Figure 41 A become b_{3g} and b_{2g} in Figure 42 A, while the a_{1u} and a_{2u} orbitals become a_u and b_{1u}, respectively. For the LUMO orbitals, the b_{2g}

energy is lower than the b_{3g} energy, while for the HOMO orbitals, the b_{1u} energy is lower than the a_u energy[156].

The ground state electronic configuration for D_{2h} symmetry is $(a_u)^2(b_{1u})^2$ which is labeled as A_{1g}. In this case, we obtain the following four excited configurations: $(a_u)^2(b_{1u})(b_{3g})$ and $(a_u)(b_{1u})^2(b_{2g})$, which can be labeled as B_{2u}, and $(a_u)^2(b_{1u})(b_{2g})$ and $(a_u)(b_{1u})^2(b_{3g})$, which can be labeled as B_{3u}. Note that x and y are associated with B_{3u} and B_{2u}, respectively. According to symmetry, $\left|b_{1u}b_{3g}\right\rangle$ can mix with $\left|a_u b_{2g}\right\rangle$, while $\left|b_{1u}b_{2g}\right\rangle$ can mix with $\left|a_u b_{3g}\right\rangle$[156]. However, these orbitals cannot be assumed to be two pairs of degenerate orbitals. Protonation along the x axis leads to lowering the energy of b_{2g} compared to b_{3g}, and increasing the energy of a_u compared to b_u[156].

As a natural extension of two linear combinations given by Eq. (6.1) for the D_{4h} case, we can write for the D_{2h} case the following four linear combinations[156]:

$$
\begin{aligned}
\left|B_x\right\rangle_0 &= \frac{1}{\sqrt{2}}\left(\left|b_{1u}b_{2g}\right\rangle + \left|a_u b_{3g}\right\rangle\right) \\
\left|B_y\right\rangle_0 &= \frac{1}{\sqrt{2}}\left(\left|b_{1u}b_{3g}\right\rangle + \left|a_u b_{2g}\right\rangle\right) \\
\left|Q_x\right\rangle_0 &= \frac{1}{\sqrt{2}}\left(\left|b_{1u}b_{2g}\right\rangle - \left|a_u b_{3g}\right\rangle\right) \\
\left|Q_y\right\rangle_0 &= \frac{1}{\sqrt{2}}\left(\left|b_{1u}b_{3g}\right\rangle - \left|a_u b_{2g}\right\rangle\right)
\end{aligned}
\tag{6. 3}
$$

where we explicitly distinguish the x from the y states. The "0" subscripts indicate that these four wavefunctions do not take into account degeneracy loss. This can be included by applying perturbation theory. More accurate wavefunctions for the Q states are given by[156]

$$\left|Q_x\right\rangle = \left|Q_x\right\rangle_0 + \lambda_x \left|B_x\right\rangle_0$$
$$\left|Q_y\right\rangle = \left|Q_y\right\rangle_0 + \lambda_y \left|B_y\right\rangle_0 \qquad (6.\ 4)$$

were λ_x and λ_y are perturbation coefficients and we have omitted the normalization factors. It can be shown that $\lambda_y > \lambda_x$[156]. This implies that $\left|Q_y\right\rangle$ possesses a higher B character compared to $\left|Q_x\right\rangle$ and allows us to associate $\left|Q_y\right\rangle$ with a higher energy and band intensity compared to $\left|Q_x\right\rangle$. The energy diagram of FBP is shown in Figure 38 B.

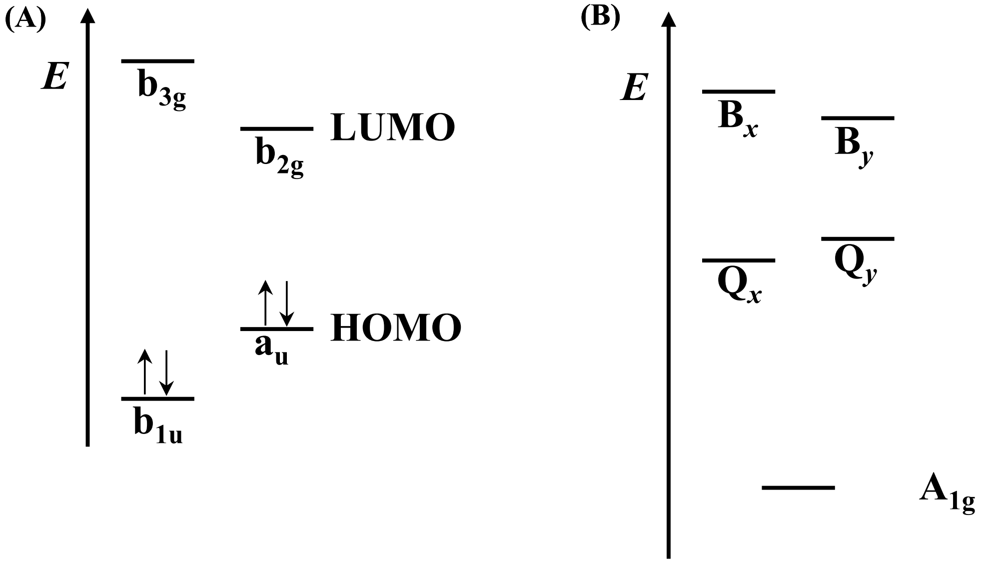

Figure 42. Energy diagram for the (A) four-orbital model and (B) electronic states of FBP.

Experimentally, the absorption spectra region between 450 and 700 nm includes the lowest energy absorption Q-bands[135,141,156]. These are of medium intensity (molar absorptivities, ε, are in order of 10^4 $M^{-1}cm^{-1}$). In the case of the FBP, the Q-bands appear as two pairs of peaks (0,0) and (1,0) denoted as Q_y (1,0), Q_y (0,0), Q_x (1,0) and Q_x (0,0). The more intense transitions to B states are located between 380 and 420 nm (Soret band) and may include different vibronic components[141,156].

6.3. Porphyrin Aggregation

Self-aggregation of porphyrins in aqueous systems is very common and it involves the formation of dimers and/or larger aggregates of various structures[143,158,160–164]. This process depends on physicochemical properties such as solution pH, ionic strength, temperature and the presence of additives such as polymers[143,165,166]. Self-association plays a significant role in porphyrin spectroscopy properties and, consequently, the porphyrin aggregation state is of interest for applications such as sensors, catalyst sand photodynamic therapy[167]. Since self-aggregation makes porphyrins less effective photosensitizers and catalysts, fundamental studies aimed at characterizing and modulating the aggregation state of porphyrins are very valuable. For instance in photodynamic therapy, aggregation shortens the triplet-state lifetime and decreases the singlet-oxygen quantum yield by dissipating the energy through internal conversion[147].

Porphyrin aggregates have been mainly investigated by examining red-shifted (J-aggregates, edge-to-edge stacking) and blue-shifted (H-aggregates, face-to-face stacking) porphyrins absorption spectra[168]. Exciton theory can be used to explain the effect of aggregation on the spectroscopic properties of porphyrins[143,164,168]. We will focus on the porphyrin dimer, AB, formation described by the reaction A + B→ AB, where A and B are two identical porphyrin units. The groundstate of AB and its excited state can be described by the dimer wavefunction, ψ_{AB}, as a product of both monomers wavefunctions, ψ_{A} and ψ_{B} (first-order perturbation). If we apply the variational method to the dimer wavefunctions we can obtain[164,168]:

$$\psi_{\mathrm{AB}} = \frac{1}{\sqrt{2}}(\psi^*_{\mathrm{A}}\psi_{\mathrm{B}} + \psi_{\mathrm{B}}\psi^*_{\mathrm{A}}) \text{ and } E^*_{+} = \alpha + \beta$$
$$\psi_{\mathrm{AB}} = \frac{1}{\sqrt{2}}(\psi^*_{\mathrm{A}}\psi_{\mathrm{B}} - \psi_{\mathrm{B}}\psi^*_{\mathrm{A}}) \text{ and } E^*_{+} = \alpha - \beta \tag{6. 5}$$

where α and β are interaction-energy parameters with $\alpha = \left\langle \psi^*_{\mathrm{A}}\psi_{\mathrm{B}} \middle| \hat{H} \middle| \psi^*_{\mathrm{A}}\psi_{\mathrm{B}} \right\rangle =$ $= \left\langle \psi_{\mathrm{A}}\psi^*_{\mathrm{B}} \middle| \hat{H} \middle| \psi_{\mathrm{A}}\psi^*_{\mathrm{B}} \right\rangle$ and $\beta = \left\langle \psi^*_{\mathrm{A}}\psi_{\mathrm{B}} \middle| \hat{H} \middle| \psi_{\mathrm{A}}\psi^*_{\mathrm{B}} \right\rangle = \left\langle \psi_{\mathrm{A}}\psi^*_{\mathrm{B}} \middle| \hat{H} \middle| \psi^*_{\mathrm{A}}\psi_{\mathrm{B}} \right\rangle$.

From the interaction between two dipoles[169], we can relate the interaction energy β with two transition dipoles, $\vec{\mu}_{\mathrm{A}}$ and $\vec{\mu}_{\mathrm{B}}$, separated by a distance R as follows:

$$\beta = \frac{(\vec{\mu}_{\mathrm{A}} \cdot \vec{\mu}_{\mathrm{B}})R^2 - 3(\vec{\mu}_{\mathrm{A}} \cdot \vec{R})(\vec{\mu}_{\mathrm{B}} \cdot \vec{R})}{R^5} \tag{6. 6}$$

where $\vec{R}$ is the position vector describing the relative location of the centers of the two porphyrins and R the corresponding distance. We will now consider the two limiting cases of parallel and aligned dipoles[164]. In the case of parallel dipoles, we have $\mu = |\vec{\mu}_{\mathrm{A}}| = |\vec{\mu}_{\mathrm{B}}|$ perpendicular to $\vec{R}$ and $\beta = \mu^2 / R^3$. For aligned dipoles, we have $\mu = |\vec{\mu}_{\mathrm{A}}| = |\vec{\mu}_{\mathrm{B}}|$ parallel to $\vec{R}$ and $\beta = -2\mu^2 / R^3$. These two limiting expressions for β allows us to identify two types of energy diagrams as shown in Figure 43. The transition dipole-moment of the dimer, $\vec{\mu}$, can be calculated as the linear combination of dipole moments of the monomers following the same approach as that of the corresponding dipoles. These two types of aggregates are denoted as H-aggregates, those resulting in parallel dipoles and $\beta > 0$, and J-aggregates, those resulting in aligned dipoles and $\beta > 0$. The analysis of the energy diagrams, in Figure 43 allows us to deduce that the spectrophotometric bands of H- and J-aggregates are blue and red shifted with respect to the monomer, respectively.

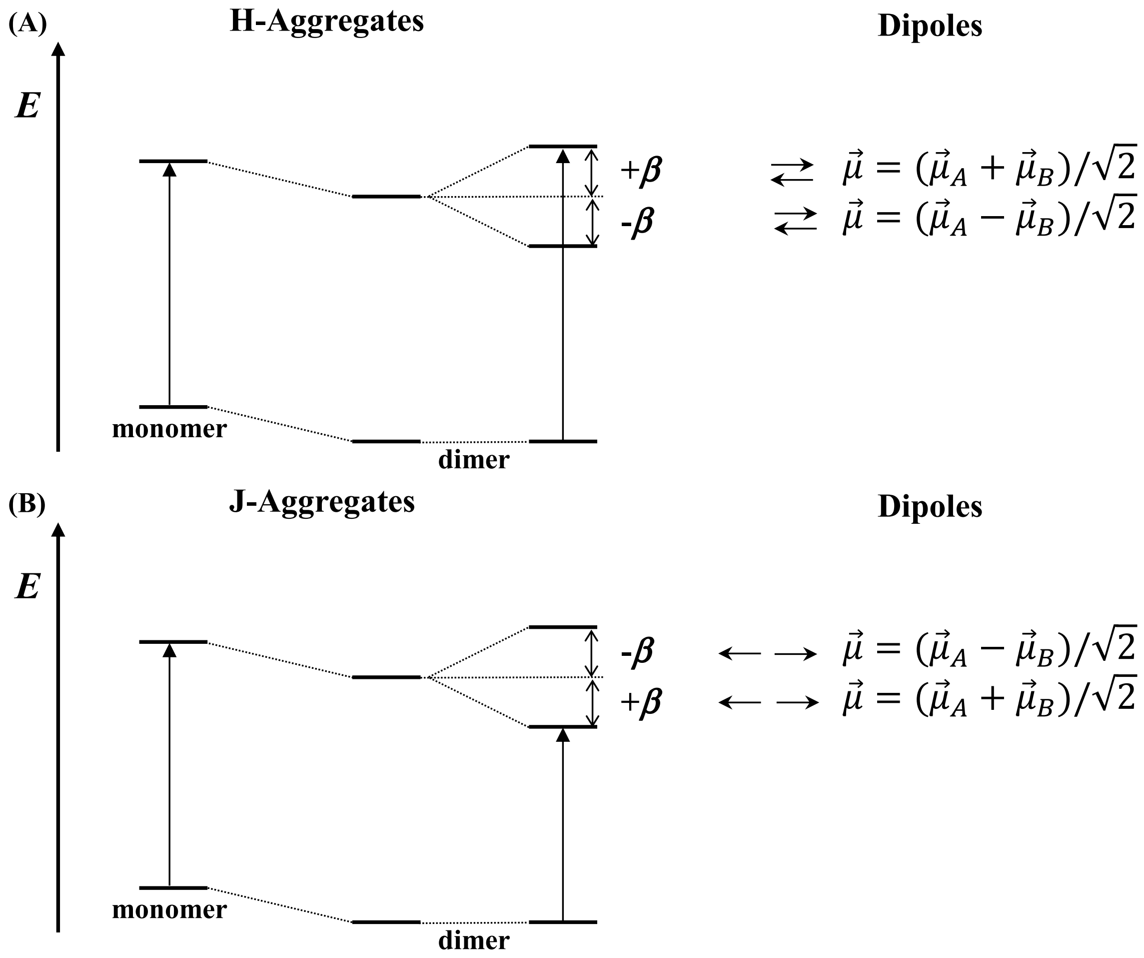

Figure 43. Energy diagram for (A) H-aggregates and (B) J-aggregates.

6.4. Meso-tetrakis(4-sulfonatophenyl) porphyrin (TPPS)

One of the most investigated porphyrin is the water-soluble meso-tetrakis(4-sulfonatophenyl) porphyrin (TPPS). TPPS has four negatively charged sulfonate groups that compensate for the hydrophobicity of the aromatic tetra-pyrrolic system and the attached four phenyl groups[163]. The amphiphilic properties of this porphyrin lead to complex self-association behavior in aqueous solutions, depending on physicochemical parameters such as concentration, temperature, ionic strength and pH. The porphyrin ring possesses two pKa values, with pKa1=pKa2=4.9 at 25 °C[137]. TPPS displays a net charge of -4 at pH ≈ 7 (FBP) and -2 at pH ≈ 3 (DAB) (see Figure 44).

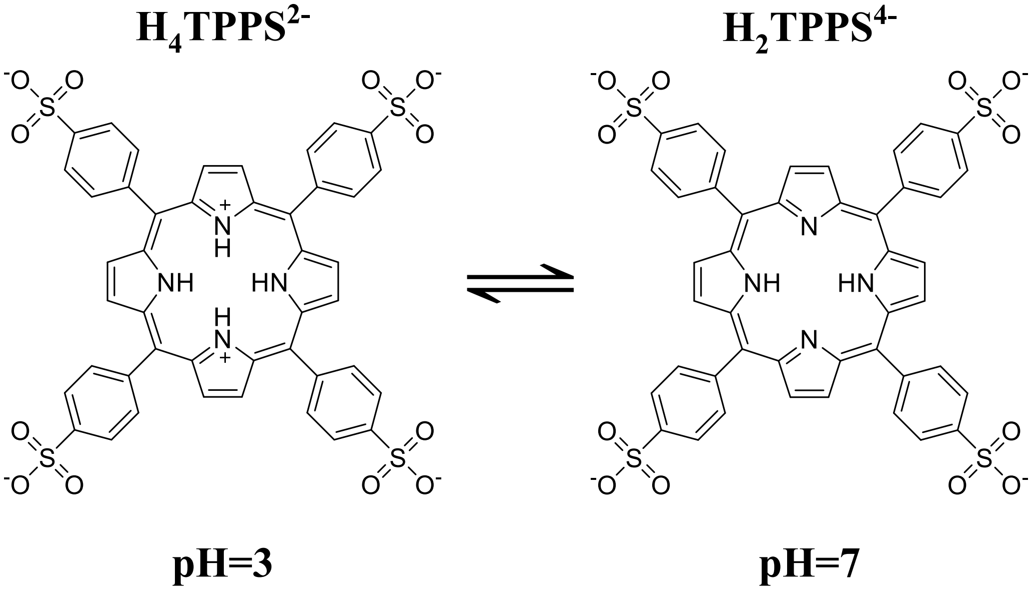

Figure 44. Acid-base equilibrium for TPPS.

The reduction of electrostatic repulsion at low pH facilitates self-association of the diacid form compared to that of the free base porphyrin at neutral and high pH[163]. TTPS diacid form is known to self-aggregate leading to the formation of ordered nanowires of J-aggregates with interesting photophysical properties for optoelectronic applications[158,163,170]. In particular, the J-aggregates form has been proposed to be stabilized through a network of electrostatic and hydrogen-bonding interactions mainly involving the negatively charged sulfonate groups and the positively charged inner nitrogen core[143].

The spectroscopic behaviour of TPPS in aqueous solutions has been utilized to characterize TPPS self-association in aqueous solutions[158,163]. This process may be described by employing a dimerization model at neutral and high pH, while the self-association occurring at low pH is more complex and normally involves the formation of large J-aggregates as mentioned above.

6.5. Polymer

The polymer used in Part II of this dissertation is polyvinyl pyrrolidone (PVP). PVP is a hydrophilic neutral, non-toxic biocompatible polymer extensively employed in pharmacological applications as well as in food, textile and biomedical industry[171]. PVP is used as a binder in tablet formulations and as a solubilizing agent for active ingredients with poor aqueous solubility[171]. The addition of PVP or PVP-copolymers to active substances forms water-soluble complexes with increased bioavailability and chemical stability during drug formulation[171].

This polymer is available in a range of molecular weights from 40,000 to 360,000 and it is composed of repeating units of the monomer polyvinylpyrrolidone (see Figure 45).

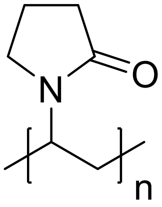

Figure 45. Structure of polyvinyl pyrrolidone (PVP).

6.6. Binding Models

We will now consider an important model describing reversible host-guest association, where host-guest affinity is described by multiple equilibrium binding[172]. In this model, we will consider that the host molecule (P) has *n* binding sites with the following reaction scheme:

$$\begin{aligned}
&\mathrm{P}+\mathrm{L} \rightleftharpoons \mathrm{PL}\\
&\mathrm{PL}+\mathrm{L} \rightleftharpoons \mathrm{PL}_2\\
&\mathrm{PL}_2+\mathrm{L} \rightleftharpoons \mathrm{PL}_3\\
&\cdots\cdots\cdots\cdots\cdots\cdots\cdots\\
&\mathrm{PL}_{n-1}+\mathrm{L} \rightleftharpoons \mathrm{PL}_n
\end{aligned} \tag{6. 7}$$

where L is the guest molecule (ligand) and PL_i (with i=1,2,…n) the host–guest bound species.

For each generic step i equilibrium associative step, we can write the corresponding mass-action law[172]:

$$K_i = \frac{[\mathrm{PL}_i]}{[\mathrm{PL}_{i-1}][\mathrm{L}]} \tag{6. 8}$$

where K_i is the stepwise association constant, $[\mathrm{PL}_i]$ is the concentration of bound ligand and [L] is the concentration of free ligand in solution. We can also introduce the cumulative association constant, β_i, by considering the following reaction[172]:

$$\mathrm{P} + i\ \mathrm{L} \rightleftharpoons \mathrm{PL}_i \tag{6. 9}$$

where the related mass-action law is,

$$\beta_i = \frac{[\mathrm{PL}_i]}{[\mathrm{P}]\,[\mathrm{L}]^i} \tag{6. 10}$$

It is important to recognize that the two sets of constants, K_i and β_i, are directly related to each other i.e. $\beta_i = \prod_{j=1}^{i} K_j$. If one set of constants is known, the other set can be straightforwardly calculated. To derive a relation between bound and free ligand we consider the average number of ligand bound to one P macromolecule, ν ,

$$\nu = \frac{C_{\mathrm{L}} - [\mathrm{L}]}{C_{\mathrm{P}}} \qquad (6.\ 11)$$

where C_{L} and C_{P} are the total ligand and host concentrations, respectively. Both C_{L} and C_{P} can be related to $[\mathrm{L}]$ and $[\mathrm{PL}]$ by applying the following mass balances:

$$C_{\mathrm{L}} = [\mathrm{L}] + [\mathrm{PL}] + 2[\mathrm{PL}_2] + 3[\mathrm{PL}_3] + \ldots + n[\mathrm{PL}_n] \qquad (6.\ 12)$$

$$C_{\mathrm{P}} = [\mathrm{P}] + [\mathrm{PL}] + [\mathrm{PL}_2] + [\mathrm{PL}_3] + \ldots + [\mathrm{PL}_n] \qquad (6.\ 13)$$

If we insert these two equations (Eqs. (6. 12) and (6. 13)) into Eq. (6. 11) we can derive the following relation between ν and $[\mathrm{L}]$:

$$\nu = \frac{[\mathrm{PL}] + 2[\mathrm{PL}_2] + 3[\mathrm{PL}_3] + \ldots + n[\mathrm{PL}_n]}{[\mathrm{P}] + [\mathrm{PL}] + [\mathrm{PL}_2] + [\mathrm{PL}_3] + \ldots + [\mathrm{PL}_n]} = \frac{\sum_{i=1}^{n} i\beta_i [\mathrm{L}]^i}{1 + \sum_{i=1}^{n} \beta_i [\mathrm{L}]^i} \qquad (6.\ 14)$$

This equation is known as the Adair equation[172] and it is a general equation for host-guest binding that can be used to determine the set of stepwise constants K_i by measuring ν as a function of $[\mathrm{L}]$. However, if n is large (even as large as 4), there are too many adjustable parameters to determine which requires many extremely precise experimental data. To overcome this problem, assumptions are usually introduced in order to obtain simplified models. We will consider the simplest case of multiple equilibria where all the n biding sites on the host have the same affinity for the ligand (equivalent sites) and the affinity of any site is independent of whether or not the other sites are occupied (independent sites)[172]. In this case, the multiple equilibria problem can be described by two parameters only: the intrinsic dissociation constant, K, of a host site and the total number of sites, n [172].

It is important to remark that these assumptions do not imply that all stepwise equilibrium constants, K_i, are identical. To appreciate this, we need to observe that the label PL_i does not refer to one chemical state only. For example, in the case of PL_2 with $n = 4$, we have six possible "isomers" related to the different arrangements of the two ligands. In general, the number of possible arrangements, $g_{i,n}$, for the species PL_i can be calculated by,

$$g_{i,n} = \begin{pmatrix} n \\ i \end{pmatrix} = \frac{n!}{i!(n-i)!} \quad \text{with } 1 \le i \le n \tag{6. 15}$$

In this macroscopic approach, we do not make distinctions between such chemical species, and the macroscopic equilibrium association constant K_i simply group all of them together as PL_i [172]. Thus the cumulative constant for the formation of $[\mathrm{PL}_i]$ corresponds to the sum of the concentrations of individual isomers. To take into account this effect (see Eq. (6. 15)) and keeping in mind that dissociation constants are the reciprocal of association constants, we can write:

$$\beta_i = \prod_{j=1}^{i} K_j = g_{i,n} / K^i \tag{6. 16}$$

Note that in the limiting case of $n = 1, \beta_1 = 1/K$. Using this result, the Adair equation can be rewritten in the following way[172]:

$$\nu = \frac{\sum_{i=1}^{n} i \frac{n!}{i!(n-i)!} \left([\mathrm{L}]/K\right)^i}{1 + \sum_{i=1}^{n} \frac{n!}{i!(n-i)!} \left([\mathrm{L}]/K\right)^i} \tag{6. 17}$$

We can use the binomial theorem to rewrite Eq. (6. 17) as:

$$\nu = \frac{n[\mathrm{L}]}{K + [\mathrm{L}]} \tag{6. 18}$$

This simple equation is known as the Scatchard equation[172] and it can be used to characterize host-guest binding processes.

As described in Section 6.1 of this chapter, porphyrins are known to self-associate in solution. Therefore, it is also convenient to examine reversible self-associative processes starting from the case of dimerization[172]. The corresponding mass-action law for the dimer dissociation process is,

$$\alpha_{\mathrm{dim}} = \frac{[\mathrm{P}]^2}{[\mathrm{P}_2]} \tag{6. 19}$$

where $[\mathrm{P}]$ and $[\mathrm{P}_2]$ are the concentration of free monomer and dimer species, respectively and α_{dim} is the dimer dissociation constant.

The total concentration of P is given by the mass balance,

$$C_{\mathrm{P}} = [\mathrm{P}] + 2[\mathrm{P}_2] \tag{6. 20}$$

By inserting the mass-action law (Eq. (6. 19)) into the mass balance (Eq. (6. 20)), we obtain an expression of C_{P} as a function of free monomer concentration, $[\mathrm{P}]$:

$$C_{\mathrm{P}} = [\mathrm{P}] + 2\,[\mathrm{P}]^2 / \alpha_{\mathrm{dim}} \tag{6. 21}$$

This quadratic equation can be solved with respect to $[\mathrm{P}]$ yielding:

$$[\mathrm{P}] = \alpha_{\mathrm{dim}} \frac{-1 + \sqrt{1 + 8C_{\mathrm{P}} / \alpha_{\mathrm{dim}}}}{4} \tag{6. 22}$$

Note that the concentration of the dimer can calculated from $[\mathrm{P}]$ directly using Eq. (6. 19). In Figure 46 we can see the dependence of the fractions $[\mathrm{P}]/C_{\mathrm{P}}$ and $2[\mathrm{P}_2]/C_{\mathrm{P}}$ on total concentration C_{P}. We note that $[\mathrm{P}]/C_{\mathrm{P}} \to 1$ in the limit of $C_{\mathrm{P}} \to 0$, and $[\mathrm{P}]/C_{\mathrm{P}} \to 0$ in the limit of $C_{\mathrm{P}} \to \infty$. Thus, the reaction will tend toward total dissociation or complete dimerization as the total concentration becomes very small or very large, respectively.

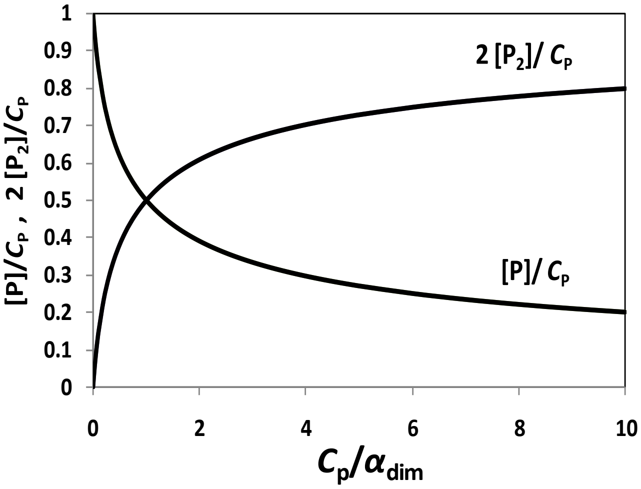

Figure 46. Dimerization process.

We can also have the case of equal-constant self-association model[172], where polymerization is assumed to occur without an upper limit. In other words, each molecule is assumed to have two equivalent binding sites. We start by writing the following scheme:

$$\begin{aligned} &2\,\mathrm{P} \rightleftharpoons \mathrm{P}_2 \\ &\mathrm{P}_2 + \mathrm{P} \rightleftharpoons \mathrm{P}_3 \\ &\mathrm{P}_3 + \mathrm{P} \rightleftharpoons \mathrm{P}_4 \\ &\cdots\cdots\cdots\cdots\cdots \\ &\mathrm{P}_{i-1} + \mathrm{P} \rightleftharpoons \mathrm{P}_i \\ &\cdots\cdots\cdots\cdots\cdots \end{aligned} \qquad (6.\,23)$$

In this model, it assumes that the binding affinity is independent of the degree of association and we can write:

$$\beta_i = \frac{1}{\alpha_{\mathrm{olig}}} = \frac{[\mathrm{P}_i]}{[\mathrm{P}]^i} \text{ with } i = 2,3,... \qquad (6.\,24)$$

where α_{olig} is the dissociation constant of one molecule from the oligomer. By inserting the mass-action law (Eq. (6. 24)) into the mass balance, we obtain an expression of C_{P} as a function of free monomer concentration, $[\mathrm{P}]$:

$$C_{\mathrm{P}} = \sum_{i=1} i[\mathrm{P}_i] = \sum_{i=1} \beta_i [\mathrm{P}]^i = [\mathrm{P}] \sum_{i=1} i([\mathrm{P}]/\alpha_{\mathrm{olig}})^{i-1} = \frac{[\mathrm{P}]}{(1-[\mathrm{P}]/\alpha_{\mathrm{olig}})^2} \qquad (6.\ 25)$$

which can be rewritten in the following way:

$$C_{\mathrm{P}}[\mathrm{P}]^2 - \alpha_{\mathrm{olig}}(\alpha_{\mathrm{olig}} + 2C_{\mathrm{P}})[\mathrm{P}] + \alpha_{\mathrm{olig}}{}^2 C_{\mathrm{P}} = 0 \qquad (6.\ 26)$$

This quadratic equation can be solved with respect to $[\mathrm{P}]$ yielding:

$$[\mathrm{P}] = \alpha_{\mathrm{olig}} \frac{(1+2C_{\mathrm{P}}/\alpha_{\mathrm{olig}}) - \sqrt{1+4C_{\mathrm{P}}/\alpha_{\mathrm{olig}}}}{2C_{\mathrm{P}}/\alpha_{\mathrm{olig}}} \qquad (6.\ 27)$$

Note that the concentrations of the P oligomers can be calculated from $[\mathrm{P}]$ directly using the mass-action law. Specifically, we have: $[\mathrm{P}_i] = \alpha_{\mathrm{olig}}([\mathrm{P}]/\alpha_{\mathrm{olig}})^i$.

Chapter 7: Materials and Experimental Techniques

7.1. Materials

5,10,15,20-Tetraphenyl-21*H*, 23*H*-porphine-*p*,*p′*,*p″*,*p‴*-tetrasulfonic acid tetrasodium hydrate (TPPS) was purchased from Sigma-Aldrich, and used as supplied, without further purification. Poly(vinylpyrrolidone) (PVP) with nominal molecular weight of 40 kg mol^{-1}, citric acid and sodium acetate were purchased from Sigma-Aldrich and used as without further purification. Sodium phosphate dibasic dyhydrate and sodium phosphate monobasic anhydrous was purchased from Fisher Scientific. Deionized water was passed through a four-stage Millipore filter system to provide higher purity water for all the experiments.

7.2. Solution Preparation

TPPS-water stock solutions with a composition of ≈1% (w/w) were prepared by weight. PVP-water stock solutions with a composition of ≈10% (w/w) were prepared by weight.

All the solutions were gravimetrically prepared by mixing known amounts of TPPS and/or PVP stock solutions with water and buffer. A 0.10-M, of the chosen buffer (sodium phosphate buffer at pH 7.1, sodium acetate buffer at pH 4.5 or citric acid buffer at pH 3.0) was also added so that the final buffer concentration was 0.010 M. TPPS and PVP weight fractions were converted into the corresponding molar concentrations using the molecular weights of 1023 kg mol^{-1} and 111.14 kg mol^{-1} for TPPS and PVP monomer respectively and the solution specific volume calculated using the specific volumes of 0.80 cm^3 g^{-1} and 0.999 cm^3 g^{-1} for PVP and 0.010-M aqueous buffer respectively. The small contribution of TPPS to the solution specific volume was neglected.

7.3. Isothermal Titration Calorimetry

ITC measurements were performed using the MicroCal iTC200 System from GE Healthcare Life Sciences. All experiments were performed at 12, 25 and 37 °C.

For dissociation experiments, small aliquots (2.0 μL) of a TPPS aqueous solution (titrant, 3.69 mM) were sequentially injected (≈20 injections) from a rotating syringe into the vigorously stirred sample cell (syringe rotation, 1000 rpm) containing porphyrin-free 0.010-M buffer (titrand

For PVP-TPPS binding experiments, small aliquots (2.0 μL) of a PVP aqueous solution (titrant, 91.0 mM) were sequentially injected into the ITC cell containing a TPPS aqueous solution (titrand, 0.244 mM). The choice of PVP instead of TPPS as the titrant was imposed by the large contribution of TPPS dilution to the recorded heat (due to porphyrin dissociation). On the other hand, blank experiments, in which PVP solutions were injected into pure buffer, showed that the contribution of PVP dilution to the overall heat involved in the PVP-TPPS mixing process is very small.

Each injection corresponds to an exothermic peak on a plot showing the power required to maintain the sample and reference cells at the same temperature as a function of time. The differential heat associated is calculated using Eq. (2. 36) in terms of dendrimer volume fraction:

$$q^{(k)} = \left[\left(V + v/2\right)\left(Q^{(k)}/V\right) - \left(V - v/2\right)\left(Q^{(k-1)}/V\right)\right] / \, vC'_{\text{TITRANT}} \tag{7. 1}$$

where $Q^{(0)} = 0$ and C'_{TITRANT} is the titrant concentration.

Theoretical binding models are then used to obtain mathematical expressions linking $Q^{(k)}/V$ to the total concentrations of titrant, $C_{\text{titrant}}^{(k)}$ (see Eq. (2. 32)), and titrand, $C_{\text{titrand}}^{(k)}$ (see Eq. (2. 35)), inside the sample cell after injection k. We then use the mathematical expressions for $Q^{(k)}/V$ developed in Chapter 8 and insert them into Eq. (7. 1), and apply the method of least squares to the experimental $q^{(k)}$ using MATLAB to yield the values of the relevant model parameters. Note that $Q^{(k)}/V$ is a continuum function of the sample composition. Hence the superscript "(*k*)" will be omitted in Chapter 8.

7.4. Absorption Spectra

Absorption spectra were obtained at room temperature (≈21-22 °C) with a Beckman DU 800 using two cuvettes with path length of $l = 1\text{ cm}$ and $l = 0.1\text{ cm}$ for experiments in the wavelength range of 500-700 nm (Q bands) and in the wavelength range of 400-450 nm (Soret band), respectively. The obtained results were reported as normalized absorption spectra by calculating the molar absorption coefficient: $\varepsilon = Abs/(lC)$, where Abs is the corresponding sample absorbance and C is the corresponding TPPS concentration.

Chapter 8: Formation and Thermodynamic Stability of (PVP+TPPS) Supramolecular Structures in Aqueous Solutions at pH 7.0

8.1. Introduction

In this chapter, the binding of polymer-porphyrin porphyrin self-association for meso-tetrakis(4-sulfonatophenyl) porphyrin (TPPS) in water at pH 7.0 was successfully characterized by isothermal titration calorimetry (ITC) and UV/visible spectromotometric techniques. Compared to spectroscopic techniques, ITC has the advantage of providing both the equilibrium constant (or standard reaction Gibbs free energy) of a reversible chemical reaction and the corresponding reaction enthalpy. Note that reaction enthalpies can be also obtained by determining equilibrium constants from spectroscopic measurements as a function of temperature (Van't Hoff plot). Consequently, if equilibrium constants are measured by ITC as a function of temperature, two independent means of determining the same reaction enthalpy become available from ITC. This unique feature is very important for assessing the accuracy of the binding models chosen to describe complex chemical equilibria. Furthermore, reaction enthalpies extracted from individual ITC measurements as a function of temperature offers a precise way to determine the reaction heat capacity. This thermodynamic parameter is known to be important for evaluating the contribution of hydrophobic interactions to binding processes in aqueous solutions. To our knowledge, there is only one qualitative ITC study related to TPPS binding to ferric myoglobin[166], and there are only few ITC investigations on porphyrins, in general[173]. In relation to spectroscopic studies there is one reporting on (PVP-TPPS) binding[174]. However, this investigation was limited to acidic pHs and neglects the very important contribution of TPPS self-association.

8.2. TPPS self-association

In Figure 47A, we show differential-heat plots for our ITC dissociation experiments at 12, 25 and 37 °C. In all three cases, we obtain positive heat values consistent with dissociation being an endothermic process. Our data were examined using the dimerization model $\mathrm{L_2} \rightleftarrows 2\mathrm{L}$ [172,175]where L and $\mathrm{L_2}$ denote the TPPS monomer and dimer respectively. In this section, we will also apply the equal-constant self-association model to TTPS[176]. We will first review the dimerization model, while the other model will be discussed at the end of this section. The cumulative heat for TPPS dimer dissociation is given by

$$Q/V = \left([\mathrm{L_2}]-[\mathrm{L_2}]_0\right)\Delta_\mathrm{d}H^0_\mathrm{dim} \tag{8. 1}$$

where $[\mathrm{L_2}]$ is dimer concentration in the ITC sample cell, $[\mathrm{L_2}]_0$ is the hypothetical concentration of dimers in the sample cell calculated by assuming that all dimers transferred from the titrant solution do not dissociate, and $\Delta_\mathrm{d}H^0_\mathrm{dim}$ is the standard enthalpy for dimer dissociation. Note that the value of Q/V is directly related to the dimer concentration because there is one binding interaction per dimer molecule. The dimer concentration is then related to the monomer concentration, $[\mathrm{L}]$, according the mass-action law:

$$\alpha_\mathrm{dim} = \frac{[\mathrm{L}]^2}{[\mathrm{L_2}]} \tag{8. 2}$$

where α_dim is the dissociation equilibrium constant. The monomer concentration is related the known total concentration of TPPS, C_L, by the mass balance:

$$\frac{C_{\mathrm{L}}}{[\mathrm{L}]} = 1 + 2\frac{[\mathrm{L}]}{\alpha_{\mathrm{dim}}} \tag{8. 3}$$

For this model, the following analytical expression for [L] can be obtained (see Section 6.6):

$$[\mathrm{L}] = \frac{\alpha_{\mathrm{dim}}}{4}\left[\left(1 + \frac{8C_{\mathrm{L}}}{\alpha_{\mathrm{dim}}}\right)^{1/2} - 1\right] \tag{8. 4}$$

Equations (8. 2) and (8. 4) are then used to obtain an expression for $[\mathrm{L}_2]$ in Eq. (8. 1). The corresponding expression of $[\mathrm{L}_2]_0$ is obtained by first calculating the dimer concentration in the titrant solution and then applying the dilution factor (see Eq. (2. 32)).

In Table 8, we report the determined values of α_{dim} and $\Delta_{\mathrm{d}}H^0_{\mathrm{dim}}$. Note that α_{dim} increases with temperature. This is qualitatively consistent with dissociation being an endothermic process. The corresponding values of standard Gibbs free energy and entropy were then calculated using $\Delta_{\mathrm{d}}G^0_{\mathrm{dim}} = -RT\ln\alpha_{\mathrm{dim}}$ and $\Delta_{\mathrm{d}}S^0_{\mathrm{dim}} = (\Delta_{\mathrm{d}}H^0_{\mathrm{dim}} - \Delta_{\mathrm{d}}G^0_{\mathrm{dim}})/T$ respectively, where R is the ideal-gas constant and T the absolute temperature. As shown in Table 8 and in the inset of Figure 48, $\Delta_{\mathrm{d}}H^0_{\mathrm{dim}}$ increases with temperature. Thus, the constant-pressure heat capacity of dissociation, $\Delta_{\mathrm{d}}C^0_{p,\mathrm{dim}} = (0.45 \pm 0.06)\ \mathrm{kJ \cdot mol^{-1} \cdot K^{-1}}$, was determined by applying the method of least squares based on $\Delta_{\mathrm{d}}H^0_{\mathrm{dim}} = \Delta_{\mathrm{d}}H^0_{\mathrm{dim,R}} + \Delta_{\mathrm{d}}C^0_{p,\mathrm{dim}}(T - T_{\mathrm{R}})$, where $T_{\mathrm{R}} = 298.15\ \mathrm{K}$ is our chosen reference temperature and $\Delta_{\mathrm{d}}H^0_{\mathrm{dim,R}} = (39.3 \pm 0.6)\ \mathrm{kJ \cdot mol^{-1}}$ is its corresponding $\Delta_{\mathrm{d}}H^0_{\mathrm{dim}}$ value extracted from the fit.

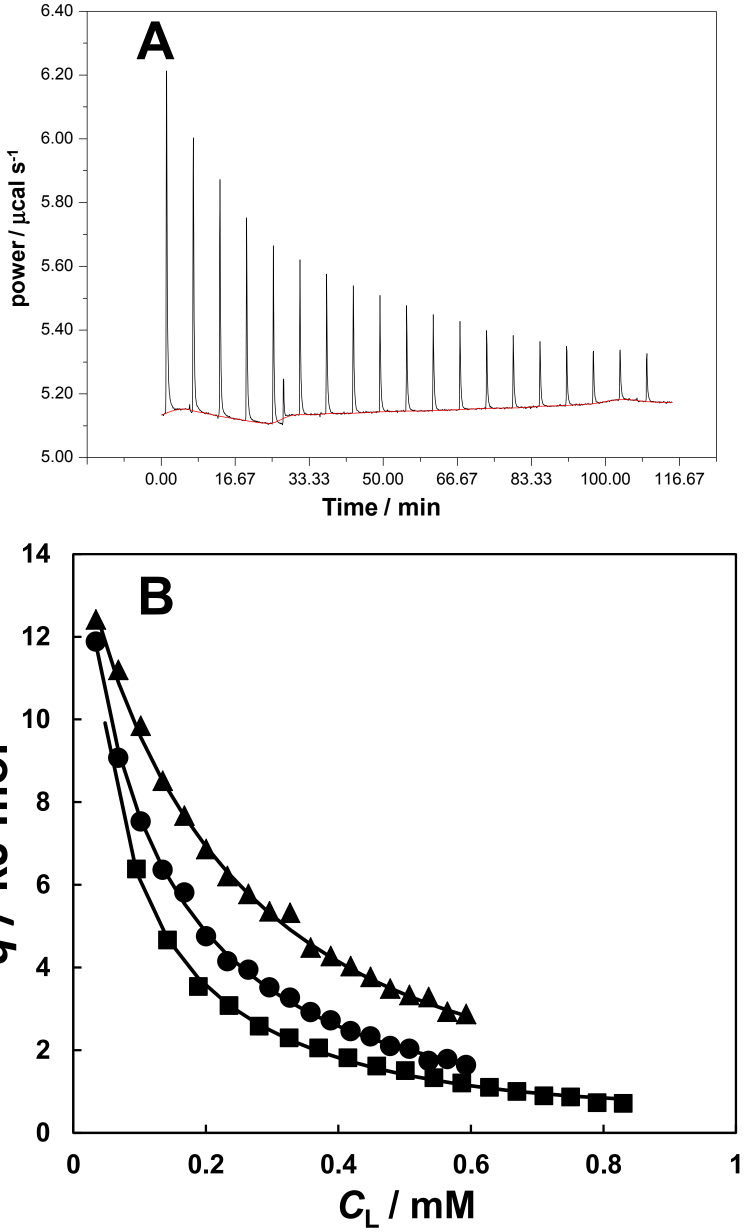

Figure 47. (A) Representative plot of power as a function of time for the titration at 25 °C. (B) Differential heat, *q*, associated with consecutive injections of titrant solution (TPPS, 3.69 mM; sodium phosphate buffer, 10 mM, pH 7.0) into the titrand solution (sodium phosphate buffer, 10 mM, pH 7.0) as a function of TPPS concentration after injection in the ITC cell, C_L, at 12 °C (triangles), 25 °C (circles) and 37 °C (squares).

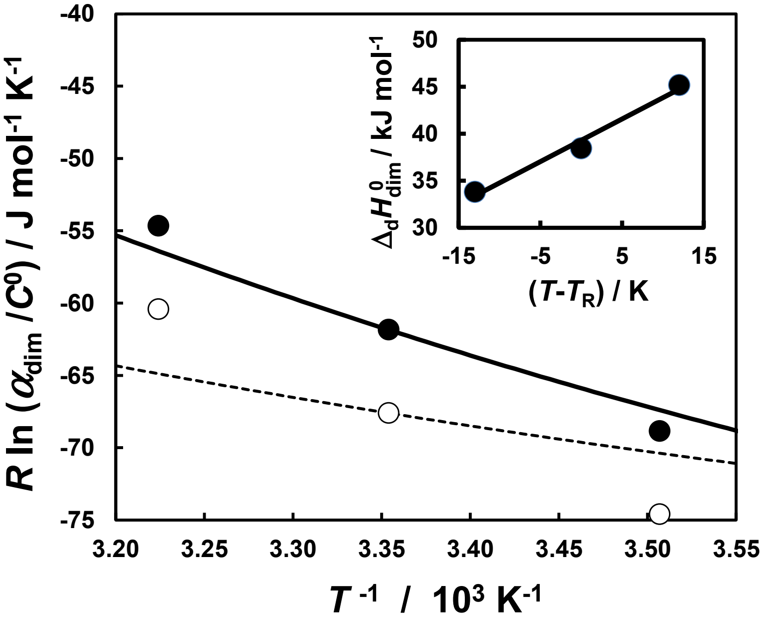

Figure 48. Van’t Hoff plot for the TPPS dimer dissociation constant, α_{dim}, as a function of temperature (solid circles). The solid curve describes the behavior of α_{dim} predicted starting from its experimental value at 25 °C and the corresponding reaction enthalpy and heat capacity values extracted from ITC experiments. The Van’t Hoff plot for the dissociation constants obtained by applying the equal-constant self-association model (open circles) and the predicted behavior (dashed curve) from the corresponding reaction enthalpy and heat capacity values is also included. $C^0 \equiv 1$ M is the standard concentration and $T_{\mathrm{R}} \equiv 25$ °C is the chosen reference temperature. The inset shows the standard dissociation enthalpy for TPPS dimers as a function of temperature.

The dependence of the dissociation constant on temperature can be described using the following thermodynamic relation derived by assuming that $\Delta_{\mathrm{d}} C^0_{p,\mathrm{dim}}$ is independent of temperature:

$$R \ln \alpha_{\mathrm{dim}} = \Delta_{\mathrm{d}} S^0_{\mathrm{dim,R}} - \frac{\Delta_{\mathrm{d}} H^0_{\mathrm{dim,R}}}{T} - \Delta_{\mathrm{d}} C^0_{p,\mathrm{dim}} \left(\frac{T - T_{\mathrm{R}}}{T} - \ln \frac{T}{T_{\mathrm{R}}} \right) \tag{8. 5}$$

where $\Delta_{\mathrm{d}} S^{0}_{\mathrm{dim,R}} = (70 \pm 3)\ \mathrm{J \cdot mol^{-1} \cdot K^{-1}}$ is the dissociation entropy value at T_{R} calculated from $\Delta_{\mathrm{d}} H^{0}_{\mathrm{dim,R}}$ and the value of $\Delta_{\mathrm{d}} G^{0}_{\mathrm{dim}}$ at 298.15 K in Table 8. In Figure 48, the experimental values of $R \ln \alpha_{\mathrm{dim}}$ are plotted together with the theoretical curve generated by using Eq. (8. 5). The values of α_{dim} calculated from Eq. (8. 5) (see last row in Table 8) exhibit an error lower than 20% compared to those directly obtained from ITC experiments. We believe that this is an acceptable level of accuracy for experimental equilibrium-constant data.

Table 8. Thermodynamic parameters associated with TPPS dimerization.

T / K	285.15	298.15	310.15
α_{dim} / mM	0.25±0.01	0.58±0.02	1.4±0.01
$\Delta_{\mathrm{d}} H^{0}_{\mathrm{dim}}$ / $\mathrm{kJ \cdot mol^{-1}}$	33.9±0.4	38.4±0.4	45.2±0.4
$\Delta_{\mathrm{d}} G^{0}_{\mathrm{dim}}$ / $\mathrm{kJ \cdot mol^{-1}}$	19.6±0.08	18.5±0.08	16.9±0.17
$\Delta_{\mathrm{d}} S^{0}_{\mathrm{dim}}$ / $\mathrm{kJ \cdot mol^{-1} \cdot K^{-1}}$	50±1	67±1	91±1
α_{dim} / mM (calc)	0.300		1.13

Spectroscopic studies have shown that TPPS aggregates are formed through edge-to-edge stacking[158]. Specifically, to minimize electrostatic repulsion between two parallel porphyrins, a sulfonate group of a porphyrin interacts with the center of the other porphyrin. However, steric considerations indicate that higher-order linear oligomers can be also formed through edge-to-edge stacking. Thus, we have also examined our ITC dissociation experiments using a equal-constant self-association model, in which higher-order soluble aggregates (oligomers) can also occur according to $\mathrm{L}_n \rightleftarrows \mathrm{L}_{n-1} + \mathrm{L}$ [176,177], were n is the number of monomers and equal to $n = 2, 3, 4, \ldots$. The basic assumption of this second model is that the dissociation constant, α_{olig}, of a monomeric unit from an oligomer is independent of the degree of oligomerization:

$$\alpha_{\mathrm{olig}} = \frac{[\mathrm{L}][\mathrm{L}_{n-1}]}{[\mathrm{L}_n]}, \text{ with } n = 2,\ 3,\ 4, \ldots \tag{8. 6}$$

where [L] is the concentration of monomer and $[\mathrm{L}_n]$ is the concentration of oligomer (see Section 6.6).

This model is consistent with the hypothesis that stacking of a third porphyrin molecule can also occur on one of the two dimer sides, leading to the formation of linear oligomers of the J-aggregate type. The cumulative heat for the dissociation of TPPS oligomers is given by

$$Q / V = \left(\sum_{n=2} (n-1)[\mathrm{L}_n] - \sum_{n=2} (n-1)[\mathrm{L}_n]_0 \right) \Delta_{\mathrm{d}} H^0_{\mathrm{olig}} \tag{8. 7}$$

where $[\mathrm{L}_n]$ is the concentration of oligomer n in the sample cell, $[\mathrm{L}_n]_0$ is the corresponding hypothetical concentration in the sample cell calculated by assuming that all oligomers transferred from the titrant solution do not dissociate, and $\Delta_{\mathrm{d}} H^0_{\mathrm{olig}}$ is the standard enthalpy for the dissociation of a monomer unit from the oligomers, also assumed to be independent of the degree of oligomerization. Note that the $(n-1)$ factor in Eq. (8. 7) implies that there are $(n-1)$ bonds in the linear oligomer L_n and neglects the formation of cyclic assemblies.

The monomer concentration is related to $\mathrm{C_L}$, by the mass balance: $\mathrm{C_L} = [\mathrm{L}_k] + \sum_{k=2} k[\mathrm{L}_k]$.

The second term on the right side of the mass balance can be rewritten as a geometric series, leading to the following expression:

$$\frac{\mathrm{C_L}}{[\mathrm{L}]}=\left(1-\frac{[\mathrm{L}]}{\alpha_{\mathrm{olig}}}\right)^{-2} \tag{8. 8}$$

For this model, the following analytical expression for $[\mathrm{L}]$ can be obtained:

$$[\mathrm{L}]=\frac{\alpha_{\mathrm{olig}}{}^{2}}{2\mathrm{C_L}}\left[1+\frac{2\mathrm{C_L}}{\alpha_{\mathrm{olig}}}-\left(1+\frac{4\mathrm{C_L}}{\alpha_{\mathrm{olig}}}\right)^{1/2}\right] \tag{8. 9}$$

Equations (8. 6) and (8. 9) can be then used to obtain an expression for $[\mathrm{L}_k]$ in Eq. (8. 7).

We now observe that the mathematical structure of Eq. (8. 7) is the same as that of Eq. (8. 1). This can be appreciated by comparing the obtained expressions for $[\mathrm{L}_2]$ and $\sum_{n=2}(n-1)[\mathrm{L}_n]$:

$$[\mathrm{L}_2]=\frac{[\mathrm{L}]^2}{\alpha_{\mathrm{dim}}}=\frac{\alpha_{\mathrm{dim}}}{8}\left[1+\frac{4\mathrm{C_L}}{\alpha_{\mathrm{dim}}}-\left(1+\frac{8\mathrm{C_L}}{\alpha_{\mathrm{dim}}}\right)^{1/2}\right] \tag{8. 10}$$

$$\sum_{n=2}(n-1)[\mathrm{L}_n]=\frac{\alpha_{\mathrm{olig}}[\mathrm{L}]^2}{(\alpha_{\mathrm{olig}}-[\mathrm{L}])^2}=\frac{\alpha_{\mathrm{olig}}}{2}\left[1+\frac{2\mathrm{C_L}}{\alpha_{\mathrm{olig}}}-\left(1+\frac{4\mathrm{C_L}}{\alpha_{\mathrm{olig}}}\right)^{1/2}\right] \tag{8. 11}$$

The comparison of Eq. (8. 10) with Eq. (8. 11) allows us to deduce that these two equations lead to identical expressions of Q/V (see Eq. (8.7) if $\alpha_{\mathrm{olig}}=\alpha_{\mathrm{dim}}/2$ and $\Delta_{\mathrm{d}}H^{0}_{\mathrm{olig}}=\Delta_{\mathrm{d}}H^{0}_{\mathrm{dim}}/2$. Since reaction enthalpy is linked to the equilibrium-constant logarithm, it allows us to appreciate that the discrepancy between the enthalpy values directly extracted from the ITC experiments with those obtained from the Van't Hoff plot can be used as a decisive criterion in assessing the relative accuracy of the two proposed models.

In Figure 48, we also included the experimental values of $R\ln\alpha_{\text{olig}}$ together with the corresponding theoretical curve based on the Van't Hoff equation. The relatively large deviation between experimental values and calculated curve shows how ITC data can be used to deduce that dimerization is the more accurate model for TPPS self-association. Hence, electrostatic repulsions play a critical role in hindering the formation of highly-charged oligomers.

The value of $\Delta_{\text{d}}H^{0}_{\text{dim, R}}$ is comparable with those extracted from spectroscopic experiments[178] and indicates that porphyrin dimerization is an enthalpically driven process. However ITC experiments have also allowed us to characterize the observed dependence of $\Delta_{\text{d}}H^{0}_{\text{dim, R}}$ on temperature (see inset in Figure 48). The observed increase of $\Delta_{\text{d}}H^{0}_{\text{dim, R}}$ with temperature is consistent with the presence of hydrophobic interactions. For instance, it has been estimated that the involvement of one water molecule to the reaction heat capacity in the ice-like cage around hydrophobic moieties of biomolecules is about $13\ \text{J}\cdot\text{mol}^{-1}\cdot\text{K}^{-1}$[179]. Our value of $\Delta_{\text{d}}C^{0}_{p,\text{dim}}$ is about 30-fold higher, thereby indicating significant hydrophobic interactions to the dimer dissociation.

Contrary to $\Delta_{\text{d}}H^{0}_{\text{dim, R}}$ and $\Delta_{\text{d}}C^{0}_{p,\text{dim}}$, the value of $\Delta_{\text{d}}S^{0}_{\text{dim, R}}$ is of more difficult interpretation. Indeed, even the sign of $\Delta_{\text{d}}S^{0}_{\text{dim, R}}$ will depend on the choice of the standard state due to the effect of solution volume on the translational entropy of individual solute particles. Assuming that the solvent can be treated as a continuum, the standard translational entropy of $160\ \mathrm{J \cdot mol^{-1} \cdot K^{-1}}$ can be calculated using the Sakur-Tetrode equation[180]. This value can be compared to the experimental $\Delta_{\mathrm{d}} S^{0}_{\mathrm{dim,\,R}}$. Note that the rotational entropy, which is independent of the choice of the standard state, is also expected to positively contribute to the net reaction entropy for dissociative processes. On the other hand, effects related to the solvent molecular structure such as excluded-volume and hydrophobic effects are expected to negatively contribute to $\Delta_{\mathrm{d}} S^{0}_{\mathrm{dim,\,R}}$. That the experimental values of reaction entropy in Table 8 are significantly lower than $160\ \mathrm{J \cdot mol^{-1} \cdot K^{-1}}$ is also consistent with the presence of significant hydrophobic interactions.

8.3. PVP-TPPS Supramolecular Structures

In Figure 49, we show differential-heat plots for our ITC polymer-porphyrin binding experiments at $T = 12,\ 25$ and $37\ ^{\mathrm{o}}\mathrm{C}$, demonstrating the formation of polymer + porphyrin supramolecular structures. In all three cases, we obtain negative heat values consistent with binding being an exothermic process. Our data were examined using the Scatchard model based on equivalent and independent sites[172]: $\mathrm{PL}_k \rightleftharpoons \mathrm{PL}_{k-1} + \mathrm{L}$ with $k = 1,2,3,\ldots,n$, where P denotes PVP and n is the total number of sites on the host polymer. Note that this reaction scheme assumes that only TPPS monomer binds to PVP. This assumption will be further discussed at the end of this section. The cumulative heat for polymer-porphyrin binding is given by

$$Q/V = ([\mathrm{L}_2] - [\mathrm{L}_2]_0)\Delta_{\mathrm{d}} H^{0}_{\mathrm{dim}} - \nu C_{\mathrm{P}} \Delta_{\mathrm{d}} H^{0}_{\mathrm{PL}} \tag{8. 12}$$

where here $[\mathrm{L}_2]_0$ is the hypothetical concentration of dimers in the sample cell calculated by assuming that all dimers in the titrand solution do not dissociate after the addition of polymer, and v is the number of porphyrin molecules bound per polymer unit. According to the Scatchard model (see Eq. (6. 18)) v can be linked to the free monomer concentration, $[\mathrm{L}]$.

The thermodynamic parameters $\Delta_{\mathrm{d}} H^0_{\mathrm{PL}}$ in Eq. (8. 12) and K in Eq. (6. 18) are the standard enthalpy and equilibrium constant for polymer + porphyrin dissociation, respectively. The total polymer concentration, C_{P}, is defined with respect to PVP monomer molecular weight. This implies that formally n is a fractional number if the polymer binding site consists of several PVP monomer units; *i.e.*, the number of PVP monomers involved in a binding site is $1/n$. Equation (8. 12) shows that the observed Q/V has to take into account not only the heat associated with polymer-porphyrin binding (second term of RHS) but also that contribution coming from porphyrin dimer dissociation, which is promoted by porphyrin-polymer binding (first term of RHS).

The free monomer concentration, $[\mathrm{L}]$, is related to C_{L}, by the mass balance: $C_{\mathrm{L}} = [\mathrm{L}] + 2[\mathrm{L}_2] + vC_{\mathrm{P}}$, which can be rewritten in the following way:

$$\frac{C_{\mathrm{L}}}{[\mathrm{L}]} = 1 + 2\frac{[\mathrm{L}]}{\alpha_{\mathrm{dim}}} + \frac{nC_{\mathrm{P}}}{K + [\mathrm{L}]} \tag{8. 13}$$

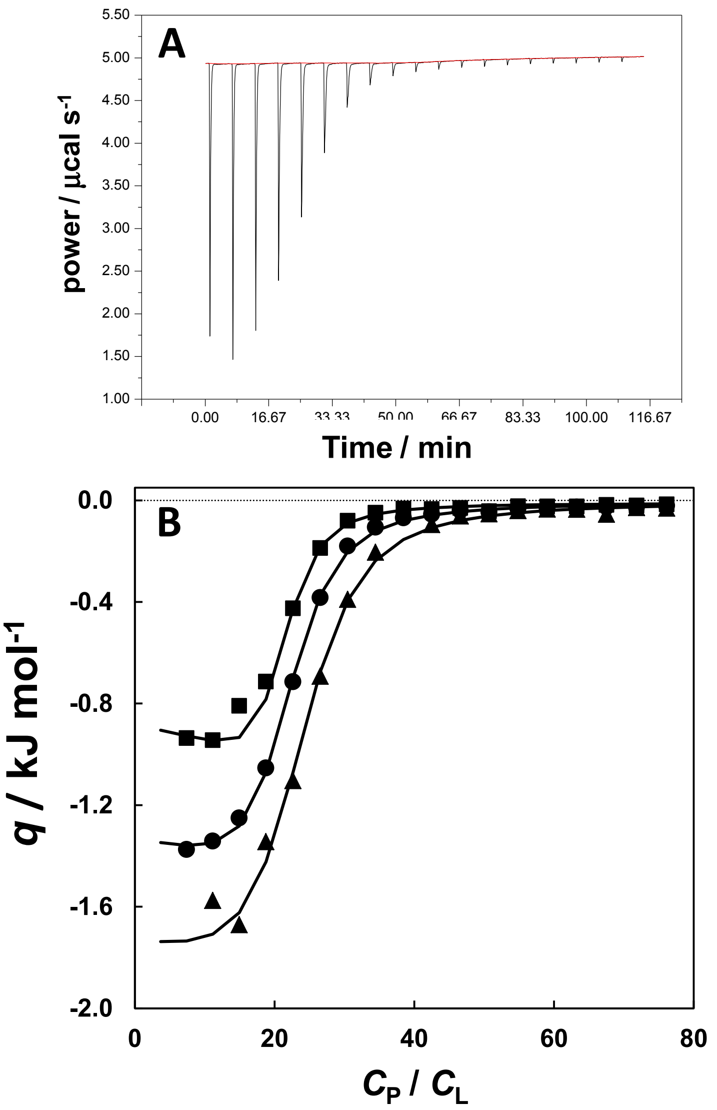

Figure 49. (A) Representative plot of power as a function of time for the titration at 25 °C. (B) Differential heat, q, associated with consecutive injections of titrant solution (PVP, 91.0 mM; sodium phosphate buffer, 10 mM, pH 7.0) into the titrand solution (TPPS, 0.244 mM; sodium phosphate buffer, 10 mM, pH 7.0) as a function of the PVP to TPPS concentration ratio after injection, C_P/C_L, at 12 °C (squares), 25 °C (circles) and 37 °C (triangles).

Equation (8. 13) can be rearranged as a cubic equation with respect to [L], and its three roots were numerically calculated as a function of $\alpha_{\dim}$, K and n using MATLAB. Clearly, the free monomer concentration must be low enough so that all concentrations satisfying the mass balance are positive. Thus, the value of [L] was taken as the lowest real positive root. The method of least squares was then applied to Eq. (8. 12) by using the values of $\Delta_d H^0_{\mathrm{dim}}$ and α_{dim} from Table 8 and by systematically calculating the deviation between experimental Q/V and that calculated from Eq. (8. 12) by systematically varying the values of $\Delta_d H^0_{\mathrm{PL}}$, K and n.

In Table 9, we report the determined values of $\Delta_d H^0_{\mathrm{PL}}$, K and n. Note that K increases with temperature consistent with polymer-porphyrin dissociation being an endothermic process. These values can be used to deduce that substantial formation of PVP + TPPS supramolecular structures is obtained when the porphyrin concentration in the surrounding aqueous medium is of the order 10 μM or higher. From the obtained values of n, we deduce that there are about 20 PVP monomers involved in binding one TPPS molecule. This implies that the molecular weight of the saturated PVP + TPPS supramolecular structures is ≈50% larger than that of the polymeric scaffold. Note that $1/n$ was found to slightly increase with temperature. This behavior can be related to the effect of temperature on solvent quality. Specifically, according to thermodynamic and viscosity experiments[181], the hydrodynamic volume of PVP chains decreases as temperature increases. As temperature increases, polymer chains contract making PVP monomer units less accessible to other molecules. Hence, more PVP units contribute to one binding site.

We now compare the thermodynamic strength of PVP+TPPS binding with that of TPPS dimerization. Note that the values of $\Delta_d H^0_{\mathrm{PL}}$ were found to be comparable with those of

$\Delta_{\rm d} H^0_{\rm dim}$, while the values of K were found to be two order of magnitude smaller that those of $\alpha_{\rm dim}$. This implies that polymer+porphyrin is stronger than porphyrin dimerization due to entropic effects. The corresponding values of standard Gibbs free energy and entropy were then calculated using $\Delta_{\rm d} G^0_{\rm PL} = -RT \ln K$ and $\Delta_{\rm d} S^0_{\rm PL} = (\Delta_{\rm d} H^0_{\rm PL} - \Delta_{\rm d} G^0_{\rm PL}) / T$, respectively.

Table 9. Thermodynamic parameters associated with PVP + TPPS binding.

T / K	285.15	298.15	310.15
$1/n$	18.7±0.2	19.6±0.2	21.8±0.4
K / μM	3.9±0.5	7.5±0.5	9.5±1.5
$\Delta_{\rm d} H^0_{\rm PL}$ / $\rm kJ \cdot mol^{-1}$	28.5±0.3	37.4±0.3	47.7±1.0
$\Delta_{\rm d} G^0_{\rm PL}$ / $\rm kJ \cdot mol^{-1}$	29.5±0.3	29.3±0.2	29.8±0.4
$\Delta_{\rm d} S^0_{\rm PL}$ / $\rm kJ \cdot mol^{-1} \cdot K^{-1}$	-4±2	27±1	58±4
$\alpha_{\rm dim}$ / mM (calc)	3.73		13.6

As shown in Table 9 and in the inset of Figure 50, $\Delta_{\rm d} H^0_{\rm PL}$ increases with temperature. Thus, the constant-pressure heat capacity of dissociation, $\Delta_{\rm d} C^0_{p,\rm PL} = (0.77 \pm 004)$ $\rm kJ \cdot mol^{-1} \cdot K^{-1}$, was determined by applying the method of least squares based on $\Delta_{\rm d} H^0_{\rm PL} = \Delta_{\rm d} H^0_{\rm PL,R} + \Delta_{\rm d} C^0_{p,\rm PL} (T - T_{\rm R})$, where $\Delta_{\rm d} H^0_{\rm PL,R} = (38.1 \pm 0.5)$ $\rm kJ \cdot mol^{-1}$ is its corresponding $\Delta_{\rm d} H^0_{\rm PL}$ value extracted from the fit. The dependence of the dissociation constant on temperature can be described as previously shown for porphyrin dimerization (see Eq. (8. 5). The standard dissociation entropy at $T_{\rm R}$ was calculated to be $\Delta_{\rm d} S^0_{\rm PL,R} = (30 \pm 2)$ $\rm J \cdot mol^{-1} \cdot K^{-1}$ from $\Delta_{\rm d} H^0_{\rm PL,R}$ and the value of $\Delta_{\rm d} G^0_{\rm PL}$ at 25 °C in Table 9.

The value of $\Delta_{\mathrm{d}} C^{0}_{p,\mathrm{PL}}$ was found to be about 60% higher than that of $\Delta_{\mathrm{d}} C^{0}_{p,\mathrm{dim}}$. This indicates that hydrophobic interactions contribute more to polymer-porphyrin binding than to porphyrin-porphyrin dimerization. This is also consistent with $\Delta_{\mathrm{d}} S^{0}_{\mathrm{PL,R}}$ being significantly lower than $\Delta_{\mathrm{d}} S^{0}_{\mathrm{dim,R}}$. A more significant contribution of hydrophobic interaction in the case of polymer-porphyrin binding is consistent with both sides of a porphyrin molecule being involved in the interaction with the polymer chain. On the other hand, only one side per porphyrin is involved in the formation of a dimer.

Consideration on molecular sizes can be used to assess that the estimated lengths of the PVP binding site and porphyrin molecule are consistent with PVP chains interacting with both sides of TPPS. Specifically, we can estimate that the binding segment of PVP is ≈ 6 nm based on the assumption that one PVP monomer contributes ≈ 0.3 nm to the chain length and that there are about 20 PVP units contributing to a binding site. On the other hand, the diameter of TPPS, including the four peripheral groups, can be estimated to be ≈ 2 nm [182]. Thus, the estimated lengths of the biding site and porphyrin are consisted with the PVP chains interacting with both sides of TPPS.

In Figure 50, the experimental values of $R \ln K$ are plotted together with the theoretical curve generated by using the Van't Hoff equation. The corresponding calculated values of K (see last row in Table 9) exhibit an error of 5% compared to the experimental value at $T = 12\,^{\circ}\mathrm{C}$ and 40% compared to the experimental value at $T = 37\,^{\circ}\mathrm{C}$. These are acceptable discrepancies considering system relative complexity due to the presence of two binding processes. Note that an error of 40% in K corresponds to an error of $1\ \text{kJ}\cdot\text{mol}^{-1}$ in $\Delta_{\text{d}}G^{0}_{\text{PL}}$. This error remains comparable with the typical errors of $\Delta_{\text{d}}H^{0}_{\text{PL}}$ data extracted by ITC.

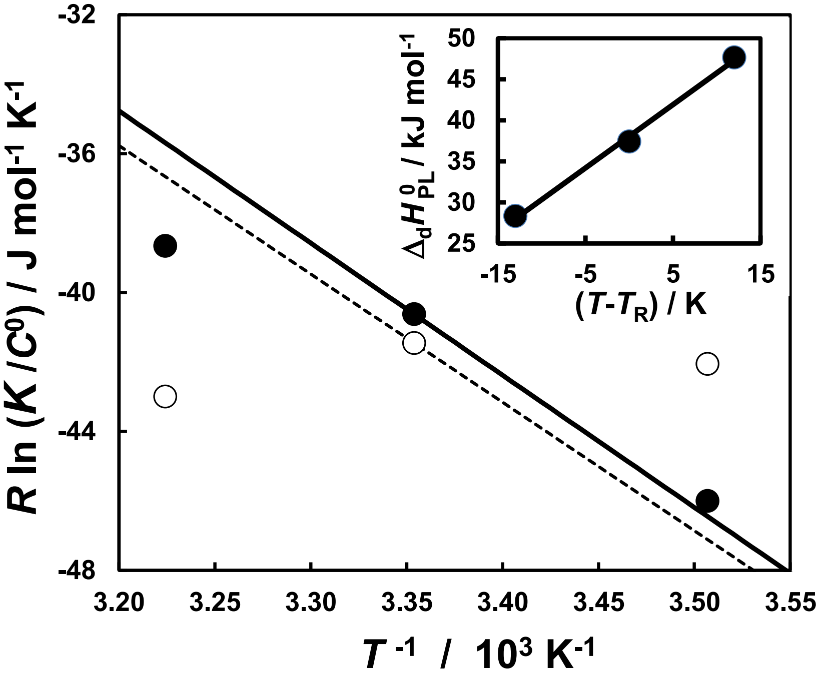

Figure 50. Van't Hoff plot for the PVP-TPPS dissociation constant, K, as a function of temperature (solid circles), obtained by assuming that TPPS binds to PVP in its monomeric state only. The solid curve describes the behavior of K predicted from its experimental value at 25 °C and the corresponding reaction enthalpy and heat capacity values extracted from ITC experiments. The Van't Hoff plot for the PVP-TPPS dissociation constants (open circles), obtained by assuming that TPPS dimers bind to PVP in the same way as TPPS monomers, and the predicted behavior (dashed curve) from the corresponding reaction enthalpy and heat capacity values is also included. $C^0 \equiv 1$ M is the standard concentration and $T_{\text{R}} \equiv 25$ °C is the chosen reference temperature. The inset shows the standard dissociation enthalpy for PVP-TPPS complexes as a function of temperature.

For comparison, we have also examined our ITC binding experiments by assuming that both monomers and dimers equally bind to the polymer sites. The only modification to the previous model is that Eq. (6. 18) is replaced by

$$\nu = \frac{n([\mathrm{L}]+[\mathrm{L}_2])}{K+([\mathrm{L}]+[\mathrm{L}_2])} \tag{8. 14}$$

where L and L_2 are treated as two distinct competing ligands with same binding properties. By following the same approach applied to Eq. (8. 12), the extracted values of $\Delta_{\mathrm{d}} H^0_{\mathrm{PL}}$ and n were found to be slightly different ($\approx 5\%$) from those reported in Table 9. However, the corresponding K values, which are shown in Figure 50, were found to be virtually independent of temperature contrary to the prediction from Van't Hoff plot (see Figure 50). We therefore deduce that the model based on Eq. (6. 18) represents a more accurate description of PVP-TPPS binding. That the interaction of PVP with L is favored compared to that with L_2 is also consistent with the idea that PVP chains interact with both sides of the porphyrin molecule.

8.4. Absorption Spectra

In Figure 51, we show normalized absorption spectra in the visible wavelength range for TPPS (Figure 51A) and TPPS-PVDP aqueous solutions (Figure 51B-D) taken at room temperature (22-23 °C). In Figure 51A, we can see the characteristic four Q bands of FBP. As TPPS concentration increases, these bands shifts towards higher wavelengths as expected for a J-type aggregation. Clearly, the existence of several isosbestic points is consistent with presence of chemical equilibrium between two different porphyrin species, *i.e.* monomer and dimer.

We can use the dimer dissociation constant determined by ITC to describe the behaviour of TPPS absorption spectra. At a given wavelength, the observed extinction coefficient of TPPS, ε, can be expressed as the weighted average between that of the monomer, ε_1, and dimer, ε_2, according to

$$\varepsilon = \frac{[\mathrm{L}]}{C_\mathrm{L}}\varepsilon_1 + \frac{2[\mathrm{L}_2]}{C_\mathrm{L}}\varepsilon_2 \tag{8. 15}$$

where ε_2 is defined with respect to the monomer molecular weight. The concentrations [L] and $[\mathrm{L}_2]$ can be calculated as a function of C_L by using α_dim. We have used $\alpha_\mathrm{dim} = 0.54\ \mathrm{mM}$, which was calculated at 22.5 °C by linear interpolation of $\ln\alpha_\mathrm{dim}$ (data taken from Table 8) as a function of $1/T$. The values of ε_1 and ε_2 (see Figure 51 caption) were then determined by applying the method of least squares. The graph on the right side of Figure 51A shows $\varepsilon/\varepsilon_1$ as a function of C_L at three chosen wavelengths (515, 580 and 634 nm). These wavelengths correspond to the largest observed variations in ε. This graph shows that the curvature of $\varepsilon/\varepsilon_1$ is accurately described by our ITC thermodynamic data.

In Figure 51 (B-D), we show porphyrin spectra as a function of PVP concentration at three constant TPPS concentrations. Here, we can use both the dimerization and PVP-TPPS binding data determined by ITC to describe the behaviour of TPPS absorption spectra. At a given wavelength, the observed extinction coefficient of TPPS, ε, can be expressed as the following weighted average:

$$\varepsilon = \frac{[\mathrm{L}]}{C_\mathrm{L}}\varepsilon_1 + \frac{2[\mathrm{L}_2]}{C_\mathrm{L}}\varepsilon_2 + \varepsilon_\mathrm{PL}\frac{\nu C_\mathrm{P}}{C_\mathrm{L}} \tag{8. 16}$$

where $\varepsilon_{\mathrm{PL}}$ is extinction coefficient of bound TPPS. The values of $[\mathrm{L}]$, $[\mathrm{L}_2]$ and ν can be calculated as a function of C_{L} provided that α_{dim}, K and n are known. We have used $K = 6.1\ \mu$M and $n = 0.051$ at 22.5 °C from the linear interpolation of $\ln K$ and n (data taken from Table 9) as a function of $1/T$. The values of $\varepsilon_{\mathrm{PL}}$ (see Figure 51B-D caption) were then determined by applying the method of least squares. The graphs on the right side of Figure 51B-D shows $\varepsilon / \varepsilon_0$ as a function of $C_{\mathrm{P}} / C_{\mathrm{L}}$ at the three investigated TPPS concentrations. Here, ε_0 is the corresponding value of ε at $C_{\mathrm{P}} = 0$. As we can see on the right side of Figure 51B-D, the curvature of $\varepsilon / \varepsilon_0$ is accurately described by our ITC thermodynamic data at three chosen wavelengths. One of these three wavelengths (515 nm) was chosen to be the same as that in Figure 51A. The other two wavelengths correspond to two isosbestic points (571 and 642 nm) for the monomer-dimer equilibrium, i.e. $\varepsilon_1 = \varepsilon_2$ and show significant variations in ε as PVP concentration increases. On the other hand, the other two wavelengths (580 and 634 nm) in Figure 51B-D were not considered because the corresponding variations in ε were small.

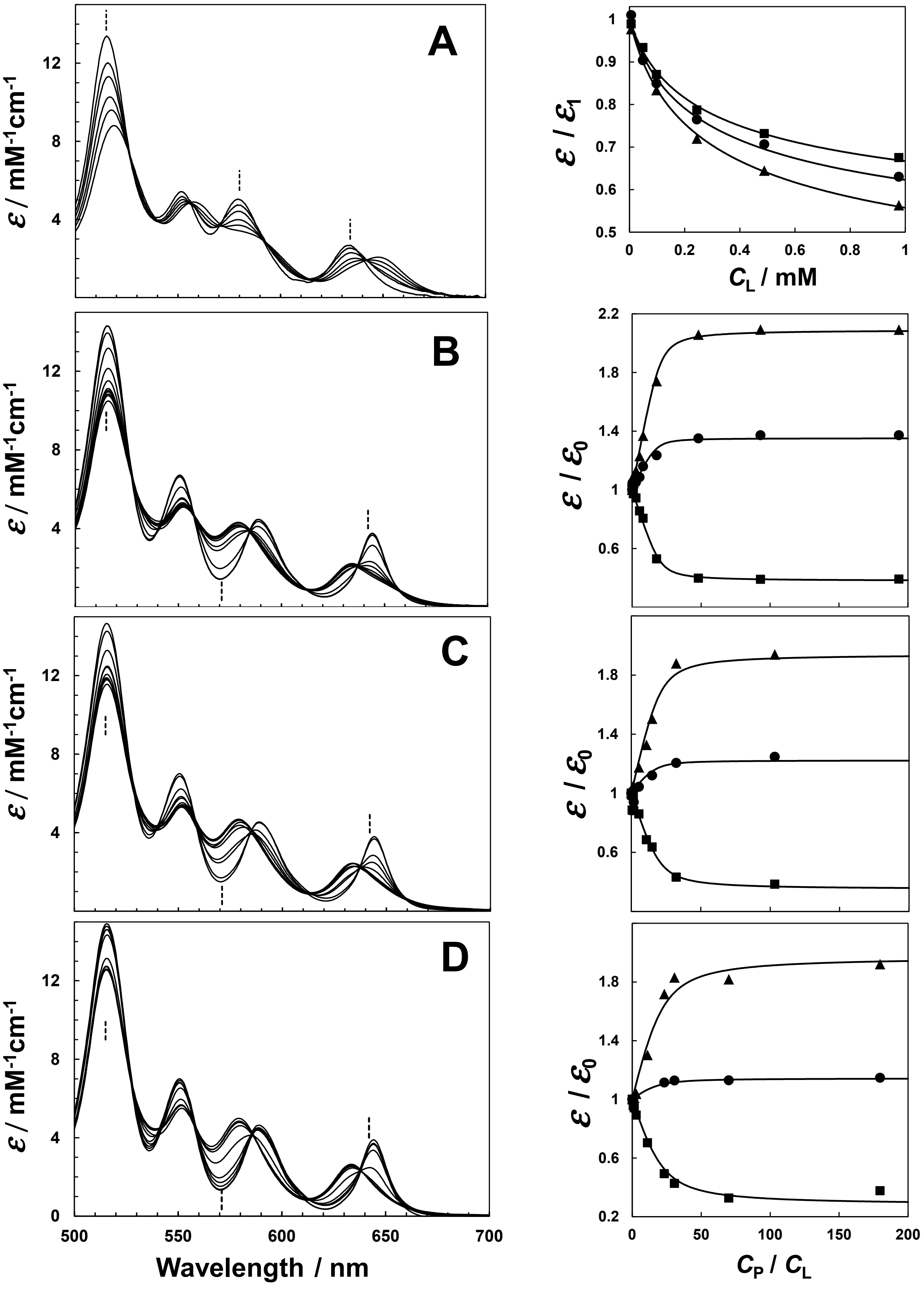
A
B
C
D
ε / mM^{-1}cm^{-1}
Wavelength / nm
500
550
600
650
700
0
4
8
12
ε / ε_1
C_L / mM
0
0.2
0.4
0.6
0.8
1
0.5
0.6
0.7
0.8
0.9
1
ε / ε_0
0.2
0.6
1
1.4
1.8
2.2
C_P / C_L
0
50
100
150
200

Figure 51. Normalized absorption spectra (extinction coefficient, ε) showing the four *Q* bands of TPPS in sodium phosphate buffer, 10 mM, pH 7.0, 22.5 °C. **(A)** Spectra obtained at several TPPS concentrations, C_L in the absence of PVP. The dashed vertical bars identify three chosen wavelengths: (515, 580 and 634) nm. The effect of C_L on ε is described by the graphs on the right side showing the ratio, $\varepsilon/\varepsilon_1$, as a function of C_L at 515 nm (circles), 580 nm (squares) and 634 nm (triangles). The infinite-dilution values of the ε_1 = (13.3, 5.07 and 2.75) $mM^{-1}cm^{-1}$ at (515, 580 and 634) nm were determined by applying the method of least squares with α_{dim}= 0.54 mM. The corresponding determined values of $\varepsilon_2/\varepsilon_1$ were 0.37, 0.44 and 0.26 respectively. **(B, C, D)** Spectra obtained at several PVP concentrations, C_P, for three constant TPPS concentrations: 93.6 µM (B), 47.9 µM (C) and 23.2 µM (D). The dashed vertical bars identify three chosen wavelengths: (515, 571 and 642) nm. The effect of the molar ratio, C_P/C_L, on ε is described by the corresponding graphs on the right side showing the ratio, $\varepsilon/\varepsilon_0$, as a function of C_P/C_L at 515 nm (circles), 571 nm (squares) and 642 nm (triangles). The values of $\varepsilon_{PL}/\varepsilon_1$ = 1.17, 0.38 and 2.09 (B), 1.12, 0.35 and 1.94 (C), and 1.09, 0.28 and 1.97 (D) at (515, 571 and 642) nm were determined by applying the method of least squares with α_{dim}= 0.54 mM, K = 6.1 µM and n = 0.051. The wavelengths 571 nm and 642 nm corresponds to two isosbestic points in fig 5A with ε_2=ε_1= (5.07 and 2.75) $mM^{-1}cm^{-1}$ respectively.

Our values of α_{dim}, K and n were also used to extract the limiting spectra for monomer, dimer and bound forms of TPPS. These spectra, which are shown in Figure 52, allow us to examine the relative positions of the four Q bands. The observed shift between the four Q bands of monomer and dimer is 0.04-0.05 eV (see inset in Figure 52). In the case of bound TPPS, the two Q_x bands displays an intermediate location with a ≈ 0.03 eV shift with respect to the monomer, while the two Q_y bands display no appreciable shift with respect to the monomer. Since the *x* axis is located along the direction of the two protonated pyrrole nitrogens of a porphyrin by convention[157], the observed shifts indicates that the interaction of

PVP and TPPS mainly occurs along the *x* axis. This interaction is expected to involve hydrogen bonding between the two pyrrole hydrogens of TPPS and the PVP oxygens, as indicated by the resonance form in which a negative charge is located on PVP oxygens and a corresponding positive charge on the PVP nitrogens. The π character of the N–C bond may favor π– π interactions between polymer and porphyrin.

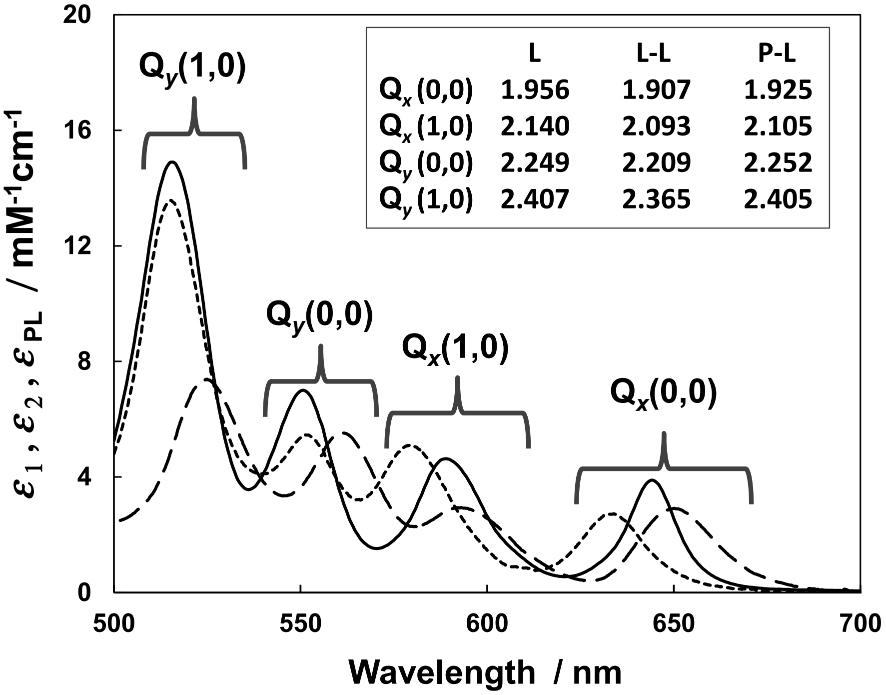

	L	L-L	P-L
$Q_x(0,0)$	1.956	1.907	1.925
$Q_x(1,0)$	2.140	2.093	2.105
$Q_y(0,0)$	2.249	2.209	2.252
$Q_y(1,0)$	2.407	2.365	2.405

Figure 52. Limiting normalized absorption spectra (extinction coefficient, ε) for TPPS in the monomeric (short dashed curve), dimeric (long dashed curve) and bound (solid curve) states. Each spectrum consists of four Q bands denoted as $Q_x(0,0)$, $Q_x(1,0)$, $Q_y(0,0)$ and $Q_y(1,0)$ as we move from high to low wavelengths. The inset shows the corresponding transition energy values in eV associated with the band maxima for the monomer (L), dimer (L-L) and bound (P-L) TPPS.

For completeness, we have also examined the Soret band of TPPS. The corresponding normalized spectra in the UV range are shown in Figure 53. Since the intensity of this band is significantly stronger than those of the Q bands, spectra were collected at relatively low TPPS concentrations. Within this range of dilute concentrations, the effect of TPPS dimerization on the Soret band is small (see inset of Figure 53). On the other hand, the effect of PVP on the TPPS Soret band could be clearly investigated resulting into a shift towards high wavelength (≈ 0.05 eV), which is qualitatively consistent with the shift observed for Q_x.

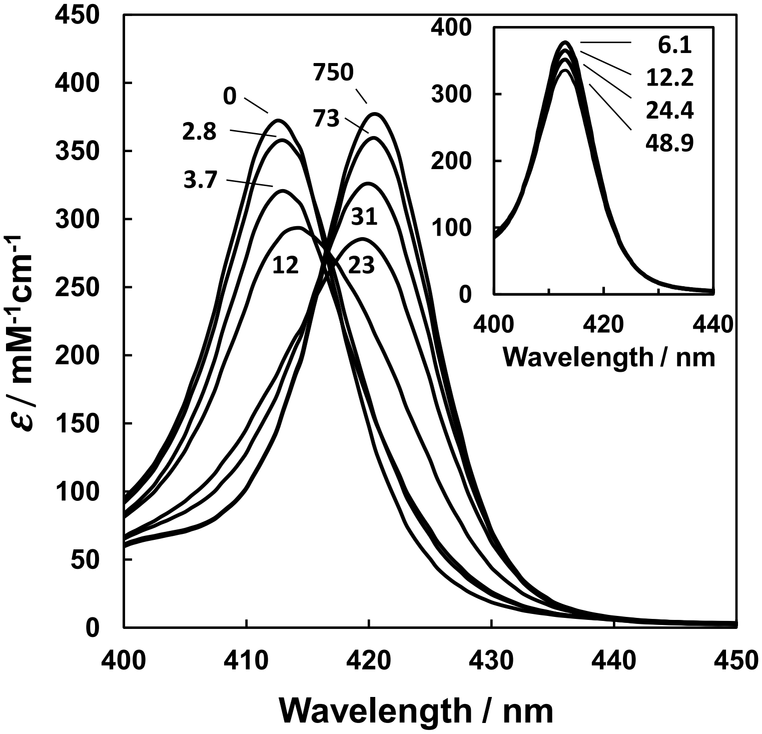

Figure 53. Normalized absorption spectra (extinction coefficient, ε) showing the Soret band for TPPS (sodium phosphate buffer, 10 mM, pH 7.0, 22.5 °C) at C_L= 23 μM for several PVP concentrations, C_P. The numbers associated with individual spectra denote the corresponding values of PVP to TPPS concentration ratio, C_P/C_L. The inset shows normalized absorption spectra for TPPS taken at several C_L values in the absence of PVP. The numbers associated with individual spectra denote the corresponding C_L in μM.

8.5. Conclusions

Supramolecular PVP-TPPS structures with a maximum molecular weight ≈50% higher than that of the PVP scaffold are obtained in the presence of TPPS concentrations of the order of 10 μM or higher in the surrounding aqueous medium. The comparison between the experimental Van't Hoff plot and that calculated from experimental reaction enthalpies was used to show that TPPS self-association is limited to the formation of dimers and that TPPS binds to PVP in its monomeric state. ITC reaction enthalpies have also allowed us to determine accurate reaction heat capacities. These were related to hydrophobic interactions. Our ITC results show that PVP-TPPS binding is stronger than TPPS dimerization due to the difference in reaction entropy. Thermodynamic parameters were used to extract the normalized absorption spectra of monomeric, dimeric and bound states of TPPS. The observed spectral shifts in the two Qx bands can be explained by considering that the two hydrogens in the central porphyrin bind to the PVP oxygens.

Chapter 9: Effect of PVP on TPPS Spectrophotometric Properties in Acidic Conditions

9.1. Introduction

In this chapter, we examine the effect of PVP concentration on TPPS spectrophotometric properties at pH 4.5 and 3.0 and compare them with our results at pH 7.0. We observed significant changes in TPPS spectral properties compared to those observed at neutral pH. At these low pH values, TPPS samples appear green. As PVP concentration increases, sample color turned red as it is observed at pH 7.0. TPPS spectra are presented in Section 9.2 while the relation of the observed spectrophotometric behavior to TPPS-PVP binding is examined in Section 9.3.

9.2. TPPS Spectrophotometric Properties at low pH in the presence of PVP

We obtained TPPS spectra at pH 4.5 (10 mM of sodium acetate buffer) and pH 3.0 (10 mM of sodium citrate buffer) as a function of PVP concentration at room temperature (22.5 ºC ± 0.5 ºC). Our results are shown in Figure 54A-C (pH 4.5) and Figure 54D-F (pH 3.0) for the visible range. In Figure 54, we can see that the TPPS spectrum in the absence of PVP at pH 4.5 still presents the characteristic four Q bands (from 500 to 700 nm) of FBP although the intensity of the Q_y bands is significantly smaller than that of Q_x bands, contrary to what we observe at pH 7.0. On the other hand, at pH 3.0, we observe only two Q bands approximately at the location of the two Q_x bands observed at higher pH values. At pH 3.0, TPPS spectra in the absence of PVP also show a sharp intense peak at lower wavelengths (480 nm). This is associated with the formation of J-aggregates (see Section 6.3).

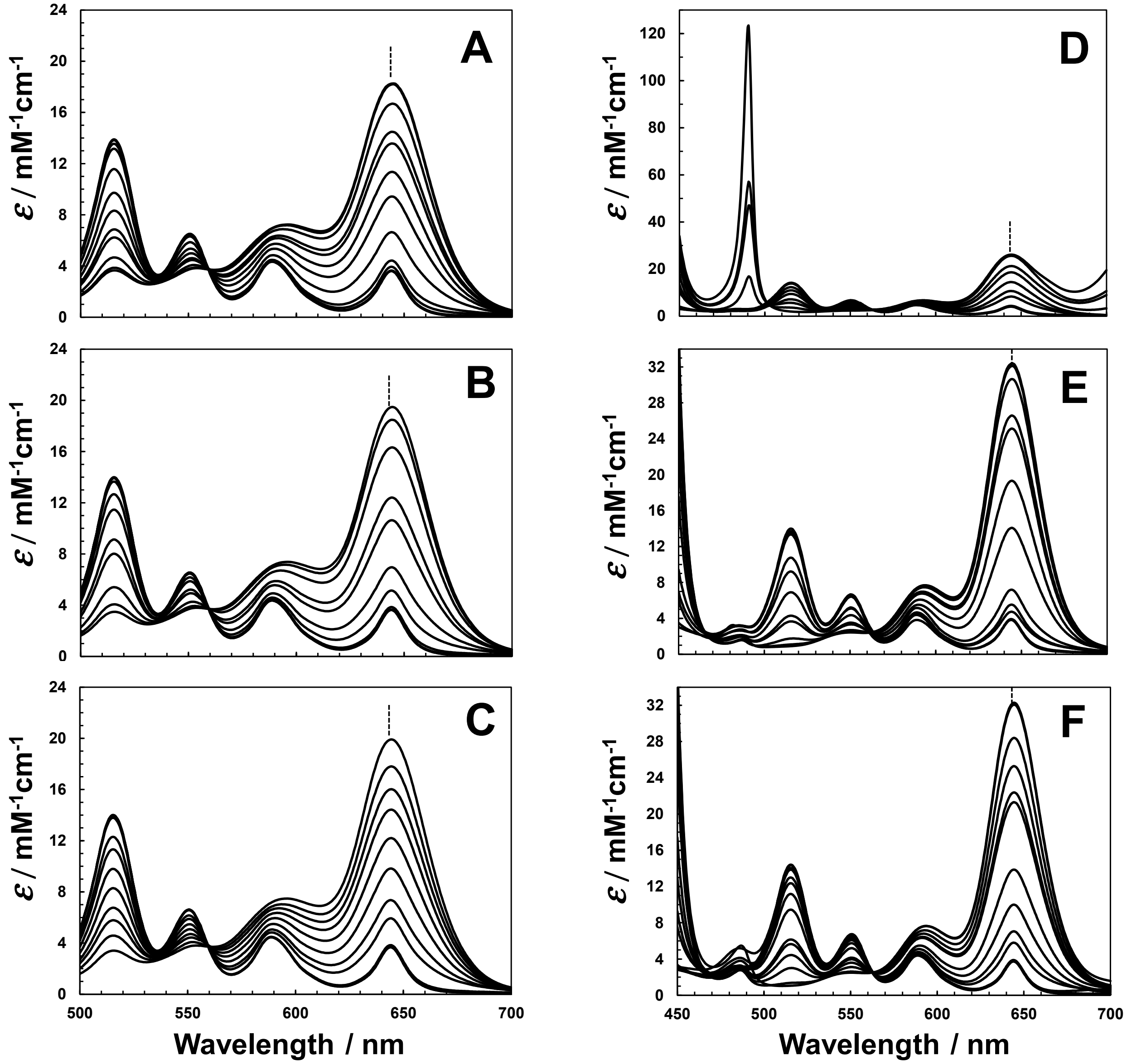

Figure 54. Normalized absorption spectra (extinction coefficient, ε) showing the four Q bands of TPPS at 22.5 ºC and in (A)-(C) acetate buffer, 10 mM, pH 4.5, for three constant TPPS concentrations: C_L= 98.4 μM (A), C_L= 48.6 μM (B) and C_L= 24.1 μM (C) and (D)-(F) sodium citrate buffer, 10 mM, pH 3.0, for three constant TPPS concentrations: C_L= 97.8 μM (D), C_L= 49.5 μM (E) and C_L= 24.1 μM (F). Values for C_P / C_L can be seen in Figure 57 (for pH 4.5) and Figure 58 (for pH 3.0).

The observed behavior is consistent with the FBP species (D_{2h} symmetry) dominating at pH 7.0 and the DAB species (D_{4h} symmetry) dominating at pH 3.0. For all TPPS concentrations in Figure 54, we can observe the existence of an isosbestic point ($\varepsilon_{563} = 2.88$ mM^{-1}cm^{-1} at pH 3.0, $\varepsilon_{559.5} = 3.67$ mM^{-1}cm^{-1} at pH 4.5 and $\varepsilon_{557.5} = 4.65$ mM^{-1}cm^{-1} at pH 7.0), which we can relate to the presence of a TPPS bounded species in solution, with its fraction increasing with PVP concentration. As PVP concentration increases, we observe that the intensity of the Q_y bands increases while that of Q_x bands correspondly decreases. This implies that the TPPS spectrum of the bound state in acidic conditions recovers the main features of the FBP spectrum observed at neutral pH. Moreover, the peak associated with the J aggregates at pH 3.0 (see Figure 54F) rapidly decreases as PVP concentration increases and disappears at the intermediate experimental polymer concentrations.

To further examine the spectrophotometrics properties of bound TPPS compared to free TPPS in the visible range, we plot the spectra obtained at the three investigated pH values in the absence of PVP (see Figure 55A) and in excess of PVP (see Figure 55B). According to Figure 55A, the isosbestic point between the FBP (pH 7.0) and DAP (pH 3.0) spectra is predicted to be located at 578 nm. The experimental spectrum at pH 4.5 cannot be simply described as a linear combination of the other two spectra. This can be attributed to the presence of a third TPPS species, the monoacid form of the porphyrin (MAP). In Table 10, we report the fractions of FBP and DAP calculated at the three experimental pH values assuming that pKa1=pKa2=4.9[137]. In this table, we can see, as expected, that the DAP and FBP species contribute to 99% of the total TPPS at pH 3.0 and 7.0, respectively. At pH 4.5, DAP is the most abundant species (64%), with the amount of FBP being significantly smaller (10%). Note that MAP contributes more than FBP (26%) at pH 4.5. This analysis, which shows that all three TPPS species contribute at pH 4.5, is consistent with the absence of an isosbestic point in Figure 55A.

Table 10. Fractions of DAP, MAP and FBP.

pH	3.0	4.5	7.0
DAB (%)	99	64	0.0063
MAP (%)	1.2	26	0.79
FBP (%)	0.016	10	99

In Figure 55B, we show the spectra obtained in excess of PVP at the three investigated pH values. The spectra virtually overlap thereby demonstrating that the spectrophotometric properties of bound TPPS become independent of pH in the visible range. This result indicates that the chemical state of bound TPPS does not change with pH. Furthermore, similarities between the spectrum of bound TPPS and that of free TPPS at pH 7.0, suggest that the TPPS bound species is closely related to FBP.

We now examine the TPPS spectrophotometric properties in the UV range (from 400 nm to 450 nm, Soret band). In Figure 56A-C (pH 4.5) and Figure 56D-F (pH 3.0), we show normalized spectra in the UV range at constant TPPS concentration and different concentrations of PVP. Because of the high intensity of the Soret band compared to the Q bands, spectra were collected at relatively low TPPS concentration. In the absence of PVP, we can see that the Soret band has a maximum at 433 nm at pH 3.0 (DAB), which is red shifted with respect to that observed at pH 7.0 (412 nm, FBP (see Figure 53). At pH 4.5, the TPPS spectrum shows two bands that reflect the coexistence of all TPPS species. In excess of PVP, the TPPS spectrum consists of a band with a maximum at 422 nm, at all three investigated pHs. Note that the addition of PVP to TPPS at pH 3.0, blue shifts the Soret band. This is the opposite of what it is observed at pH 7.0.

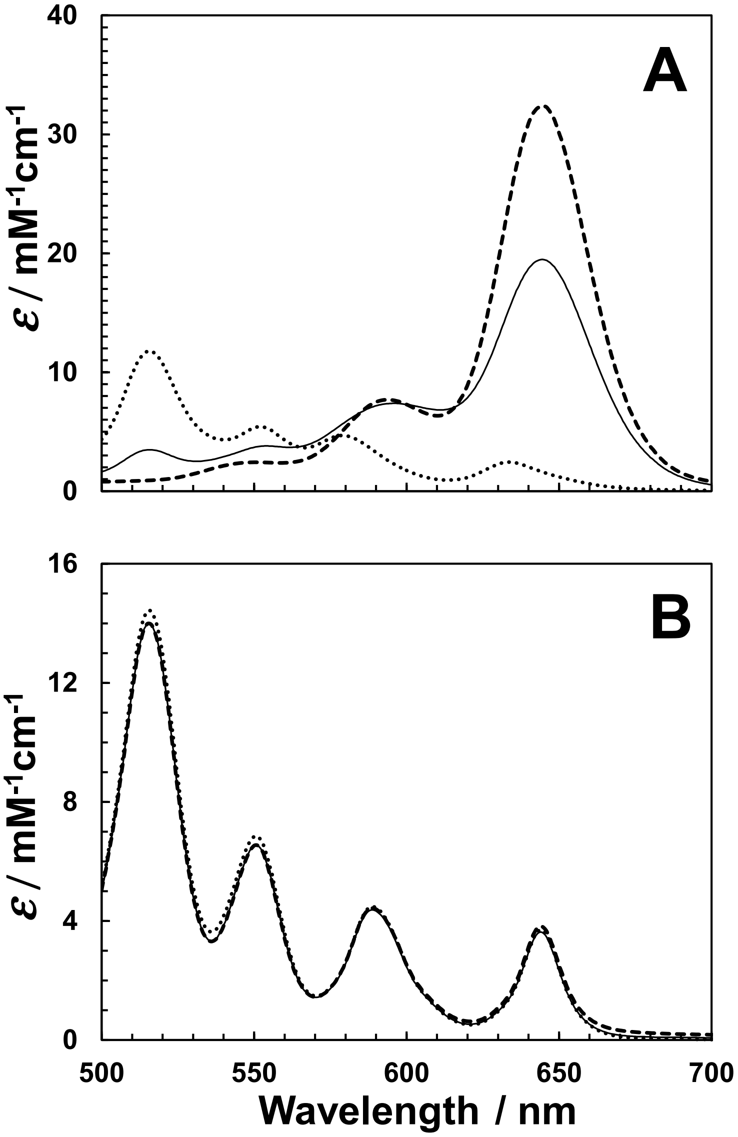

Figure 55. Normalized absorption spectra (extinction coefficient, ε) showing the Q bands for TPPS (C_L= 48±1 μM) at (A) pH 7.0 (short dash line), pH 4.5 (full line) and pH 3.0 (long dash line) in the absence of PVP (in this comparison the normalized spectra of TPPS can be regarded as independent of TPPS concentration) and (B) pH 7.0 (short dash line), pH 4.5 (full line) and pH 3.0 (long dash line) in excess of PVP (C_p = 45.2, 26.4 and 18.3 M for pH = 3.0, 4.5 and 7.0, respectively).

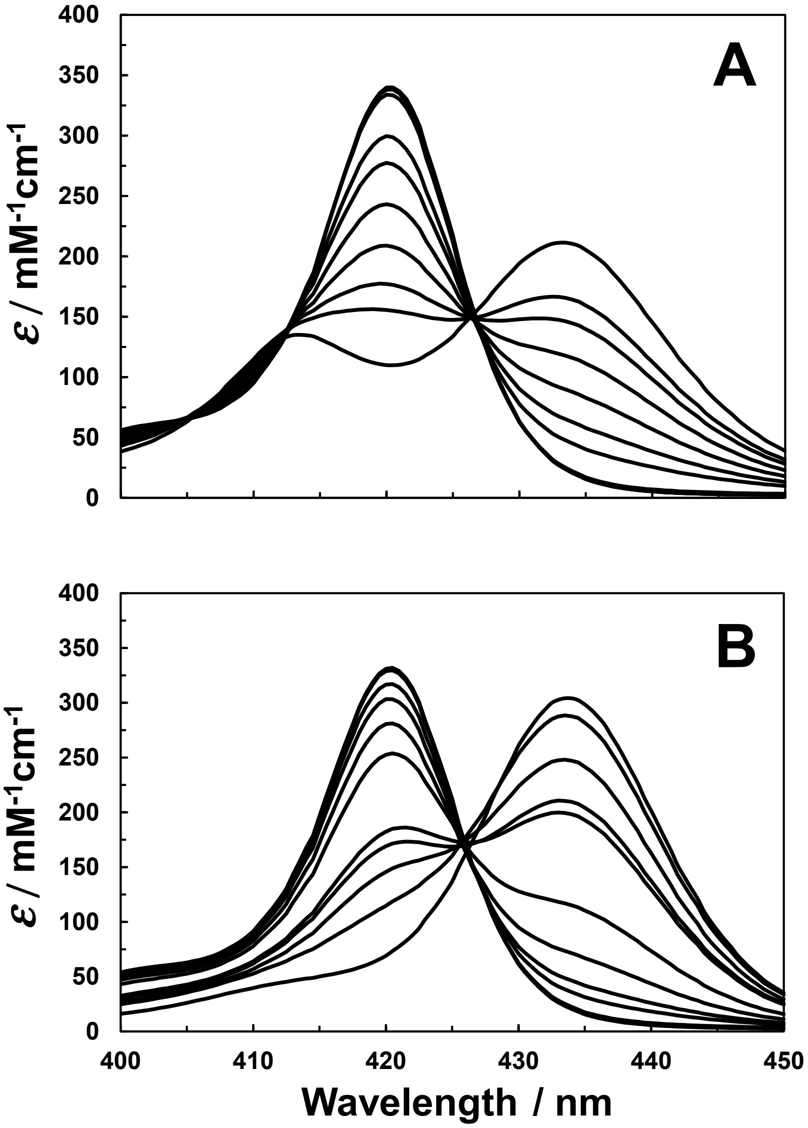

Figure 56. Normalized absorption spectra (extinction coefficient, ε) showing the Soret band for TPPS at 22.5 ºC and in (A) acetate buffer, 10 mM, pH 4.5 at C_L= 24.1 μM and (B), sodium citrate buffer, 10 mM, pH 3.0, at C_L= 24.1 μM.

In conclusion, the TPPS spectrophotometric properties in the UV and visible range, in the presence of sufficient PVP become pH independent.

9.3. Effect of pH on the PVP-TPPS binding affinity

In Figure 57 and Figure 58, we show the normalized extinction coefficient, $\varepsilon / \varepsilon_0$ of TPPS as a function of the molar ratio $C_\mathrm{P} / C_\mathrm{L}$ at constant C_L. Note that ε_0 is the value of the TPPS extinction coefficient in the absence of PVP. The values of $\varepsilon / \varepsilon_0$ in these figures were determined at the wavelength of 642 nm. This wavelength corresponds to the largest observed variations of ε with PVP concentration.

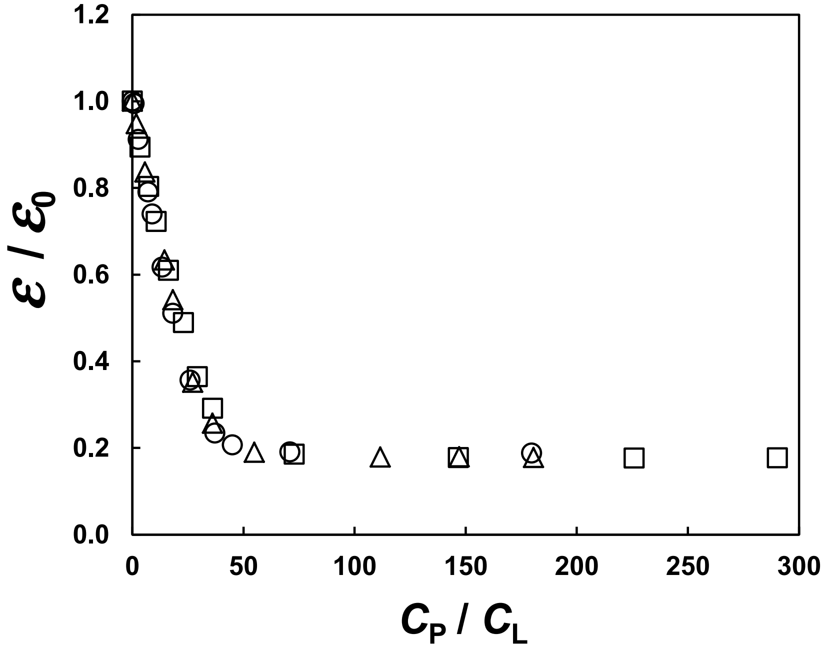

Figure 57. Normalized extinction coefficient at 642 nm, $\varepsilon / \varepsilon_0$, of TPPS in acetate buffer, 10 mM, pH 4.5 and 22.5 ºC as a function of $C_\mathrm{P} / C_\mathrm{L}$ for three constant TPPS concentrations of 98.4 µM (open circles), 48.6 µM (open triangles) and 24.1 µM (open squares). ε_0 is the TPPS extinction coefficient in the absence of PVP. The corresponding value of $\varepsilon_\mathrm{PL} / \varepsilon_0$ is 0.17.

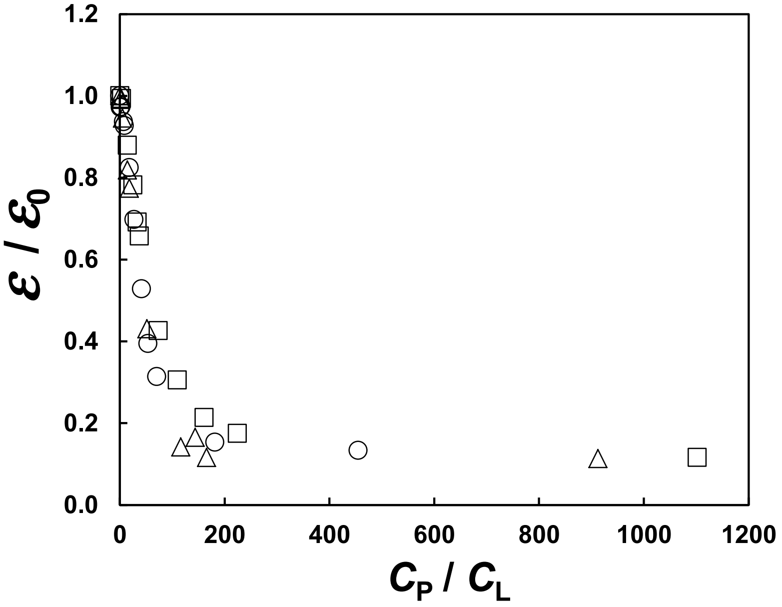

Figure 58. Normalized extinction coefficient at 642 nm, $\varepsilon / \varepsilon_0$, of TPPS in sodium citrate buffer, 10 mM, pH 3.0 and 22.5 ºC as a function of C_P / C_L for three constant TPPS concentrations of 97.8 μM (open circles), 49.5 μM (open triangles) and 24.1 μM (open squares). ε_0 is the TPPS extinction coefficient in the absence of PVP. The corresponding value of $\varepsilon_{PL} / \varepsilon_0$ is 0.11.

At a given wavelength, the observed normalized extinction coefficient of TPPS, $\varepsilon / \varepsilon_0$ can be expressed as the following weighted average:

$$\frac{\varepsilon}{\varepsilon_0} = (1-\alpha) + \alpha \frac{\varepsilon_{PL}}{\varepsilon_0} \tag{9. 1}$$

where $\varepsilon_{PL} / \varepsilon_0$ is the extinction coefficient ratio of bound TPPS to ε_0, and α is the fraction of bound TPPS. We set $\varepsilon_{PL} / \varepsilon_0$ to be equal to the value of $\varepsilon / \varepsilon_0$ found at the highest PVP concentrations and calculate α from Eq. (9.1).

From the data in Figure 57 and Figure 58, it is possible to calculate the values of $C_\mathrm{P} / C_\mathrm{L}$ at which 50% of the porphyrin is bound ($\alpha = 0.5$). The lower the value of $C_\mathrm{P} / C_\mathrm{L}$ at $\alpha = 0.5$, the stronger the affinity of PVP to TPPS is. We obtain: $C_\mathrm{P} / C_\mathrm{L} = 41 \pm 4$ at pH 3.0 and $C_\mathrm{P} / C_\mathrm{L} = 16 \pm 2$ at pH 4.5 by linear interpolation of our experimental data. These values show that PVP has a greater affinity for TPPS at pH 4.5 compared to pH 3.0. Furthermore, the value obtained at pH 7.0 is $C_\mathrm{P} / C_\mathrm{L} = 14 \pm 2$. This implies that the PVP affinity to TPPS found at pH 4.5 is equal or just slightly smaller than that found at pH 7.0.

At any calculated α we determined the corresponding concentration of unbound TPPS, $[\mathrm{L}]_\mathrm{unb}$. Note that this is the total concentration of all monomeric and aggregated porphyrin in solution. In the limit of $[\mathrm{L}]_\mathrm{unb} \to 0$, this concentration becomes equal to that of monomeric porphyrin, $[\mathrm{L}]$. To calculate $[\mathrm{L}]_\mathrm{unb}$, we used

$$[\mathrm{L}]_\mathrm{unb} = (1-\alpha)C_\mathrm{L} \tag{9. 2}$$

The number of porphyrin molecules bound per polymer, ν, can be also linked to α using the following expression (see Chapter 8):

$$\nu = \alpha \frac{C_\mathrm{L}}{C_\mathrm{P}} \tag{9. 3}$$

In Figure 59, we show ν as a function of $[\mathrm{L}]_\mathrm{unb}$ at the three investigated pH values. Note that the experimental points at low $[\mathrm{L}]_\mathrm{unb}$ correspond to high $C_\mathrm{P} / C_\mathrm{L}$ values in Figure 57 and Figure 58. In Figure 59, we observe that ν increases with pH at constant $[\mathrm{L}]_\mathrm{unb}$. Note that the change in binding affinity from pH 3.0 to pH 4.5 is significantly larger than that from pH

4.5 to pH 7.0 consistent with the comparison of the $C_\mathrm{P} / C_\mathrm{L}$ values at $\alpha = 0.5$. Furthermore, at pH 3.0, we observe that ν starts decreasing at values of $[\mathrm{L}]_\mathrm{unb}$ higher than 0.04 mM. This can be explained by considering the presence of an increasing amount of J-aggregates as the polymer concentration decreases (low $C_\mathrm{P} / C_\mathrm{L}$). These aggregates contribute to the value of $[\mathrm{L}]_\mathrm{unb}$ and do not participate in the PVP-TPPS binding process.

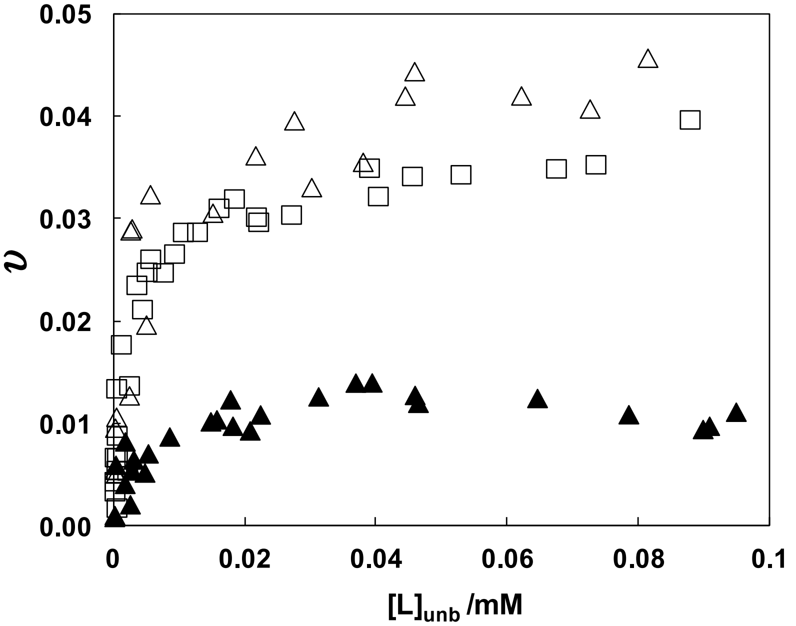

Figure 59. Number of porphyrin molecules bound per polymer, ν, as a function of free ligand concentration [L] at pH 7.0 (open triangles), 4.5 (open squares) and 3.0 (closed triangles).

9.4. Conclusions

Our spectrophotometric data shows that PVP-TPPS binding occurs at neutral and acidic pH. Furthermore, the comparison between the spectra for PVP+TPPS solutions at three different pH values of 7.0, 4.5, 3.0 and in the presence of PVP excess shows that the porphyrin bound state is independent of pH.

The shape of the spectra obtained in excess of PVP suggests that the chemical state of bound TPPS is closely related to the free base porphyrin.

Chapter 10: Summary

The objective of the second part of this dissertation was to investigate polymer–porphyrin binding in aqueous solutions. In Chapter 8, we focused on the thermodynamic characterization of supramolecular PVP-TPPS structures in aqueous solution at pH 7.0 by ITC. These supramolecular structures, which have a maximum molecular weight ≈50% higher than that of the PVP scaffold, are obtained in the presence of TPPS concentrations of the order of 10 μM or higher. ITC, compared to spectroscopic techniques, provides two independent means to determine reaction enthalpies: direct measurements and Van't Hoff plot. In our case, the comparison of the Van't Hoff plot obtained from equilibrium constants to that calculated from experimental reaction enthalpies was used to show that TPPS self-association is limited to the formation of dimers and that TPPS binds to PVP in its monomeric state. ITC reaction enthalpies have also allowed us to determine accurate reaction heat capacities. These were related to hydrophobic interactions. Our ITC results show that PVP-TPPS binding is stronger than TPPS dimerization due to the difference in reaction entropy. Thermodynamic parameters were used to extract the normalized absorption spectra of monomeric, dimeric and bound states of TPPS. The observed spectral shifts in the two Q_x bands can be explained by considering that the two hydrogens in the central porphyrin bind to the PVP oxygens.

In Chapter 9, we focused on the effect of pH on the spectrophotometric properties of TPPS in the presence of PVP. Specifically the TPPS absorption spectra obtained at pH 7.0 were compared with those obtained at pH 3.0 and pH 4.5. The absorption spectrum of TPPS is significantly affected by pH in the absence of PVP, due to the acid-base properties of TPPS. On the other hand, the TPPS spectrum becomes independent of pH in the presence of sufficient PVP to produce TPPS-PVP supramolecular nanostructures.

This work not only provides valuable information on thermodynamic stability of polymer-porphyrin supramolecular nanostructures, but it also delivers general strategies for the thermodynamic characterization of complex reaction equilibria in solution based on ITC. Further work is needed for understanding the thermodynamic behavior of TPPS+PVP aqueous solutions in acidic conditions. This has to take into account not only TPPS-PVP binding but also TPPS self-association, including the formation of larger J-aggregates, and chemical equilibrium among FBP, DAP and MAP. Fluorescence properties of TPPS-PVP systems must be also characterized. This information is valuable for the application of these systems to photodynamic therapy. Here, it will be important to examine how TPPS-PVP binding, the reduced porphyrin mobility[183] and the intrinsic fluorescence of PVP, which has been recently discovered[183], affect fluorescence intensity, fluorescence quantum yield and ultimately the capability of TPPS-PVP systems to produce excited singlet oxygen through intersystem crossing. These supramolecular systems can be further improved if they can selectively target tumor tissues. This can be achieved by preparing PVP chains that are partially functionalized with tumor-specific target ligands such as folic acid[184].

Finally, we observe that the method discussed in Chapter 4 for the formation of dendrimer globular nanoparticles can be also extended to TPPS-PVP systems. Specifically, salting-out agents such as Na_2SO_4 may be used to bring about LLPS of PVP aqueous sytstems. PVP crosslinking can then be coupled to LLPS to produce PVP-TPPS nanogels.

References

(1) Liu, C.; Lomakin, A.; Thurston, G. M.; Hayden, D.; Pande, A.; Pande, J.; Ogun, O.; Asherie, N.; Benedek, G. B. *J. Phys. Chem.* **1995**, *99*, 454–461.

(2) Liu, C.; Asherie, N.; Lomakin, A.; Pande, J.; Ogun, O.; Benedek, G. B. *Proc. Natl. Acad. Sci. U. S. A.* **1996**, *93*, 377–382.

(3) Annunziata, O.; Ogun, O.; Benedek, G. B. *Proc. Natl. Acad. Sci. U. S. A.* **2003**, *100*, 970–974.

(4) Thomson, J. A.; Schurtenberger, P.; Thurston, G. M.; Benedek, G. B. *Proc. Natl. Acad. Sci.* **1987**, *84*, 7079–7083.

(5) Lekkerkerker, H. N. W.; Tuinier, R. *Colloids and the Depletion Interaction*; Springer: New York, 2011.

(6) Flory, P. J. *Principles of Polymer Chemistry*; Cornell University Press: Ithaca, New York, 1953.

(7) Keating, C. D. *Acc. Chem. Res.* **2011**, *45*, 2114–2124.

(8) Hatti-Kaul, R. *Mol. Biotechnol.* **2001**, *19*, 269–277.

(9) Gunton, J. D.; Shiryayev, A.; Pagan, D. L. *Protein Condensation: Kinetic Pathways to Crystallization and Disease*; Cambridge University Press: Cambridge, 2007.

(10) McPherson, A. *Crystallization of Biological Macromolecules*, 1st ed.; Cold Spring Harbor Laboratory Press: New York, 1999.

(11) Shultz, A. R.; Flory, P. J. *J. Am. Chem. Soc.* **1952**, *73*, 4760–4767.

(12) Elbert, D. L. *Acta Biomater.* **2011**, *7*, 31–56.

(13) Wang, Y.; Annunziata, O. *Langmuir* **2008**, *24*, 2799–2807.

(14) Lima, A. C.; Sher, P.; Mano, J. F. *Expert Opin. Drug Deliv.* **2012**, *9*, 231–248.

(15) Nichols, M. D.; Scott, E. A.; Elbert, D. L. *Biomaterials* **2009**, *30*, 5283–5291.

(16) Willauer, H. D.; Huddleston, J. G.; Rogers, R. D. *Ind. Eng. Chem. Res* **2002**, *41*, 1892–1904.

(17) Albertsson, P. A. *Partition of Cell Particles and Macromolecules*; Wiley: New York, 1986.

(18) Behr, A.; Henze, G.; Schomäcker, R. *Adv. Synth. Catal.* **2006**, *348*, 1485–1495.

(19) Joo, F. *Acc. Chem. Res.* **2002**, *35*, 738–745.

(20) Bitan, G.; Kirkitadze, M. D.; Lomakin, A.; Vollers, S. S.; Benedek, G. B.; Teplow, D. B. *Proc. Natl. Acad. Sci.* **2003**, *100*, 330–335.

(21) Galkin, O.; Chen, K.; Nagel, R. L.; Hirsch, R. E.; Vekilov, P. G. *Proc. Natl. Acad. Sci.* **2002**, *99*, 8479–8483.

(22) Aprelev, A.; Weng, W.; Zakharov, M.; Rotter, M.; Yosmanovich, D.; Kwong, S.; Briehl, R. W.; Ferrone, F. A. *J. Mol. Biol.* **2007**, *369*, 1170–1174.

(23) Galkin, O.; Nagel, R. L.; Vekilov, P. G. *J. Mol. Biol.* **2007**, *365*, 425–439.

(24) Broide, M. L.; Berland, C. R.; Pande, J.; Ogun, O. O.; Benedek, G. B. *Proc. Natl. Acad. Sci. U. S. A.* **1991**, *88*, 5660–5664.

(25) Galkin, O.; Pan, W.; Filobelo, L.; Hirsch, R. E.; Nagel, R. L.; Vekilov, P. G. *Biophys. J.* **2007**, *93*, 902–913.

(26) Abbott, N. L.; Blankschtein, D.; Hatton, T. A. *Macromolecules* **1991**, *24*, 4334–4348.

(27) Abbott, N. L.; Blankschtein, D.; Hatton, T. A. *Macromolecules* **1992**, *95*, 5192–5200.

(28) Harrisson, R. G. *Protein Purification Process Engineering*; Marcel Dekker, Inc: New York, 1993.

(29) Persson, J.; Johansson, H.-O.; Tjerneld, F. *J. Chromatogr. A* **1999**, *864*, 31–48.

(30) Wang, X.; Okada, M.; Matsushita, Y.; Furukawa, H.; Han, C. C. *Macromolecules* **2005**, *38*, 7127–7133.

(31) Nephew, J. B.; Nihei, T. C.; Carter, S. A. *Phys. Rev. Lett.* **1998**, *80*, 13–16.

(32) Tran-Cong, Q.; Harada, A. *Phys. Rev. Lett.* **1996**, *76*, 4–7.

(33) Schoevaart, R.; Wolbers, M. W.; Golubovic, M.; Ottens, M.; Kieboom, A. P. G.; Rantwijk, F. Van; van der Wielen, L. A. M.; Sheldon, R. A. *Biotechnol. Bioeng.* **2004**, *87*, 754–762.

(34) Kimura, K.; Kohama, S.-I.; Yamazaki, S. *Polym. J.* **2006**, *38*, 1005–1022.

(35) Dumetz, C.; Brien, A. N. N. M. S.; Kaler, E. W.; Lenhoff, A. M. *Protein Sci.* **2007**, *16*, 1867–1877.

(36) Dumetz, A. C.; Chockla, A. M.; Kaler, E. W.; Lenhoff, A. M. *Biophys. J.* **2008**, *94*, 570–583.

(37) Galkin, O.; Vekilov, P. G. *Proc. Natl. Acad. Sci.* **2000**, *97*, 6277–6281.

(38) Muschol, M.; Rosenberger, F.; Muschol, M.; Rosenberger, F. *J. Chem. Phys.* **2013**, *107*, 1953–1962.

(39) Stradner, A.; Sedgwick, H.; Poon, W. C. K.; Egelhaaf, S. U.; Schurtenberger, P. *Nature* **2004**, *432*, 198–201.

(40) Gebauer, D.; Kellermeier, M.; Gale, J. D.; Bergstro, L. *Chem Soc Rev* **2014**, *43*, 2348–2371.

(41) Zhang, F.; Roosen-Runge, F.; Sauter, A.; Roth, R.; Skoda, M. W. A.; Jacobs, R. M. J. *Faraday Discuss.* **2012**, *159*, 313–325.

(42) Annunziata, O.; Asherie, N.; Lomakin, A.; Pande, J.; Ogun, O.; Benedek, G. B. *Proc. Natl. Acad. Sci.* **2002**, *99*, 14165–14170.

(43) Tian, H.-Y.; Yan, J.-J.; Wang, D.; Gu, C.; You, Y.-Z.; Chen, X.-S. *Macromol. Rapid Commun.* **2011**, *32*, 660–664.

(44) Amemori, S.; Kokado, K.; Sada, K. *J. Am. Chem. Soc.* **2012**, *134*, 8344–8347.

(45) Van Durme, K.; Rahier, H.; Van Mele, B. *Macromolecules* **2005**, *38*, 10155–10163.

(46) Gong, G.; Huang, Y.; Macknight, W. J.; Karasz, F. E. *Macromolecules19* **1986**, *19*, 2765–2770.

(47) Mori, T.; Nakashima, M.; Fukuda, Y.; Minagawa, K.; Tanaka, M.; Maeda, Y. *Langmuir* **2006**, *22*, 4336–4342.

(48) Zhang, Y.; Furyk, S.; Bergbreiter, D. E.; Cremer, P. S. *J. Am. Chem. Soc.* **2005**, *127*, 14505–14510.

(49) Koningsveld, R.; Stockmayer, W. H.; Nies, E. *Polymer Phase Diagrams. A textbook*; Oxford University Press: New York, 2008.

(50) Qian, C.; Mumby, S. J.; Eichinger, B. E. *Macromolecules* **1991**, *24*, 1655–1661.

(51) Solc, K. *J. Phys. Chem.* **1992**, *96*, 4056–4068.

(52) Liu, X.-Y.; Mu, X.-R.; Liu, Y.; Liu, H.-J.; Chen, Y.; Cheng, F.; Jiang, S.-C. *Langmuir* **2012**, *28*, 4867–4876.

(53) Bosman, A. W.; Janssen, H. M.; Meijer, E. W.; Bosman, A. W.; Janssen, H. M.; Meijer, E. W. *Chem. Rev* **1999**, *99*, 1665–1688.

(54) Tomalia, D. A.; Naylor, A. M.; Goddard, W. A. *Angew. Chemie Int. Ed.* **1990**, *29*, 138–175.

(55) Boas, U.; Christensen, J. B.; Heegaard, P. M. H. *J. Mater. Chem.* **2006**, *16*, 3785–3798.

(56) Astruc, D.; Boisselier, E.; Ornelas, C. *Chem. Rev.* **2010**, *110*, 1857–1959.

(57) Caminade, A.; Ouali, A.; Majoral, J.; Caminade, A. *Chem Soc Rev* **2012**, *41*, 4113–4125.

(58) Crooks, R. M.; Zhao, M.; Sun, L.; Chechik, V.; Yeung, L. K. *Acc. Chem. Res.* **2001**, *34*, 181–190.

(59) Scott, R. W. J.; Wilson, O. M.; Crooks, R. M. *J. Phys. Chem. B* **2005**, *109*, 692–704.

(60) Astruc, D. *Nat. Chem.* **2012**, *4*, 255–267.

(61) Diallo, M. S.; Christie, S.; Swaminathan, P.; Johnson, J. H.; Goddard, W. A. *Environ. Sci. Technol.* **2005**, *39*, 1366–1377.

(62) Lee, C. C.; MacKay, J. a; Fréchet, J. M. J.; Szoka, F. C. *Nat. Biotechnol.* **2005**, *23*, 1517–1526.

(63) Fischer, M.; Vogtle, F. *Angew. Chemie Int. Ed.* **1999**, *38*, 884–905.

(64) Kaminskas, L. M.; McLeod, V. M.; Porter, C. J. H.; Boyd, B. J. *Mol. Pharm.* **2012**, *9*, 355–373.

(65) Boas, U.; Heegaard, P. M. H. *Chem. Soc. Rev.* **2004**, *33*, 43–63.

(66) Tomalia, D. A. *Mater. Today* **2005**, *8*, 34–46.

(67) Maiti, P. K.; Çağın, T.; Wang, G.; Goddard, W. A. *Macromolecules* **2004**, *37*, 6236–6254.

(68) Tomalia, D. A.; Baker, H.; Dewald, J.; Hall, M.; Kallos, G.; Martin, S.; Roeck, J.; Ryder, J.; Smith, P. *Polym. J.* **1985**, *17*, 117–132.

(69) Svenson, S.; Tomalia, D. A. *Adv. Drug Deliv. Rev.* **2005**, *57*, 2106–2129.

(70) Esfand, R.; Tomalia, D. A. *DDT* **2001**, *6446*, 427–436.

(71) Lim, J.; Kostiainen, M.; Maly, J.; da Costa, V. C. P.; Annunziata, O.; Pavan, G. M.; Simanek, E. E. *J. Am. Chem. Soc.* **2013**, *135*, 4660–4663.

(72) Stechemesser, S.; Eimer, W. *Macromolecules* **1997**, *30*, 2204–2206.

(73) Liu, Y.; Bryantsev, V. S.; Diallo, M. S.; Goddard, W. A. *J. Am. Chem. Soc.* **2009**, *131*, 2798–2799.

(74) Nourse, A.; Millar, D. B.; Minton, A. P. *Biopolymers* **2000**, *53*, 316–328.

(75) Welch, P.; Muthukumar, M. *Macromolecules* **1998**, *31*, 5892–5897.

(76) Maiti, P. K.; Çağın, T.; Lin, S.-T.; Goddard, W. A. *Macromolecules* **2005**, *38*, 979–991.

(77) Muratt, M.; Grest, G. S. *Macromolecules* **1996**, *29*, 1278–1285.

(78) Topp, A.; Bauer, B. J.; Tomalia, D. A.; Amis, E. J. *Macromolecules* **1999**, *32*, 7232–7237.

(79) Lee, I.; Athey, B. D.; Wetzel, A. W.; Meixner, W.; Baker, J. R. *Macromolecules* **2002**, *35*, 4510–4520.

(80) Maiti, P. K.; Goddard, W. A. *J. Phys. Chem. B* **2006**, *110*, 25628–25632.

(81) Parrott, M. C.; Valliant, J. F.; Adronov, A. *Langmuir* **2006**, *22*, 5251–5255.

(82) Koga, T.; Iimura, M.; Higashi, N. *Macromol. Biosci.* **2012**, *12*, 1043–1047.

(83) Shen, Y.; Ma, X.; Zhang, B.; Zhou, Z.; Sun, Q.; Jin, E.; Sui, M.; Tang, J.; Wang, J.; Fan, M. *Chemistry* **2011**, *17*, 5319–5326.

(84) Jia, Z.; Chen, H.; Zhu, X.; Yan, D. *J. Am. Chem. Soc.* **2006**, *128*, 8144–8145.

(85) Li, W.; Zhang, A.; Chen, Y.; Feldman, K.; Wu, H.; Schlüter, A. D. *Chem. Commun.* **2008**, *45*, 5948–5950.

(86) Haba, Y.; Harada, A.; Takagishi, T.; Kono, K. *J. Am. Chem. Soc.* **2004**, *126*, 12760–12761.

(87) Kojima, C.; Yoshimura, K.; Harada, A.; Sakanishi, Y.; Kono, K. *J. Polym. Sci. Part A Polym. Chem.* **2010**, *48*, 4047–4054.

(88) Lue, L.; Prausnitz, J. M. *Macromolecules* **1997**, *30*, 6650–6657.

(89) Rissanou, A. N.; Economou, I. G.; Panagiotopoulos, A. Z. *Macromolecules* **2006**, *39* (18), 6298–6305.

(90) Jang, J. G.; Noh, S.; Bae, Y. C. *J. Phys. Chem. A* **2000**, *104*, 7404–7407.

(91) Migneault, I.; Dartiguenave, C.; Bertrand, M. J.; Waldron, K. C. *BioTecniques* **2004**, *37*, 370–802.

(92) Wang, Y. Protein Condensation in Crowded Aqueous Solutions, Texas Christian University, 2008.

(93) Levine, I. N. *Physical Chemistry*, 6th ed.; The McGraw-Hill Companies, Inc.: New York, 2009.

(94) Annunziata, O. *J. Phys. Chem. B* **2008**, *112*, 11968–11975.

(95) Lomakin, A.; Asherie, N.; Benedek, G. B. *J. Chem. Phys.* **1996**, *104*, 1646–1656.

(96) Hansen, J.-P.; McDonald, I. R. *Theory of Simple Liquids*, 4th ed.; Academic Press: Oxford, 2013.

(97) Asherie, N. R. The Phase Diagram of Globular Protein Solutions: the Role of the Range of Interaction, MIT, 1998.

(98) Carnahan, N. F.; Starling, K. E. *J. Chem. Phys.* **1969**, *51*, 635.

(99) Zhang, Y.; Cremer, P. S. *Proc. Natl. Acad. Sci.* **2009**, *106*, 15249–15253.

(100) Zhang, Y.; Cremer, P. S. *Curr. Opin. Chem. Biol.* **2006**, *10*, 658–663.

(101) Zhang, Y.; Cremer, P. S. *Annu. Rev. Phys. Chem.* **2010**, *61*, 63–83.

(102) Flores, S. C.; Kherb, J.; Cremer, P. S. *J. Phys. Chem. C* **2012**, *116*, 14408–14413.

(103) Cho, Y.; Zhang, Y.; Christensen, T.; Sagle, L. B.; Chilkoti, A.; Cremer, P. S. *J. Phys. Chem. B* **2008**, *112*, 13765–13771.

(104) Zhang, Y.; Furyk, S.; Sagle, L. B.; Cho, Y.; Bergbreiter, D. E.; Cremer, P. S. *J. Phys. Chem. C* **2007**, *111*, 8916–8924.

(105) Lund, M.; Jungwirth, P. *J. Phys. Condens. Matter* **2008**, *20*, 1–4.

(106) Bostro, M.; Tavares, F. W.; Finet, S.; Skouri-Panet, F.; Tardieu, A.; Ninham, B. W. *Biophys. Chem.* **2005**, *117*, 217–224.

(107) Curtis, R. A.; Ulrich, J.; Montaser, A.; Prausnitz, J. M.; Blanch, H. W. *Biotechnol. Bioeng.* **2002**, *79*, 367–380.

(108) Hey, M.; Jackson, D.; Yan, H. *Polymer* **2005**, *46*, 2567–2572.

(109) Record, M. T.; Anderson, C. F. *Biophys. J.* **1995**, *68*, 786–794.

(110) Parsegian, V. A.; Rand, R. P.; Rau, D. C. *Proc. Natl. Acad. Sci.* **2000**, *97*, 3987–3992.

(111) McAfee, M. S.; Zhang, H.; Annunziata, O. *Langmuir* **2014**, *30*, 12210–12219.

(112) Timasheff, S. N. *Proc. Natl. Acad. Sci.* **2002**, *99*, 9721–9726.

(113) Arakawa, T.; Timasheff, S. N. *Meth. Enzym.* **1985**, *114*, 49-77.

(114) Rard, J. A.; Albright, J. G.; Miller, D. G.; Zeidler, M. E.; Worth, F. *J. Chem. Soc., Faraday Trans.* **1996**, *92*, 4187–4197.

(115) Zhao, M.; Sun, L.; Crooks, R. M. *J. Am. Chem. Soc.* **1998**, *120*, 4877–4878.

(116) Pecora, R. *Dynamic Light Scattering: Applications of Photon Correlation Spectroscopy*; Plenum Press: New York, 1985.

(117) Lomakin, A.; Teplow, D. B.; Benedek, G. B. In *Methods in Molecular Biology*; Humana Press Inc.: Totowa, NJ.

(118) Tyrell, H. J. V.; Harris, K. R. *Diffusion in Liquids: A theoretical and experimental study*; Butterworth & Co: London, 1984.

(119) Serdyuk, I. N.; Zaccai, N. R.; Zaccai, J. *Methods in Molecular Biophysics*; Cambridge University Press: Cambridge, 2007.

(120) da Costa, V. C. P.; Hwang, B. J.; Eggen, S. E.; Wallace, M. J.; Annunziata, O. *J. Chem. Thermodyn.* **2014**, *75*, 119–127.

(121) Richter-Egger, D. L.; Landry, J. C.; Tesfai, A.; Tucker, S. A. *J. Phys. Chem. A* **2001**, *105* (28), 6826–6833.

(122) Kline, K. K.; Morgan, E. J.; Norton, L. K.; Tucker, S. A. *Talanta* **2009**, *78*, 1489–1491.

(123) Pethig, R. *Annu. Rev. Phys. Chem* **1992**, *43*, 177–205.

(124) Korosi, A.; Fabuss, B. M. *J. Chem. Eng. Data* **1968**, *13*, 548–552.

(125) Muschol, M.; Rosenberger, F. *J. Chem. Phys.* **1995**, *103*, 10424–10432.

(126) Fine, B. M.; Lomakin, A.; Ogun, O. O.; Benedek, G. B. *J. Chem. Phys.* **1996**, *104*, 326–335.

(127) Rard, J. A.; Clegg, S. L.; Palmer, D. A. *J. Sol. Chem.* **2000**, *29*, 1–49.

(128) Mansoori, G. A.; Carnahan, N. F.; Starling, K. E.; Leland Jr, T. W. *J. Chem. Phys.* **1971**, *54*, 1523–1525.

(129) Amokrane, S.; Regnaut, C. *Phys. Rev. E Stat. Phys., Plasmas, Fluids, Relat. Interdiscip. Top.* **1996**, *53*, 1990–1993.

(130) Li, P.; Banjade, S.; Cheng, H. C.; Kim, S.; Chen, B.; Al., E. *Nature* **2012**, *483*, 336–340.

(131) Pusey, P. N.; wan Megen, W. *Nature* **1986**, *320*, 264–265.

(132) Niu, Y.; Sun, L.; Crooks, R. M. *Macromolecules* **2003**, *36*, 5725–5731.

(133) Annunziata, O.; Paduano, L.; Pearlstein, A. J.; Miller, D. G.; Albright, J. G. *J. Phys. Chem. B* **2006**, *110*, 1405–1415.

(134) Buzatu, D.; Annunziata, O.; Petrescu, E.; Popa, C.; Buzatu, F. D. *J. Optoelectron. Adv. Mater.* **2005**, *7*, 3161–3168.

(135) Kadish, K. M.; Smith, K. M.; Guilard, R. *The Porphyrin Handbook*; Academic Press: New York, 1999.

(136) Gharib, F.; Soleimani, F.; Farajtabar, A.; Aghaei, H. *J. Chem. Eng. Data* **2009**, *54*, 2060–2066.

(137) Farajtabar, A.; Gharib, F.; Jamaat, P.; Safari, N. *J. Chem. Eng. Data* **2008**, *53*, 350–354.

(138) Král, V.; Králová, J.; Kaplánek, R.; Bríza, T.; Martásek, P. *Physiol. Res.* **2006**, *55*, 3–26.

(139) Medforth, C. J.; Wang, Z.; Martin, K. E.; Song, Y.; Jacobsen, J. L.; Shelnutt, J. A. *Chem. Commun.* **2009**, *47*, 7241–7428.

(140) Beletskaya, I.; Tyurin, V. S.; Tsivadze, A. Y.; Guilard, R.; Stern, C. *Chem. Rev.* **2009**, *109*, 1659–1713.

(141) Dolphin, D. *The Porphyrins*; Academic Press: New York, 1978.

(142) Drain, C. M.; Varotto, A.; Radivojevic, I. *Chem. Rev.* **2009**, *109*, 1630–1658.

(143) Kobayashi, T. *J-Aggregates*; World Scientific Publishing Co: Singapore, 2012.

(144) Li, L.-L.; Diau, E. W.-G. *Chem. Soc. Rev.* **2013**, *42*, 291–304.

(145) Monti, D.; Nardis, S.; Stefanelli, M.; Paolesse, R.; Di Natale, C.; D'Amico, A. *J. Sensors* **2009**, *2009*, 1–10.

(146) Nyman, E. S.; Hynninen, P. H. *J. Photochem. Photobiol. B Biol.* **2004**, *73*, 1–28.

(147) Sternberg, E. D.; Dolphin, D.; Brickner, C. *Tetrahedron* **1998**, *54*, 4151–4202.

(148) Sortino, S.; Mazzaglia, A.; Monsù Scolaro, L.; Marino Merlo, F.; Valveri, V.; Sciortino, M. T. *Biomaterials* **2006**, *27*, 4256–4265.

(149) Bonnett, R. *Chem. Soc. Rev.* **1995**, 19–33.

(150) Ethirajan, M.; Chen, Y.; Joshi, P.; Pandey, R. K. *Chem. Soc. Rev.* **2011**, *40*, 340–362.

(151) Berg, K.; Selbo, P. K.; Weyergang, A.; Dietze, A.; Prasmickaite, L.; Bonsted, A.; Engesaeter, B.; Angell-Petersen, E.; Warloe, T.; Frandsen, N.; Høgset, A. *J. Microsc.* **2005**, *218* (2), 133–147.

(152) Macdonald, I. J.; Dougherty, T. J. *J. Porphyrins Phthalocyanines* **2001**, *5*, 105–129.

(153) DeRosa, M. C.; Crutchley, R. J. *Coord. Chem. Rev.* **2002**, *233-234*, 351–371.

(154) Gouterman, M. *J. Chem. Phys.* **1959**, *30*, 1139–1161.

(155) Gouterman, M.; Wagnière, G. H. *J. Mol. Spectrosc.* **1963**, *11*, 108–127.

(156) Gouterman, M. *J. Mol. Spectrosc.* **1961**, *6*, 138–163.

(157) Hashimoto, T.; Choe, Y.-K.; Nakano, H.; Hirao, K. *J. Phys. Chem. A* **1999**, *103*, 1894–1904.

(158) Aggarwal, L. P. F.; Borissevitch, I. E. *Spectrochim. Acta. A. Mol. Biomol. Spectrosc.* **2006**, *63*, 227–233.

(159) Levine, I. N. *Quantum Chemistry*; Prentice-Hall: New Jersey, 1999.

(160) Pasternack, R. F.; Huber, P. R.; P, B.; Engasser, G.; Francesconi, L.; Gibbs, E.; Fasella, P.; Cerio Venturo, G. *J. Am. Chem. Soc.* **1971**, *669*, 4511–4517.

(161) Ribo, J. M.; Crusats, J.; Farrera, J.; Valero, M. L. *J. Am. Chem. Soc. Chem. Commun.* **1994**, *7*, 681–682.

(162) Rubires, R.; Crusats, J.; El-hachemi, Z.; Jaramillo, T.; Lo, M.; Valls, E.; Farrera, J.-A.; Ribo, J. M. *New J. Chem.* **1999**, 189–198.

(163) Hollingsworth, J. V; Richard, A. J.; Grac, M.; Vicente, H.; Russo, P. S. *Biomacromolecules* **2011**, *13*, 60–62.

(164) Ohno, O.; Kaizu, Y.; Kobayashi, H. *J. Chem. Phys.* **1993**, *99*, 4128.

(165) Egawa, Y.; Hayashida, R.; Anzai, J. *Langmuir* **2007**, *23*, 13146–13150.

(166) Kano, K.; Watanabe, K.; Ishida, Y. *J. Phys. Chem. B* **2008**, *112*, 14402–14408.

(167) Maiti, N. C.; Ravikanth, M.; Mazumdar, S.; Periasamy, N. *J. Phys. Chem.* **1995**, *99*, 17192–17197.

(168) Ribó, J. M.; Bofill, J. M.; Crusats, J.; Rubires, R. *Chem. Eur. J.* **2001**, *7*, 2733–2737.

(169) Daune, M. *Molecular Biophysics Structures in Motion*; Oxford University Press, 1999.

(170) Zhao, L.; Ma, R.; Li, J.; Li, Y.; An, Y.; Shi, L. *Biomacromolecules* **2008**, *9*, 2601–2608.

(171) Kadajji, V. G.; Betageri, G. V. *Polymers (Basel).* **2011**, *3*, 1972–2009.

(172) van Holde, K. E. *Physical Biochemistry*; Prentice-Hall: Englewood Clifs, NJ, 1985.

(173) Vippagunta, S. R.; Dorn, A.; Ridley, R. G.; Vennerstrom, J. L. *Biochim. Biophys. Acta* **2000**, *1475*, 133–140.

(174) Manna, B. K.; Sen, D.; Bera, S. C.; Rohatgi-Mukherjee, K. K. *Chem. Phys. Lett.* **1991**, *176*, 191–197.

(175) Draper, N. R.; Smith, H. *Applied Regression Analysis*; Wiley: New York, 1966.

(176) Martin, R. B. *Chem. Rev.* **1996**, *96*, 3043–3064.

(177) Oosawa, F. *Thermodynamics of the Polymerization of Protein*; Academic Press: Waltham, MA, 1975.

(178) Kemnitz, K.; Sakaguchi, T. *Chem. Phys. Lett.* **1992**, *196*, 497–503.

(179) Sharp, K. A.; Madan, B. *J Phys Chem B* **1997**, *5647*, 4343–4348.

(180) Yu, Y. B.; Privalov, P. L.; Hodges, R. S. *Biophys. J.* **2001**, *81*, 1632–1642.

(181) Sadeghi, R.; Zafarani-Moattar, M. T. *J. Chem. Thermodyn.* **2004**, *36*, 665–670.

(182) da Costa, V. C. P.; Ribeiro, A. C. F.; Sobral, A. J. F. N.; Lobo, V. M. M.; Annunziata, O.; Santos, C. I. a. V.; Willis, S. a.; Price, W. S.; Esteso, M. a. *J. Chem. Thermodyn.* **2012**, *47*, 312–319.

(183) Song, G.; Lin, Y.; Zhu, Z.; Zheng, H.; Qiao, J.; He, C.; Wang, H. *Macromol. Rapid Commun.* **2015**, *36*, 278−285

(184) Liang, R.; You, S.; Ma, L.; Li, C.; Tian, R.; Wei, M.; Yan, D.; Yin, M.; Yang, W.; Evans, D. G.; Duan, X. *Chem. Sci.* **2015**, *6*, 5511-5518

Appendices

Appendix A

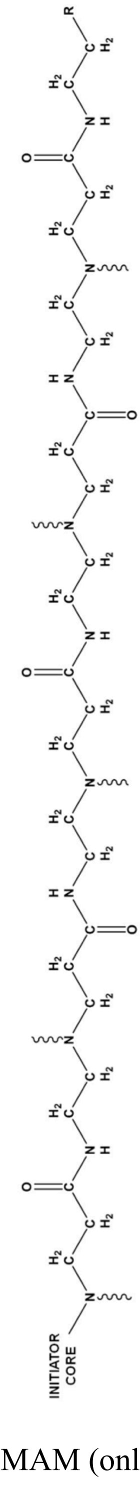

Figure A. 1. Chemical structure of PAMAM (only one branch is represented). Where the initiator core is ethylene diamine ($NH_2C_2H_4NH_2$) R is equal to –OH or $–NH_2$.

Appendix B: Experimental Data for Chapter 3

LLPS Experimental Data for Turbidity Experiments

Tables B1. LLPS temperature (T_{ph}) as a function of salt molar concentration (C_S) at several dendrimer volume fractions (ϕ_D) obtained from turbidity experiments.

Table B1a. T_{ph} at ϕ_D=0.38

ϕ_D	C_S/M	T_{ph}/°C
0.384	0.289	4.0
0.383	0.305	13.2
0.384	0.309	16.5
0.384	0.313	19.6
0.383	0.320	24.8
0.383	0.336	34.2

Table B1b. T_{ph} at ϕ_D=0.29

ϕ_D	C_S/M	T_{ph}/°C
0.292	0.372	9.4
0.291	0.374	12.5
0.291	0.377	15.0
0.291	0.378	17.8
0.291	0.380	21.8
0.291	0.385	29.8

Table B1c. T_{ph} at ϕ_D=0.27

ϕ_D	C_S/M	T_{ph}/°C
0.265	0.412	4.8
0.266	0.413	10.0
0.266	0.415	21.0
0.267	0.417	42.0

Table B1g. T_{ph} at ϕ_D=0.14

ϕ_D	C_S/M	T_{ph}/°C
0.140	0.691	36
0.142	0.690	32
0.143	0.690	28

Table B1h. T_{ph} at ϕ_D=0.084

ϕ_D	C_S/M	T_{ph}/°C
0.0834	0.806	33.2
0.0835	0.814	27.6
0.0836	0.822	22.9
0.0835	0.830	17.8
0.0835	0.837	13.8

Table B1i. T_{ph} at ϕ_D=0.049

ϕ_D	C_S/M	T_{ph}/°C
0.0492	0.958	35.4
0.0495	0.964	31.4
0.0492	0.970	28.2
0.0493	0.974	26.6
0.0493	0.978	24.4

Table B1d. T_{ph} at ϕ_D=0.24

ϕ_D	C_S/M	T_{ph}/°C
0.237	0.475	0.2
0.235	0.477	3.2
0.235	0.484	12.4
0.234	0.486	12.8

Table B1e. T_{ph} at ϕ_D=0.22

ϕ_D	C_S/M	T_{ph}/°C
0.224	0.500	-4.4
0.224	0.501	-2.0
0.223	0.504	0.8
0.223	0.507	5.0
0.223	0.508	9.2

Table B1f. T_{ph} at ϕ_D=0.21

ϕ_D	C_S/M	T_{ph}/°C
0.208	0.526	-8.0
0.208	0.527	-5.8
0.208	0.529	-2.5
0.208	0.531	-0.4

Table B1j. T_{ph} at ϕ_D=0.00126

ϕ_D	C_S/M	T_{ph}/°C
0.0125	0.994	36.8
0.0127	1.002	33.4
0.0125	1.010	30.4
0.0126	1.022	25.3
0.0127	1.026	23.0

Table B1k. T_{ph} at ϕ_D=0.0096

ϕ_D	C_S/M	T_{ph}/°C
0.0096	1.267	35.0
0.0096	1.269	34.0
0.0096	1.271	32.0
0.0097	1.271	32.0
0.0096	1.274	30.0

Table B1l. T_{ph} at ϕ_D=0.0091

ϕ_D	C_S/M	T_{ph}/°C
0.0092	1.384	32.0
0.0091	1.387	27.0
0.0091	1.392	26.0
0.0091	1.396	20.0
0.0091	1.401	19.0

ITC Experimental Data

In Table B2, we report the corresponding plot of the differential heat per mole of titrant, $q^{(k)}$, as a function of dendrimer volume fraction inside the ITC cell , $\phi_{\mathrm{D}}^{(k)}$, after injection k .

Table B2. Differential molar heat, $q^{(k)}$, associated with consecutive injections, *k*, of the titrant solution containing PAMAM-OH with volume fraction, ϕ_{D}^{0}, into the titrand solution with increasing dendrimer volume fraction, ϕ_{D}. These heat of dilution experiments were performed in aqueous salt buffer (ACES, pH7.0, 0.10M; sodium sulfate, 0.03 M; ionic strength, 0.14M) and 25.0 °C.

Table B2a. $q^{(k)}$ values at ϕ_{D}^{0}=0.191.

k	ϕ_{D}	$q^{(k)}$ / (kJ mol^{-1})	k	ϕ_{D}	$q^{(k)}$ / (kJ mol^{-1})
1	0.0019	–	11	0.0195	-2.992
2	0.0037	-3.159	12	0.0212	-2.967
3	0.0055	-3.201	13	0.0228	-2.915
4	0.0073	-3.142	14	0.0244	-2.881
5	0.0091	-3.098	15	0.0260	-2.885
6	0.0109	-3.100	16	0.0276	-2.865
7	0.0127	-3.035	17	0.0292	-2.827
8	0.0144	-3.067	18	0.0307	-2.815
9	0.0161	-3.001	19	0.0323	-2.764
10	0.0178	-3.017			

Table S2b. $q^{(k)}$ values at ϕ_{D}^{0}=0.173.

k	ϕ_{D}	$q^{(k)}$ / (kJ mol^{-1})	k	ϕ_{D}	$q^{(k)}$ / (kJ mol^{-1})
1	0.0017	–	11	0.0177	-2.560
2	0.0034	-2.830	12	0.0193	-2.624
3	0.0050	-2.817	13	0.0207	-2.576
4	0.0067	-2.774	14	0.0222	-2.507
5	0.0083	-2.740	15	0.0237	-2.438
6	0.0099	-2.710	16	0.0251	-2.402
7	0.0115	-2.692	17	0.0266	-2.433
8	0.0131	-2.670	18	0.0280	-2.421
9	0.0147	-2.613	19	0.0294	-2.259
10	0.0162	-2.575			

Table S2c. $q^{(k)}$ values at ϕ_{D}^{0}=0.130.

k	ϕ_{D}	$q^{(k)}$ / (kJ mol^{-1})
1	0.0013	–
2	0.0025	-1.690
3	0.0038	-1.681
4	0.0050	-1.711
5	0.0063	-1.683
6	0.0075	-1.628
7	0.0087	-1.626
8	0.0099	-1.648
9	0.0110	-1.619
10	0.0122	-1.556
11	0.0133	-1.538
12	0.0145	-1.546
13	0.0156	-1.567
14	0.0167	-1.577
15	0.0178	-1.489
16	0.0189	-1.505
17	0.0200	-1.486
18	0.0210	-1.422
19	0.0221	–

Table S2d. $q^{(k)}$ values at ϕ_{D}^{0}=0.103.

k	ϕ_{D}	$q^{(k)}$ / (kJ mol^{-1})
1	0.0010	–
2	0.0020	-1.181
3	0.0030	-1.219
4	0.0040	-1.207
5	0.0050	-1.141
6	0.0059	-1.113
7	0.0069	-1.135
8	0.0078	-1.167
9	0.0087	-1.097
10	0.0097	-1.104
11	0.0106	-1.087
12	0.0115	-1.072
13	0.0124	-1.021
14	0.0132	-1.049
15	0.0141	-0.990
16	0.0150	-1.012
17	0.0158	-1.020
18	0.0167	-0.995
19	0.0175	-0.944

Salt Osmotic Coefficient Data

According to[127], the salt osmotic coefficient at 25 °C is given by

$$\varphi_{\mathrm{S}}(25\,^{\circ}\mathrm{C}) = 1 - 2\frac{0.391475\,I^{1/2}}{1+1.2\,I^{1/2}} + \frac{4}{3}\frac{m_{\mathrm{S}}}{m^{0}}\left[0.011976 + 0.951276\times\exp(-2I^{1/2})\right] + \\ + \frac{16}{3}\left(\frac{m_{\mathrm{S}}}{m^{0}}\right)^{2}\left[0.0024359 + 0.236044\times\exp(-2.5\,I^{1/2})\right]$$

where $m_\mathrm{S} = \dfrac{C_\mathrm{S}^*}{M_\mathrm{W} C_\mathrm{W}^*}$ and $I = 3\,\dfrac{m_\mathrm{S}}{m^0}$.

For other temperatures, we fit the experimental data to the following empirical expression:

$$\varphi_\mathrm{S}(T) = \varphi_\mathrm{S}(25\,^\circ\mathrm{C}) + 1000\frac{m_\mathrm{S}}{m^0}\left[21.377 - 9.1906\,\frac{m_\mathrm{S}}{m^0} + 0.95293\left(\frac{m_\mathrm{S}}{m^0}\right)^2\right][(T/^\circ\mathrm{C})^{1/2} - (25/^\circ\mathrm{C})^{1/2}]$$

where T is in Celsius. In Figure B1, the plots of φ_S as a function of C_S^* at 5, 15, 25 and 37 °C show that φ_S increases with temperature at a given C_S^*.

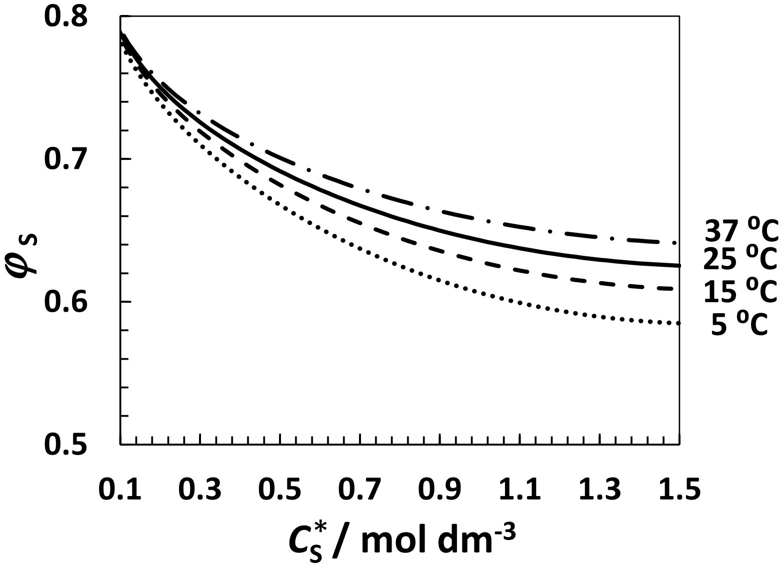

Figure B1. Osmotic coefficient for the Na_2SO_4-water system.

Diffusion Coefficient Data

Table B3. DLS dendrimer diffusion coefficient, D, as a function of dendrimer volume fraction, ϕ_D, at two salt concentrations (C_S / mol dm^{-3} = 0.044 and 0.949) and two temperatures (25.0 and 37.0 °C).

Table B3a. Values of $D/10^{-9}$ m^{2}s^{-1} at 25.0 and 37.0 °C for C_S / mol dm^{-3} =0.044.

ϕ_D	25.0 °C	37.0 °C
0.0067	0.0924	0.1248
0.0100	0.0947	0.1268
0.0149	0.0944	0.1268
0.0183	0.0945	0.1265
0.0205	0.0955	0.1293

Table B3b. Values of $D/10^{-9}$ m^{2}s^{-1} at 25.0 and 37.0 °C for C_S / mol dm^{-3} =0.044.

ϕ_D	25.0 °C	37.0 °C
0.0076	0.0562	0.0774
0.0102	0.0537	0.0733
0.0133	0.0526	0.0715
0.0169	0.0493	0.0671
0.0212	0.0463	0.0622

Appendix C: Experimental Data for Chapter 4

LLPS Experimental Data for Turbidity Experiments

Tables C1. LLPS temperature (T_{ph}) as a function of salt molar concentration (C_{S}) at several dendrimer volume fractions (ϕ_{D}) obtained from turbidity experiments.

Table C1a. T_{ph} at ϕ_{D}=0.22

ϕ_{D}	C_{S}/M	T_{ph}/°C
0.218	0.567	15.1
0.217	0.582	18.6
0.218	0.586	21.2
0.217	0.587	20.2
0.217	0.598	23.7
0.216	0.603	25.6

Table C1b. T_{ph} at ϕ_{D}=0.19

ϕ_{D}	C_{S}/M	T_{ph}/°C
0.189	0.623	9.4
0.188	0.629	11.0
0.189	0.637	13.8
0.188	0.644	16.0
0.188	0.652	18.2
0.188	0.660	21.0
0.188	0.667	24.0
0.188	0.675	26.4

Table C1c. T_{ph} at ϕ_{D}=0.14

ϕ_{D}	C_{S}/M	T_{ph}/°C
0.143	0.817	16.8
0.144	0.826	20.2
0.143	0.833	22.5
0.144	0.845	27.0
0.144	0.854	30.6

Table C1d. T_{ph} at ϕ_{D}=0.12

ϕ_{D}	C_{S}/M	T_{ph}/°C
0.120	0.861	7.7
0.120	0.879	14.6
0.120	0.885	17.5
0.120	0.893	21.1
0.119	0.909	25.3
0.120	0.914	28.8
0.120	0.918	31.1

Table C1e. T_{ph} at ϕ_{D}=0.080

ϕ_{D}	C_{S}/M	T_{ph}/°C
0.0798	0.965	2.4
0.0799	0.981	7.5
0.0797	0.988	11.1
0.0796	0.996	13.3
0.0797	1.004	17.2
0.0797	1.013	20.5
0.0796	1.020	23.5
0.0797	1.028	27.9
0.0798	1.044	34.7

Table C1f. T_{ph} at ϕ_{D}=0.062

ϕ_{D}	C_{S}/M	T_{ph}/°C
0.0623	1.075	-5.1
0.0622	1.097	5.2
0.0622	1.106	7.9
0.0623	1.116	11.6
0.0622	1.121	14.4

Table C1g. T_{ph} at ϕ_{D}=0.049

ϕ_{D}	C_{S}/M	T_{ph}/°C
0.0489	1.125	3.0
0.0489	1.133	5.6
0.0489	1.149	12.0
0.0489	1.156	15.4
0.0490	1.164	19.0
0.0490	1.180	26.2

LLPS Experimental Data for the Binodal Curve

Linear fits through turbidity data were used to calculate binodal data at four representative temperatures. Calculated values are reported in Table S2 together with the corresponding slopes, $(\partial C_{\text{S}} / \partial \phi_{\text{D}})_T$, extracted by assuming that C_{S} linearly varies with ϕ_{D}.

Table C2. Binodal data.

T_{ph}/°C	5	15	25	35
ϕ_{D}	C_{S}/M	C_{S}/M	C_{S}/M	C_{S}/M
0.217	0.635	0.602	0.568	0.534
0.188	0.702	0.671	0.641	0.610
0.144	0.866	0.839	0.812	0.785
0.120	0.930	0.905	0.879	0.854
0.080	1.047	1.022	0.998	0.974
0.062	1.171	1.147	1.123	1.099
0.049	1.201	1.178	1.155	1.131
$(\partial C_{\text{S}} / \partial \phi_{\text{D}})_T$/M	-3.41±0.16	-3.46±0.15	-3.52±0.15	-3.58±0.14

ITC Experimental Data

In Table C3, we report the corresponding plot of the differential heat per mole of titrant, $q^{(k)}$, as a function of the dendrimer volume fraction inside the ITC cell ,$\phi_{\text{D}}^{(k)}$, after injection k.

Table C3. $q^{(k)}$ values at ϕ_{D}^{0}=0.095 and 25.0 °C.

k	$\phi_{\mathrm{D}}^{(k)}$	$q^{(k)}$ / (kJ mol^{-1})
13	0.978	-5.89
14	1.048	-5.65
15	1.117	-5.46
16	1.185	-5.16
17	1.253	-4.96
18	1.319	-4.75
19	1.385	-4.57

Salt Osmotic Coefficient Data

See Appendix B for equations.

.In Figure C.1, the plots of φ_{S} as a function of C_{S}^{*} at 5, 15, 25 and 35 °C show that φ_{S} increases with temperature at a given C_{S}^{*}.

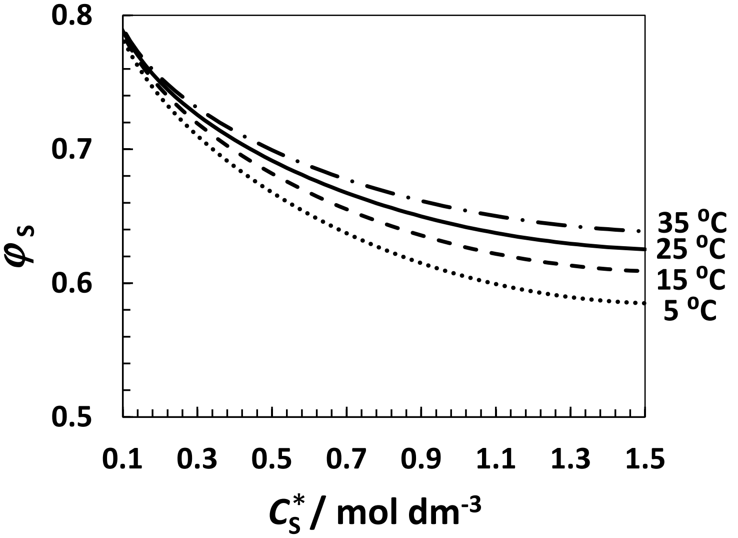

Figure C.1 Osmotic coefficient for the Na_2SO_4-water system.

VITA

Viviana Cecília Pereira da Costa was born November 22, 1982, in Tarouca, Viseu, Portugal. She is the daughter of Fernando Vasco Pinto Ribeiro da Costa and Anália de Almeida Pereira da Costa. A 2000 graduate of Escola Secundária da Sé, Lamego, Viseu, Portugal, she received a *Licenciatura* in Chemical Engineering from the University of Coimbra, Coimbra, Portugal, in 2005.

After receiving her *Licenciatura* she joined the department of Chemical Engineering from the University of Coimbra, Portugal, in 2007, as a scientific researcher. During this time, she enrolled in graduate studies at the University of Coimbra, Portugal, where she received, in 2009, her Master of Science degree in Chemical Engineering.

In August 2010, she enrolled in the chemistry Ph.D. program at Texas Christian University, Fort Worth, Texas, where she worked on her doctorate in Chemistry under supervision of Dr. Onofrio Annunziata and served as a graduate teaching assistant for four semesters. She won 1st place for the best graduate research poster in chemistry, in 2012, at the Michael and Sally McCracken Annual Student Research Symposium and the graduate student teaching award, in 2015, from the College of Science and Engineering at Texas Christian University. She is a member of the American Chemical Society.

ABSTRACT

STUDIES OF PHASE BEHAVIOR AND HOST-GUEST BINDING IN AQUEOUS SYSTEMS CONTAINING MACROMOLECULES

by Viviana Cecília Pereira da Costa, Ph.D., 2015
Department of Chemistry
Texas Christian University

Dissertation Advisor: Onofrio Annunziata, Associate Professor of Chemistry

The two dissertation goals were to investigate 1) liquid-liquid phase separation (LLPS) of dendrimer solutions and 2) thermodynamic stability of polymer-porphyrin supramolecular structures in solutions.

LLPS is important in separation and materials science. However, no experimental studies have been reported on LLPS of dendrimer solutions. Dendrimers are hyperbranched macromolecules that find applications in these fields. We focused on the LLPS of aqueous solutions of poly(amido amine) dendrimers of forth generation with hydroxyl- (PAMAM-OH) and amino- (PAMAM-NH2) functionality. LLPS was observed in the presence of sodium sulfate. In the case of PAMAM-OH, LLPS switches from being induced by cooling to being induced by heating as the salt concentration increases while, in the case of PAMAM-NH2, LLPS is observed by cooling only. To explain our findings, a thermodynamic model based on two parameters, describing dendrimer-dendrimer interaction energy and salt salting-out strength, was developed. This model successfully describes the observed LLPS behavior including the unusual thermal behavior of PAMAM-OH. We showed that coupling dendrimer oligomerization with LLPS leads to the formation of

globular dendrimer nanoparticles. This provides the basis for the preparation of nanoparticles of low-generation dendrimers, which may circumvent the need of preparing high-generation dendrimers.

Porphyrin optical properties can be tuned through polymer-porphyrin host-guest binding in solution, giving rise to the formation of supramolecular structures. The formation, thermodynamic stability and spectroscopic properties of polymer-porphyrin supramolecular structures and their competition with porphyrin self-association were investigated by isothermal titration calorimetry (ITC) and absorption spectroscopy. Reaction enthalpies and equilibrium constants were measured for meso-tetrakis(4-sulfonatophenyl) porphyrin (TPPS) self-association and TPPS binding to poly(vinylpyrrolidone) (PVP) in aqueous solutions at pH 7 and three temperatures (12-37°C). ITC provides two independent means to determine reaction enthalpies: direct measurements and Van't Hoff plot. This was used to assess that self-association of TPPS is limited to the formation of dimers and TPPS binds to PVP in its monomeric state. TPPS dimerization and PVP-TPPS supramolecular structures are enthalpically driven. However, polymer-porphyrin binding was found to be entropically favored compared to dimerization. Finally, we show that TPPS spectrophotometric properties become independent of pH in the presence of a large excess of PVP.